Characterization of Laser-Induced Plasmas with Terahertz Pulses

by

Aran J. N. McDowell

A thesis submitted in partial fulfillment of the requirements for the degree of
Master of Science

Department of Physics
University of Alberta

Abstract

Laser-induced breakdown spectroscopy (LIBS) is a method of material analysis used to determine the composition of a sample by ablating it with an ultrafast laser pulse. By monitoring the light emission from the resulting plasma, the elemental composition of the sample and the concentration of constituents can be determined from the spectral emission lines. This makes it suitable for industrial applications where quick-standoff detection of constituents is required, such as in agriculture. However, matrix effects arising from the water content in soils complicate LIBS analysis for agricultural applications, making it more difficult to determine constituent concentrations from the spectral lines. Proper calibration of the LIBS spectra requires information regarding the water content. A possible optical means by which to isolate water content is to use terahertz (THz) frequency band pulses. This is because water molecule vibrational and rotational modes oscillate at THz frequencies and are attenuated by the presence of water. In addition to possible applications as a probe for water content in soil samples, it could also be possible to provide a direct means to measure plasma conductivity with picosecond resolution. Thus, a hybrid THz-LIBS approach could provide both water content information, plasma conductivity with picosecond resolution, and elemental composition.

In this thesis, the feasibility of using terahertz (THz) pulses to study laser-induced breakdown plasmas (LIBPs) produced in LIBS is investigated. Two approaches were used in this work, the first being a transmissive approach (i.e., THz pulse is sent through the plasma plume) and the second being an emissive approach (i.e., THz emission from a plasma plume is monitored). Plasma formation in both cases was achieved using a copper (Cu) ring that was ablated using a Ti:Sapphire laser of wavelength, $\lambda = 795$ nm, a pulse-width, $\tau_p = 70$ fs, and typical pulse energies of $E_p \approx 200\,\mu$J. Both approaches were tested first using photoexcited (PE) semiconductors, as photoexcitation of a semiconductor results in the formation of an electron-hole plasma (EHP) which has analogous behavior to the space-charge separation in LIBPs. This benchmarked the two approaches.

While a measurable $\Delta\mathcal{T}/\mathcal{T}_0$ was observed for the case of a PE semiconductor EHP, there was no discernible $\Delta\mathcal{T}/\mathcal{T}_0$ detected for the Cu-LIBP plume. The reason for this is the difficulty encountered synchronizing the THz pulse arrival with Cu-LIBP evolutionary timescales. The emissive approach yielded THz emission in both the photoexcited semiconductor EHP and the femtosecond (fs) ablated Cu cases. To eliminate the possibility that the THz emission in the latter was from a bulk nonlinear process (e.g., optical rectification), the Cu sample was oriented to be at normal incidence with respect to the oncoming fs-laser pulse. This resulted in subsequent frequency components vanishing, but THz emission was still observed. This indicated that most of the THz emission arises from the rapid separation and recombination of charge carriers in the plume, like the photo-Dember effect in semiconductors. To understand this effect, a general model of the charge carrier separation is proposed.

With regards to the development of a hybrid THz-LIBS approach, the results here indi-

cate that for the transmissive approach to work, proper timing between the ablation pulse arrival, the plasma plume timescales, and the THz probe needs further development. While for the emissive approach, it is yet to be determined if the water molecule vibrational and rotational mode oscillations present in the THz pulse come from the ambient environment, the sample, or both. If it solely comes from the ambient environment, the emissive approach for THz-LIBS is non-viable. However, if it is from the latter two, the emissive approach is potentially viable. Future experiments are proposed for both approaches.

Preface

This thesis is an original work by Aran J. N. McDowell

This work is supported by Alberta Innovates through the Smart Agriculture and Food Digitalization and Automation Challenge (Agreement No. 202100740). This thesis was done under the supervision of Frank Hegmann in the Department of Physics and Amina Hussein in the Department of Electrical and Computer Engineering at the University of Alberta.

Dr. Richard Sydora advised me on how to incorporate collisional scattering into the simulation results shown in fig. 2.4-2.6.

Dr. Bandyopadhay from the Indian Institute of Technology at New Dehli first introduced the possibility of adopting an emissive rather than transmissive approach to the THz spectroscopy. Dr. Frank Hegmann suggested varying the orientation of the Cu sample.

I designed both the transmissive and emissive experiments. Setup was aided by Jesus "Alex" Alejandro Marin Calzada and Charles Jensen. Jesus "Alex" Alejandro Marin Calzada trained me on the LabVIEW program used to interface between the lock-in amplifier, the photoconductive antennae, and the electro-mechanical delay stage.

Charles Jensen brought to my attention the work of Gao et al., which was instrumental in motivating the emissive terahertz spectroscopy approach. In addition to this, many of the measurements specifically the spectral emission, terahertz pulse characterization, photoexcitation/ablation pulse characterization, and the transmissive measurements were performed with help from Charles Jensen. At many points he has also helped in alignment of the laser and experimental setup. The convolution model for the space-charge separation was motivated in part by a private discussion I had with Charles Jensen.

I performed the emissive THz measurements for the photoexcited semiconductors.

I performed the emissive THz measurements for the Cu-LIBP.

The ambient and purged terahertz pulses shown in fig. 1.2-1.3 were obtained using a lithium niobate source provided by Dr. David Purschke.

All schematics and diagrams shown in this work were made using the Inkscape Program.

I performed the analysis and interpretation of the photoluminescencent plasma spectra and photoluminescent signal duration.

I performed the analysis and interpretation of the terahertz pulse emission from the semiconductors GaAs and InAs.

I performed the analysis and interpretation of the terahertz pulse emission from the copper laser-induced breakdown plasma.

Acknowledgements

Science is a collaborative process involving many people. This thesis is no exception. I'd like to thank my supervisors Dr.'s Frank Hegmann and Amina Hussein for their feedback and criticism; forcing me to examine, re-examine and re-think what I thought I knew. To Dr. Richard Sydora I have to thank for his feedback on this thesis and for his suggestions regarding collisional effects in my simulations of the optical properties of the plasma plume. This thesis would not have been possible without the generous financial support of Alberta Innovates through the Smart Agriculture and Food Digitalization and Automation Challenge (Agreement No. 202100740).

To the members of my lab, I owe a particular debt to Charles Jensen, David Purschke, Cameron Hough, and Jesus "Alex" Alejandro Marin Calzada. To David Purschke and Cameron Hough I have to thank for teaching me the basics of ultrafast laser operation. To David Purshke in paricular, his assistance in acquiring the terahertz waveforms shown in fig.1.2-1.3 which were taken using his experimental setup. Yet most crucial of all D. Purschke reminded me to ask questions when I do not understand something. To Jesus "Alex" Alejandro Marin Calzada, I owe my knowledge to the basics of photoconductive antennae operation, lock-in amplifier operation, and the fine delay stage operation. To Charles Jensen, his timely aid in further refining my skills, allowing me to bounce ideas off of him, and assisting me in my experiments. Without C. Jensen, this work would've been delayed significantly. C. Jensen has over the course of the compilation of this work, gone above and beyond what would be expected of a senior colleague with respect to their junior.

To my collaborators in Alberta Innovates, I'd like to thank Shoubo Mohajan and Dr. Aparajita Bandyopadhyay. To Shoubo Mohajan, for clarifying my misconceptions about laser induced breakdown spectroscopy and discussion regarding laser produced plasmas. To

Dr. Bandyopadhyay, for her questions and encouragement which I needed at a critical juncture of my Master's thesis.

For my friends and family, my Mother and Father, for their support both personal and at times, financial. I'd like to thank Hemenato "Orko" Bairagi and Blake Mitchell for encouraging me to go to the gym, our numerous late night discussions on everything from anthropology to metaphysics. Without them, my health would have deteriorated over the duration of my masters.

Table of Contents

List of Tables

List of Figures

List of Symbols & Acronyms

$\Delta\mathcal{T}$ Differential transmission.

λ Wavelength

$\omega = 2\pi f$ Angular frequency

Φ Fluence

τ_p Pulse width

$\tilde{\mathcal{E}}$ Complex conjugate of the field

$\tilde{\sigma}$ Complex conductivity

$\vec{J}$ Current density

$\vec{\mathcal{E}}$ Electric field

$c = 3 \times 10^8\,\mathrm{m/s}$ Speed of light in vacuum

$e = 1.6 \times 10^{-19}\,\mathrm{C}$ Elementary charge

E_p Laser pulse energy

f Linear frequency

j The principle quantum number

$k_B = 8.62 \times 10^{-5}\,\mathrm{eV/K} = 1.38 \times 10^{-23}\,\mathrm{J/K}$ Boltzmann's constant

n Charge carrier number density

P	Power
q	Net charge
R	Reflectivity
r_0	Gaussian beam waist radius at the focus
T_p	Period between pulses
T_t	Transmissivity
U	Potential energy
U_I	Ionization energy
w	Probability
EHP	electron-hole plasma
fs	femtosecond
LIBP	laser-induced breakdown plasma
LIBS	laser-induced breakdown spectroscopy
LIP	laser-induced plasma
MPI	multiphoton ionization
ns	nanosecond
PCA	photoconductive antenna/antennae
PE	photoexcitation
PL	photoluminescent
ps	picosecond
THz	Terahertz
VMRA	Verdi Micra + Regenerative Amplifier

Chapter 1

Introduction

Laser-induced breakdown spectroscopy (LIBS) is an all-optical means of determining sample elemental composition and the relative concentrations of those elements [1–6]. This proves applicable in areas where quick stand-off detection of elemental constituents is required, such as space exploration, mining, and agriculture [1–4]. A schematic of a typical LIBS setup is shown in fig. 1.1. At its most basic, LIBS requires a spectrometer, some collection optics, and a focused high power ultrafast laser with pulse-widths ranging from the femtosecond (fs) to nanosecond (ns) duration [4–12].

The basic operation of LIBS is as follows: light from an ultrafast laser with pulse-widths ranging from $\tau_p \sim 10\,\text{fs} - 1\,\text{ns}$ duration is focused down to a spot-size, $2r_0$, on the order of $2r_0 \sim 10\,\mu\text{m} - 100\,\mu\text{m}$ on the sample [4–11]. Doing this induces optical breakdown in the sample, resulting in plasma formation on the sample surface [4–6; 6–11]. Light from the sample is then collected and routed to a spectrometer, and the resulting spectral lines correspond to atomic and ionic lines which give the elemental composition of the material [4–11]. The intensity of these lines atomic emission lines are then proportional to the concentration of constituents in the sample, however the presence of matrix effects complicates the picture [3; 4].

Matrix effects are changes in the signal that arise when the components of the sample (termed "the matrix") alter the signal intensity of a particular constituent [3; 4]. For example, the signals from silicon (Si) in water, steel, and soil vary in intensity quite drastically even though the concentration of Si can be the same in all three matrices [4]. Historically the

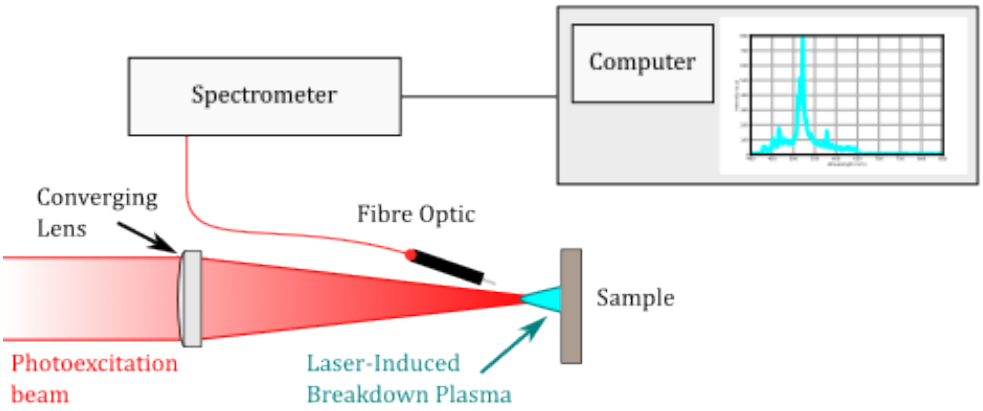

Figure 1.1: Schematic of a typical LIBS setup. A sample is ablated with a focused laser pulse of femtosecond to nanosecond duration giving a fluence above the ablation threshold, Φ_0, leading to plasma formation. Light emission from the plasma is then collected using a fibre optic which routes the light to a spectrometer. After some internal spectrometer time delay, the plasma spectrum can then be measured by the spectrometer and collected by a computer.

presence of matrix effects and the difficulty associated with correcting them prevented LIBS from being used extensively [3]. While many of the issues regarding matrix effects have been addressed to the point where LIBS is viable, in agriculture specific applications, a challenge remains in understanding matrix effects in soils [3]. Matrix effects in soils, broadly speaking, have their origin in two sources: first, water content in the soil and second, in grain size [3]. Of the two contributions to matrix effects water concentration in a soil sample is by far the greater contributor [3]. Knowing the soil sample water concentrations would make it feasible to calibrate the soil plasma spectra for matrix effects [4].

For the identification of water, a technique is required that gives rise to a signature that is unique to water molecules themselves, not their constituent elements. Such a signature is seen in the terahertz (THz) pulses shown in fig. 1.2-1.3. Fig. 1.2-1.3 show THz pulses from a lithium niobate source travelling through an enclosure under ambient lab conditions (labelled in fig. 1.2-1.3 as the "ambient" pulse) and when the enclosure is flooded with diatomic nitrogen, which removes water from the enclosure (labelled in fig. 1.2-1.3 as the "purged" pulse). In the time domain, shown in fig. 1.2, the presence of water molecules (the ambient pulse) gives rise to a "ringing" in the tail of the pulse that is absent when the enclosure is purged with diatomic nitrogen. Fourier transforming these pulses gives rise

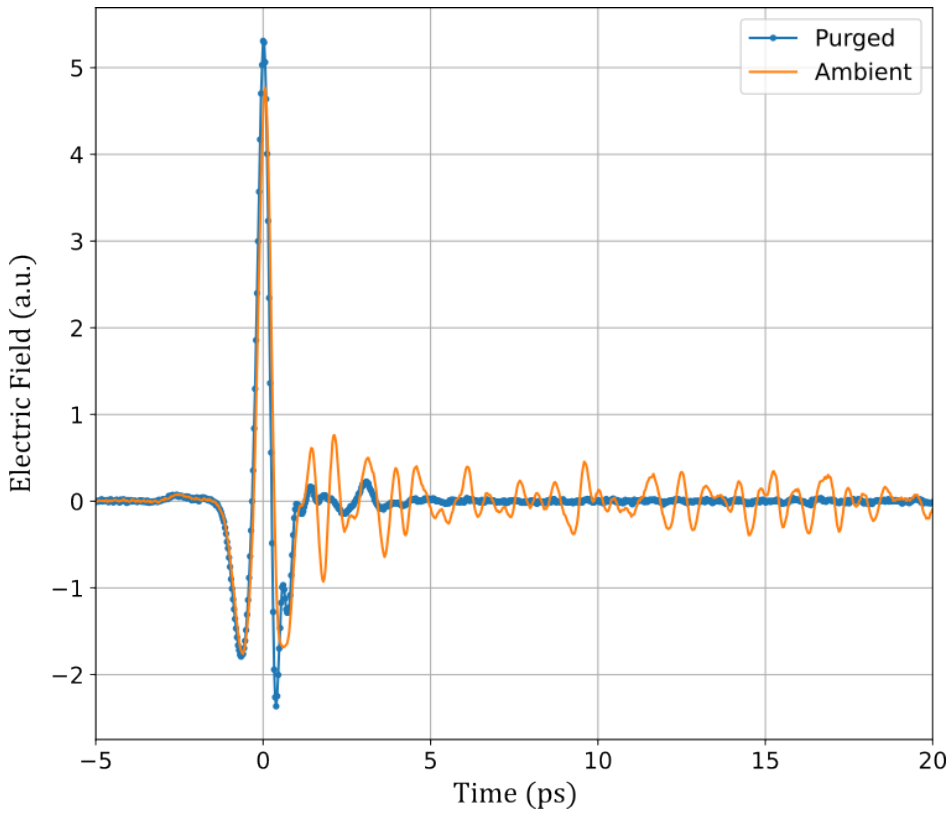

Figure 1.2: The electric field of a single-cycle THz pulse from a lithium niobate source travelling through an enclosure. The purged pulse was sampled when the enclosure was flooded with diatomic nitrogen, removing the presence of water molecules in the enclosure. The ambient pulse was measured without a diatomic nitrogen purge of the enclosure. The oscillations in the ambient pulse tail correspond to a real signal arising from the "ringing" of water molecule vibrational and rotational modes.

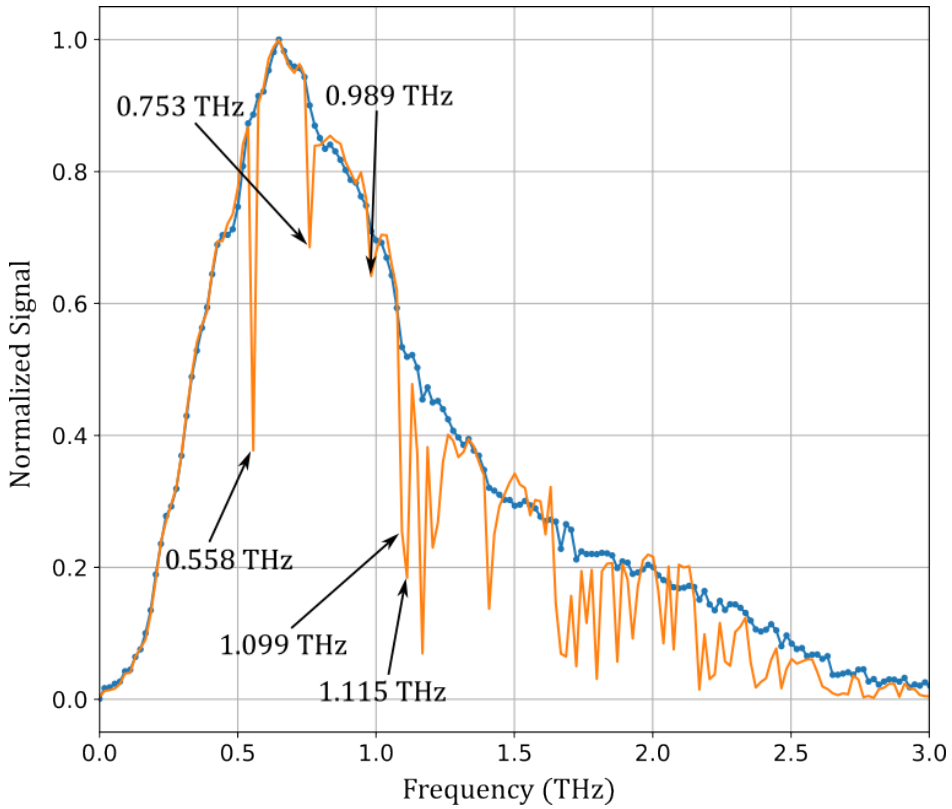

Figure 1.3: The Fourier-transformed frequency domain of fig. 1.2. The first five labelled dips in the spectra are the water molecule vibrational and rotational modes identified by Van Exeter et al. in ref. [13]. The depth of these dips can be used to estimate water content in the medium the THz pulse travels through.

to fig. 1.3 and reveals "dips" or "troughs" at certain frequencies in the ambient pulse that are absent from the purged pulse. The troughs shown in fig. 1.3 are not random; they correspond directly to water molecule rotational and vibrational modes like the ones shown in fig. 1.4 [13–17].

It is specifically because the resonant frequencies of the water molecule rotational and vibrational modes shown in fig. 1.4 lie within the THz band, a frequency range corresponding to $f \sim 0.1 - 10$ THz, that THz band pulse light is a strong candidate for the detection of water molecules [13–17]. More importantly though, the depth of the troughs shown in fig. 1.3 can be used to detect and measure water content in the medium the THz pulse travelled through [13; 16; 17].

Even under extreme conditions, such as combustion of a propane flame, as was done by Cheville and Grischkowsky in ref. [16], these traces still remain. While a LIBS plasma might seem more extreme than a propane flame, and that water molecules would split under the conditions of a LIBS plasma, it is worth noting that LIBS plasmas are not fully ionized [18]. This necessitates in LIBS analysis the inclusion of a parameter termed the degree of ionization, κ_i, given by [18; 19],

$$\kappa_i = \frac{n_{Z+1}}{n_Z + n_{Z+1}}. \tag{1.1}$$

Where n_{Z+1} and n_Z are the number density concentrations for particles in states $Z+1$ and Z respectively [18; 19]. Thus, depending on the particular plasma value of κ_i, there could exist a population of neutral molecular species, including water molecules.

There exists another more general application of the LIBS setup shown fig. 1.1. If the plasma exists in a state called local-thermodynamic equilibrium (LTE) (see Appendix A for details), the intensity of an emission line, I, then corresponds to the temperature according to the Boltzmann method [6; 8; 11],

$$\ln\left(\frac{I\lambda}{A_{ul}g_u}\right) \propto -\frac{E_u}{k_B T}, \tag{1.2}$$

where I is the intensity of a given line, λ the wavelength, A_{ul} the atomic transition probability between the upper-to-lower levels, g_u the degeneracy associated with the upper level, and T the plasma temperature. From repeated measurements of multiple lines at different

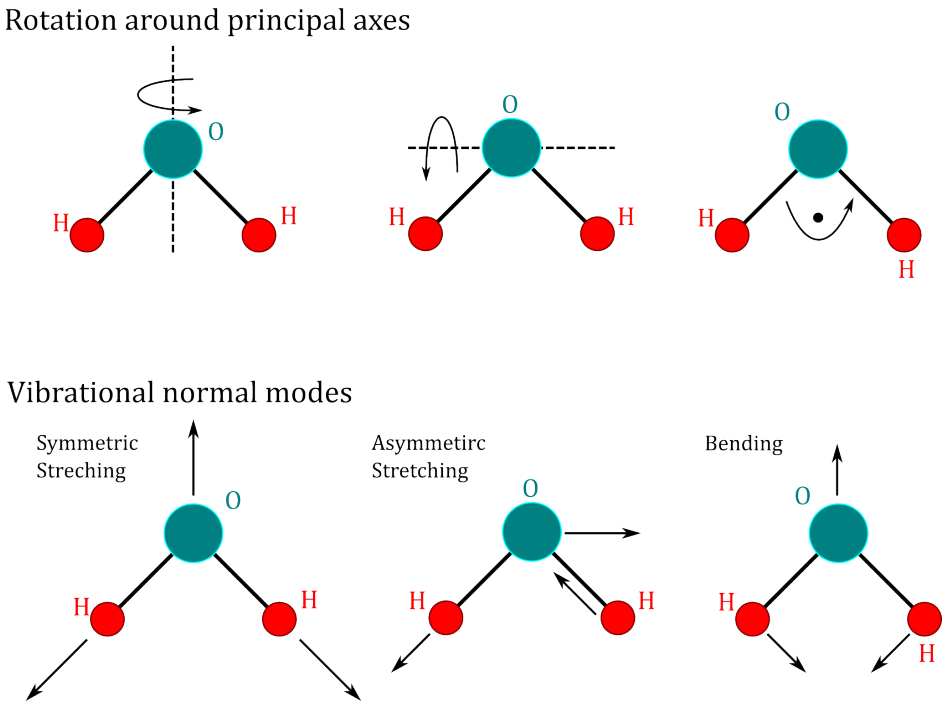

Figure 1.4: Examples of water molecule rotational and vibrational modes. The frequencies at which these modes oscillate can lie within the THz range ($f \sim 0.1 - 10$ THz). Subsequently this will cause THz band light to be absorbed in the presence of water molecules. This gives rise to the "ringing" seen in the time-domain of the THz pulse (see fig. 1.2) and the corresponding dips in the frequency-domain spectrum (see fig. 1.3). Based off of a similar figure from ref. [15].

timesteps, T can be resolved on nanosecond (ns) timescales [6; 8; 11]. By measuring the stark-broadended lines, one could also obtain a time-resolved electron density n_e [6; 8; 11]. Alternatively, T maybe obtained by comparing the intensities of two lines I and I' through the Saha-Boltzmann method [6]. However, the assumption upon which both the Saha-Boltamann method and eqn. 1.2 are based upon relies on the existence of the LTE regime, which tends to break down at both earlier and later times [6; 8; 11; 18; 20; 21]. THz pulses could help in this regard, by acting as a secondary probe that could measure the conductivity, $\tilde{\sigma}$, with picosecond resolution [22–34]. From this, it should be possible to obtain information on related optical properties (e.g., the dielectric constant, $\tilde{\epsilon}$) and n_e [28–32]. As such, there is great promise for combining the two methods for the study of laser-induced plasmas. For not only would THz pulses provide a non-contact means of measuring $\tilde{\sigma}$, it could in the process, verify the LTE state. To understand why, consider that the DC conductivity is given by [35],

$$\sigma_0 = \frac{e^2 n_e \tau}{m_e}, \tag{1.3}$$

where τ is some scattering time. Assuming that electron-ion collisions predominate, this time is then given by [36],

$$\tau_{e,i} = \frac{1}{n_e s_c \langle v_e \rangle}, \tag{1.4}$$

where s_c is a scattering cross-sectional area and $\langle v_e \rangle$ is the average electron velocity. Furthermore, $\langle v_e \rangle \propto T$ [36]. Thus, by measuring σ_0 it is then possible to estimate the temperature. If T measurements from a THz probe match those obtained from a time-resolved LIBS spectrum, then the LTE state is verified. However, if there exists a strong discrepancy between the THz probe measurements and the time-resolved LIBS measurements, then it would cast doubt upon the LTE state existing within that particular time window.

To add more credence to the claim that THz pulses could be combined with LIBS; THz pulses have been used to study electron-hole plasmas (EHPs) and inductively coupled plasmas (ICPs) [22–30]. There have also been applications of THz pulses to the study of liquid, gaseous, and solid target laser-induced breakdown plasmas, similar to those found in a LIBS process, in ref. [31–34]. EHPs arise from photoexcitation (PE) of semiconductors at or above energies greater than the band gap energy, E_G [37–41]. In the case of an EHP,

holes act as the secondary species in a two-species plasma with their own temperature and mobility, just as ions do in a gaseous plasma [26; 38; 42; 43]. The key difference here is that holes, unlike ions, are "quasi-particles" [43]. Quasi-particles are not particles themselves but arise from some intrinsic process in a physical system that gives rise to particle-like behaviour [44]. In the case of holes, a hole arises when one considers the absence of an electron from a valence band in a semiconductor, the empty state can be described as behaving like a positively charged particle of mass m_h and energy $\hbar^2 k^2/2m_h$ [43].

ICPs are created through the ionization of a gaseous target achieved via voltage breakdown [27–30; 45]. ICPs are then sustained by energy provided by electromagnetic induction through an induction circuit element either adjacent to, or immersed in, the discharge region [27–30; 45]. The validity of using THz pulses to study ICPs was affirmed by Ando et al. in ref. [30]. Ando et al. found that the measured electron densities, n_e, they obtained using transmissive THz approaches (specifically terahertz time-domain spectroscopy) matched the measurements performed with Langmuir probes within error [30].

It is important to note though that both EHPs and ICPs are categorically distinct from the plasmas found in LIBS; EHPs are created for example, through PE of a semiconductor wafer and the material does not undergo any sort of optical breakdown [22–26; 39–41]. In contrast to EHPs, LIBS plasmas are formed through optical breakdown of either a solid, liquid, or gaseous target [4; 6–11; 11; 31; 34; 46; 47]. While ICPs are exclusively gaseous targets and require an induction element, LIBS plasmas can be formed from, in addition to gaseous targets, solids and liquids and there is no induction element to be found [4; 7–11; 27–30; 45; 46]. Despite these differences, the results obtained from EHPs and ICPs do demonstrate that plasma phenomenon can be studied with THz pulses.

As a last word on the comparison between EHPs and LIBS plasmas, it is important to note that EHPs and LIBS plasmas are both induced using lasers [4; 7–11; 22–26; 38; 40; 41]. However, the term "laser-induced plasma" and "laser-produced plasma" are typically used within the LIBS literature to refer to plasmas arising from optical breakdown of materials (see ref. [4; 7; 8; 10; 11]), however this nomenclature is confusing and cumbersome as both laser-induced plasma and laser-produced plasma could also refer to EHPs arising from PE (see ref. [41] for example) as both are technically "laser produced" or "laser-induced."

To avoid confusion, this thesis will opt to use the term laser-induced breakdown plasma (LIBP) to refer exclusively to plasmas arising from the optical breakdown of matter, while "electron-hole plasma" will refer exclusively to semiconductor EHPs arising from the PE of semiconductors. If the term laser-induced plasmas (LIPs) is used in this thesis, it is in reference to both EHPs and LIBPs.

Despite the previously mentioned differences, it has been shown prior that THz pulses can be used to study plasmas arising from optical breakdown similar to those seen in LIBS experiments [31–34; 48–55]. Of note is the work of Kim et al. who was able to obtain a quasi-DC conductivity for a laser heated aluminum plasma using a reflection geometry [32]. Using a single-shot transmissive THz approach, Chen et al. extracted a time-resolved conductivity for gold warm dense matter formed with an extreme ultra-violet pulse [33]. Sagisaka et al. and Hamster et al. were both able to detect THz emission from a solid target copper (Cu) LIBP that was formed from an amplified stimulated emission pulse and pre-pulse, that was subsequently driven by a proceeding fs-pulse [50–52]. Gao et al. claimed to observe a coherent half-cycle THz pulse from a Cu-LIBP, informing the basis for emissive spectroscopy [49]. Gao et al.'s results were later corroborated by Li et al. (ref. [55]), while THz radiation detected from fs-ablated solid targets as measured by a bolometer, has been noted by authors in ref. [50; 53; 54; 56]. For the transmissive approach, a noteworthy mentions are Mics et al. in ref. [31] and Chen et al. in ref. [33]. Mics et al. performed transmissive THz spectroscopy on a diatomic oxygen gas target LIBP using a fs-pulse pump laser and a THz probe [31]. More crucially gold warm-dense matter has been probed with THz pulses by Chen et al. in ref. [33]. The success Chen et al. had in the probing of gold-target warm dense matter indicates that the transmissive THz probing of solid-target plasmas is feasible or at the very least, not that far fetched [33].

This brief overview of the literature presents two paths that a THz-LIBS approach could take: transmissive and emissive. The transmissive approach is shown in fig. 1.5(a) and follows the lead of Van Exeter et al. (ref. [13]) and Cheville at al. (ref. [16]) with the key difference between this thesis and Cheville et al.'s work being that a LIBP plume replaces the propane plume respectively. The emissive approach is shown in fig.1.5(b) follows the lead of Gao et al. (ref. [49]) where THz emission from the plasma plume is monitored. The

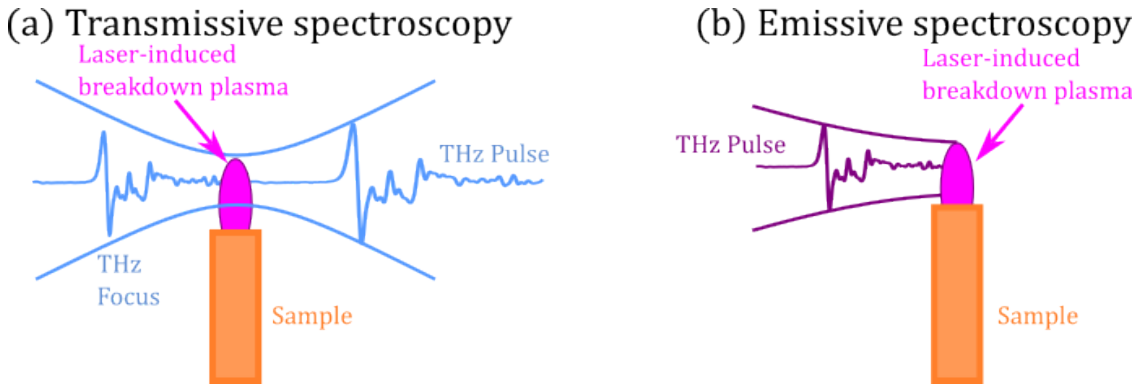

Figure 1.5: Fig. (a) outlines a transmissive approach to the THz spectroscopy. In approach (a) a THz pulse is sent through the LIBP plume and is attenuated by the plume. Fig. (b) outlines an emissive approach to the THz spectroscopy. In approach (b) the LIBP plume is the source of THz emission.

advantage of the emissive approach over the transmissive approach is that it is simpler to implement and requires less synchronization. Whereas the advantage of the transmissive approach over the emissive approach is that the spectroscopic methods for identifying and determining water content are already developed (see ref. [13; 16; 17]). There is also the possibility of retrieving a conductivity spectra, as is done for EHPs in semiconductors [57; 58]. For the emissive approach to be used in the context of detecting water content in THz-LIBS, it must be shown that the water molecule rotational and vibrational modes appearing in the frequency spectra such as those shown in fig. 1.3 arise from the target sample, not from the ambient environment. As of writing, this remains to be proven.

In this thesis, the feasibility of using THz spectroscopy to study LIBPs for the development of a hybrid all-optical THz-LIBS system is assessed. This hybrid THz-LIBS system would be hypothetically capable of determining water content and measuring plasma conductivity with picosecond resolution; in addition to element detection, and time resolved measurements of the plasma temperature and electron density of LIBS. Furthermore, it would open the possibility for the development of an all-optical in-situ device capable of element detection and water content measurement in soil targets for agricultural applications. This will be done by implementing the two approaches illustrated in fig. 1.5 and benchmarking both approaches against EHPs present in photoexcited semiconductors.

If the transmissive approach is viable, a differential transmission, $\Delta\mathcal{T}$, should be observed

in a LIBP similar to that of what is seen in a semiconductor EHP (see ref. [22; 23; 25; 59]). This $\Delta\mathcal{T} \equiv \mathcal{T}_{\text{Pump}} - \mathcal{T}_{\text{Ref}}$, is defined as the difference between the presence of photo-induced effects (denoted $\mathcal{T}_{\text{Pump}}$) in the sample and the nominal THz transmission through the sample in the absence of these effects (denoted $\mathcal{T}_{\text{Ref}}$ or $\mathcal{T}_0$) [57; 58]. In the context of this thesis, $\mathcal{T}_{\text{Ref}}$ would refer to the THz transmissivity in the absence of a LIBP, while a $\mathcal{T}_{\text{Pump}}$ would refer to THz transmissivity in the presence of a LIBP. If such a transmissive approach like the one shown in fig. 1.5(a) is possible for LIBPs, it would indicate that water content measurements such as those done by Yang et al. in ref. [17] are indeed possible for LIBPs. In addition to this, the same methods used to measure $\tilde{\sigma}$ in ref. [22; 23; 25; 59] would also be applicable to LIBPs.

Conversely, if the emissive approach shown in fig. 1.5(b) is viable, THz emission commonly documented in photoexcited semiconductors (see ref. [60–66]) should also appear in solid-target LIBPs. Caution should be exerted when studying THz emission from solid-target LIBPs as THz emission can occur in photoexcited metal targets, due bulk nonlinear processes (e.g., optical rectification), as opposed to the rapid charge separation in LIBPs [67–69]. There is also the possibility of a photocurrent arising from free-electrons in the metal being driven by the incident laser pulse as discussed by Fei et al. in ref. [54]. In this thesis a solid-target Cu sample is mounted first at an angle to the oncoming photoexcitation beam as per Gao et al. (ref. [49]) and then at normal incidence to the oncoming beam as per fig. 1.6. This is because as noted by Liu et al., contributions from optical rectification possess an angular dependence according to $\mathcal{E}_{\text{OR}} = \mathcal{E}_0 \cos(z\theta)$ where z is some fit parameter and θ is the angle between the sample plane and the oncoming beam [62]. Therefore, if $\theta = 90°$ to the oncoming pulse, and a coherent THz pulse is still detected, this would imply that the signal observed is from the LIBP plume, not from optical rectification (see fig. 1.6). This eliminates the possibility of optical rectification, as a process. De-coupling a possible bulk photocurrent from the THz emission is beyond the scope of this work, but should be considered for future work.

To understand the reasoning for emissive and transmissive THz approaches for the study of laser-induced plasmas in both LIBP and EHP cases necessitates a background regarding the optical properties of both systems in the THz region and the picosecond dynamics

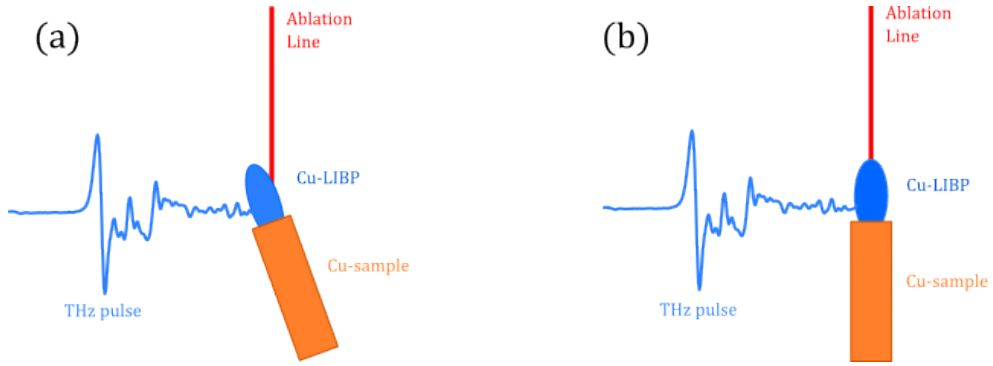

Figure 1.6: Fig.(a) the orientation of a Cu-target sample at an angle to the oncoming ablation beam used to induce optical breakdown. Fig.(b) the orientation of a Cu-target sample normal to the oncoming ablation beam used to induce optical breakdown. The reason for the different Cu-target sample orientations is to check if any THz emission arises from the laser-induced breakdown plasma plume as opposed to nonlinear effects from the bulk. This is because one such bulk process, optical rectification, has an angular dependency that can be eliminated by changing the sample orientation. If coherent single-cycle THz emission disappears when the sample is re-orientated between fig.(a) to fig.(b) it would imply that any THz emission seen in fig.(a) was not from the plasma, but rather the bulk.

associated with them. To this end, chapter 2 of this thesis covers laser-induced breakdown plasmas. This chapter covers how LIBPs form, descriptions of the charge carrier dynamics as it pertains to notions of a plasma lifetime and picosecond scale phenomenon are given. This is followed by a simple model detailing how rapid charge separation in a LIBP, similar to the photo-Dember effect in semiconductors, can result in the emission of a single-cycle THz pulse. The inclusion of this section is necessary as to motivate how THz emission can occur in solid-target plasmas. Simulation results of the optical properties, particularly the transmissivity, reflectivity, and penetration depths of a LIBP in the THz region assuming the predominance of electron-ion collisions are also presented. The inclusion of this section is necessary to understand why in conjuction with the aforementioned literature, it was thought that transmissive THz approaches were feasible.

Chapter 3 discusses electron-hole plasmas and their applications to photoconductive antennae. This chapter discusses their formation and descriptions of the charge carrier dynamics as it pertains to obtaining a $\Delta\mathcal{T}/\mathcal{T}_0$ measurement. This is followed by a section on the various processes that occur in semiconductors that can give rise to THz emission. This includes both linear processes such as, drift currents and the photo-Dember effect and

briefly covers nonlinear processes, such as optical rectification. Branching off from the prior discussion on linear processes, this chapter is concluded by a discussion on photoconductive antennae theory and operation. The inclusion of this section is necessary as photoconductive antennae were used for the generation of THz pulses for the transmissive measurements.

Chapter 4 covers experimental methods and materials used in this thesis. This encompasses descriptions of the lasers used, the photoconductive antennae, and the two spectrometers used in this thesis. Electro-optic sampling (EOS) is discussed in detail as it is the basis for THz detection in both the transmissive and emissive cases. Some material is also provided on laser-induced breakdown spectroscopy. It should be noted though that for the LIBS measurements performed here, no attempt was made to time-resolve the spectra collected. The spectra displayed in this thesis were gathered for benchmarking purposes and for estimation of the photoluminescent (PL) lifetimes presented in chapter 5. This is followed by a section on the implementation of the emissive THz approaches and the chapter concludes with a discussion on the implementation of the transmissive THz approaches.

Chapter 5 covers results from the THz transmission experiments for laser-induced plasmas. This includes a section on the PL lifetimes and the spectra from a Cu target. These results were crucial in determining why there was much difficulty with the transmissive approach, and brings attention to difficulties that researchers in the future must be aware of if they wish to pursue a transmissive style approach. A proposal involving a Herriot cell is introduced to remedy some of the difficulties encountered in this thesis. It concludes with a discussion of the results for THz transmission in semiconductors.

Chapter 6 covers THz emission experiments for laser-induced plasmas. This includes both the results from a solid target Cu-LIBP and the semiconductor THz emission from EHPs. Of note in this chapter is the disappearance of frequency components in the THz pulse when the plane of the target sample is at normal incidence to the laser as per fig. 1.6. To the best of the author's knowledge, this has not been observed in literature before. After comparing these results to prior work, the chapter concludes with a proposed future experiment for gauging the feasibility of using THz emission in solid target plasmas to measure water content in the target.

Finally, chapter 7 concludes this thesis. Summarizing what was covered in chapters 5-6

and outlining possible directions for a hybrid THz-LIBS style device that engineers need to consider.

Chapter 2

Laser-Induced Breakdown Plasmas

In this chapter laser-induced breakdown plasmas (LIBPs) are introduced. This chapter is intended to give a qualitative understanding of LIBPs, as such, it will cover how LIBPs are formed, how they dissipate, and the processes that could possibly enable the probing of LIBPs using THz pulses and THz emission from LIBPs. This is intended to prime the reader for the author's answer to two key questions; first, do standard theoretical and experimental results permit the emission of THz band radiation from LIBPs? Second, can a THz pulse be used to probe a LIBP?

To answer the first question, the literature surrounding how LIBPs are formed is introduced using the work of Shen and Park et al. (ref. [70; 71]). While Shen's model is rather simple, it does motivate the processes involved in laser-matter interactions, including multi-photon ionization (MPI) and avalanche ionization. Park et al. meanwhile presents insights into experimental behaviour, which emphasizes multi-photon ionization and notes a saturation effect in the measured ionic charge [71]. This is followed up by a brief discussion of Nolte et al. and Furusawa et al.'s work which estimates that ablation thresholds for Cu, Φ_0, range from $140\,\mathrm{mJ/cm^2} \leq \Phi_0 \leq 460\,\mathrm{mJ/cm^2}$ [72; 73]. Hashida et al. meanwhile estimates that for pulse-widths of $\tau_p = 70\,\mathrm{fs}$ the ablation threshold for Cu as, $\Phi_0 = 18\,\mathrm{mJ/cm^2}$ [74]. This gives the range of fluences over which LIBP formation occurs for solid-target Cu. This is then concluded by a simple model developed to motivate how a space-charge could give rise to a single-cycle THz pulse. Note though, this model is not meant to be a complete picture of the early-time picosecond dynamics and this section is accompanied by a brief discussion

of the theoretical work done by J.P. Girardeau-Montaut and C. Girardeau-Montaut on the Fowler-Dubridge model (ref. [75]) and Fei et al.'s proposal of a photocurrent effect in metals (ref. [54]).

To answer the second question, previous work done by Ando et al. and others is highlighted. These results showed that THz spectroscopy has been successful for at least the case of inductively-coupled plasmas, which while categorically distinct from LIBPs do show that transmissive THz spectroscopy is feasiable for plasma phenomenon [27–30]. However, there is a notable discrepancy in the orders of magnitude for electron density between what is reported in LIBPs ($n_e \sim 10^{16} - 10^{19}\text{cm}^{-3}$) vs what is seen in inductively-coupled plasmas ($n_e \sim 10^{11} - 10^{16}\text{cm}^{-3}$) [7; 8; 11; 27–30; 76; 77]. More suggestive is the work reported in ref. [31–34]. For example, though different from a transmissive approach, Kim et al. used a reflective THz probe to obtain a quasi-DC conductivity in a warm-dense aluminum target [32]. Chen et al. measured the conductivity of a warm-dense gold target that was induced by an extreme ultraviolet pulse with a single-shot THz pulse [33]. The experiments most similar to the transmissive ones seen here, were those performed by Mics et al. in ref. [31] and Tan et al. in ref. [34]. In both works a target had a fs-pulse incident upon it to induce optical breakdown in the target leading to a plasma. This LIBP was placed at the focus of two off-axis parabolics which focused an oncoming THz pulse probe unto the LIBP. In both instances, the author's reported seeing a $-\Delta\mathcal{T}/\mathcal{T}_0$ and measured electron densities, $n_e \simeq 10^{14} - 10^{16}\text{cm}^{-3}$ [31; 34]. Mics et al. was able to obtain a dielectric spectra for the diatomic oxygen plasma they were studying [31]. However, none of these previous works have attempted to perform a transmissive THz approach for fs-ablated solid targets.

This means that literature alone does not provide enough precedent for whether or not transmission through a fs-ablated LIBP is feasible at some fixed time; as the aforementioned discrepancy could indicate that the electron densities are such that, the LIBP is too opaque in the THz band. To remedy this, a simulation assuming a Drude-like LIBP slab of thickness $l = 1.5\,\text{mm}$ was performed for various electron densities to see if LIBPs are transmissive within the THz range given typical LIBS densities. These simulation results indicated that a transmission geometry is feasible for LIBPs on the order of $n_e \sim 10^{16} - 10^{17}\text{cm}^{-3}$, with strong attenuation occurring beyond these densities.

The issue of synchronization is touched upon in the final section of this chapter, highlighting plasma recombination and lifetime. Note that the term "plasma lifetime" is ill-defined within the literature. In light of this, this thesis will use the photoluminescent (PL) lifetime to estimate the duration of a Cu-LIBP. Keep in mind though, that this does not represent the total duration of plasma effects, only the duration of light emission measured with a photodiode. A notable example of how this is not sufficient for estimating the total duration of a plasma is found in the ICCD imaging results of Wang et al., in ref. [11]. Wang et al.'s results indicate that Cu-LIBPs could last longer and this will be further discussed in detail in Chapter 5. However, PL lifetime is used in this thesis because of the ease of implementation and the time over which PL lasts is the time over which the plasma state can be verified. It is further justified when considering the fact that it is over the time that a LIBP is emitting light, that there exists a large quantity of charge-carriers in an excited state that have yet to complete recombination processes [78–83].

2.1 Optical Breakdown and Plasma Formation

Optical breakdown refers to catastrophic evolution by a strong laser field leading to ionization and plasma formation in a target [70]. It is the basis of laser-induced breakdown spectroscopy (LIBS), and is the means by which LIBPs are formed and hence a discussion of its principles are worth examining. A myriad of processes occur when an ultrafast fs-pulse is incident on matter, including multiphoton ionization (MPI), tunnelling ionization, and thermionic emission, to name a few [70; 75; 84]. To establish a basis, it helps to consider the model laid out by Shen in ref. [70]. Shen describes the production rate of charge carriers in a solid as being dependent on three key parameters: avalanche/impact ionization rate η, the recombination processes r, and multiphoton excitation contributions [70]. Altogether this gives,

$$\frac{\partial n}{\partial t} = (\eta - r)\, n + \left(\frac{\partial n}{\partial t}\right)_{\mathrm{MPI}}. \tag{2.1}$$

Here $(\partial n/\partial t)_{\mathrm{MPI}}$ is the multiphoton ionization rate. Note η and r are both assumed to be constant over the period of observation [70]. In Shen's model the charge carrier production is due to two processes: (1) MPI (designated in eqn. 2.1 by the $(\partial n/\partial t)_{\mathrm{MPI}}$ term) and (2)

avalanche ionization (designated by the $(\eta - r)\, n$ term in eqn. 2.1). Both (1) and (2) are in direct competition with recombination processes. Since the pulsewidth Park et al. used in their letter was $\tau_p = 10\,\text{ps}$, they claimed that contributions from avalanche ionization are negligible over these timescales [71]. Subsequently, the $(\eta - r)\, n$ term in eqn. 2.1 was dropped in their study of Aluminum (Al) and Cu-target LIBPs [71]. Park et al. writes a form of eqn. 2.1 as [71],

$$\frac{\mathrm{d}n_i}{\mathrm{d}t} = w_{\text{MPI}}\,(n_n - n_i) - r n_i. \tag{2.2}$$

Here n_i is the ion density, n_n the neutral atom density, w_{MPI} is the probability of MPI which is defined as [71; 85],

$$w_{\text{MPI}} = s_j \mathcal{E}^{2j} = s_j \Phi^j. \tag{2.3}$$

Where, Φ is the fluence, $\mathcal{E}$ is the electric field, s_j is some cross-sectional area and j is the number of quanta sufficient for ionization which is found according to [71; 85],

$$j = \left\langle \frac{U_I}{\hbar\omega} + 1 \right\rangle_{\text{int}} \quad \text{where} \quad j \in \mathbb{Z}^+. \tag{2.4}$$

Where U_I is the ionization potential, which for Cu is $U_I^{\text{Cu}} = 7.726\,\text{eV}$ [71]. Eqn. 2.4 gives the minimum number of photons as $j = 5$ for the onset of ionization for the case of a ruby laser with $\hbar\omega = 1.785\,\text{eV}$ [71]. For this thesis, the laser used for ablation is a Ti:Sapphire laser which has parameters of $\tau_p = 70\,\text{fs}$, a pulse energy of $E_p \approx 2 \times 10^{-4}\,\text{J} = 200\,\mu\text{J}$, and a wavelength of $\lambda = 795\,\text{nm}$ which maps to a photon energy of $\hbar\omega = 1.56\,\text{eV}$ giving the minimum number of photons required for ionization as $j = 6$. Park et al. was able to further simplify eqn. 2.2 by noting that the inter-pulse period, T_p, used in their work was $T_p = 7\,\text{ns}$ which is significantly shorter than their quoted recombination rate of $r^{-1} = \tau_R \simeq 500\,\text{ns}$ [71]. This means that Park et al. was able to neglect the recombination term (represented by $r n_i$ in eqn. 2.2) and the decay during inter-pulse separation could be neglected (meaning that $r n_i \approx 0$) [71]. With this thesis assuming an equivalent recombination time, such effects cannot be neglected due to the relatively long period between pulses $T_p = 1\,\text{ms}$.

Of particular note in Park et al.'s work is the existence of three distinct fluence regimes which they term as low-fluence (which they defined as fluences between $\Phi \leq 8\,\text{J}\cdot\text{cm}^{-2}$),

intermediate fluence (which they defined $8\,\mathrm{J}\cdot\mathrm{cm}^{-2} < \Phi < 50\,\mathrm{J}\cdot\mathrm{cm}^{-2}$), and high-fluence (which they defined as $\Phi \geq 50\,\mathrm{J}\cdot\mathrm{cm}^{-2}$) [71]. Park et al. found that these regions had different cross-sectional areas, s_j. For Cu in the low-fluence regime $s_j = 9.58 \times 10^{-47}\,\mathrm{cm}^{10}\mathrm{s}^4\mathrm{J}^{-5}$ and in the high-fluence regime as $s_j = 1.48 \times 10^{-49}\,\mathrm{cm}^{10}\mathrm{s}^4\mathrm{J}^{-5}$ [71].

The astute reader will note that the ionization potential for Cu quoted by Park et al. is much higher than the work function of Cu, W_{Cu}, which is around $W_{\mathrm{Cu}} \simeq 4 - 4.5\,\mathrm{eV}$ [86]. What this means in practice is that electron emission via the photoelectric effect could be occurring concurrently with ionization [75; 84]. Anisimov et al. in ref. [84] and J. P. Giradeau-Montaut and C. Giradeau-Montaut in ref. [75] discuss these contributions in more detail. It is worth emphasizing that decoupling electron emission processes is a non-trivial process [75; 84]. J. P. Giradeau-Montaut and C. Giradeau-Montaut for instance discuss intermediary regimes between thermionic and multiphoton emission [75]. This effect is sometimes called thermally assisted multiphoton photoemssion [75]. Decoupling these individual processes is beyond the scope of this thesis. What is important to note is that they could contribute to optical breakdown and ultimately plasma formation and that the multiplicity of these processes present a formidable challenge to researchers.

To add to the difficulty of studying ionization in solids, Shen notes solid targets are far more difficult to study than their gaseous counterparts because optical breakdown of solids leaves permanent damage [70]. Furthermore, local deformities along the surface can lead to strong deviations from what is predicted from eqn. 2.1 as the local field around a structure could be significantly higher [70]. For example, dust particles can absorb the oncoming light lowering the threshold required for optical breakdown and the coarseness of a surface can create pockets of confined fields which can lower the threshold [70]. This explains in part the wide variety of fluence thresholds for Cu that are reported in literature [72–74; 87]. This is in addition to the wide parameter space available to researchers which include pulse-width, laser-wavelength, and even number of shots on a surface can raise or lower a fluence threshold [72–74; 87]. This creates an issue of repeatability between measurements as the act of optical breakdown destroys the sample being studied, thus a study of optical breakdown requires a large chunk of material of similar quality, ideally very smooth and without surface deformities [70].

This is not to say that a means to decouple ionization processes does not exist. For example, an explicit way of decoupling tunnelling ionization from MPI can be seen in the work of Keldysh [88]. Keldysh defines a parameter γ which is called the Keldysh parameter and it is defined as [88],

$$\gamma \equiv \sqrt{\frac{U_I}{2U_p}} = \frac{\omega}{e\mathcal{E}_0}\sqrt{2m_e U_I}. \tag{2.5}$$

Where U_p is the ponderomotive energy and is equal to [88],

$$U_p = \frac{e^2\mathcal{E}_0^2}{(4m_e\omega^2)}. \tag{2.6}$$

Where $e = 1.6 \times 10^{-19}\,\mathrm{C}$ is the elementary charge, n_e is the electron density, and $m_e = 9.11 \times 10^{-31}\,\mathrm{kg}$ is the electron mass. The Keldysh parameter defined in eqn. 2.5 can be used to determine whether MPI or tunnelling ionization dominates [88]. For example, if $\gamma \gg 1$ tunnelling processes are negligible and MPI dominates [88]. Conversely if $\gamma \ll 1$ tunnelling ionization dominates over MPI, and in the intermediate regime, $\gamma \sim 1$, tunnelling and MPI co-exist [88].

While there are many other pathways for both photoionization and electron emission, decoupling them all is beyond the scope of this work. What is important for this thesis is that regardless of how ionization occurs in solid targets, ionization is required for the formation of a LIBP and that many pathways exist for a solid target to experience ionization. Furthermore, even if the energy quanta within the laser is below the ionization potential energy, U_I, ionization can indeed occur under the influence of a strong laser field as per eqn. 2.2 and 2.4. Lastly, from eqn. 2.2 it is apparent that for the formation of a plasma from a solid target requires that $w_{\mathrm{MPI}} > r$.

Having described the necessity of ionization and the ways in which it can occur briefly, consider now how the transition between a solid and plasma happens. Such a transition in solid targets can be best thought of as a two-temperature system, wherein energy from the incident pulse is exchanged between the electrons in the solid target and the lattice of the solid target [72; 73; 75; 84]. The energy transferred by electrons to the lattice of the metal

per unit time is in 1-dimension [72; 73; 75; 84],

$$\Delta E = \gamma_{e,L}\left(T_e - T_L\right) \quad \text{where} \quad \gamma_{e,L} \equiv \frac{\pi^2}{6}\frac{m n_e v_s^2}{\langle \tau_{e,ph} \rangle T_L}$$

is the electron-lattice coupling coefficient, Where v_s is the speed of sound in the metal, $\langle \tau_{e,ph} \rangle$ is the mean electron-phonon relaxation time, T_e, is the electron temperature, and T_L is the lattice temperature [75; 84]. The temperature evolution of the electrons-lattice system is then described by the following set of coupled equations [72; 73; 75; 84],

$$C_e \frac{\partial T_e}{\partial t} = \frac{\partial}{\partial x}\left(K_e \frac{\partial T_e}{\partial x}\right) - \frac{\partial \Delta E}{\partial x} + G\left(x,t\right) \tag{2.7}$$

$$C_L \frac{\partial T_L}{\partial t} = \Delta E; \quad \text{where} \quad G\left(x,t\right) \equiv \left(1-R\right)\alpha I\left(x,t\right). \tag{2.8}$$

Where C_e and C_L are the heat capacities of the electrons and lattice respectively, R the reflectivity of the solid target, α is the absorption coefficient, the K_e the thermal conductivity of electrons, and $G\left(x,t\right)$ is the time-intensity pulse shape function [72; 73; 75; 84]. Such a model is difficult to solve analytically without making a few assumptions, Anisimov et al. for example approached the problem numerically focusing on a few limiting cases of physical significance [84].

Nolte et al. were able to analytically solve the system of PDEs described by eqn. 2.7 - 2.8 by making a few simplifying assumptions about the material and are as follows: (1) heat capacity of the electrons is constant, (2) electron relaxation time decreases rapidly with increasing temperature and reaches a minimum at $\sim a/v_F$, where a is the inter-atomic spacing and v_F is the Fermi velocity, (3) a/v_F is broad which implies that at $T_e \gg T_F$, the relaxation time, τ, grows as $\tau \sim T_e^{3/2}$ (4) the diffusion coefficient $D = K_e/C_e$ is constant throughout [72]. Furusawa et al., following Nolte et al.'s work later confirmed these observations [72; 73]. The details of the derivation is given in ref. [72], what is pertinent for this thesis is by using this modified two-temperature model given by eqn. 2.7-2.8 Nolte et al. found two regimes for ablation in solid materials: (1) a skin-effect dominated regime ($\propto \delta e^{-z/\delta}$) and (2) a bulk dominated one ($\propto l e^{-z/l}$). By relating these two different regimes to the fluence of the laser, Nolte et al. was able to estimate threshold fluences, Φ_0, in Cu

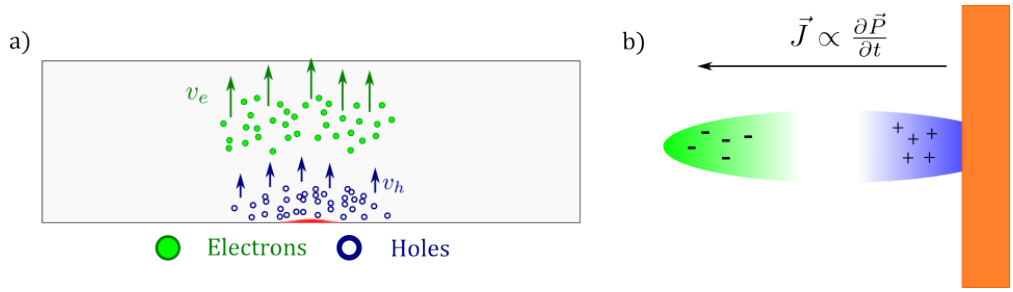

Figure 2.1: Charge carrier separation in (a) photoexcited semiconductors via the photo-Dember effect and (b) laser-induced breakdown plasmas. Both systems are alike in that they induce a transient plasma where electrons advance before their positively charged counterparts (holes in the case of (a) and ions in the case of (b)).

for these regimes as $\Phi_0^\delta = 140\,\mathrm{mJ/cm^2}$ & $\Phi_0^l = 460\,\mathrm{mJ/cm^2}$ [72]. By following Holte et al.'s reasoning, Furusawa et al. obtained a threshold fluence in the bulk dominated regime for Cu as $\Phi_0^l = 430\,\mathrm{mJ/cm^2}$ in their experiments [73]. This discrepancy can be explained in part by Furusawa et al.'s observation that varying the pulse widths from $120\,\mathrm{fs} \leq \tau_p \leq 800\,\mathrm{fs}$ yields a non-linear dependency of Φ_0 on τ_p; with smaller pulse-widths resulting in lower thresholds for ablation and the subsequent formation of LIBPs [73]. For plasma ignition to occur the fluence at the focus in this thesis must either exceed, or fall within, this range of fluences ($140\,\mathrm{mJ/cm^2} \leq \Phi_0 \leq 460\,\mathrm{mJ/cm^2}$). Measurements done by Hashida et al. give the threshold fluence for Cu to be at $\Phi_0 = 18\,\mathrm{mJ/cm^2}$ for the case of $\tau_p = 70\,\mathrm{fs}$ [74].

The formation of a LIBP leads to a charge separation of between ions and electrons [89; 90]. With the electrons initially leading followed by slower ions [89; 90]. Since this charge separation occurs over picosecond timescales, as it does in the case of the diffusion dominated photo-Dember effect (see fig.2.1), this charge separation should give rise to a THz pulse in the far field [61; 63; 91–93]. Further discussion of transient picosecond behaviour is described in section 2.4.

After formation of the LIBP, the plasma itself has its own internal fields and collective behaviour [42; 50; 91–94]. Modelling the behaviour after ignition in an LIBP is crucial for the optimization of LIBS and interpreting results from it therein. The most common approach used is the assumption of local thermodynamic equilibrium (LTE) [20; 21]. LTE is discussed in greater detail in Appendix A. In brief though, LTE states that the temperature of the electrons, T_e, the ions, T_i, and neutrals, T_n, in the plasma can all be described by the same

temperature T, i.e., $T_e = T_n = T_i = T$ [20; 21; 83; 95]. However, the emitted photons from the plasma are characterized by a different temperature, T_ω, hence the LTE assumption asserts that $T_e = T_n = T_i \neq T_\omega$ [20; 21; 83; 95]. Under LTE, this implies that spatial and temperature gradients are minimal, and that the plasma as a whole can be characterized using a partition function from Boltzmann statistics [20; 21; 83; 95].

While there are concerns with the assumption, and even outright disagreement over the appropriate timescale for its validity (see ref. [18; 20; 21; 96] and the discussion in Appendix A section A.1). Despite these criticisms, in this thesis, the LTE assumption is used in the calculation of the LIBP optical properties in section 2.3 for the ease of calculation. This can be justified in that the concern with this thesis is not the interpretation of spectral lines, but given typical orders of magnitude of T and n_e is whether or not THz transmission through the LIBP plume feasible.

In the following section, plasma evolution timescales with reference to recombination are discussed. The reason for this is because the timescales over which recombination processes occur in part contribute to the overall duration of a LIBP plume. The reason why plasma evolutionary timescales are a concern, is that if the evolutionary timescales are too fast, transmissive THz spectroscopy becomes difficult. For example, Verhoff et al. noted that light emission becomes very weak after 100 ns in the case of fs-ablated brass [8]. Taking 100 ns to be the order of magnitude where the bulk of the plasma dynamics occurs, means that to properly sample the LIBP requires a stage delay of,

$$\Delta x = \frac{c\Delta t}{2} = \frac{(300\,\mathrm{mm/ns})\,(100\,\mathrm{ns})}{2} = 1.5 \times 10^4\,\mathrm{mm} = 15\,\mathrm{m}.$$

This means that a stage delay of $\Delta x \simeq 15\,\mathrm{m}$ is required to even sample the plume, which is not feasible using classical approaches for THz spectroscopy. What this back of the envelope calculation shows, is that if the plasma lifetime is too short, transmissive probing with a THz pulse becomes difficult. Thus in assessing the feasibility of transmissive THz approaches for LIBPs, it is necessary to define and quantify LIBP plume duration which is the subject of the next section.

2.2 Charge Carrier Recombination & Plasma Lifetime

In the prior sections, the focus has been on how LIBPs are formed. How LIBPs dissipate is through the process of charge carrier recombination (CCR) [79]. As stated by Shen ionization and recombination are two competing processes which can exist simultaneously as per eqn. 2.1 [70]. Under the LTE framework, these processes should be balanced and $dn/dt = 0$ in eqn. 2.1 [20; 83]. This balance is violated at the initial stages of optical breakdown and at later timescales [18; 20; 96]. During the initial stages of optical breakdown, the reason for this imbalance is because the presence of a strong electric field provided by the laser pulse increases the likelihood of ionization events [88]. Under the influence of this strong laser field, $w_{\mathrm{MPI}} > r$ and a LIBP plume is formed.

Recombination works in reverse, requiring the capture of a free particle [97]. As discussed by Hemenway et al., the direct capture of an electron by a heavy ion is very unlikely [97]. This is because bound particles may possess only discrete values of energy and momentum [97]. Free particles, meanwhile, may have any value of energy and momentum on a continuum so the odds that they have the exact energy and momentum required to occupy a bound state is very small [97]. This necessitates the presence of a third particle to aid in the recombination process [97]. Naively, this might imply that recombination is a rare event and ionized gases whether they are an arc discharge or a LIBP should be very long lived. This is not the case however, because the density of electrons alone tends to be on the order of $n_e \sim 10^{16} - 10^{19}\mathrm{cm}^{-3}$ [7; 8; 11; 76; 77]. Furthermore, these numbers neglect ionic or neutral atom density, meaning that the overall total density is much higher. Therefore, it follows that what is a "rare event" then becomes substantially more significant just because of how many interactions the plasma constituents have with one another. Thus, it is not a question of if recombination will occur but when and how recombination will occur.

As with ionization, the possible routes for recombination are numerous in a LIBP, and include radiative recombination, dielectronic recombination, and three body recombination to name just a few [79; 83; 98–100]. Rumsby and Paul in ref. [100] separate collisional-radiative recombination into radiative recombination and three-body recombination with

the rates given respectively as,

$$r_R = \left(\frac{\mathrm{d}n_e}{\mathrm{d}t}\right)_R = -\alpha_R n_e n_i \quad r_{3B} = \left(\frac{\mathrm{d}n_e}{\mathrm{d}t}\right)_{3B} = -\alpha_{3B} n_e^2 n_i. \tag{2.9}$$

Where,

$$\alpha_R \equiv 2.7 \times 10^{-19} Z^2 T_e^{-3/4} \quad \alpha_{3B} \equiv 9.2 \times 10^{-39} Z^3 T_e^{-9/2} \ln\left(\sqrt{Z^2+1}\right),$$

are the recombination rates [100]. Rumsby and Paul observed that in collisional-radiative recombination that $n_e = \sum Z_i n_i \propto t^{-3}$ while $T_i = T_e \propto t^{-2}$ all the while collisional times would remain constant as the expansion proceeds [100]. Rumsby and Paul ascribe this phenomena to their observation that in the expansion of the LIBP, is does not exchange heat with the environment i.e., it is adiabatic [100].

This strong dependence upon the temperature discussed by Rumsby and Paul implies via eqn. 2.9 that as the plasma cools, recombination events become more likely leading to what Kuznetsov and Raizer term "low temperature cascade recombination" [79; 100]. In this case, electrons may move slow enough that they attach themselves to neutral atoms and molecules forming heavy negative ions [97]. Regardless of the pathway taken for recombination, the basic form of a recombination process is [97],

$$\frac{\mathrm{d}n_e}{\mathrm{d}t} = \gamma_{ei} - r n_e n_i. \tag{2.10}$$

Where γ_{ei} is the ion-electron pair production rate per unit volume and r is the recombination rate [97]. If quasi-neutrality holds (implying $n_e = n_i = n$) and as $\gamma_{ei} \to 0$ the solution to eqn. 2.10 is [97],

$$n\left(t\right) = \frac{n_0}{1 + n_0 r t}. \tag{2.11}$$

As to what a value r is in a fs-abalted Cu-LIBP is beyond the scope of this work. What is pertinent is that from eqn. 2.11, it is apparent that as $t \to \infty \implies n\left(t\right) \to 0$. This means that over a long enough timescale, the charge carrier density, and with it the plasma, does dissipate. The task then is to determine over what timescales does the plume dissipate and what the exact value of this lifetime is. However, for this thesis in the absence of detailed knowledge or means to directly measure what r is, PL emission duration is measured instead

and is used as a proxy for the LIBP lifetime.

The reasoning for this decision is as follows: LIBPs can be a source of both continuum and discrete sources of light [96]. While light emission is occurring, the LIBP is in a sufficiently highly excited state such that it is emitting light [78–83]. It follows then, that when PL ceases, there are not enough highly excited atoms undergoing relaxation processes, nor are there enough collisional radiative or dielectronic recombination events for light emission to be detected. Furthermore, while the processes that give rise to light emission in LIBPs are vast and varied (for details see Appendix B) they all contribute to the bulk PL emission. Thus, it is over the duration of PL emission that regardless of the recombination or emission processes ongoing within the LIBP, that the existence of the LIBP can be verified to at least a first order approximation.

A sketch of a typical LIBP PL curve is shown in fig. 2.2. It is evident from fig.2.2 that the PL emission follows a mono-exponential decay. This implies that the PL signal, I_{PL}, is $\propto \mathrm{e}^{-t/\tau_0}$, where τ_0 is the $1/e$ lifetime of the PL. If the oscilloscope response is taken to be a Gaussian, $g\left(t\right)$, with a standard deviation, t_w, this means that the signal measured in total, $I\left(t\right)$, is,

$$I\left(t\right) = g\left(t,\tau\right) * I_{\mathrm{PL}}\left(\tau\right) = A_0 \int_{-\infty}^{+\infty} d\tau \mathrm{e}^{-\frac{\left(t-\tau-t_0\right)^2}{2t_w^2}} \mathrm{e}^{-\frac{\tau}{\tau_0}} \theta\left(\tau - t_0\right). \tag{2.12}$$

Where $\theta\left(\tau - t_0\right)$ is the Heaviside step function, A_0 is a constant, and t_0 is the time at which PL emission is detected. By numerically fitting the convolution integral given by eqn. 2.12 to LIBP-PL data acquired from a photodiode, one can estimate τ_0. Note though the integral given by eqn. 2.12 can be solved analytically, and the solution is shown in full in Appendix D and the answer is given later in chapter 5 section 5.1. For now what is important is that eqn. 2.12 provides a means to obtain extract a τ_0 from a PL curve similar to the one sketched out in fig. 2.2.

The importance of τ_0 is that it forms the basis for the definition of a full PL lifetime. In analogy to RC circuits which are said to be discharged after a period of five time constants have passed [101], it is assumed that after a period of $5 \times \tau_0$ all PL emission ceases. This $5 \times \tau_0$ period is termed the full PL-lifetime and is designated here as t_{PL} and is equal to $t_{\mathrm{PL}} = 5\tau_0$. Fig. 2.2 is a sketch of a typical LIBP-PL curve with τ_0 and t_{PL} labelled.

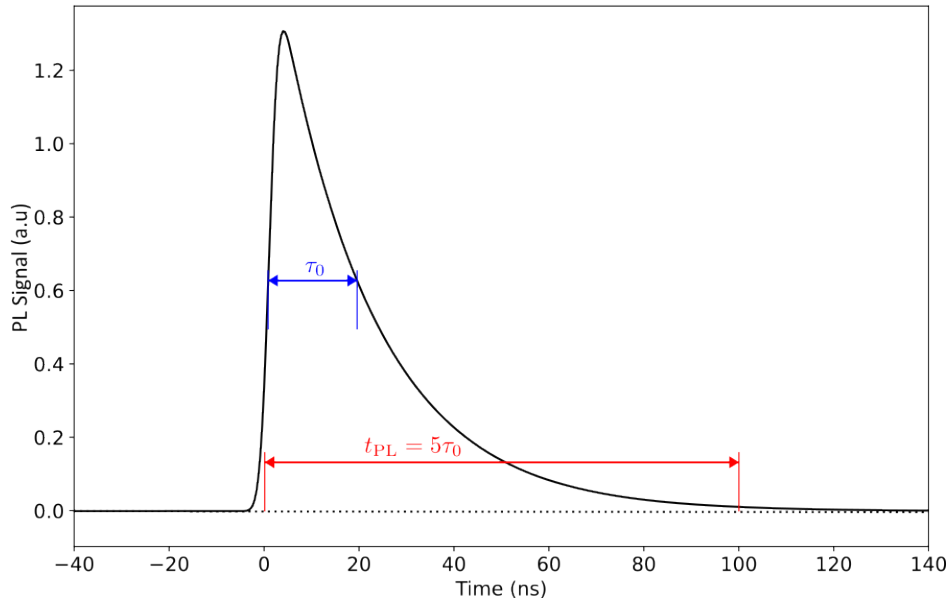

Figure 2.2: A sketch of PL a curve with the $1/e$ lifetime, τ_0 and the full PL-lifetime, t_{PL}. In this thesis, τ_0 is estimated by numerically evaluating convolving the Gaussian scope response with the PL signal, $I_{\mathrm{PL}} \propto \mathrm{e}^{-t/\tau_0}$.

In this thesis, the PL duration τ_0 will be used to estimate the lifetime of the LIBP plume. The author does not claim that this metric represents the totality of plasma phenomena duration (see ref. [11]). However, it is sufficient to use as a first order estimate to gauge the viability of transmissive THz spectroscopy in LIBPs for the reasons stated prior. The question of plasma duration and synchronization will be re-visited in chapter 5 section 5.1. However, even if synchronization could be solved, there remains the issue of whether or not the optical properties of the LIBP plume are such that they are transmissive over the THz range. Which is the subject of the next section.

2.3 Terahertz Transmission in Laser-Induced Breakdown Plasmas

As mentioned prior, there were two experimental approaches which informed this thesis. The first approach is a transmission geometry where a LIBP is probed with single-cycle THz pulses that would lay the ground work for using transmissive approaches in conjunction

with LIBS to measure and model LIBPs. The second approach is to use the LIBP itself as an "antennae" which would produce THz radiation that would then be measured. The reasoning for the former approach stems from van Exter et al. in ref. [13] and Cheville and Grischkowsky in ref. [16]. Van Exter et al. showed that THz pulses were strongly absorbed by water molecules [13]. Furthermore, the absorption coefficient can be used to estimate the water content [17].

There was further precedent for this approach in the literature as THz pulses have already been used to study inductively coupled plasmas (ICPs) in a transmissive geometry [27–30]. The electron density, n_e, measured using transmissive THz approaches when compared to Langmuir probes, as done by Ando et al., showed strong agreement with the Langmuir probes affirming the validity of this technique [30]. Just as significant, Mics et al. performed transmissive THz spectroscopy on a diatomic oxygen gas target plasma using a fs-pulse pump and a THz probe [31] and Chen et al.'s single-shot THz probing of warm dense gold [33].

However, this alone is not enough to indicate that transmissive THz approaches are feasible. This is because in ref. [27–30] the plasmas are formed from gaseous targets which are broken down by an RF arc discharge, with the notable exception of ref. [31] which uses fs-pulses. This is an issue because the electron densities of gaseous targets such as those reported in ref. [27–31] have electron densities ranging from $n_e \sim 10^{11} - 10^{16}\text{cm}^{-3}$. Electron densities from solid targets reported in LIBS papers are $n_e \sim 10^{16} - 10^{19}\text{cm}^{-3}$ [7; 8; 11; 76; 77]. This large difference in the orders of magnitude could imply that densities in LIBPs are simply too high for transmissive THz approaches. To investigate this claim, a simulation was performed assuming a free-electron model and typical LIBS parameters reported in ref. [7; 8; 11; 76; 77]. Assuming a free electron model entails that the plasma behaviour is Drude-like and the plasma frequency is given by [35],

$$\omega_p = \sqrt{\frac{n_e e^2}{\epsilon_0 m_e}} \implies f_p = \frac{1}{2\pi}\sqrt{\frac{n_e e^2}{\epsilon_0 m_e}}, \tag{2.13}$$

where $e = 1.6 \times 10^{-19}\,\text{C}$ is the elementary charge, n_e is the electron density, and $m_e =$

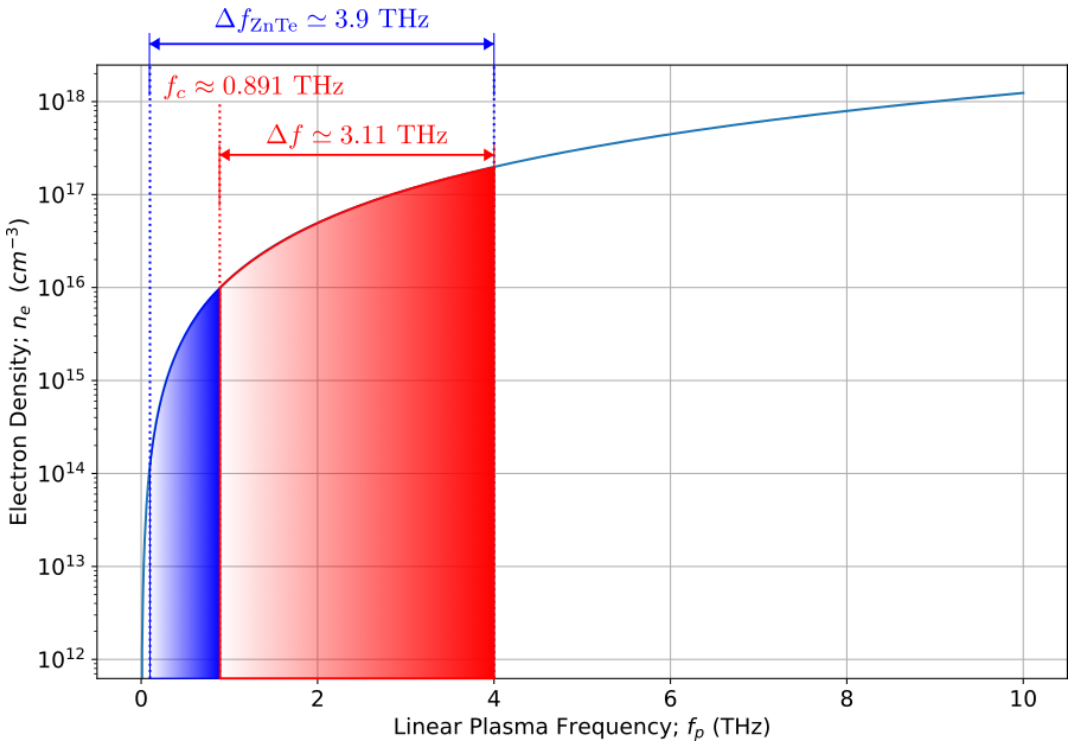

Figure 2.3: Graph of eqn. 2.14. These results hint that there should exist some THz transmission in a LIBP. Δf_{ZnTe} represents the approximate bandwidth of the ZnTe crystal used in this work. f_c is the frequency beyond which, the order-of-magnitude densities of the plasmas seen in LIBPs appear. Δf is the approximate bandwidth over which THz transmission in LIBPs could occur. This Δf covers the lower order band of typical LIBS densities ($n_e \sim 10^{16} - 10^{17}\mathrm{cm}^{-3}$).

9.11×10^{-31} kg and is the electron mass. Re-arranging eqn. 2.13 for n_e gives,

$$n_e = \epsilon_0 m_e \left(\frac{2\pi f_p}{e}\right)^2 . \tag{2.14}$$

In analogy to solids, one can assert that at ω_p a LIBP becomes transparent [102]. To see if the densities given in LIBS literature even permit transmission within the ZnTe detection crystal bandwidth used in this thesis shown in fig. 2.3, amounted to choosing values of f_p such that they fall within the range $f \simeq 0.1 - 4$ THz and back solving for the associated densities using eqn. 2.14. For linear plasma frequencies of $f_p = 0.3, 1, 2, 3\,\mathrm{THz}$, this gives electron densities of $n_e = 1.1 \times 10^{15}, 1.2 \times 10^{16}, 5.0 \times 10^{16}, 1.1 \times 10^{17}\,\mathrm{cm}^{-3}$ which indicates that for at least the lower bounds of typical LIBPs reported in literature, THz transmission could be possible.

To see how transmissive an LIBP is, the transmission coefficient, T_t, reflection coefficient, R, and penetration depth, δ, over the THz range are plotted in fig. 2.4 - 2.6. The LIBP in this case is treated as a slab of length $l = 1.5\,\text{mm}$, consisting of one ionic species and electrons, is considered static in time, and under vacuum. In addition density and temperature are isotropic, satisfying the conditions for LTE given by criteria A.6-A.7. The final assumption is that electron-ion collisions dominate over other collision types (e.g. electron-electron or electron-neutral collisions) if this is so, the Coloumb logarithm for electron-ion collisions, $\Pi_{e,i}$ is [103],

$$\Pi_{e,i} = 23 - \ln\left(Z\sqrt{\frac{n_e}{T_e}}\right) \quad \text{where} \quad T_i\frac{m_e}{m_i} < T_e < 10Z^2 \ \text{ eV}. \tag{2.15}$$

Where n_e is in units of cm^{-3} and T_e in units of eV in eqn. 2.15. The momentum scattering time τ is then estimated to be [103],

$$\tau \simeq 3.44 \times 10^5 \frac{T_e^{3/2}}{n_e \Pi_{e,i}} \quad [\text{s}] \tag{2.16}$$

in eqn. 2.16, the units of T_e are in K and n_e are in m^{-3}. The parameters for the simulation are tabulated in table 2.1. For all cases the electron temperature is $T_e = 1 \times 10^4\,\text{K}$, an the ion charge of $Z = 2$ and a cross-sectional length $l = 1.5\,\text{mm}$. The reasoning for the choice of T_e and l, is because these parameters are the order of magnitude for LIBP as measured by LIBS experiments [7; 8; 11; 76; 77]. The choice of $Z = 2$ is arbitrary. While in truth there could be multiple ionic species present in a LIBP, they are ignored here for both the sake of simplicity and that changing the ionic charge did not cause significant deviations from the results presented here. Note that the simulation was far more sensitive to changes in l and T_e.

Details outlining the simulation algorithm are shown in Appendix C. To summarize briefly, after calculating n_e and τ from eqn. 2.14 and 2.16, the optical properties are then calculated by propagating through the relations shown in Appendix C, with the imaginary and real components of the index of refraction being given by [102],

$$n_1 = \frac{1}{\sqrt{2}}\left(\sqrt{\epsilon_1^2 + \epsilon_2^2} + \epsilon_1\right)^{1/2}, \quad n_2 = \frac{1}{\sqrt{2}}\left(\sqrt{\epsilon_1^2 + \epsilon_2^2} - \epsilon_1\right)^{1/2}. \tag{2.17}$$

The results of 2.17 can then be used to calculate the reflectivity R and transmissivity T_t [102],

$$R = \frac{(n_1 - 1)^2 + n_2^2}{(n_1 + 1)^2 + n_2^2}, \quad T_t = \frac{(1 - R)^2 \, \mathrm{e}^{-\alpha l}}{1 - R^2 \mathrm{e}^{-2\alpha l}}. \tag{2.18}$$

Where α is the absorption coefficient. Note T_t is the transmission through the plume accounting for multiple internal reflections, while R is the reflectivity for both sides of the plasma surface. Note that the form of T_t used here is valid for when the coherence length, $l_c = c/\Delta f$, is negligible in comparison to the cross-sectional length, l [102]. For a typical THz pulse from a photoconductive antenna, $\Delta f \simeq 2 \times 10^{12}\,\mathrm{Hz}$ giving an l_c of $l_c = 1.5 \times 10^{-4}\,\mathrm{m}$ which is significantly smaller than the cross-sectional length $l = 1.5 \times 10^{-3}\,\mathrm{m}$ used here. This means that the form of T_t quoted here is a reasonable approximation [102]. To obtain the penetration depth, δ, and with it the absorption coefficient, α, requires only n_2 from eqn. 2.17 giving [102; 104],

$$\delta = \frac{1}{\alpha} = \frac{c}{2 n_2 \omega} = \frac{c}{4\pi n_2 f}. \tag{2.19}$$

The plots of eqn. 2.18 - 2.19 are shown in fig.2.4-2.6. As expected, the higher n_e is, the harder it is for a THz pulse to travel through the cross-sectional length of $l = 1.5\,\mathrm{mm}$ which even at ω_p proves difficult for a waveform to traverse (fig. 2.6-2.6). This is further shown in fig. 2.4 as higher n_e entails a slower convergence towards $T_t \to 1$.

f_p (THz)	n_e ($\times 10^{15}$ cm^{-3})	$\Pi_{e,i}$	τ (ps)
0.3	1.1	4.8	65
1.0	12	3.6	7.8
2.0	50	2.9	2.4
3.0	110	2.5	1.3

Table 2.1: Simulation parameters for fig.2.4-2.6. For all cases $T_e = 1 \times 10^4\,\mathrm{K}$, $Z = 2$ and $l = 1.5\,\mathrm{mm}$.

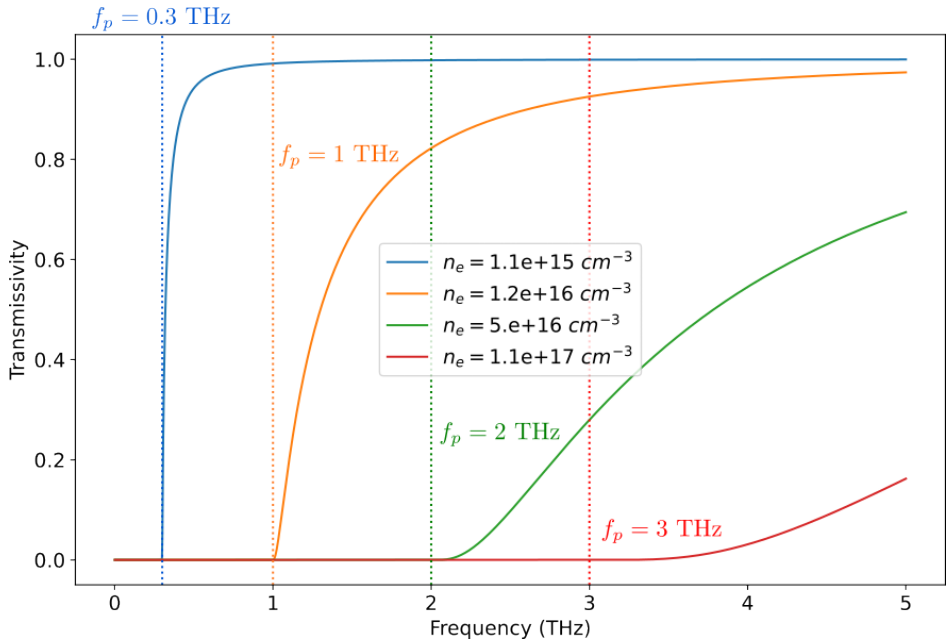

Figure 2.4: THz transmissivity (T_t) spectra through a LIBP slab with densities varying from $n_e \sim 10^{15} - 10^{16}$ cm^{-3}. This means, that transmissive spectroscopy is feasible for at least the lower bound on the typical LIBP electron densities quoted in literature ($n_e \sim 10^{16} - 10^{19}$cm^{-3}), while THz transmission would be strongly suppressed for $n_e \gtrsim 10^{-17}$ cm^{-3}. The dashed lines correspond to the linear plasma frequency, $f_p = \omega_p/2\pi$ used.

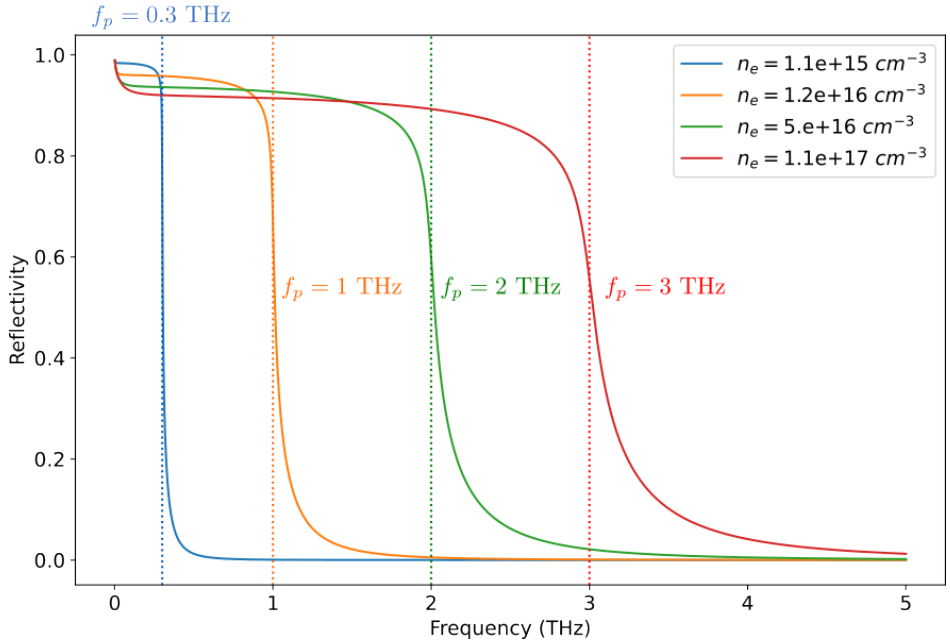

Figure 2.5: The reflectivity (R) spectra for a LIBP of $n_e \sim 10^{15} - 10^{16}$ cm^{-3} for a single side of a LIBP slab surface. The dashed lines correspond to the linear plasma frequency, $f_p = \omega_p/2\pi$ used.

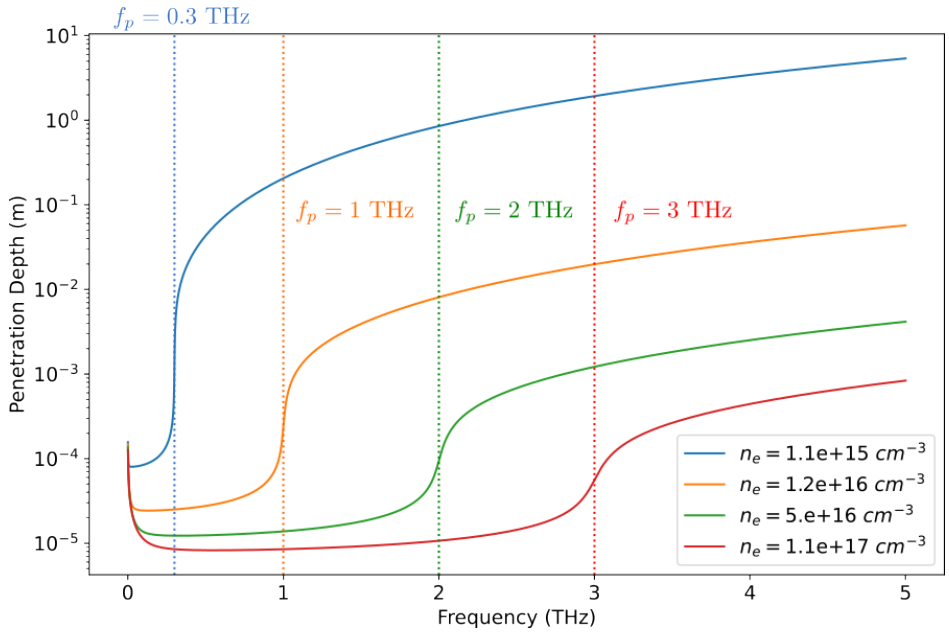

Figure 2.6: The penetration depth, δ, over the ZnTe frequency bandwidth. Coloured-dashed lines indicate plasma frequencies, $f_p = \omega_p/2\pi$ used. As expected, the higher the plume density the harder it is for THz band light to traverse the LIBP plume.

Considering the case where the LIBP is weakly collisional or collisionless, in the space-charge picture illustrated in fig. 2.1(b) the electrons precede the ions in the early times within the first few picoseconds [91–93]. Li et al. for example, estimated based on the hemispherical shadow that appeared in their work, that electrons were ejected at a speed of $v_e \sim 1.4 \times 10^7\,\mathrm{m/s}$ [93]. J.S. Pearlman and G.H. Dahlbacka note that on average the electrons lead the ions at the front of the expansion in the early time [89]. If this is so, this would mean that within the first few picoseconds, a LIBP under vacuum is collisionless. In light of this, $1/\tau \to 0$ and the expression for the relative dielectric constant reduces down to [15; 35],

$$\epsilon_r(\omega) = 1 - \frac{\omega_p^2}{\omega^2}. \tag{2.20}$$

The reflectivity can then be calculated using eqn. 2.20 according to [102],

$$R = \left|\frac{\tilde{n}-1}{\tilde{n}+1}\right|^2 = \frac{\epsilon_r - 2\sqrt{\epsilon_r}+1}{\epsilon_r + 2\sqrt{\epsilon_r}+1} \tag{2.21}$$

where the relation $n = \sqrt{\epsilon_r}$ has been used. The transmissivity shown in eqn. 2.18 still holds,

but the absorption coefficient is now re-defined as [15],

$$\alpha(\omega) = \frac{1}{\delta} = \frac{2\sqrt{\omega_p^2 - \omega^2}}{c} \quad \text{for} \quad \omega < \omega_p. \tag{2.22}$$

Plotting eqn. 2.21 along with δ defined according to eqn. 2.22, and the transmissivity in eqn. 2.18 using absorption coefficient defined in eqn. 2.22 gives fig. 2.9-2.9.

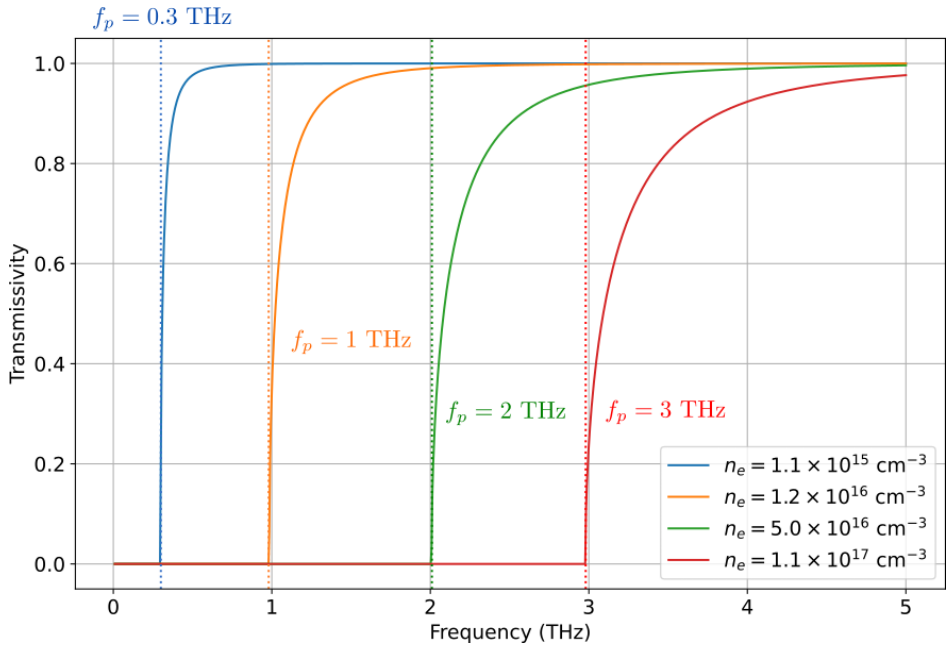

Figure 2.7: The transmissivity in the collisionless limit. T_t here represents the transmissivity through the plasma slab in the THz region. The absorption coefficient, α used in the calculation of T_t is given by eqn. 2.22. The collisionless transmissivity converges much faster towards unity than the collisional counterpart shown in fig. 2.4.

These simulation results show an even greater degree of transmissivity in the THz band than the previous simulation results which included the effects of collisions (fig. 2.4-2.6). With the penetration depth rapidly approaching infinity in the case of fig. 2.9 and an even quicker convergence to unity than it's collisional counterpart shown in fig. 2.4. Regardless in both the later-time collisional shown in fig. 2.4-2.6, and the earlier time collisionless cases, shown in fig. 2.7-2.9 seem to indicate that some degree of transmissivity is feasible. In both cases higher n_e indicates slower convergence towards unity.

An implication of fig. 2.4-2.9 is that due to the higher n_e at earlier times (see ref. [7; 8; 11; 76; 77]), the THz pulse should experience a large $-\Delta\mathcal{T}$. This follows from the

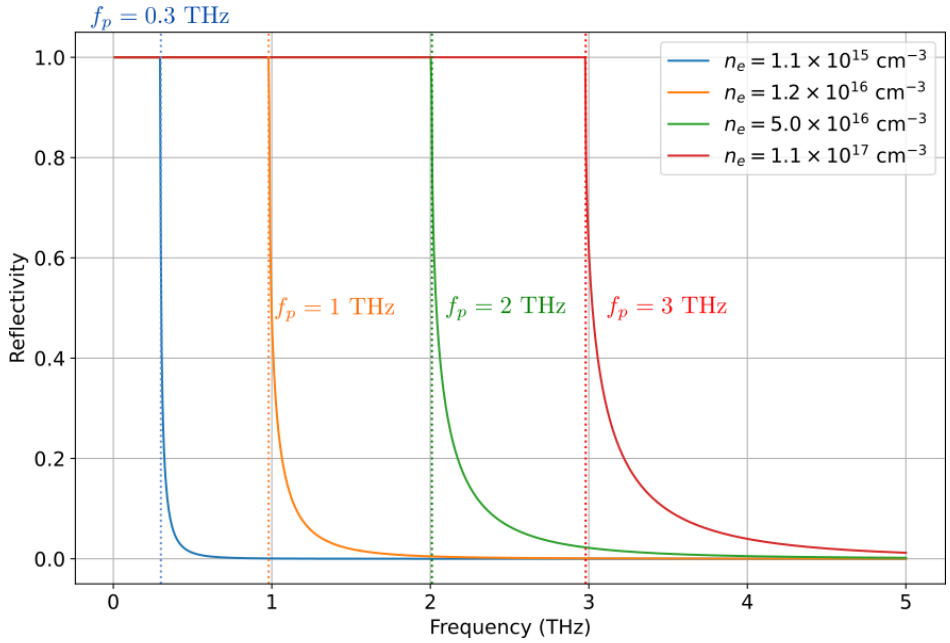

Figure 2.8: Reflectivity in the collisionless limit. The reflectivity here represents the reflectivity of a single side of the plasma slab. The curves in this figure were calculated using eqn. 2.20-2.21.

definition of $-\Delta\mathcal{T}$, which states that $-\Delta\mathcal{T} \equiv \mathcal{T}_{\text{Pump}} - \mathcal{T}_{\text{Ref}}$ [57; 58]. In the context of LIBPs, $\mathcal{T}_{\text{Pump}}$ would refer to the THz pulse travelling through a LIBP, while the $\mathcal{T}_{\text{Ref}}$ would refer to the THz pulse travelling through air. In light of this fig. 2.4-2.9 would indicate that LIBP would totally screen the THz pulse in the early times resulting in a very large $\Delta\mathcal{T}$. However, $\Delta\mathcal{T} \longrightarrow 0$, as the LIBP undergoes recombination and transmission would become feasible.

In practice though when performing the measurement, no $\Delta\mathcal{T}$ was observed. There are two possible reasons for this: (1) lack of spatial overlap and (2) lack of synchronization. Spatial overlap refers to the alignment of the LIBP plume at the THz focus. The lack of spatial overlap comes from misalignment of the sample surface with the THz focus. Spatial overlap can be solved with relative ease with the use of guiding lasers and a fine adjust translation stage mount. Synchronization though requires careful consideration of the plasma duration, the arrival of the ablation/PE pulse, and the arrival of the THz probe pulse. Issues with synchronization arise if the LIBP dissipates before the arrival of the THz pulse, or alternatively, if the THz pulse arrives long before the ablation pulse necessary for optical breakdown. In this thesis the issues with synchronization proved difficult to surmount within the period of investigation as the LIBP was both relatively short-lived (see chapter 5) and

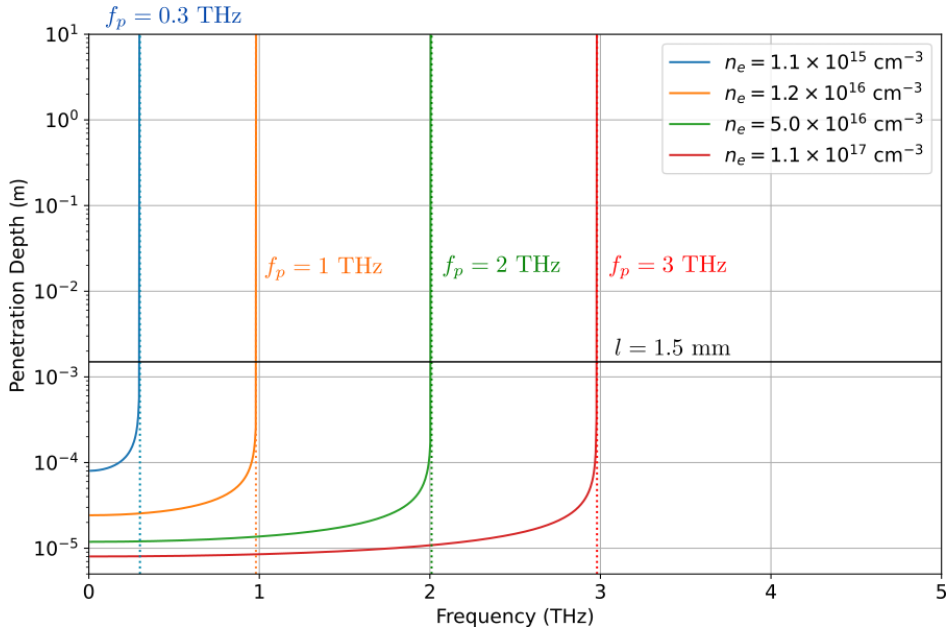

Figure 2.9: The optical penetration depth in the collisionless limit. The solid black line represents the cross-sectional length of the LIBP plume. These results indicate that at $\omega = \omega_p$ the penetration depth diverges quite quickly.

the asynchronicity between the two laser systems means that the arrival of the THz pulse with respect to the ablation pulse was constantly shifting. It is for these reasons that the transmissive approach was abandoned.

2.4 Terahertz Emission in Laser-Induced Breakdown Plasmas

There are two main models of THz emission in LIBPs: the first of which is the ponderomotive model proposed by Hamster et al. in ref. [51; 52] and the second model is the photocurrent model proposed by Sagisaka et al. in ref. [50]. In the ponderomotive model, THz emission arises from a ponderomotive potential under a strong electric field provided by the laser pulse [51; 52]. This strong electric field drives charge carriers in the plasma resulting in THz emission [51; 52]. In addition Hamster et al. posits, that in addition to the ponderomotive driving force, difference and sum frequency mixing between the oscillations inside the plasma and the laser pulse bandwidth contribute to a non-linear current density

which in the far field gives rise to THz emission [51; 52]. In the photocurrent model, the magnetic field of the optical excitation pulse produces a driving force on the photoexcited electrons within the plasma or by electrons moving along the target surface [49; 50; 54]. Neither of these approaches are sufficient for the findings in this thesis. For in the both sets of experiments, the authors used a pre-pulse and an amplified-spontaneous emission pulse to make a preformed plasma which was subsequently driven by the proceeding main fs-pulse [50–52; 54].

In this thesis the THz emission seen in fig. 6.1-6.4 cannot be sufficiently explained by either model. For as noted in LIBS literature, for the case of femtosecond ablation, the fs-pulse does not interact with the plasma [8; 10]. This means that in the absence of a pre-pulse with sufficient energy to induce ablation, there can be no preformed plasma and therefore, no ponderomotive effect. This means that any THz emission that is seen must arise either from some nonlinear bulk process or from the LIBP plume itself. For this thesis, the experiment performed for emissive THz detection of LIBPs, the only pulse used for the LIBP formation was a $\lambda_0 = 795\,\text{nm}$ femtosecond pulse with a pulsewidth, τ_p, of $\tau_p = 70\,\text{fs}$. However, even assuming that there was non-negligable pre-pulse, for the Ti:Sapphire system used in this thesis the typical contrast ratio between the main pulse and any pre-pulse is $E_{pp}/E_p \approx 1/500$. This implies that the corresponding absorbed fluence (estimated here to be $\Phi \approx 3.82\,\text{J/cm}^2$ for the main pulse) would be $\Phi \approx 7.64\,\text{mJ/cm}^2$ for the pre-pulse. $\Phi \approx 7.64\,\text{mJ/cm}^2$ is well below the minimum ablation threshold fluence found by both Nolte et al. ($\Phi_0 = 140\,\text{mJ/cm}^2$) and Hashida et al. ($\Phi_0 = 18\,\text{mJ/cm}^2$) for Cu [72; 74]. This indicates that there is a limited possibility of a preformed plasma appearing before the arrival of the main pulse, and thus a need for a different approach to understanding the THz emission shown in fig. 6.1-6.4.

The mechanism that the author proposes is a rapid space-charge separation occurring on picosecond timescales in a manner analogous to the photo-Dember effect. This speculation has grounding in that rapid space-charge separation in LIBPs has been documented before in the literature [89; 91–93]. Femtosecond electron shadow imaging measurements in ref. [91–93] even show rapid picosecond behaviour. In ref. [93] for example, Li et al. used femtosecond electron shadow imaging to show that there appears a transient electric field within the first $\sim 10\,\text{ps}$ of the LIBP lifetime [93]. Li et al estimated based on the hemispherical shadow that

appeared in their work that electrons were ejected at a speed of $v_e \sim 1.4 \times 10^7\,\mathrm{m/s}$ with electric fields up to $\mathcal{E} \simeq 2.4 \times 10^5\,\mathrm{V/m}$ at a distance of around $\sim 140\,\mu\mathrm{m}$ from the Cu-target surface under a vacuum of $1 \times 10^{-9}\,\mathrm{torr}$[93]. Such a rapid charge expulsion in the first few picoseconds of the LIBP plume lifetime should give rise to a THz transient.

To account for the results seen here in fig. 6.1-6.4, the following toy model considers first the density of incident photons from a Gaussian pulse in the ablation volume given by,

$$n_p(t) = n_0 \exp\left(-\frac{t^2}{\tau_p^2}\right) \quad \text{where} \quad n_0 = \frac{N_0}{V_A} = \frac{1}{V_A}\frac{E_p}{\hbar\omega_0}(1-R)\,. \tag{2.23}$$

Where τ_p is the pulse duration on the order of $\sim 10^{-13}$ s, $V_A = \pi w_0^2 \delta$ is the ablation volume of the sample, and δ is given by eqn. 2.19, E_P the energy of the pulse, and $\hbar\omega_0$ is the energy of the central laser wavelength. There exists some relation between the photon density described by eqn. 2.23 amd the charge carrier density, n_c, since the absorption of photons corresponds to the production of charge carriers through either multiphoton-ionization, the photoelectric effect, or thermionic emission is directly related to the initial laser pulse as it provides the energy [75]. However, not all the photons in the distribution described by eqn. 2.23 contribute to the charge carrier production process. To account for this, assume that there exists a constant of proportionality η_C such that the relation between $n_p(t)$ and $n_c(t)$ is,

$$\eta_C \equiv \frac{n_c(t)}{n_p(t)} \implies \therefore n_c(t) = \eta_C n_p(t) = \eta_C n_0 \exp\left(-\frac{t^2}{\tau_p^2}\right). \tag{2.24}$$

Where $0 \leq \eta_C \leq 1$ with $\eta_C \to 0$ corresponds to no charge carrier production, while $\eta_C \to 1$ implies that all the incident photons in the ablation volume contribute to charge carrier production. This parameter is a direct analog to the quantum efficiency of semiconductors (see ref. [105] for details regarding the quantum efficiency). In semiconductors, the quantum efficiency is a dimensionless constant which indicates how good the semiconductor is at emitting light [105]. Likewise, η_C is termed the charge carrier production efficiency of the sample and is a dimensionless parameter which indicates the degree of charge carrier production that occurs in the ablation volume. The velocity of the charge carriers after plasma

formation is assumed to be an exponential decay, i.e.,

$$\vec{v}\,(t) = \vec{v}_0 \exp\left(-\frac{t}{\tau_v}\right). \tag{2.25}$$

Where $\vec{v_0} = v_0\hat{n}$ is a constant velocity vector which is normal to the surface of the sample. τ_v is a constant that corresponds to some velocity relaxation processes in the charge carriers. The space-charge current density of the LIBP can then be calculated by the convolution of eqn. 2.24-2.25,

$$\begin{aligned}\vec{J} = e\,(n_c * v)\,(t) &= eA_0\eta_C n_0 v_0 \int_{-\infty}^{+\infty} d\tau\theta\,(\tau - t_0)\,\mathrm{e}^{-\frac{(t-t_0-\tau)^2}{\tau_p^2}}\mathrm{e}^{-\frac{\tau}{\tau_v}}\;\hat{n} \\ \vec{J} = e\,(n_c * v)\,(t) &= \rho_0 v_0 \int_{t_0}^{+\infty} d\tau \mathrm{e}^{-\frac{(t-t_0-\tau)^2}{\tau_p^2}}\mathrm{e}^{-\frac{\tau}{\tau_v}}\;\hat{n} \quad \text{where} \quad \rho_0 = eA_0\eta_C n_0.\end{aligned} \tag{2.26}$$

Where A_0 is some arbitrary constant of integration and $\theta\,(\tau - t_0)$ is the Heaviside function and t_0 the time at which the light is incident upon the sample. The full evaluation of the integral shown in eqn. 2.26 is nearly identical to that of the one performed for the PL seen later with minor differences being the constants out front and that $t_0 = 0$ at the end. The derivation for the PL is given in full in Appendix D. For now, the result of eqn. 2.26 is,

$$\vec{J} = e\,(n_c * v)\,(t) = \frac{\sqrt{\pi}}{2}\rho_0\tau_p \mathrm{e}^{-\frac{t}{\tau_v}+\frac{\tau_p^2}{4\tau_v^2}}\left[1 + \mathrm{erf}\left(\frac{t}{\tau_p} - \frac{\tau_p}{2\tau_v}\right)\right]\vec{v}_0. \tag{2.27}$$

The magnitude of eqn. 2.27 is shown in fig. 2.10. The THz electric field $\mathcal{E}_{THz}$ can then be related to the current density according to, $\mathcal{E}_{THz} \propto \partial J/\partial t$ [60–63; 65; 66]. So taking the derivative of eqn. 2.27 with respect to time gives a function,

$$\vec{\mathcal{E}} \propto \frac{\partial\vec{J}}{\partial t} \propto \rho_0 \mathrm{e}^{-\frac{t^2}{\tau_p^2}}\vec{v_0} - \frac{\sqrt{\pi}\tau_p}{2\tau_v}\rho_0 \mathrm{e}^{-\frac{t}{\tau_v}+\frac{\tau_p^2}{4\tau_v^2}}\left[1 + \mathrm{erf}\left[\frac{t}{\tau_p} - \frac{\tau_p}{2\tau_v}\right]\right]\vec{v_0}. \tag{2.28}$$

Plotting eqn. 2.28 gives a single-cycle THz pulse shown in fig. 2.11. From this general theoretical description, one can conclude that assuming ultrafast carrier dynamics in the early times of a LIBP, THz emission can be expected. What is sketched out here is not a complete picture of the dynamics by any stretch. For example, the exact values for the constants in eqn. 2.27-2.28 are not known. Furthermore, it is not clear as to what the actual

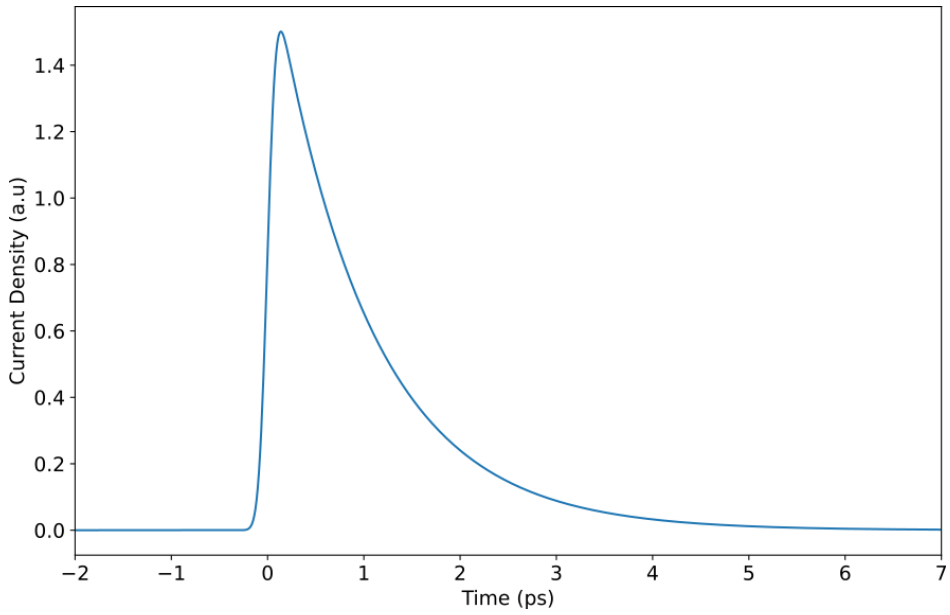

Figure 2.10: A graph of the transient current density in a LIBP based on eqn. 2.27. This transient current arises from a rapid space-charge effect. This space-charge effect gives rise to a strong internal electric field inside the plasma which drives charged particle motion. The fall time is determined by the velocity relaxation time, τ_v, which in this figure is $\tau_v = 1\,\text{ps}$. The rise time is determined by, τ_p, which in this figure is $\tau_p = 100\,\text{fs}$.

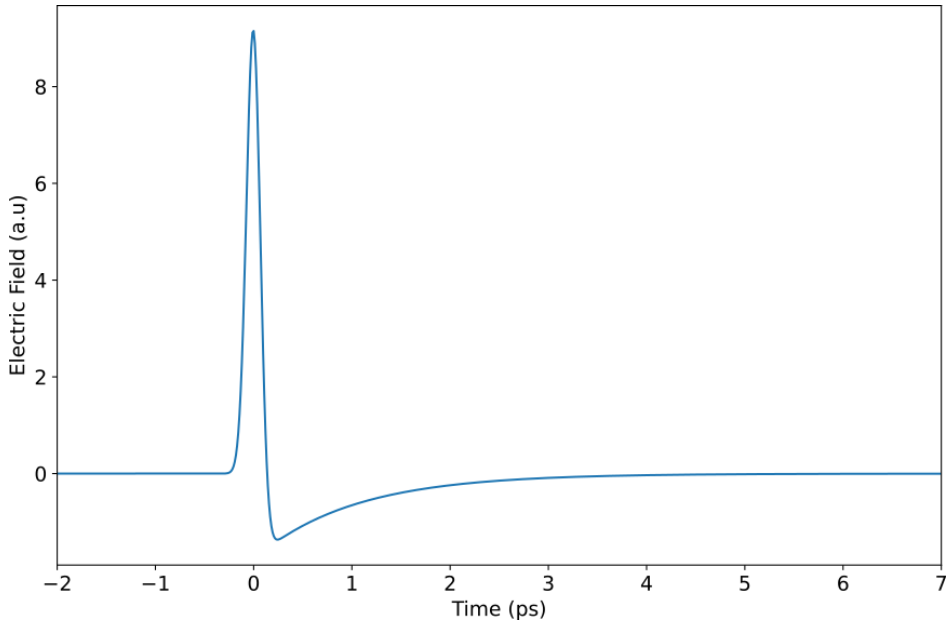

Figure 2.11: A single-cycle THz pulse obtained by taking the derivative of current density shown in fig. 2.10. This results confirms that a space-charge model can reproduce a THz pulse.

velocity relaxation processes are or how to decouple them. What the model outlined in eqn. 2.24-2.28 does demonstrate is that a space-charge effect can give rise to a THz transient in the far-field. Furthermore, this is sufficient to explain results seen in fig. 6.1-6.4. To the best of the author's knowledge there has been no attempt to explain THz transients in terms of a space-charge effect alone in the absence of a driving laser field.

Note that there could be other process from the bulk, that could contribute to THz radiation that emerges from the interaction of solid-targets with ultrafast lasers. For example, while Sagisaka et al.'s model is based on the assumption that there exists a preformed plasma, it's central argument is that there exists some free-charge that is driven by the oncoming laser pulse [50; 54]. Sagisaka assumed that this free-charge comes from the magnetic field of the fs-driven plasma which then drives the current in the Ti target [50]. Fei et al. differs from Sagisaka et al. in that they ascribe THz emission to the flow of electrons along the target surface driven by the laser field [54]. Fei et al.'s assertion the author speculates, is based on the observation that electrons in metals are free-charges that can be driven by an electric field, resulting in a current density $\vec{J} = \tilde{\sigma}\vec{\mathcal{E}}$ [35]. Fei et al. argues that the THz emission is attributable to a photocurrent along the target surface [54],

$$J = J_0 \exp\left\{-\frac{t^2}{\tau_0^2}\right\}\delta\left(\vec{r}\right), \tag{2.29}$$

where J_0 is directly proportional to the laser intensity, $\delta\left(\vec{r}\right)$ is the Dirac-delta evaluated at some coordinate $\vec{r}$, and τ_0 is a constant depending on the laser-pulse width. A limitation of Fei et al.'s approach though, is the total neglect of the aforementioned space-charge effect which has been known to occur over picosecond timescales [54; 91–93]. Decoupling potential photocurrents from the resulting space-charge effect is not within the scope of this thesis. However, they are a possible contributor that the reader should be aware of. A specific nonlinear effect of note that could contribute to THz generation arising from the bulk in metals is optical rectification [67; 68]. For more information on optical rectification see chapter 3 subsection 3.3.3.

Any future modelling of THz emission from solid-target LIBPs needs to take into account the presence of the space-charge, which to the best of the author's knowledge has not been

made explicit as of writing. Such a model should be able to re-create something akin to fig. 2.10-2.11. A possible avenue to consider is the Fowler-Dubridge Model of Photoemission. In this model, current density is represented by a superposition of partial current densities corresponding to thermionic, thermally assisted photoemission, and n-photon ionization [75; 106; 107]. J.P. Girardeau-Montaut and C. Girardeau-Montaut attempted to develop a theory of ultra-fast nonlinear multiphoton photoelectric emission from metals using the Fowler-Dubridge formalism outlined in ref. [106; 107] in their own work [75]. However, J.P. Girardeau-Montaut and C. Girardeau-Montaut claimed they were unsuccessful in their endeavour because their extension did not justify the link between processes at the microscopic scale and the macroscopic photoelectric response of the material [75]. While there were subsequent follow up studies to J.P. Girardeau-Montaut and C. Girardeau-Montaut neither J.P. Girardeau-Montaut and C. Girardeau-Montaut nor the later follow up studies make any mention of THz emission [75; 108–110]. Though all of the previously cited studies make reference to picosecond to sub-picosecond timescale phenomenon [75; 108–110].

Chapter 3

Electron-Hole Plasmas

This chapter describes Electron-Hole plasmas (EHPs). While the idea for plasma-like effects occuring within solids goes back to Kronig and Korringa in 1943 [111; 112] and Bower's makes reference to plasmas in semiconductors in particular in ref. [37]. EHPs started to be seriously investigated in light of Van Vechten and R. Tsu's proposal that an EHP could be used to account for pulsed laser annealing in semiconductors which could not be explained using thermal or simple melt models [38; 39; 41]. The annealing according to Van Vechten and R. Tsu, was instead said to arise from the presence of an EHP [39; 41]. In this thesis, EHPs are used to benchmark transmissive and emissive THz techniques. As such some background on EHPs is required. This chapter begins with a discussion on EHP formation. To describe EHPs, the Drude model is used as in the previous chapter. This is because the Drude model features describe parameters of EHPs that can be measured using single-cycle THz pulses [23; 25; 40]. The section proceeding the Drude model will then elaborate on various THz generation mechanisms that can occur within semiconductors. With a focus on the photo-Dember effect and surface currents in addition to a brief discussion on nonlinear effects that could contribute to THz generation. This will lead into a section outlining the theory of photo-conductive antennae which exploit surface currents to generate THz pulses.

3.1 Electron-Hole Plasma Formation

The formation of EHPs begins with the creation of electron-hole pairs (e-h pairs) through PE, described in fig. 3.1. When a semiconductor is PE by a photon of energy, $\hbar\omega$, at or above the band gap energy, E_G, an electron occupying the valence band is promoted into the conduction band [113; 114]. This results in a vacancy within the valence band, which is equivalent to the creation of a hole in the valence band [113]. Thus, every electron promoted to the conduction band necessitates the creation of a corresponding hole in the valence band [113; 115].

During PE, laser energy is absorbed by one of two mechanisms in semiconductors: (1) electron-hole pair creation or (2) free-carrier excitation [41]. The energy absorption comes from the imaginary part of the dielectric constant, ϵ_2 [40]. This is a consequence of free-carrier screening, where at frequencies above ω_p, $n_2 = \epsilon_2/2n_1$ and $\alpha \propto n_2 \implies \alpha \propto \epsilon_2/2n_1$ [35]. There are two contributions to this absorption: the first is from EHP absorption and the second comes from the creation of e-h pairs [40]. A rate of generation of e-h pairs can be written explicitly as [40],

$$\frac{\partial n}{\partial t} = \frac{2\pi\epsilon_0}{\hbar}\epsilon_2\mathcal{E}^2. \tag{3.1}$$

Initially, with few carriers present, the process (1) dominates so that near the surface the photon absorption rate A of [40],

$$A(\hbar\omega) = \frac{\partial n}{\partial t} = 2\pi\frac{(1-R)}{\hbar\omega}\frac{\mathcal{E}^2}{Z_0\delta}\mathrm{e}^{-z/\delta}. \tag{3.2}$$

Where $Z_0 = 377\,\Omega$ is the impedance of free-space, R the reflectivity, and δ is the optical penetration depth given by eqn. 2.19 [40].

Qualitatively, the evolution of the electronic system during PE can be understood as follows: the pulse is first absorbed over the penetration depth δ (eqn. 2.19) and creates e-h pairs with an exponential profile over δ [40]. The sample will act according to eqn. 3.2 until the surface e-h density reaches the plasma frequency density, n_p [40]. At n_p the real part of the dielectric function becomes zero and consequently, the electromagnetic field changes from a propagating wave to an exponentially decaying wave [40].

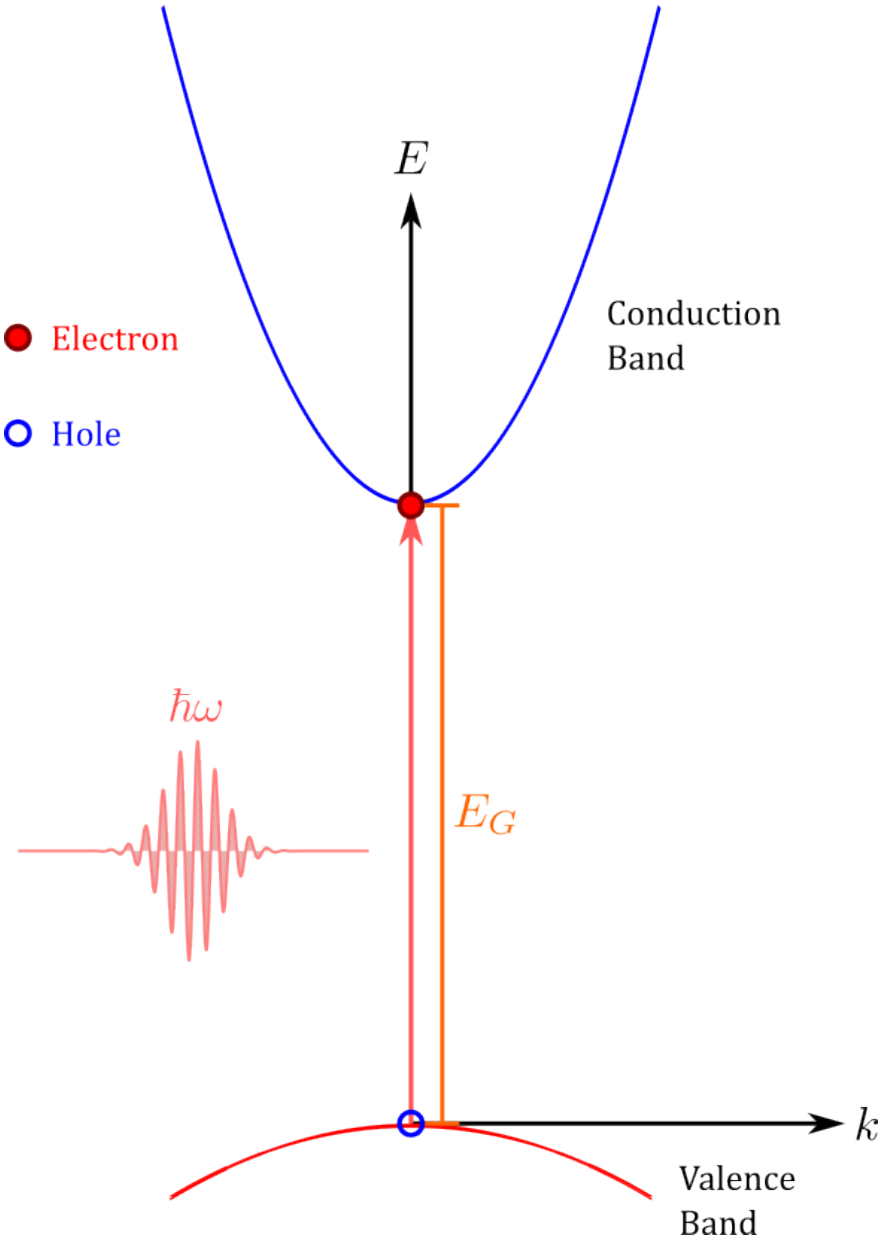

Figure 3.1: A photoexcitation (PE) by a light pulse with energy $\hbar\omega$ promoting an electron to the conduction band resulting in the appearance of a hole in the valence band. For the electron to be promoted to the conduction band, the energy of the light pulse $\hbar\omega$ must be such that, $\hbar\omega \geq E_G$. This PE of a semiconductor results in the production of electron-hole pairs.

The net result is the production of hot electrons and holes which then thermalize with other carriers and eventually the lattice [38; 41]. The primary channels for energy relaxation of these hot carriers are collisions with other carriers, plasmon production, phonon emission, and electron-hole pair production via impact ionization [41]. For high carrier densities $n >$

10^{19} cm^{-3}, the plasmon energy is typically greater than phonon energies [41]. Consequently, plasmon-phonon coupling is weak and phonon production by plasmons is negligible [41]. This means that no energy is transferred to the lattice by the creation of plasmons and their decay, the energy lost by the hot electrons remains in the carrier system [41]. Carriers though may emit phonons thereby ensuring that the energy is transferred from the e-h plasma to the lattice [41]. Beyond n_p thermalization begins, and so to do thermal processes such as diffusion and recombination [40; 41]. The description of some of the resulting optical properties of the EHP can be encompassed by the Drude model which is discussed in the next section.

3.2 Electron-Hole Plasma Evolution and Dynamics

The classical description of an EHP starts with the Drude-Lorentz model. In this model the electrons are considered to be freely moving as they collide with the surrounding lattice. The in this model, the equation of motion for the electrons is [35; 40],

$$\frac{\mathrm{d}^2\vec{x}}{\mathrm{d}t^2} + \frac{1}{\tau}\frac{\mathrm{d}\vec{x}}{\mathrm{d}t} = \frac{e\vec{\mathcal{E}}\,(t)}{m^*}. \tag{3.3}$$

Where τ is the relaxation time and m^* is the effective mass of the EHP defined as [40],

$$\frac{1}{m^*} \equiv \frac{1}{m_e} + \frac{1}{m_h}.$$

The solution to eqn.3.3 is given by the ansatz $\vec{x}\,(t) = \vec{x}_0 \exp(-i\omega t)$ [35; 40].[1]

$$\frac{\mathrm{d}^2x}{\mathrm{d}t^2} + \frac{1}{\tau}\frac{\mathrm{d}x}{\mathrm{d}t} = \frac{e\mathcal{E}\,(t)}{m^*} \implies -\omega^2 x_0 \mathrm{e}^{-i\omega t} - \frac{i\omega}{\tau}x_0\mathrm{e}^{-i\omega t} = \frac{e\mathcal{E}\,(t)}{m^*}$$
$$\therefore x\,(t) = x_0\mathrm{e}^{-i\omega t} = -\frac{e}{m^*}\frac{\mathcal{E}\,(t)}{(\omega^2 + i\omega/\tau)} = -\frac{e}{m^*}\frac{\mathcal{E}\,(t)}{(\omega^2 + i\gamma\omega)}.$$

[1] For convenience sake the vector notation is dropped in the proceeding derivation as there is minimal loss of generality.

Recall that the polarization for a dipole model is $\left|\vec{\mathcal{P}}\right| = \mathcal{P} = nex$ [35; 40]. Substituting the Ansatz derived solution gives the polarization as [35; 40],

$$\mathcal{P} = nex = -\frac{ne^2}{m^*}\frac{\mathcal{E}(t)}{(\omega^2 + i\gamma\omega)} = -ne^2\left(\frac{1}{m_e} + \frac{1}{m_h}\right)\frac{\mathcal{E}(t)}{(\omega^2 + i\gamma\omega)}$$

The displacement electric field which is defined as [35],

$$\vec{D} = \epsilon_0\vec{\mathcal{E}} + \vec{\mathcal{P}}_{fc} + \vec{\mathcal{P}}_m = \epsilon_0\epsilon_m\vec{\mathcal{E}} = \tilde{\epsilon}\vec{\mathcal{E}}.$$

Where $\vec{\mathcal{P}}_{fc}$ is the free carrier polarizability and $\vec{\mathcal{P}}_m$ is the bound electron polarizability before the addition of dopants [35]. It is from the def. of $\vec{D}$ that the dielectric constant is derived for the intraband contribution of an EHP, yielding [35; 40],

$$\begin{aligned} D = \epsilon_0\mathcal{E} + \mathcal{P} + \mathcal{P}_m &= \epsilon_0\epsilon_m\mathcal{E} - ne^2\left(\frac{1}{m_e} + \frac{1}{m_h}\right)\frac{\mathcal{E}}{(\omega^2 + i\gamma\omega)} \\ D &= \epsilon_0\epsilon_m\left[1 - \frac{ne^2}{\epsilon_0\epsilon_m m^*}\frac{1}{(\omega^2 + i\gamma\omega)}\right]\mathcal{E} \\ \implies \therefore \tilde{\epsilon} &= \epsilon_0\epsilon_m - \frac{ne^2}{m^*}\frac{1}{(\omega^2 + i\gamma\omega)} = \epsilon_0\epsilon_m\left[1 - \frac{\omega_p^2}{(\omega^2 + i\gamma\omega)}\right] \end{aligned} \tag{3.4}$$

Where ϵ_m is the background permittivity accounting for the the polarizability of an undoped semiconductor and $\omega_p^2 = ne^2/(\epsilon_0\epsilon_m m^*)$ is the plasma frequency [35; 41]. For a more elaborate calculation of the dielectric constant using the random phase approximation (RPA) see ref. [41]. The conductivity of the EHP follows a similar procedure to the one outlined for the dielectric constant. The key difference being that the velocity of an e-h pair is under consideration meaning that eqn. 3.3 becomes [35],

$$\frac{\mathrm{d}\vec{v}}{\mathrm{d}t} + \frac{1}{\tau}\vec{v} = \frac{e\mathcal{E}(t)}{m^*}$$

and the ansatz used is $\vec{v} = \vec{v}_0\exp(-i\omega t)$. Through the definition of current density, $\vec{J} = ne\vec{v} = \sigma\vec{\mathcal{E}}$, one arrives at an EHP conductivity of [35],

$$\tilde{\sigma}(\omega) = \frac{n\tau e^2}{m^*}\frac{1}{1 - i\omega\tau} = \frac{\sigma_0}{1 - i\omega\tau}. \tag{3.5}$$

Where σ_0 is the DC electric conductivity [35]. Splitting eqn. 3.5 into real and imaginary components gives,

$$\sigma_1 = \frac{\sigma_0}{1+(\omega\tau)^2} = \frac{ne^2\tau}{m^*}\frac{1}{1+(\omega\tau)^2} \quad \& \quad \sigma_2 = \sigma_0\frac{\omega\tau}{1+(\omega\tau)^2} = \frac{ne^2\tau}{m^*}\frac{\omega\tau}{1+(\omega\tau)^2}. \tag{3.6}$$

Using the results of eqn. 3.6 it can be shown that the dielectric constant real and imaginary components are in terms of σ_1 and σ_2,

$$\epsilon_1 = 1 - \frac{\sigma_2}{\epsilon_0\omega} \quad \& \quad \epsilon_2 = \frac{\sigma_1}{\epsilon_0\omega}. \tag{3.7}$$

As to how the dielectric constant and the conductivity described by eqn. 3.4-3.7 can be measured and the existence of the EHP state verified, recall that the dielectric constant given by eqn. 3.4 has an imaginary component. This imaginary component of eqn. 3.4 corresponds to a damping process in the EHP and consequently, the absorption of an electromagnetic wave [40]. If the PE is such that $\hbar\omega > E_G$, e-h pair production (process (1)) will quickly give way to free-carrier excitation/absorption (process (2)) and any subsequent electromagnetic radiation incident is then screened [35; 40; 114].

If a THz pulse is travelling through the sample sometime after the PE pulse induces free-carrier production, the THz pulse will then be attenuated by the free-carriers giving rise to a transmissivity of $\mathcal{T}_s$, which differs from the initial transmissivity through the sample in the absence of PE, $\mathcal{T}_0$ [26; 57; 58]. Taking this difference between free-carrier screened pulse and the nominal pulse then gives rise to the $-\Delta\mathcal{T}$ which is defined for this instance as $-\Delta\mathcal{T} \equiv \mathcal{T}_0 - \mathcal{T}_s$ [26; 57; 58]. This change in the THz pulse arises from free-carrier screening which can be represented as a change in the dielectric response given by eqn. 3.4 and through, eqn. 3.7, the conductivity to the oncoming THz pulse. This hints at the existence of some relation between $-\Delta\mathcal{T}/\mathcal{T}_0$ and the conductivity, $\tilde{\sigma}$. The exact nature of that relation is given by the Tinkham equation [57],

$$-\frac{\Delta\mathcal{T}}{\mathcal{T}_0} = \frac{Z_0 l\tilde{\sigma}}{n_1 + 1 + Z_0 l\tilde{\sigma}} = \frac{Z_0 l\,(\sigma_1 + i\sigma_2)}{n_1 + 1 + Z_0 l\,(\sigma_1 + i\sigma_2)} \tag{3.8}$$

where $Z_0 = 377\,\Omega$ is the impedance of free-space, l is the thickness of a thin film, n_1 is the

real part of the refractive index defined in eqn. 2.17 and is evaluated at THz wavelengths. If under strong free-carrier screening, $\epsilon_2 \gg \epsilon_1$ which implies via eqn. 3.7 that $\sigma_1 \gg \sigma_2$ reducing eqn. 3.8 down to,

$$-\frac{\Delta\mathcal{T}}{\mathcal{T}_0} \approx \frac{Z_0 l \sigma_1}{n_1 + 1 + Z_0 l \tilde{\sigma}} \implies -\frac{\Delta\mathcal{T}}{\mathcal{T}_0} \approx \frac{1}{\frac{n_1+1}{Z_0 l \sigma_1} + 1}.$$

If $(n_1 + 1)/Z_0 l \sigma_1 \gg 1$ one can write an expression for σ_1 as [57],

$$\sigma_1 \approx \frac{n_1 + 1}{Z_0 l}\left[-\frac{\Delta\mathcal{T}}{\mathcal{T}_0}\right]. \tag{3.9}$$

Eqn. 3.9 implies that by varying the delay between optical-pump pulse and the THz-probe pulse, it is then possible to obtain a time-resolved conductivity measurement [22; 24; 25; 57–59]. Eqn. 3.8 and 3.9 form the basis for optical-pump[2] and THz-probe style experiments [22; 24–26; 57; 59].

In this thesis, a optical-pump THz-probe scheme is used where a $\lambda = 795\,\text{nm}$, $\hbar\omega = 1.56\,\text{eV}$ pulse acts as the pump that is used to PE the semiconductors GaAs and Si. While a THz pulse is used as the probe to monitor the resulting dynamics. For this thesis, the goal is to simply obtain a $-\Delta\mathcal{T}$ signal for LIBPs, for if such a signal can be obtained, it would then show that techniques used in the study of EHPs can be applied to LIBPs. Finally, the presence of an EHP should manifest as a spike in the $-\Delta\mathcal{T}$ signal. It will be shown in chapter 5 section 5.2 that this spike in the $-\Delta\mathcal{T}$ signal does indeed occur (see fig. 5.5 and 5.7). For now the discussion will turn to how THz generation in an EHP occurs.

3.3 Terahertz Generation in Semiconductors

THz emission mechanisms in bulk semiconductors can be grouped into nonlinear and linear processes [60]. Nonlinear processes can arise from some inherent asymmetry in the material (e.g., the electronegativity difference between Zinc and Tellurium atoms in ZnTe gives rise to an asymmetric potential along the chemical bond) or high intensity PE at, or above, E_G [60; 116; 117]. Linear processes are explained in terms of the current surge model on the

[2]Optical refers to any non-THz band light that is photo-exciting the semiconductor.

semiconductor surface induced by PE [60]. The current surge is thought to have two origins: (1) the acceleration of PE carriers by the surface depletion region and (2) the photo-Dember effect; where charge carriers diffuse into the semiconductor bulk [60–63]. Typically more than one of these processes may exist within a semiconductor and are often difficult to decouple from one another as they often co-exist [61–63]. To start, the discussion of linear processes will proceed first. This will establish not only the means by which semiconductors typically generate THz emission, but will serve as the basis for how photoconductive antennae used in this experiment work. Nonlinear processes, particularly optical rectification, will be discussed in brief.

3.3.1 Linear Processes: The Photo-Dember Effect & Surface Current

In the photo-Dember effect THz emission arises from a diffusive current in the bulk of the material [61; 63]. This occurs if two inter-related conditions are met: (1) the mobility difference between electrons and holes in the semiconductor is very large, i.e., $\mu_e \gg \mu_h$ and (2), the structural asymmetry within the material is significant [63]. Fig. 3.2 gives a pictorial representation of the photo-Dember effect at various stages in time. In the initial stage (fig. 3.2 stage (i)), the PE creates a large number of e-h pairs [38; 40; 41; 63]. Since $\mu_e \gg \mu_h$, the electrons precede the holes and accelerate into the bulk of the semiconductor (fig. 3.2 stage (ii)) [60; 61; 63]. This rapid charge separation then gives rise to a transient photo-Dember potential, V_D (fig. 3.2 stage (ii)) [60]. Eventually, the charge carriers undergo recombination and the semiconductor returns to equilibrium (fig. 3.2 stage (iii)) [63].

In the vicinity of a surface, reflection or capture of charges results in the centre of charge for electrons and holes moving away from the surface [63]. A dipole subsequently forms perpendicular to the surface, leading to THz emission [63]. Because of this diffusion into the bulk, the photo-Dember effect is bulk dominated, changing the semiconductor doping from n- to p-type has no effect on the sign of the polarity of the THz pulse [60; 62; 63]. Examples of primarily photo-dember effect emitters include InAs and InSb; both of which have relatively large electron mobilities in comparison to their hole mobilities ($\mu_e = 7.6 \times 10^4\,\mathrm{cm^2{\cdot}V^{-1}s^{-1}}$ vs

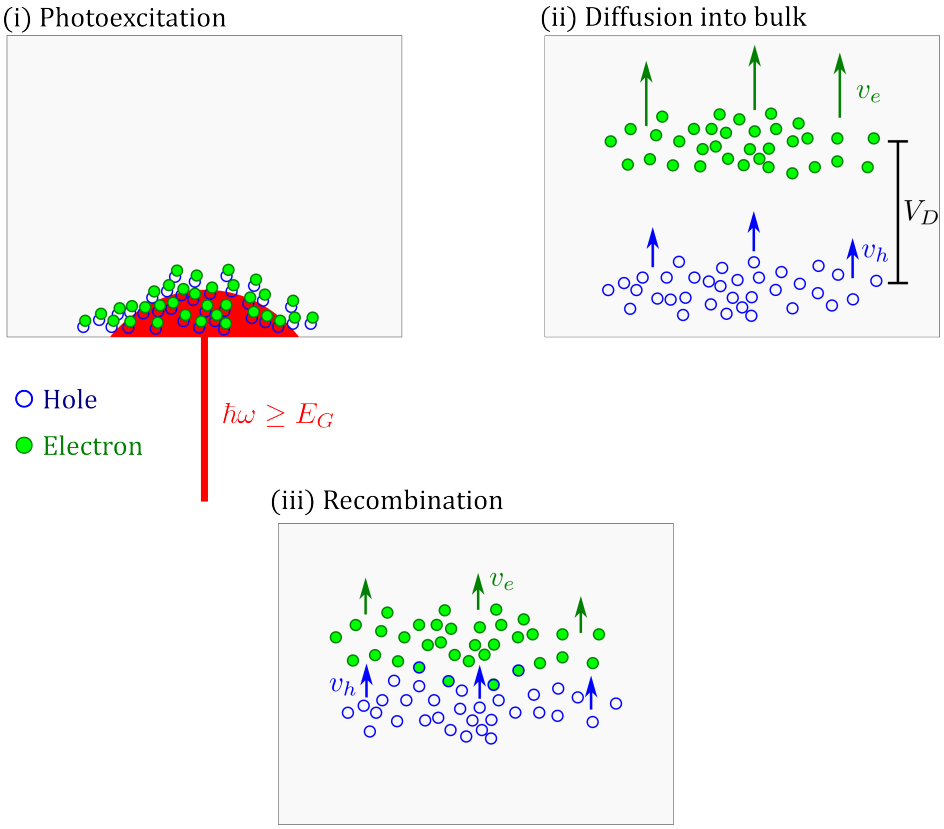

Figure 3.2: Diagram detailing the Photo-Dember mechanism. (i) PE with a laser of energy $\hbar\omega$, such that $\hbar\omega \geq E_G$ creates electron hole pairs. (ii) The mobility difference between the holes and electrons results in the electrons diffusing into the bulk and away from the holes leading to a transient photo-Dember voltage, V_D. (iii) Electrons and holes undergo recombination.

$\mu_h = 8 \times 10^2\,\mathrm{cm^2{\cdot}V^{-1}s^{-1}}$ for InSb and $\mu_e = 3 \times 10^4\,\mathrm{cm^2{\cdot}V^{-1}s^{-1}}$ vs $\mu_h = 2.4 \times 10^2\,\mathrm{cm^2{\cdot}V^{-1}s^{-1}}$ for InAs) [60].

As is implied by the fact that the carriers driving the formation of a THz pulse comes from the bulk of the material, the photo-Dember mechanism is a diffusive process and the current arising in the semiconductor is given in part by [61],

$$\vec{J}_D = e\left(D_e \boldsymbol{\nabla} n_e - D_h \boldsymbol{\nabla} n_h\right). \tag{3.10}$$

Where D_e and D_h are the coefficients of diffusion and are given by [61],

$$D_e = \frac{\mu_e k_B T_e}{e}, \quad D_h = \frac{\mu_h k_B T_h}{e}.$$

As shown in fig. 3.2, this diffusive action described by eqn. 3.10 gives rise to a photo-Dember voltage, V_D, which can be related to the THz field according to, $\mathcal{E}_{THz} \simeq V_D/\delta$ where δ is the optical penetration depth given by eqn. 2.19 [60].

Realistically though, the photo-Dember effect can co-exist with other THz generation mechanisms [60–62]. As observed by Liu et al., higher doping concentrations can effect the diffusion current [62]. For example, in n-type InAs, the doped electrons join the drift action in the opposite direction of electron diffusion [62]. Thus, the total current can be thought of as consisting of contributions from both diffusion action and the drift action meaning that [61],

$$\vec{J} = \vec{J}_{\mathcal{E}} + \vec{J}_D = e\vec{\mathcal{E}}_s \left(n_e\mu_e + n_h\mu_h\right) + e\left(D_e\boldsymbol{\nabla}n_e - D_h\boldsymbol{\nabla}n_h\right), \tag{3.11}$$

where the $\vec{\mathcal{E}}_s$ is the surface field [61]. This naturally leads to the question of whether or not THz emission from drift current arising from surface effects and the photo-Dember effect in bulk can even be decoupled from one another.

There is a very simple check that can be performed on the semiconductor: change the dopant type between n-type (or p-type) to p-type (or n-type). If the pulse like the one shown in fig. 6.7 maintains its polarity after the dopant has been swapped, then the semiconductor can be considered to be a primarily photo-Dember emitter at that wavelength [60; 62; 63]. In contrast, GaAs is primarily a surface-field emitter so the polarity of the THz pulse seen in fig. 6.5 is dopant dependent [61; 63].

As Heyman et al. pointed out though, which term dominates in eqn. 3.11 is wavelength dependent and there do exist intermediate regimes where surface current and drift are co-equal [61]. This can be seen by rewriting eqn. 3.11,

$$\begin{aligned}
\vec{J}_{\mathcal{E}} + \vec{J}_D &= e\vec{\mathcal{E}}_s \left(n_e\mu_e + n_h\mu_h\right) + e\left(D_e\boldsymbol{\nabla}n_e - D_h\boldsymbol{\nabla}n_h\right) \\
&= en_e\mu_e\vec{\mathcal{E}}_s + n_h\mu_h e\vec{\mathcal{E}}_s + eD_e\boldsymbol{\nabla}n_e - eD_h\boldsymbol{\nabla}n_h \\
&= en_e\mu_e\vec{\mathcal{E}}_s + eD_e\boldsymbol{\nabla}n_e + n_h\mu_h e\vec{\mathcal{E}}_s - eD_h\boldsymbol{\nabla}n_h \\
\vec{J}_{\mathcal{E}} + \vec{J}_D &= n_e\left(e\mu_e\vec{\mathcal{E}}_s + eD_e\frac{\boldsymbol{\nabla}n_e}{n_e}\right) + n_h\left(\mu_h e\vec{\mathcal{E}}_s - eD_h\frac{\boldsymbol{\nabla}n_h}{n_h}\right).
\end{aligned} \tag{3.12}$$

Approximating, $\boldsymbol{\nabla}n_e/n_e = \boldsymbol{\nabla}n_h/n_h = L^{-1}$, where L is the optical absorption length and

considering only the magnitudes of the vector quantities allows one to simplify eqn. 3.12 as follows [61],

$$
\begin{aligned}
J_{\mathcal{E}} + J_D &\approx n_e \left(e\mu_e \mathcal{E}_s + eD_e \frac{\boldsymbol{\nabla} n_e}{n_e} \right) + n_h \left(\mu_h e\mathcal{E}_s - eD_h \frac{\boldsymbol{\nabla} n_h}{n_h} \right) \\
&\approx n_e \left(e\mu_e \mathcal{E}_s + eD_e \frac{1}{L} \right) + n_h \left(\mu_h e\mathcal{E}_s - eD_h \frac{1}{L} \right) \\
&\approx n_e \left(e\mu_e \mathcal{E}_s + e\frac{\mu_e k_B T_e}{e} \frac{1}{L} \right) + n_h \left(\mu_h e\mathcal{E}_s - e\frac{\mu_h k_B T_h}{e} \frac{1}{L} \right) \\
&\approx n_e e\mu_e \mathcal{E}_s + n_e \frac{\mu_e k_B T_e}{L} + n_h \mu_h e\mathcal{E}_s - n_h \frac{\mu_h k_B T_h}{L} \\
J_{\mathcal{E}} + J_D &\approx \left(n_e \mu_e + n_h \mu_h \right) e\mathcal{E}_s + \left(n_e \mu_e T_e - n_h \mu_h T_h \right) \frac{k_B}{L} \\
1 + \frac{J_D}{J_{\mathcal{E}}} &\approx 1 + \frac{n_e \mu_e T_e - n_h \mu_h T_h}{n_e \mu_e + n_h \mu_h} \frac{k_B}{e\mathcal{E}_s L}
\end{aligned}
$$

Next recall that PE produces equal number of electrons and holes, this gives $J_D/J_{\mathcal{E}}$ as,

$$
\frac{J_D}{J_{\mathcal{E}}} \approx \frac{\mu_e T_e - \mu_h T_h}{\mu_e + \mu_h} \frac{k_B}{e\mathcal{E}_s L} \approx \frac{k_B T_e}{eL\mathcal{E}_s} \tag{3.13}
$$

assuming that $\mu_e \gg \mu_h$ [61]. Using eqn. 3.13 and estimating the carrier temperature according to $3/2\ k_B T_e \sim (h\nu - E_G)$, Heyman et al. were able to estimate regimes in GaAs where drift currents dominate over diffusion [61]. Corroborating what they observed experimentally when switching to the 2nd order harmonics of $\lambda = 800\,\text{nm}$ [61].

The origin of the surface field, $\vec{\mathcal{E}}_s$, that gives rise to the drift current described in eqn. 3.11 comes from dangling bonds present at the surface of a cleaved semiconductor [65; 66; 118]. A graphical representation of the dangling bonds is shown in fig. 3.3. If the electrons in the dangling bonds shown in fig. 3.3 cannot pair with nearby atoms, these dangling bonds will interact with each other giving rise to an electrostatic surface-field, $\mathcal{E}_s$ [118]. This surface field is normal to the surface of the semiconductor and the strength of it is a function of the Schottky barrier potential and the doping concentration (see eqn. 3.17) [64]. These dangling bonds also possess their own Fermi-level E_F^S [118].

If the dopant concentration at the surface exceeds that of the bulk, the surface field can penetrate into the bulk, bending the band structure of the semiconductor [118]. The Fermi

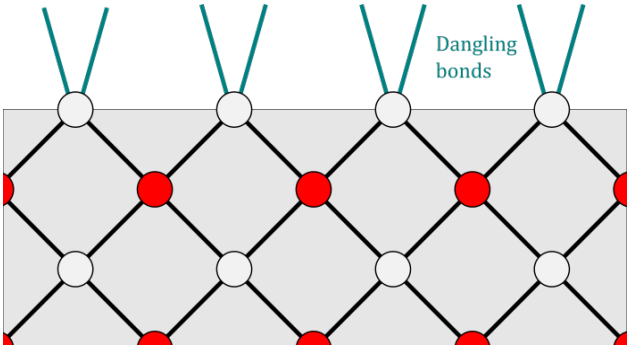

Figure 3.3: A representation of dangling bonds at the lattice-air boundary of an arbitrary semiconductor.

levels in both the bulk and surface equilibrate; resulting in band bending in both n-type and p-type semiconductors, changing the resulting band structure and subsequently "pinning" the Fermi level of the bulk [64; 66; 118]. This leads to a permanent depletion/accumulation region within the semiconductor (see fig. 3.4 - 3.5) near the surface [64; 66; 118]. This

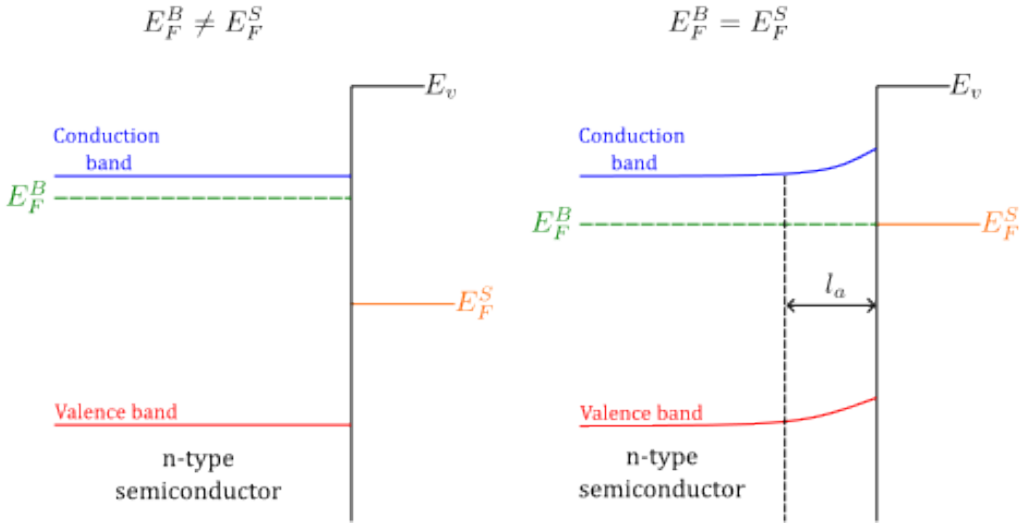

Figure 3.4: Fermi level pinning in an n-type semiconductor. Here an accumulation region l_a forms in response to the surface Fermi level E_F^S equilibrating with the bulk Fermi level E_F^B. E_v is the vacuum energy. Based on a similar figure found in ref. [118].

results in $\mathcal{E}_s$ driving electrons towards the surface (or bulk for n-type) and holes into the bulk (or surface for n-type) [64–66]. These free carriers are swept across the depletion (or accumulation) region l_d (or l_a), the photocurrent flows in, and a transient dipole forms [64–66]. This transient dipole is responsible for THz emission and is given by X.C-. Zhang as

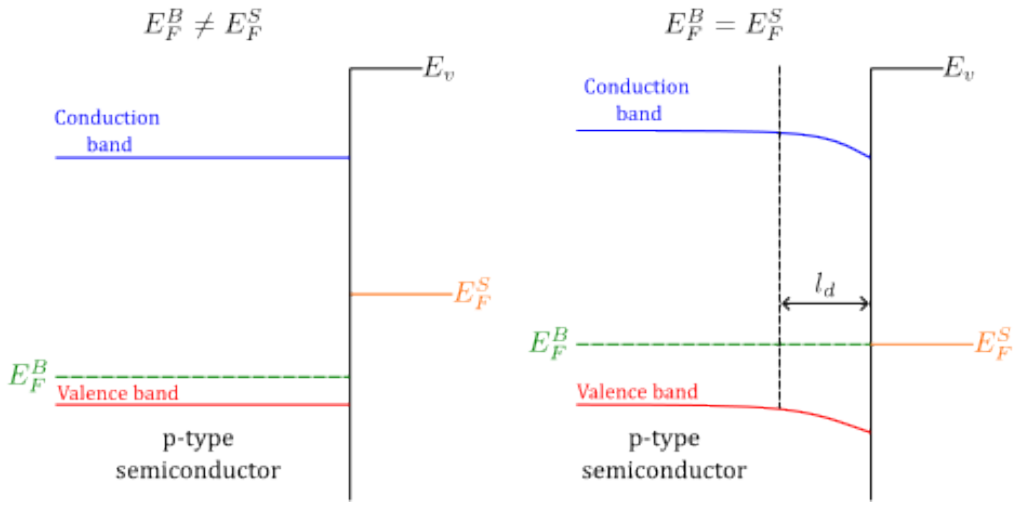

Figure 3.5: Fermi level pinning in a p-type semiconductor. Here a depletion region l_d forms in response to the surface Fermi level E_F^S equilibrating with the bulk Fermi level E_F^B. E_v is the vacuum energy. Based on a similar figure found in ref. [118].

[63; 64],

$$\mathcal{E}_{\mathrm{THz}}(\theta) = \frac{\sin\theta}{4\pi\epsilon c^2}\int_S dS\,\frac{1}{\left|\vec{r}-\vec{r}'\right|}\frac{\mathrm{d}J_s}{\mathrm{d}t}. \tag{3.14}$$

Where θ is the angle between observation direction and particle acceleration and the integral in eqn. 3.14 is performed over the entire irradiated surface area S [64]. x in this instance denotes the vertical distance between the air-semiconductor interface and the bulk [64]. The surface current density at its most general is written by X.-C Zhang et al. as [65],

$$J_s(t) = e\int_0^\infty dx\; n(x,t)\, v(\mathcal{E}_s,x,t) = e\int_0^\infty dx\; n(x,t)\,\mu(\mathcal{E}_s,x,t)\,\mathcal{E}_s(x). \tag{3.15}$$

In terms of the incident femtosecond pulse and the material parameters, J_s can be written more specifically as [64],

$$\begin{aligned} J_s(t) = \frac{e\alpha}{\hbar\omega}\left[1-R(\theta_{\mathrm{op}})\right]\int_0^{l_d} dx\;\mathcal{E}_s(x)\,\mathrm{e}^{-\alpha x}\int_{-\infty}^{t} dt'\;\mu(t-t') \\ \times\int_{-\infty}^{t'} dt''\;\mathrm{e}^{-(t'-t''/\tau_c)}I_{\mathrm{op}}(t''). \end{aligned} \tag{3.16}$$

Where α is the absorption coefficient ($\alpha \equiv 1/\delta$) for the laser light, $\hbar\omega$ is the incident photon energy in eV, $R(\theta_{\mathrm{op}})$ is the optical reflectivity at the surface with optical incident angle θ_{op},

μ is the time-domain response function of the carrier mobility, τ_c the carrier lifetime, and I_{op} is the optical pulse per unit energy [64]. The rise time of this surface photocurrent density is on the order of the laser pulse duration, and generally the decay time is the transit time of the free carriers cross the depletion (or accumulation) layer (assuming that the carrier lifetime is longer than the carrier transit lifetime) [66]. X.-C Zhang et al. gives explicit expressions for both $\mathcal{E}_s(x)$ and l_d as [66],

$$\mathcal{E}_s(x) = \frac{en_I}{\epsilon}(l_d - x) \quad \& \quad l_d = \sqrt{\frac{2\epsilon}{en_I}\left[V_S - \frac{k_B T}{e}\right]}. \tag{3.17}$$

Where n_I is the impurity concentration and V_S is the Schottky potential barrier of semiconductor [66].

3.3.2 Photoconductive Antennae Operation

Photoconductive antennas (PCAs) exploit the surface currents that arise in PE semiconductors but add to the semiconductor two biased electrodes [116]. Upon femtosecond PE, these biased electrodes drive photocarriers in an identical manner to the surface field [64; 66; 116]. The difference being in this case an external voltage is applied that then gives rise to the THz field dipole transient [64; 66; 116]. Under these conditions the equivalent to the THz dipole transient given by eqn. 3.14 is [116],

$$\vec{\mathcal{E}}_{\text{THz}}(t) = \frac{\mu_0 l_0}{4\pi}\frac{1}{r}\frac{\mathrm{d}I_{\text{pc}}}{\mathrm{d}t_r}\hat{y} \propto \frac{\mathrm{d}I_{\text{pc}}}{\mathrm{d}t} \tag{3.18}$$

Where l_0 is the gap distance between two electrodes, I_{pc} the photocurrent across the gap, and $t_r = t - r/c$ the retarded time [116]. A cross-section of the emitter structure is given by fig. 3.6. The speed and sensitivity of antennas are determined by three factors: (1) the antenna geometry, (2) the photoconductor, and (3) the optical pulse duration [116; 119]. In the case of (3), the photocurrent I_{pc} is a direct consequence of this through the convolution of optical pulse envelope, I_{op}, the charge carrier density, $n(t)$, and the speed of carriers across the gap, $v(t)$ [116]:

$$I_{\text{pc}}(t) = e\int dt\; I_{\text{op}}(t - t')\, n(t')\, v(t'). \tag{3.19}$$

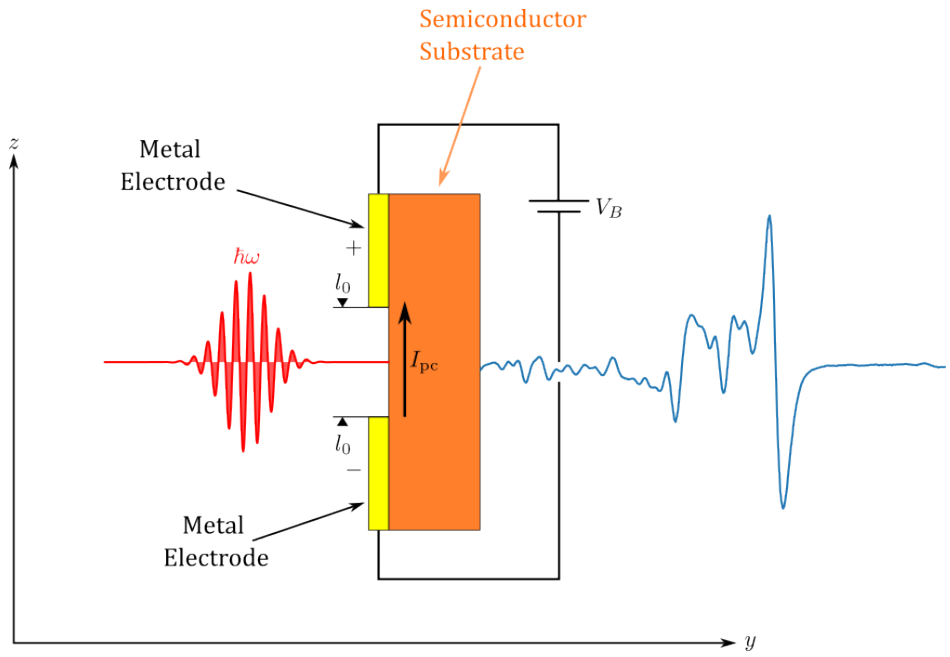

Figure 3.6: Schematic diagram of THz pulse emission from a PCA excited by a femtosecond pulse. A fs-PE pulse of energy $\hbar\omega \geq E_G$ is incident upon the semiconductor substrate resulting in photocarriers that are subsequently driven across the surface by the bias voltage, V_B, giving rise to a current given by eqn. 3.19. This current is driven over picosecond timescales resulting in a THz pulse in the far-field given by eqn. 3.18. Based on a similar figure seen in ref. [116]

Where $n(t')$ and $v(t')$ arise from dynamics of the carrier density under an impulsive excitation and the previously mentioned Drude-Lorentz model respectively giving [116]:

$$v(t) = \begin{cases} \mu_e \mathcal{E}_{\mathrm{DC}} \left[1 - e^{-t/\tau_s}\right], & t > 0 \\ 0, & t < 0 \end{cases} \qquad n_c(t) = \begin{cases} e^{-t/\tau_c}, & t > 0 \\ 0, & t < 0. \end{cases} \tag{3.20}$$

Where $\mu_e = e\tau_s/m^*$ is the electron carrier mobility, $\mathcal{E}_{\mathrm{DC}}$ is the DC electric field across the bias junction, while τ_s is the momentum relaxation time and τ_c is the carrier lifetime [116]. Experimentally, the free-carrier mobility μ in the PCA can be determined according to [116; 119],

$$\mu\tau = \frac{\hbar\omega}{e} \frac{\langle I_{\mathrm{pc}} \rangle}{\eta V_B \langle P \rangle} l_0^2 \quad \text{where} \quad \frac{1}{\tau} = \frac{1}{\tau_c} + \frac{1}{\tau_s}. \tag{3.21}$$

Where τ is the photocurrent decay time, η the illumination efficiency, and V_B the bias voltage applied [116; 119]. As is apparent from this set of equations displayed here, the output THz field strength is dependent upon the bias voltage and the optical pump pulse [116]. The amplitude of the field increases linearly with the bias voltage and pump power, however caution must be exerted when using a PCA as too high of a voltage and pump power can permanently damage the PCA placing an upper limit on the field strength that can be generated [116].

3.3.3 Nonlinear Processes: Optical Rectification

Optical rectification occurs when an applied electric field is incident on a material, which then gives rise to a pulse that is electro-static and independent of the frequency components of the applied electric field [120; 121]. What this means is that if the incident electric field varies sinusoidally in time on a material that acts as an "optical rectifier", a field with a net time average polarization will develop from the interaction that is emitted from the optical rectifier, called the "rectified pulse" [120]. If the polarity of the applied electric field switches, the polarity of the rectified pulse does not reverse when the polarization of the applied electric field is reversed [120; 122]. This process is the optical analog to that of electrical rectification, where a sinusoidal waveform when passing through a rectifier, results

in a DC signal [120]. The resulting optically rectified pulse has a polarization, $\mathcal{P}$, resulting from a second-order nonlinear process and is given by [116; 120; 121],

$$\mathcal{P}_i^{(2)}(0) = \sum_{j,k} \epsilon_0 \chi_{ijk}^{(2)}(0, \omega, -\omega)\, \mathcal{E}_j(\omega)\, \mathcal{E}_k^{\dagger}(\omega), \tag{3.22}$$

where $\chi_{ijk}^{(2)}$ is the second-order nonlinear susceptibility tensor element [123]. Optical rectification can generate THz pulses and is known to occur in semiconductors and nonlinear crystals such as ZnTe (see ref. [62; 116]). For example as discussed by Liu et al., the peak THz emission in InAs can be written as [62],

$$\mathcal{E} = \mathcal{E}_{\mathrm{PD}} + \mathcal{E}_{\mathrm{OR}} \cos(z\theta) \tag{3.23}$$

where $\mathcal{E}_{\mathrm{PD}}$ is the electric field arising from the photo-Dember effect and $\mathcal{E}_{\mathrm{OR}} \cos(z\theta)$ term represents contributions due to optical rectification. In eqn. 3.23, θ is the angle between the pulse and the surface normal and z is some fit parameter [62]. There are even documented instances of optical rectification occurring at the surface of bulk metals such as gold, silver, metallic thin films, metallic nanostructures and even gold nanoparticles [67–69; 124; 125]. Kadlec et al's detection of THz emission arising from PE of gold and silver independent of the laser polarization could indicate that similar processes can occur in bulk Cu [67; 68].

Thus, any THz emission from LIPs, including LIBPs, could have contributions from optical rectification. However, the form of eqn. 3.23 indicates that these contributions from optical rectification can be easily eliminated by simply changing the orientation of the sample plane with respect to the oncoming pulse [60; 62; 116]. This was the main motivation for changing orientation of the Cu-target from fig. 1.6(a) to 1.6(b), as the latter eliminates contributions from optical rectification. Furthermore, the presence of optical rectification could potentially account for the disappearance of frequency components seen when comparing fig. 6.2 to fig. 6.4.

Chapter 4

Experimental Methods

This chapter outlines the experiments performed to evaluate the feasibility of transmissive and emissive THz techniques for LIBPs. It begins with a discussion of electro-optic sampling (EOS), which is crucial for both the transmissive and emissive THz experiments to measure the THz pulse. This chapter then covers transmissive THz experiments, discussing the laser systems, the photoconductive antenna, the samples used and the implementation of the asynchronous method used. This is then followed by the section on emissive THz approaches. Finally, the chapter covers emissive THz approaches, explaining changes made from the transmissive setup, describing the method and how the lock-in amplifier was calibrated using semiconductor samples. The chapter aims to provide an understanding of the methods used and the reasons behind the decisions made.

4.1 Electro-optic Sampling

The technique used in this work for the detection of THz pulses is electro-optic sampling (EOS). EOS exploits the Pockel's effect in a nonlinear crystal to measure THz fields [116; 126]. The Pockel's effect states that there is a linear change in a material's refractive index with the electric field according to [117],

$$n\left(\mathcal{E}\right) = n_0 \pm \frac{1}{2} r n_0^3 \mathcal{E}, \tag{4.1}$$

where n_0 is the index of refraction at $\mathcal{E} = 0$ and r is the Pockel's coefficient of the material. The applied field, $\mathcal{E}$, leads to a phase difference between what is termed the ordinary and extraordinary rays [127]. The ordinary rays lag as the index of refraction increases for it, while the extraordinary ray travels on ahead. This phenomenon is called "birefringence." In a material undergoing birefringence, the extraordinary ray does not "see" the change in the refractive index experienced by the ordinary ray [127]. This means that by application of the Pockel's effect, a phase change, $\Delta\phi$, is induced in the incident light pulse on an electro-optic crystal with an electric field across it [117; 127]. In the context of EOS this electric field is provided by a THz pulse of magnitude, $\mathcal{E}_{\text{THz}}$, incident upon a nonlinear crystal (in this thesis the crystal used is ZnTe) prior to the arrival of an optical sampling pulse [126; 128]. This gives a phase shift, $\Delta\phi$, induced in the optical pulse of [128],

$$\Delta\phi\left(\mathcal{E}_{\text{THz}}\right) = \frac{2\pi l r_{41} n_0^3}{\lambda}\mathcal{E}_{\text{THz}}. \tag{4.2}$$

Here $r_{41} = 4\,\text{pm/V}$ and is the Pockel's coefficient for ZnTe, l is the length of the ZnTe crystal that the optical pulse traverses, $\mathcal{E}_{\text{THz}}$, is the THz electric field, and λ is the wavelength of the optical pulse [128]. In EOS, the THz field induces a phase shift, $\Delta\phi$, in the oncoming optical pulse [116; 126]. This $\Delta\phi$ is measured with three components: a quarter-wave plate (QWP), a Wollaston prism, and a pair of photodiodes, as shown in fig. 4.2 [116]. The QWP circularly polarizes the oncoming the optical emerging from the ZnTe crystal (see fig.4.1 and 4.2). The Wollaston prism breaks the components of the light pulse into its horizontal and vertical components which are then measured using a pair of photodiodes (see fig.4.1-4.3). The photodiodes are calibrated in a scenario illustrated by fig.4.1(top). In this case, there is no THz pulse to induce a phase-shift, so the optical pulse (in this thesis the optical pulse is centred around $\lambda = 795\,\text{nm}$) is circularly polarized after passing through the QWP [116]. The horizontal and vertical components are subsequently split by the Wollaston prism shown in fig. 4.1-4.3. If the photodiodes are properly calibrated, the contributions from horizontal and vertical polarizations should be equal to each other, i.e.,

$$I_h = I_v = \frac{I_0}{2}. \tag{4.3}$$

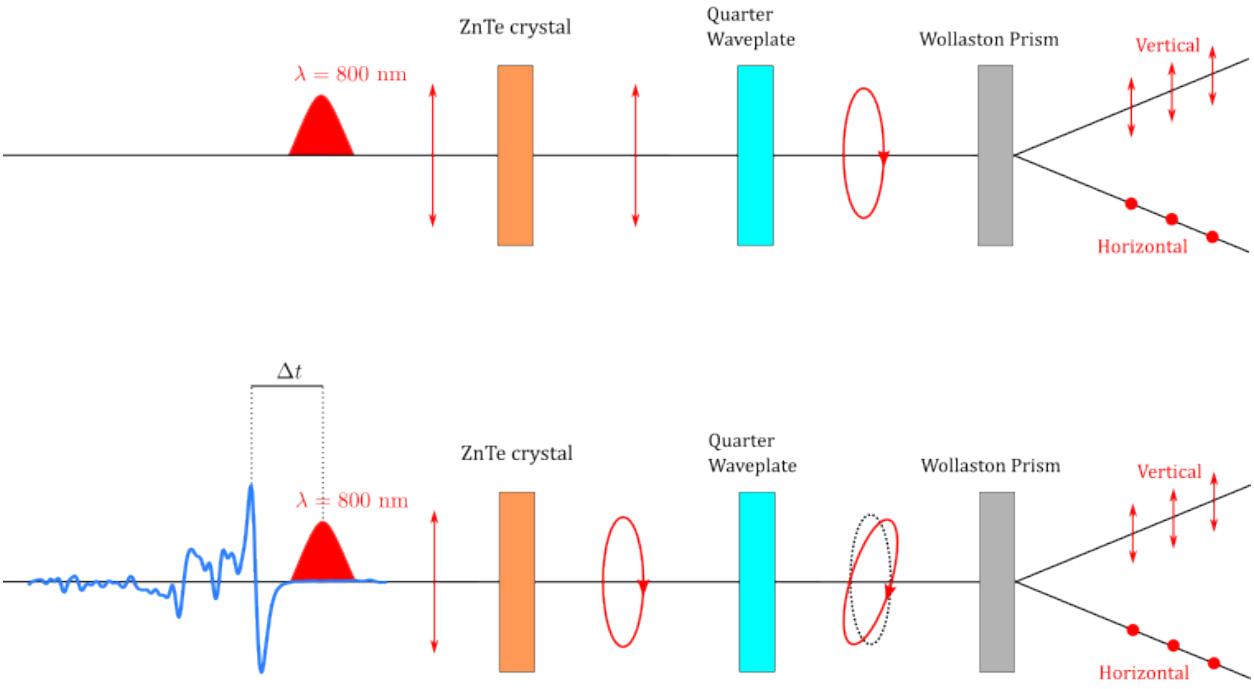

Figure 4.1: Electro-optic sampling with an 800 nm optical pulse. (Top) When there is no THz pulse, the optic pulse experiences no phase-shift and becomes circularly polarized after passing through a quarter-wave plate. In this case contributions from the horizontal and vertical components are equal to each other when measured by a photodiode. (Bottom) When a THz pulse is introduced, the ZnTe refractive index changes and induces a phase-shift in the optic pulse. After passing through the quarter-wave plate the optic pulse now has an ellipticity. This ellipticity biases the measurement of either the vertical or horizontal component of light by photodiodes after the pulse passes through a Wollaston prism. By changing the time delay between the optic and THz pulse, Δt, it is possible to sample the THz pulse at different points in time.

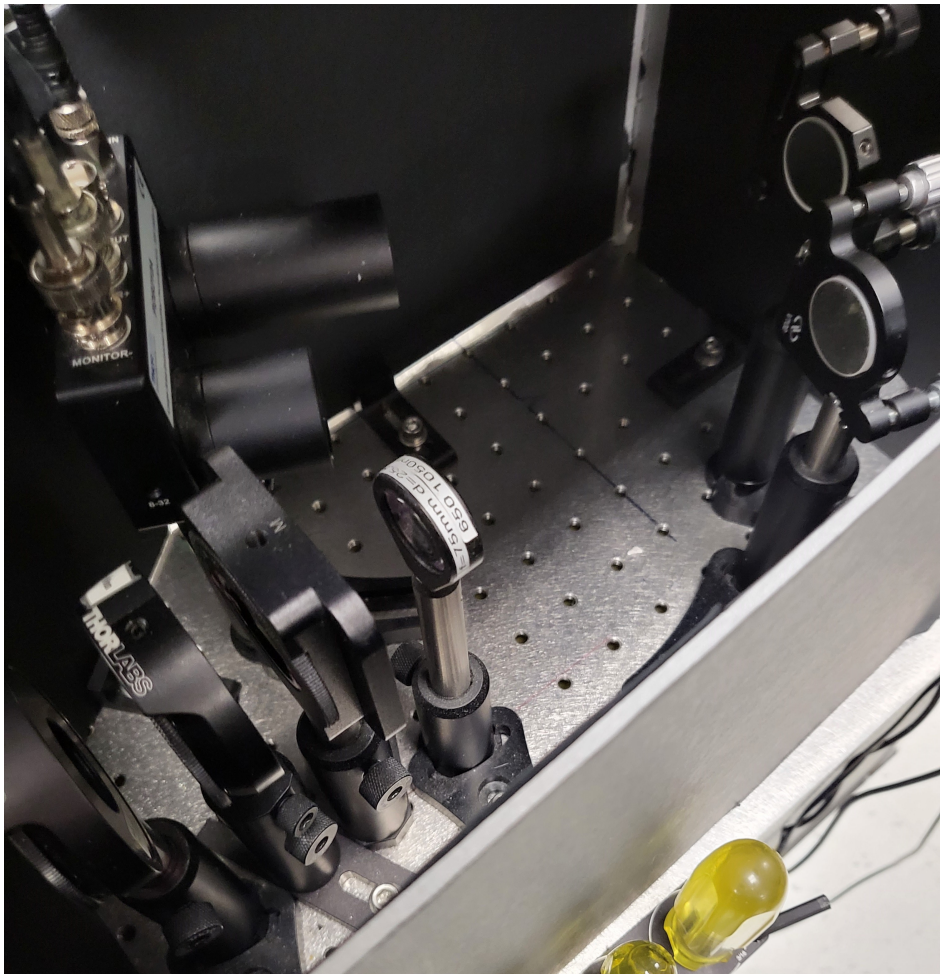

Figure 4.2: Light box enclosure of the main electro-optic sampling (EOS) apparatus. The Light box enclosure was added to prevent pollution from ambient light. A lid (not shown) with holes cut out for the photodiode connectors is placed on top. When balancing the photodiodes the only optics that are adjusted are the quarter-wave plate and the alignment of the mirrors used to guide light to the photodiodes.

If a THz pulse is absent and condition 4.3 is not satisfied, it indicates that there is some misalignment in the system or leakage from a non-THz source coupling to the photodiodes which must be addressed before proceeding further. When condition 4.3 is satisfied, the photodiodes are considered "balanced." Once the photodiodes are balanced, measurement of the THz pulse becomes possible. In the presence of a THz pulse a phase shift $\Delta\phi$ is induced in the optic pulse resulting in the vertical and horizontal components having intensities according to [116],

$$I_v = \frac{I_0}{2}\left(1 + \Delta\phi\right) \quad \& \quad I_h = \frac{I_0}{2}\left(1 - \Delta\phi\right). \tag{4.4}$$

Where $\Delta\phi$ is the phase shift determined by eqn. 4.2 [116]. Eqn. 4.4 indicates that by measuring the intensity of the horizontal and vertical components, it is possible to obtain $\Delta\phi$, as $\left(I_v - I_h\right)/I_0 = \Delta\phi$. Furthermore as per eqn. 4.2, $\Delta\phi \propto \mathcal{E}_{\mathrm{THz}}$. In full, a typical electro-optic sampling setup looks like fig. 4.3. The lock-in amplifier shown in fig. 4.3 and 4.4 is required for measuring the oncoming THz pulse. As such a brief discussion of the lock-in amplifier is warranted considering how crucial it was in obtaining the THz waveforms seen in this work. The lock-in amplifier is an amplifier and a low-pass filter in one contained unit [129]. As shown in fig. 4.3, the signal from the photodiodes is wired into two channels termed the "A-channel" and "B-channel" respectively. To measure the THz waveform, it is required that the difference between these channels is measured, this mode is termed $A - B$ and it is in this mode in which sampling is done. Mathematically, the signal the lock-in amplifier detects while in this mode is [129],

$$A - B = \frac{I_v - I_h}{I_v + I_h}.$$

By eqn. 4.4 it can be shown that the above expression is equivalent to the phase modulation of the optical probe by the THz pulse [116; 129],

$$A - B = \frac{I_v - I_h}{I_v + I_h} = \Delta\phi \propto \mathcal{E}_{THz}. \tag{4.5}$$

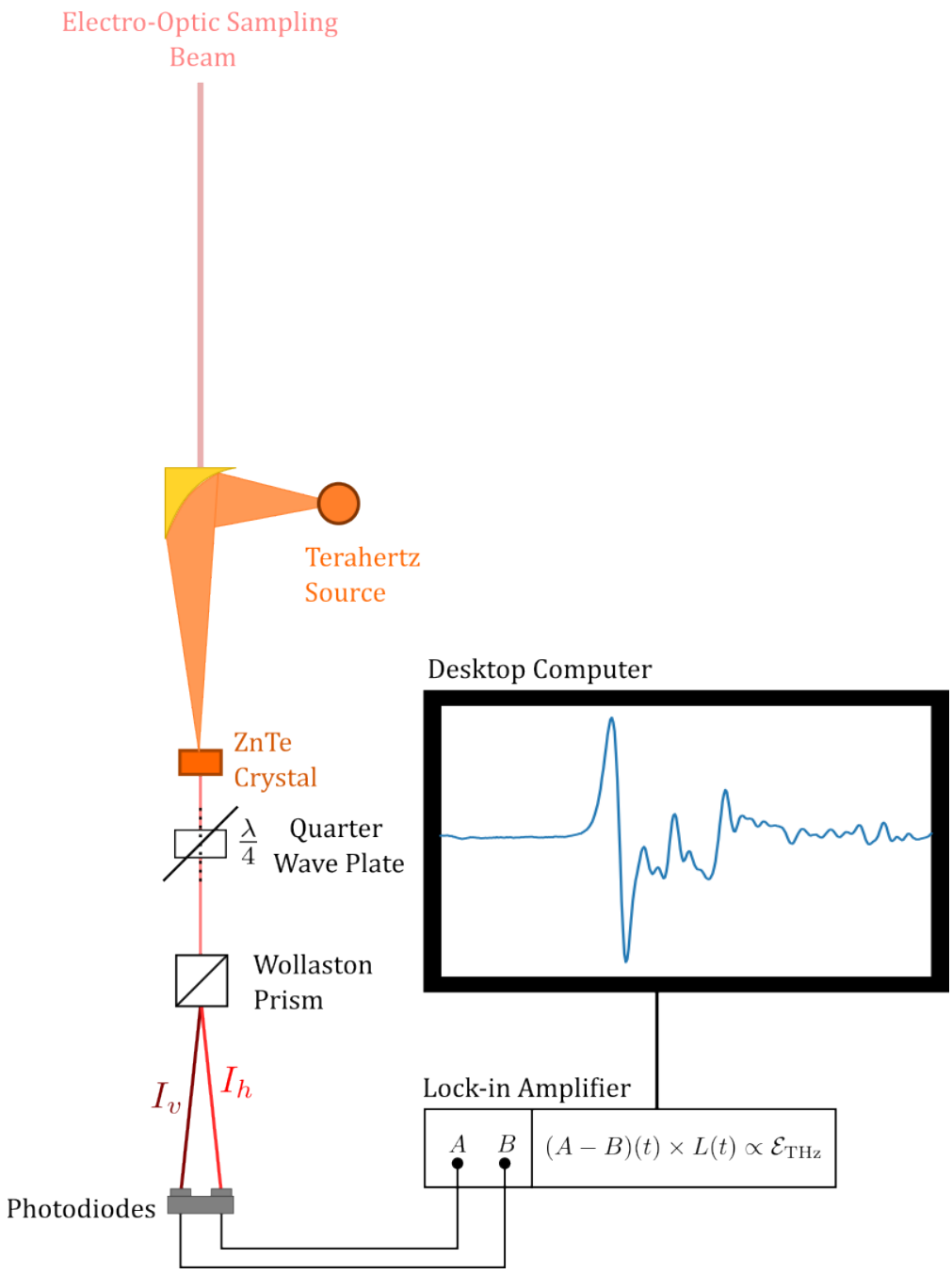

Figure 4.3: A schematic of a typical electro-optic sampling setup. A pair of balanced photodiodes measure the vertical (I_v) and horizontal (I_h) intensities of light. The signal from this measurement is then sent to a lock-in amplifier, which calculates the difference between I_v and I_h to obtain the "$A - B$" signal. The $A - B$ signal is proportional to the THz electric field, $\mathcal{E}_{\mathrm{THz}}$, at a given time, t. By adjusting the arrival time of the optic pulse in the EOS line relative to the THz pulse, it becomes possible to measure the THz pulse at different time-steps.

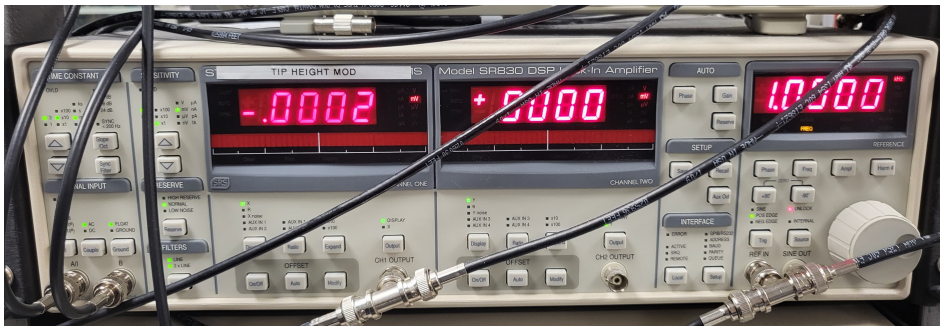

Figure 4.4: An example of an SR830 Lock-in amplifier unit used in this thesis. Settings for the lock-in amplifier were adjusted according to the needs of the particular experiment. An example of typical settings include a sensitivity of $V_L = 5\,\text{mV}$, a phase of $\theta_L = -6.78°$, a frequency of $\omega_L = 5.077\,\text{kHz}$ and a time integration constant of $\tau_L = 30\,\text{ms}$.

The $A-B$ signal can then be represented as a series of sine and cosine waves as per Fourier's theorem, this signal is then multiplied by a sine wave provided by the Lock-in amplifier [129],

$$(A-B)(t) \times L(t) = \left(\frac{V_s}{T}\sum_{n=0}^{\infty}\cos(n\omega_s t + \theta_s)\right) \times V_L \sin(\omega_L t + \theta_L). \tag{4.6}$$

Here V_L is the internal lock-in voltage, V_s is the voltage of the signal, T is the period of the signal, ω_s the angular frequency of the signal, ω_L is the angular frequency of the lock-in amplifier [129]. In a lock-in amplifier, ω_s must be set to some reference frequency at which sampling occurs meaning that, $\omega_s = \omega_L = \omega_{\text{ref}}$ [129]. The phase of the lock-in amplifier meanwhile, is locked to that of the signal, $\theta_s = \theta_L$ and is chosen such that the DC term in the series expansion of eqn. 4.6 is maximized [129]. When the series given by eqn. 4.6 is expanded and the conditions of the lock-in amplifier imposed, a low pass filter, $F(t)$ removes higher frequency leaving only a term proportional to the signal, i.e. [116; 129],

$$(A-B)(t) \times L(t)\,F(t) \propto V_s \propto \mathcal{E}_{THz}.$$

By adjusting the arrival time of the optic pulse in the EOS line relative to the THz pulse (rep. as Δt in fig. 4.1), it becomes possible to measure the THz pulse at different time-steps with the lock-in amplifier.

Measuring the THz pulse at a different time-step amounts to changing the delay, Δt, between the arrival of the optic pulse and the THz pulse. This is accomplished by the use

of electro-mechanical delay stages. In the transmissive THz experiments, the optic pulse carried along the EOS line was delayed with respect to the photoexcitation line. While in the emissive THz experiments, the PE line was delayed with respect to the optic pulse carried along the EOS line. In both cases, the relationship between electro-mechanical stage delay, Δx, and the time delay between the optical pump pulse and the THz probe pulse is given by,

$$\Delta t = \frac{2\Delta x}{c} = \frac{2\left(x_f - x_i\right)}{c}. \tag{4.7}$$

Where $c = 0.3\,\mathrm{mm/ps}$, x_f and x_i are the final and initial positions of the delay in millimetres. The factor of 2 comes from the fact that the electro-mechanical delays are retro-reflectors.

4.2 Methods of Transmissive Terahertz Characterization in Laser-Induced Plasmas

In this work, transmissive THz was to be performed asynchronously using two different lasers. The first being the Legend system firing at a repetition rate of $f_R = 1\,\mathrm{kHz} \mapsto T_p = 1\,\mathrm{ms}$ and an energy of $E_p = 200\,\mu\mathrm{J}$ which would provide the PE/ablation beam. The second system, the Verdi-Micra + Regenerative Amplifier (VMRA) firing at a repetition rate of $f_R = 250\,\mathrm{kHz} \mapsto T_p = 4\,\mu\mathrm{s}$ and an energy of $E_p = 5.2\,\mu\mathrm{J}$ provided both the THz generation beam and the EOS beam. Note that the method outlined here of using two lasers asynchronously is somewhat similar to the method outlined in ref. [130].

The parameters of both laser systems are listed in table 4.1. Note that all parameters shown in table 4.1 were measured directly, with the exception being the pulse-width, τ_p, for the VMRA. The pulse-width for the VMRA was estimated according to,

$$\tau_p \simeq 0.441 \frac{\lambda^2}{c\Delta\lambda}. \tag{4.8}$$

The derivation of eqn. 4.8 is given in Appendix D section D.2. The average power, $\langle P \rangle$, measured with a bolometer, the pulse energy can then be obtained according to $E_p = \langle P \rangle T_p = \langle P \rangle / f_R$. The wavelength bandwidth, $\Delta\lambda$ was obtained by fitting a Gaussian pulse

Laser System	λ (nm)	$\Delta\lambda$ (nm)	τ_p (fs)	f_R (kHz)	$\langle P \rangle$ (W)	E_p (μJ)
Legend Elite	795	25	70	1	0.2	200
VMRA	805	45	21	250	1.3	5.2

Table 4.1: Summary of the laser parameters used in this work. Note the pulse-duration, τ_p, for the VMRA system was estimated using eqn. 4.8. The Legend system was used for photoexcitation in semiconductors and ablation in the case of Cu-LIBPs. The VMRA system was used for EOS & THz generation. All other parameters were measured directly. Both systems are Ti:Sapphire based.

to central peak of the output spectra. The timing diagram detailing the operation of the transmissive THz experiments using these two laser systems is outlined in fig. 4.5. As shown in fig. 4.5 these experiments are contingent upon the formation of a LIP which attenuates the oncoming THz pulses. This attenuation provides the $\mathcal{T}_{\text{Pump}}$ signal, this occurs at what is termed t_0 (see fig. 4.6). At t_0, the THz pulse coincides with LIP formation. As the LIP dissipates, the THz signal rises to $\mathcal{T}_{\text{Ref}}$ as the effect of free-carrier absorption dissipates, as per fig. 4.6. Eventually the LIP would fully dissipate, returning to the $\mathcal{T}_{\text{Ref}}$ signal. $\mathcal{T}_{\text{Ref}}$ represents the absence of a LIP.

Determining the t_0 point in fig.4.6 for the transmissive THz experiments necessitated a coarse delay (in contrast with the "fine" delay provided by the electro-mechanical stages) that is held fixed throughout the duration of the experiment. The electro-mechanical delay stage which controls the arrival of the EOS pulse, is swept over the length of the stage while the PE/ablation line is blocked, and the ambient THz pulse like the one shown in fig. 4.8 is recorded. In the case of EHP, this measurement is taken with a semiconductor at the THz focus, while in the case of LIBP experiments it is recorded when the Cu-ring is close to, but not clipping the THz focus. For both cases this gives the t_0 exactly and the electro-mechanical delay stage position is then fixed at the absolute maximum of the THz pulse shown such as the one in fig. 4.8 to gurantee maximal $-\Delta\mathcal{T}$.

The THz pulses used to probe the LIP were provided by a photoconductive antenna (PCA) shown in fig. 4.7. The PCA shown in fig. 4.7, is a GaAs based THz-SED that was fitted into a rotation mount. The PCA shown in fig 4.7 was operated at bias voltage of $V_B = 30\,\text{V}$ and was never exceeded resulting in currents of $I \sim 13\,\text{mA}$ with an inhibit in. The "inhibit" here refers to a piece of external hardware that is plugged into the PCA that

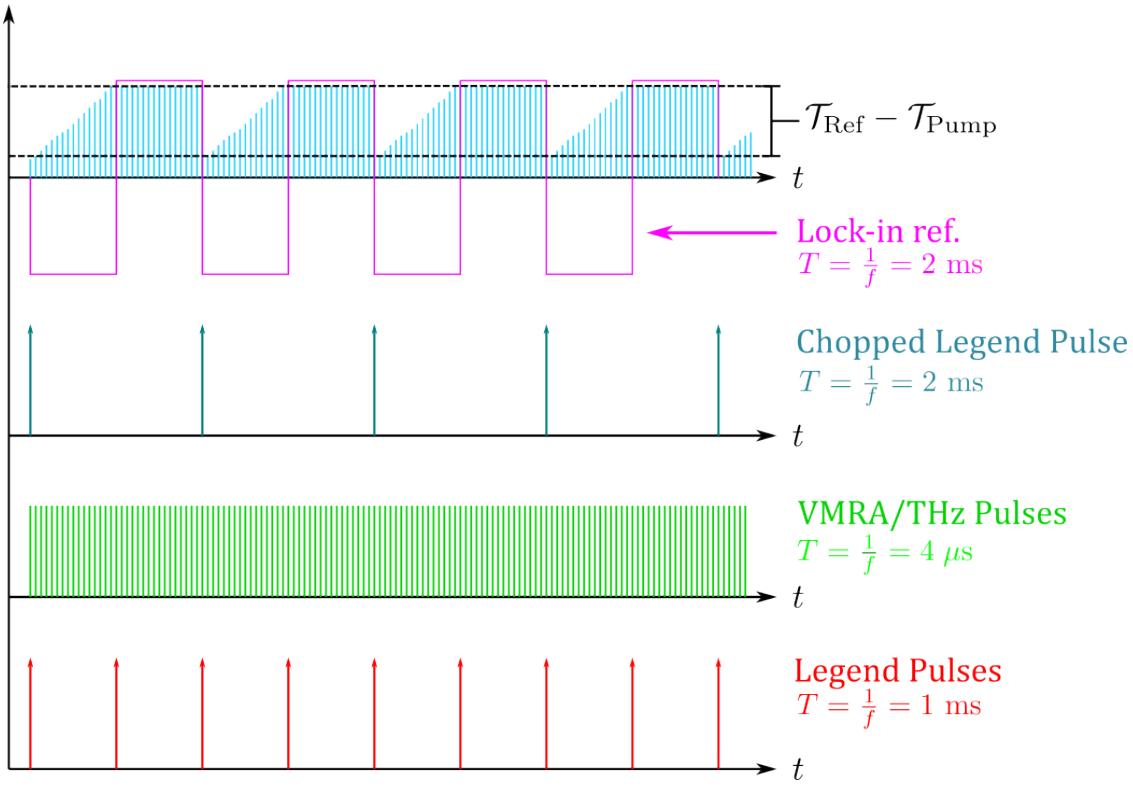

Figure 4.5: Timing diagram of the transmissive THz experiments. In these experiments, the legend was chopped at $f = 500\,\text{Hz}$ while the VMRA/THz pulses repetition rate was gated to the lock-in amplifier frequency of $f_L = 5.077\,\text{kHz}$ initially with the inhibit in and was later removed to match the repetition rate of the VMRA. The arrival of the chopped Legend pulse would coincide with the formation of a plasma. This would attenuate the oncoming THz pulses providing $\mathcal{T}_{\text{Pump}}$ signal. As the plasma dissipated THz transmission would return to it's initial value, $\mathcal{T}_{\text{Ref}}$. The difference between $\mathcal{T}_{\text{Ref}}$ and $\mathcal{T}_{\text{Pump}}$ gives $-\Delta\mathcal{T}$. If this was observed for LIBPs it would indicate that full time resolved spectroscopy would be possible.

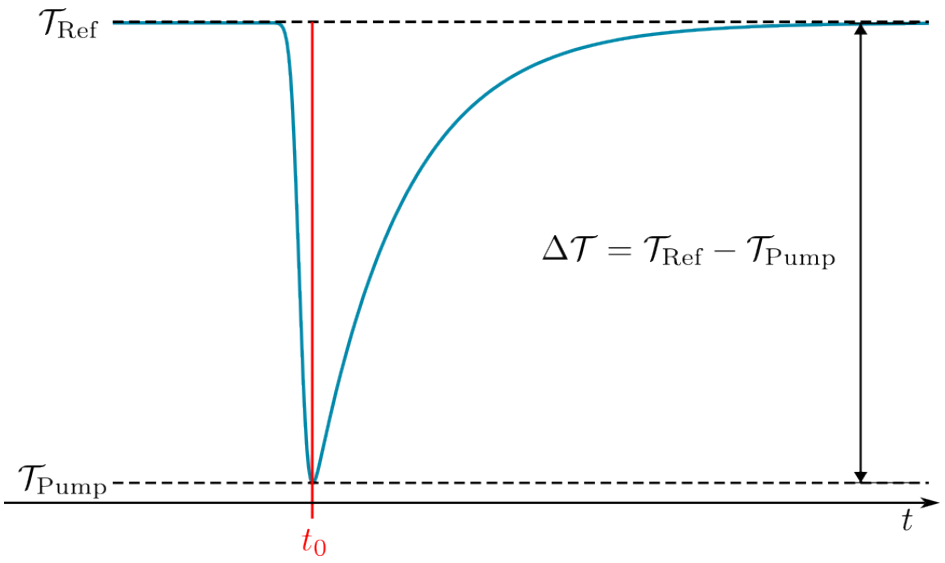

Figure 4.6: Illustration of a $\Delta\mathcal{T}$ trace on an oscilloscope. At t_0 the THz pulse overlaps with the presence of a plasma. When this happens the signal drops to $\mathcal{T}_{\text{Pump}}$. As the plasma dissipates, the THz pulse returns to it's original value $\mathcal{T}_{\text{Ref}}$. The difference between $\mathcal{T}_{\text{Ref}}$ and $\mathcal{T}_{\text{Pump}}$ gives rise to a $\Delta\mathcal{T}$ for that time-step.

limits the current to prevent damage to the PCA. The for the choice of bias voltage, V_B, is because exceeding 30 V could result in damaging the THz-SED.

For the Transmissive THz probing of LIBPs, the THz-SED inhibit which limits both the current and sets the on-off rate of the PCA to that of the lock-in amplifier ($\omega_{\text{PCA}} = \omega_L = 5.077\,\text{kHz}$) was unplugged. This resulted in the number of THz pulses per second being produced being equal to the period of the VMRA system ($T_p = 1/f_R = 4\,\mu\text{s}$). This was done to increase the number of THz pulses per second from $N = 5077\,\text{s}^{-1}$ to $N = 2.5 \times 10^5\,\text{s}^{-1}$ in the hopes of obtaining a $\Delta\mathcal{T}$ signal. For this instance the bias voltage across the PCA was capped at $V_B = 15\,\text{V}$ to prevent damage to the PCA. Values of the bias voltage and current with the inhibit in and the inhibit out are tabulated in table 4.2.

The PCA produced single-cycle THz pulses similar to the one shown in fig. 4.8-4.9. From fig. 4.9 it is apparent that the maximum bandwidth achievable with this PCA is $\Delta f \sim 2\,\text{THz}$. Theses pulses upon generation were then directed using gold coated off-axis parabolic mirrors and gold coated mirrors to the focus of two off-axis parabolics (see fig. 4.10). At the focus of the two off-axis parabolics, the spot-size of the THz pulse is $r_0 \approx 1.64\,\text{mm}$. Assuming that the LIP coincides temporally and spatially with the oncoming THz pulse, should result

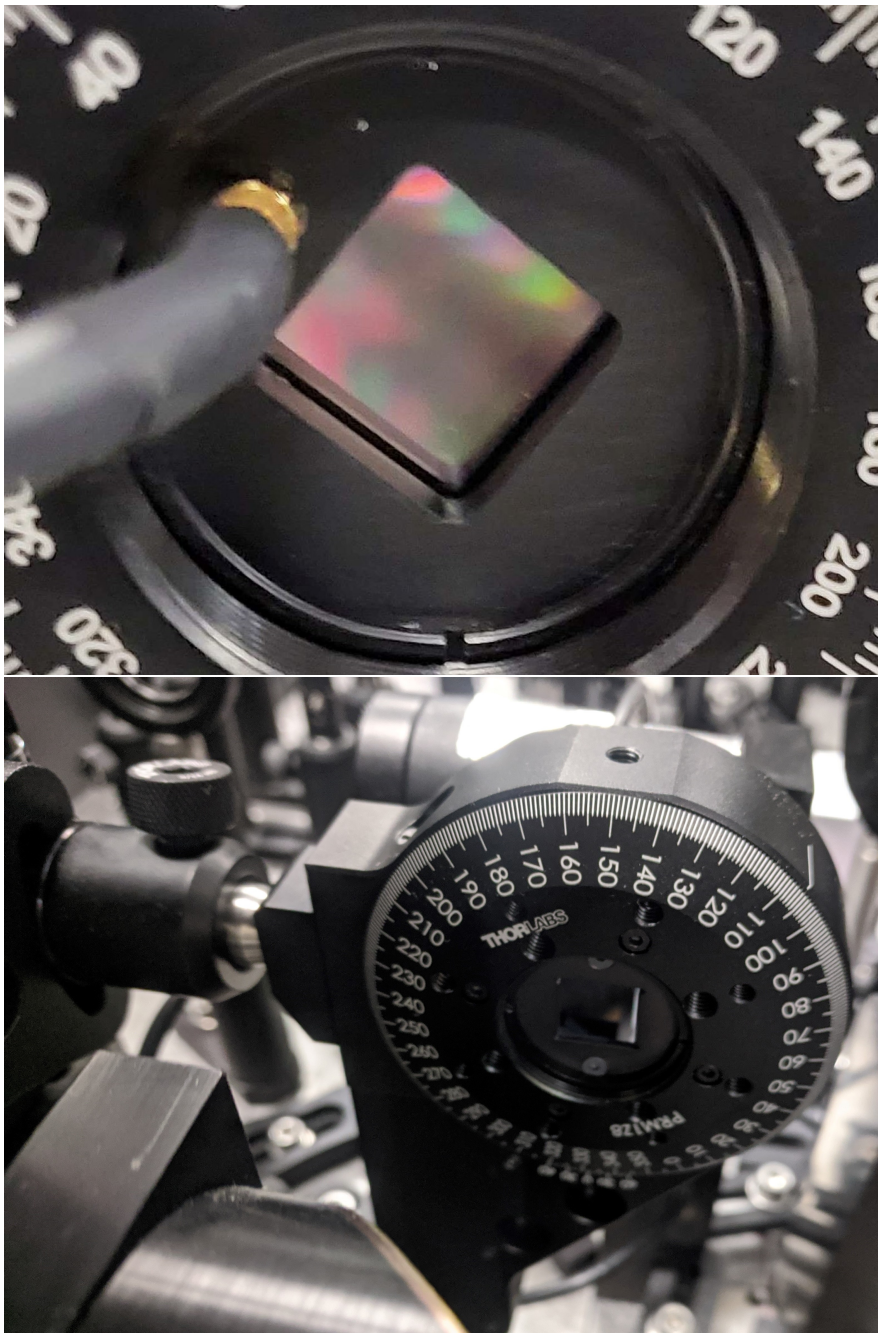

Figure 4.7: Top: a close-up of the PCA backside used in the THz transmission experiments for LIPs. The black wire is connected to an external inhibit which limits current to prevent damage to the PCA. The shiny surface, is the GaAs THz-SED that is PE by the VMRA laser system. A bias voltage of $V_B = 30\,\mathrm{V}$ and was switched on-off at a rate of $f_{\mathrm{PCA}} = 5.077\,\mathrm{kHz}$. This f_{PCA} rate is low enough that V_B is essentially a DC-bias over the timescales the experiment is running. Bottom: the PCA from the frontside and placed within a rotation mount the position of the PCA was fixed throughout the duration of experimental runs.

V_B (V)	I_{in} (mA)	I_{out} (mA)
1	1.1	2.35
2.5	1.9	3.95
5	3.1	6.3
7.5	4.2	8.5
10	5.2	10.6
12.5	6.25	12.6
15	7.25	14.65

Table 4.2: Tabulated values for the bias voltage and the resulting currents for the inhibit plugged into the PCA (I_{in}) and not plugged into the PCA (I_{out}). The inhibit is a piece of external hardware that is plugged into the PCA to prevent damage to the THz-SED emitter structure. The inhibit was unplugged during the experiments on Cu-LIBPs to increase the number of THz pulses from $N = 5077\,\text{s}^{-1}$ to $N = 2.5 \times 10^5\,\text{s}^{-1}$. The reason for this decision was done to increase the likelihood of seeing a $-\Delta\mathcal{T}$ from a Cu-LIBP.

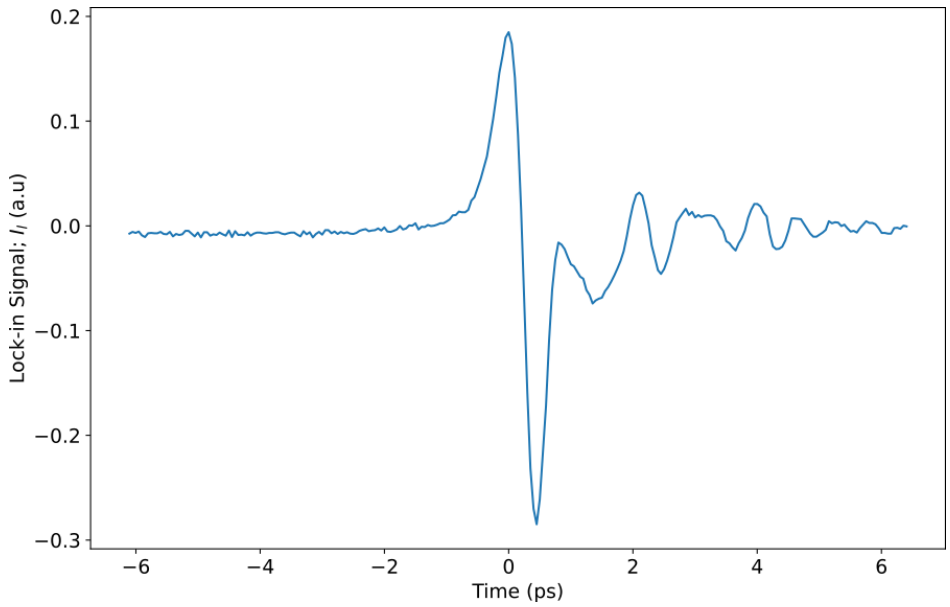

Figure 4.8: The time domain of a typical THz waveform emitted from the THz-SED shown in fig. 4.7. These single-cycle pulses were used for the transmissive THz experiments. Negative time in this plot corresponds to the time before the arrival of the THz pulse.

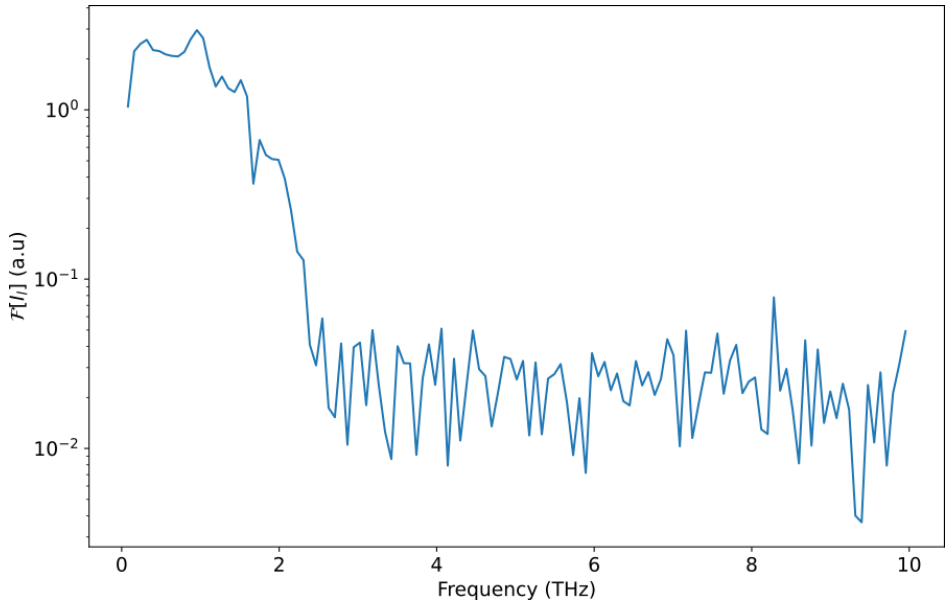

Figure 4.9: The Fourier Transform of fig 4.8. From this figure it's apparent that the THz pulse bandwidth of the PCA shown in fig. 4.7 is approx. $\Delta f \sim 2$ THz.

in attenuation of the THz pulse. EOS of the THz pulses like ones shown in fig.4.8 and 4.9 is achieved by fixing the THz generation and photoexcitation lines with respect to the EOS line. The EOS line was delayed by Δt steps in time using an electro-mechanical delay stage which is related to the physical delay through eqn. 4.7.

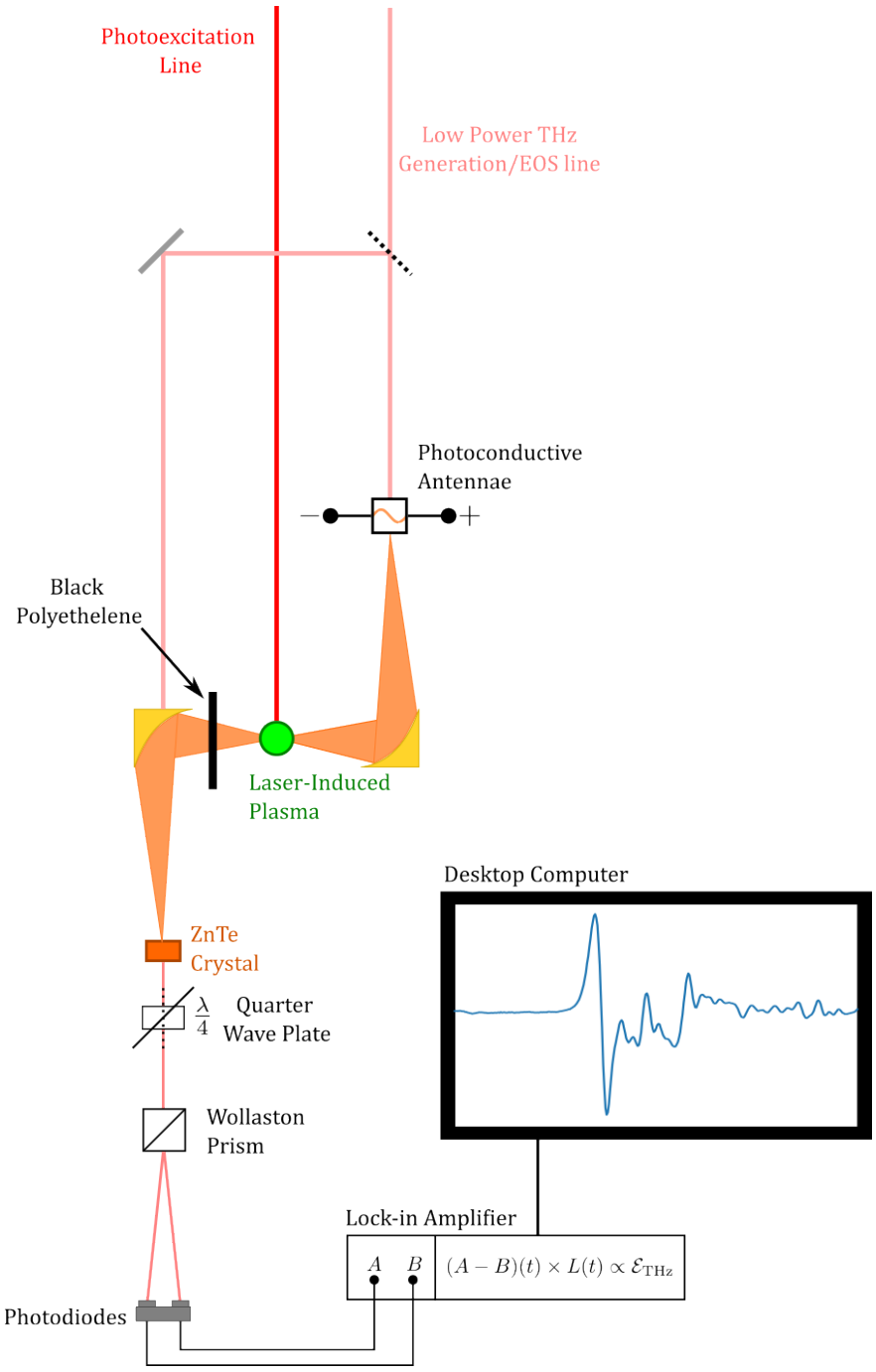

Figure 4.10: A basic schematic of the transmissive THz approach. The THz pulses are provided by a PCA, the THz pulses from which are then focused with a pair of gold off-axis parabolics. At the focus of the gold off-axis parabolics, the THz pulse has a spot-size of $r_0 \approx 1.64\,\mathrm{mm}$. The site of plasma production is placed (either an EHP or a Cu-LIBP) at the focus, and the presence of a LIP there should result in attenuating the THz pulses. Black polyethylene is placed to prevent coupling of non-THz bandwidth light into the photodiodes emitted from a LIP.

4.2.1 THz Transmission through Semiconductors

Before proceeding with Cu-LIBPs it was necessary to benchmark the transmissive approach using EHPs in PE semiconductors. This was done using the layout shown in fig.4.11 with the optical chopper set to $f_C = 500\,\mathrm{Hz}$. The lock-in amplifier meanwhile was set to a sensitivity of $V_L = 1\,\mathrm{mV}$ with a time constant of $\tau_L = 30\,\mathrm{ms}$ with a relative phase of $\theta_L = -6.78°$. Note the lock-in amplifier settings used in the PE semiconductor experiments were also used in the Cu-LIBP experiments.

Before beginning the experiment, it was necessary to see if a THz pulse from the PCA shown in fig. 4.7 could even be detected at all. To do this, required that the semiconducting wafer shown in fig.4.11 be removed from the setup. Once this was done and the pulse measured, the semiconducting wafer (either GaAs or Si) could then be added at the THz focus. A scan over the delay stage was then performed again. As seen in fig. 4.12 the addition of a semiconductor wafer could result in a shift of the THz maxima by as much as $\sim 8\,\mathrm{ps}$ this is due to the thickness of the wafer being on the order of $l \simeq 1.2\,\mathrm{mm}$.

Upon detection of the THz pulse in the presence of a semiconducting wafer, the delay stages between the THz generation beam and the EOS beam was fixed so that the THz emission from the THz-SED shown in fig. 4.7 was maximized. This must be done in order to maximize the $-\Delta\mathcal{T}$ arising from an EHP. Once the position of the delay stages were fixed, the PE beam is unblocked and the semiconductor wafer is then PE. This PE results in the emergence of an EHP. While the PE is occurring, THz pulses from the PCA shown in fig. 4.7 such as those shown in fig.4.8 travel to the focus of the off-axis parabolics shown in fig. 4.11. At this focus the THz beam has a spot-size of $r_0 \approx 1.64\,\mathrm{mm}$. Once the THz pulses are at the focus, the THz pulses are screened by the EHP giving rise to an oscilloscope trace similar to what is shown in fig. 4.6. To observe the trace shown in 4.6 it is required that the signal from the photodiodes was routed through a pre-amplifier with a high-pass frequency of $f_h = 0.03\,\mathrm{Hz}$, a low-pass frequency of $f_l = 100\,\mathrm{kHz}$ and a gain of $G = 1 \times 10^2$ for both the undoped Si and undoped GaAs samples.

Adding variable ND-filter to the PE line shown in fig. 4.11 enabled control over the PE line fluence. This enables variable control over the $\Delta\mathcal{T}$. Once the setup shown in fig.

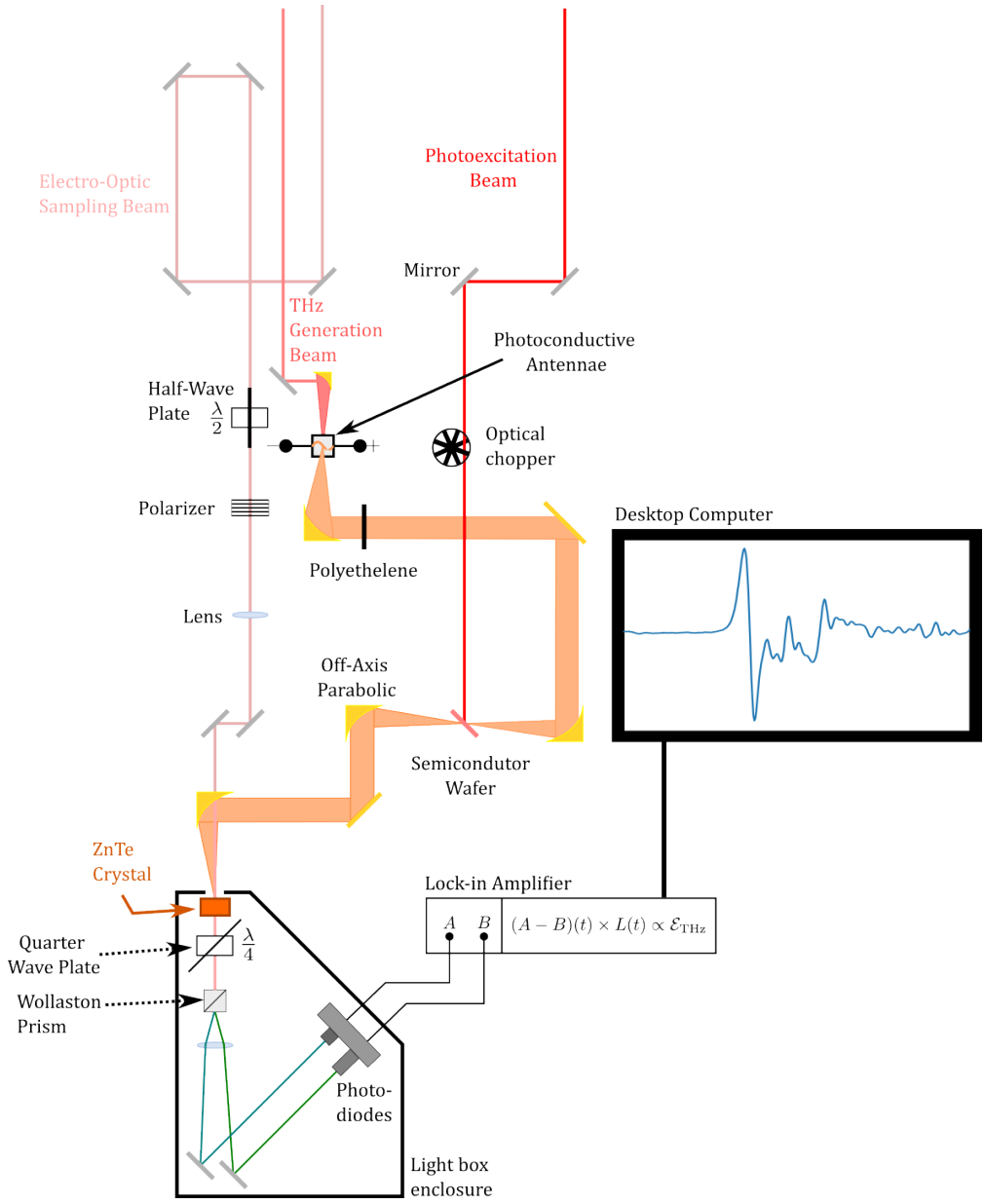

Figure 4.11: A schematic of the setup used to benchmark THz transmission with semiconductors. The optical chopper on the PE line operated at a frequency of $f_C = 500\,\mathrm{Hz}$. The half-wave plate and polarizer along the EOS line was used to attenuate the EOS beam to prevent damage to the ZnTe crystal. The semiconductor wafers used in this experiment were set at an angle shown above so that $\lambda = 795\,\mathrm{nm}$ reflection from the PE line would not couple into THz signal. The EOS optics was enclosed in a light box to prevent coupling from ambient light sources. In this setup the EOS line was delayed with respect to the THz generation and PE lines.

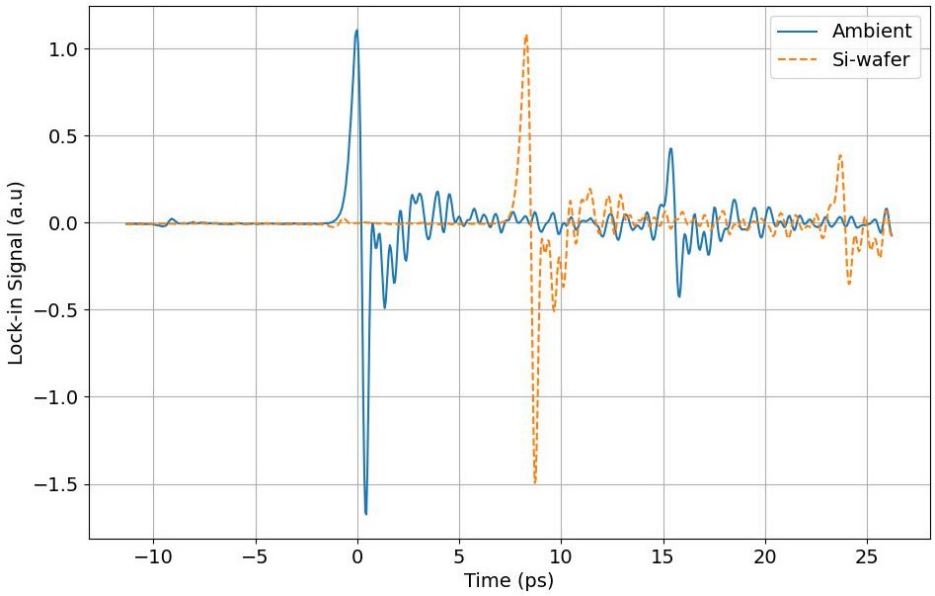

Figure 4.12: THz pulse from the PCA shown in fig. 4.7 in the absence of Si-wafer at the focus and in the presence of a Si-wafer. This shows that the THz pulse arrives later in time.

4.11 was calibrated and benchmarked to the semiconductor samples, it was then possible to proceed with experiments involving THz transmission through solid target LIBPs.

4.2.2 Terahertz Transmission through a Cu Target Laser-Induced Breakdown Plasma

To study THz transmission through a Cu-LIBP the setup was arranged according to fig. 4.14. The Legend provided the ablation beam shown in fig. 4.14. The settings for the lasers, the lock-in amplifier and the optical chopper are identical to those used in PE semiconductor case of fig. 4.11. The key differences between the setup shown in fig. 4.11 is the addition of a convex lens of a focal length, F, of $F = 200\,\text{mm}$ and a Cu-ring sample mounted on an XYZ-translation stage shown in fig. 4.13.

The knife edge measurements gave an initial spot-size of $D = 12.4\,\text{mm}$ which when focused by the $F = 200\,\text{mm}$ len in fig. 4.18, gave a spot-size at the focus, $2r_0$, of,

$$2r_0 = \frac{4\lambda}{\pi}\left(\frac{F}{D}\right) = \frac{4\,(795\,\text{nm})}{\pi}\left(\frac{200\,\text{mm}}{12.4\,\text{mm}}\right) = 1.63 \times 10^4\,\text{nm} = 16.3\,\mu\text{m}.$$

When focused on the Cu-ring shown in fig. 4.13, this gave an absorbed fluence of $\Phi = 3.82\,\mathrm{J/cm^2}$ well above the threshold fluences quoted by Nolte et al. and Furusawa et al. which range from $140\,\mathrm{mJ/cm^2} \leq \Phi_0 \leq 460\,\mathrm{mJ/cm^2}$ [72; 73]. Note that the fluence was calculated according to,

$$\Phi \simeq \frac{E_p}{\pi r_0^2}\,(1-R)\,. \tag{4.9}$$

Where E_p is the energy of the pulse and is equal to $E_p = \langle P \rangle\, T_p$ where T_p is the period of the laser pulse train and R is the reflectivity at the surface and is given by eqn. 2.18,

$$R = \frac{(n_1 - 1)^2 + n_2^2}{(n_1 + 1)^2 + n_2^2}.$$

The addition of the $(1-R)$ term is necessary to account for the fact that at $\lambda = 795\,\mathrm{nm}$ Cu is highly reflective, with an R of $R \approx 0.96$ according to the data in ref. [131]. For the fluence dependence measurements, a variable ND filter was added to the ablation line in fig. 4.18 to control the pump power, $\langle P \rangle$, with values ranging from $\langle P \rangle = 35 - 205\,\mathrm{mW}$. While lower fluences could be achieved, it was found that below $\langle P \rangle = 35\,\mathrm{mW}$ ($\Phi = 0.67\,\mathrm{J/cm^2}$) there was no plasma ignition or ablation.

The Cu-ring was placed at the focus of the THz transmission path with the help of a guiding laser (not shown in fig.4.14). To verify that it was at the focus, the delay between the THz generation beam and the EOS beam was fixed such that the THz field from the THz-SED shown in fig. 4.7 was at a maximum. The Cu-ring was then slid into the focus until a noticeable dip in the lock-in signal could be detected and then was backed off slightly using the micrometer adjust until signal was restored using the mount shown in fig. 4.13. This was done to avoid losing signal strength and higher frequency components in the THz pulse (see fig. 4.15-4.16).

Because of this loss of spectral information, it is not suitable for the Cu-ring to clip the the THz focus. Upon finishing the alignment of the Cu-sample holder with the THz focus, the ablation beam was then focused onto the Cu-ring as the sample holder rotated producing a continuous plasma plume.

Initially the inhibit for the PCA was left in for the first few attempts. However, due initial difficulties encountered with measuring a $\Delta\mathcal{T}$, the inhibit in the THz-SED shown

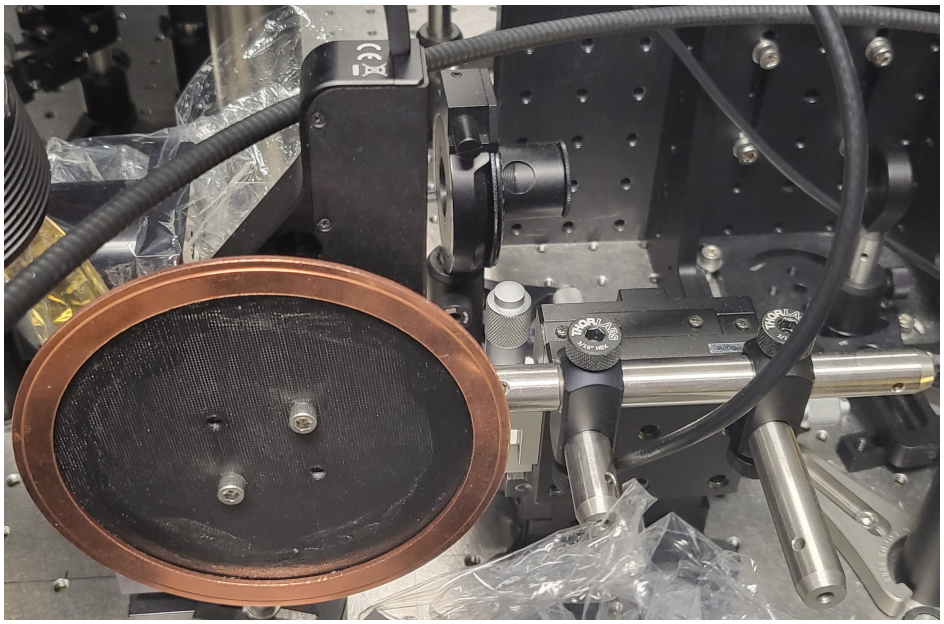

Figure 4.13: The sample mount and Cu ring used for the generation of Cu-LIBPs. The rotation mount was attached to an XYZ-translation stage enabling millimetre positional control. The mount was controlled electronically using a motorized controller and rotated at an angular velocity of $\nu = 0.06\,^{\circ}/\mathrm{s}$ to continually provide a fresh surface for ablation.

in fig. 4.7 was removed and the voltage was reduced down to $V_B = 12\,\mathrm{V}$. This resulted in the number of THz pulses per second being produced being equal to the period of the VMRA system ($T_p = 1/f = 4\,\mu\mathrm{s}$); increasing the number of THz pulses per second from $N = 5077\,\mathrm{s}^{-1}$ to $N = 2.5 \times 10^5\,\mathrm{s}^{-1}$. This though did not yield any significant $\Delta\mathcal{T}$. To understand why, necessitated a further study of the Cu-LIBP PL duration the methods for which are discussed in the next section.

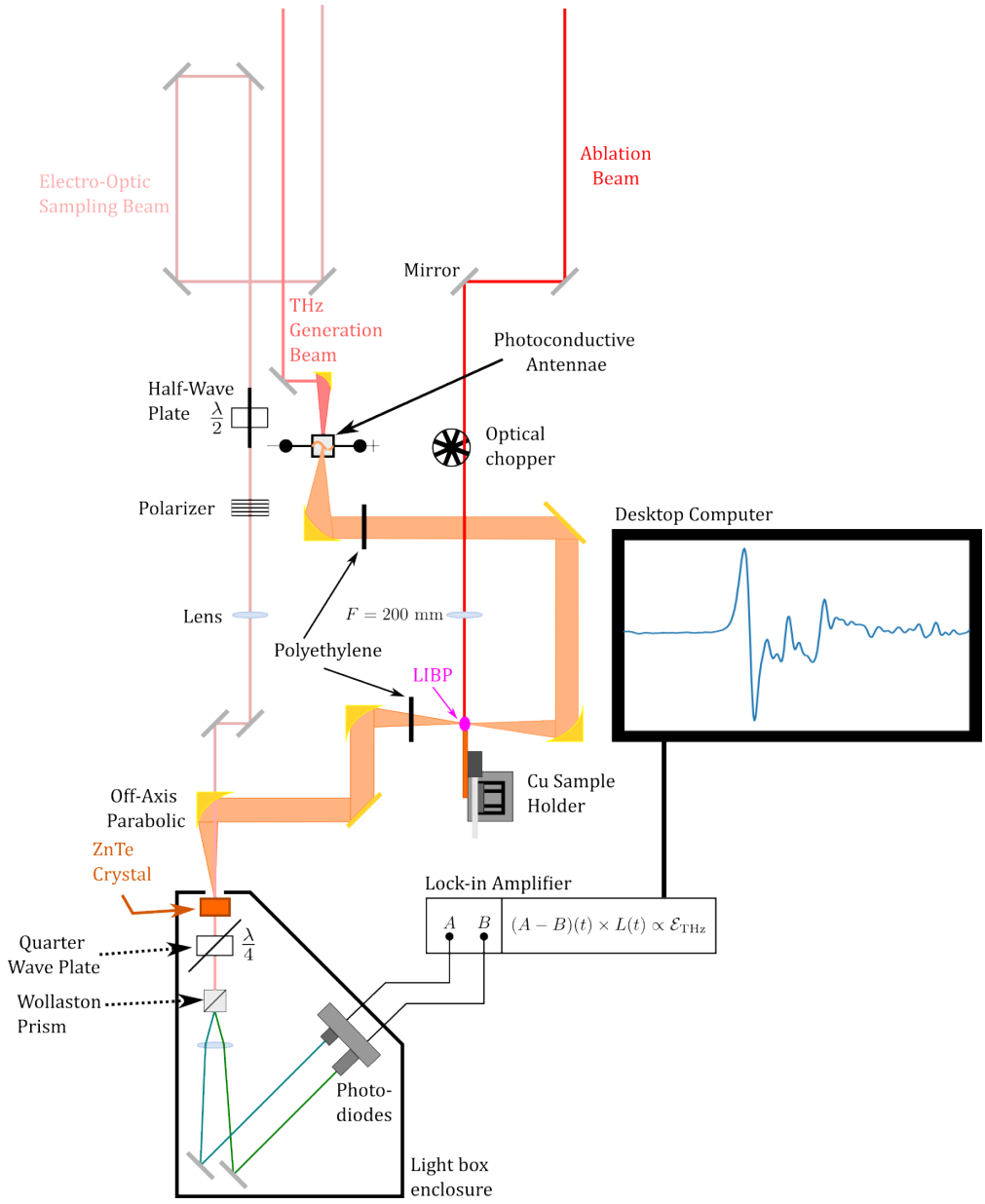

Figure 4.14: The setup used to study THz transmission in Cu-LIBP. The ablation beam was focused down to a spot-size, $2r_0$, of $2r_0 \simeq 16.3\,\mu$m using a lens with a focal length, F, of $F = 200\,$mm giving rise to a fluence, Φ_0, of $\Phi_0 = 3.82\,\mathrm{J}\cdot\mathrm{cm}^{-2}$. The polarizer and half-wave plate on the EOS line functions as a variable attenuator and is used attenuate the beam to prevent damage to the ZnTe crystal. The Cu-sample holder was mounted on an XYZ-translation stage with millimetre control and was placed at the focus of the THz pulses. Black polyethylene was required to prevent the coupling of non-THz band light into the photodiodes.

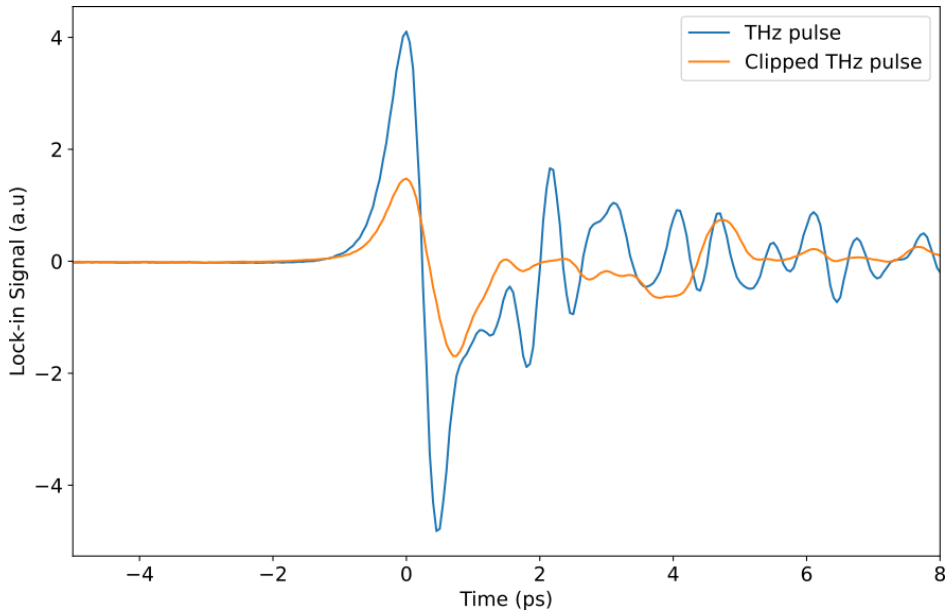

Figure 4.15: Demonstration of the effects of clipping with a Cu-ring in the time domain on a THz pulse. It is apparent from this figure that there is an immediate loss in signal due to the Cu-ring intersecting the THz focus.

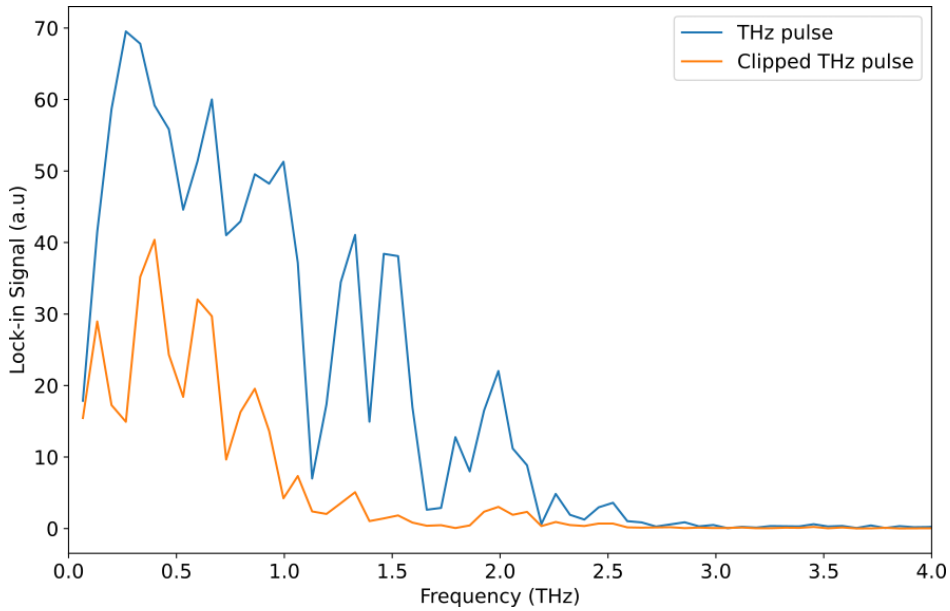

Figure 4.16: Demonstration of the effects of clipping with a Cu-ring in the frequency domain. From this figure it is apparent that there is a loss of higher frequency components in addition to the signal loss when a Cu-ring intersects the THz focus.

4.3 Photoluminescent Measurements & Spectral Characterization

PL was collected with a fibre optic with a core of diameter, D_c, $D_c = 600\,\mu$m with a numerical aperture, NA, of $NA = 0.5$ [132]. This fibre optic covered a wavelength range of $400 - 2200\,$nm [132]. Initially, the fibre optic was clamped in place and placed near the site of ablation on the Cu ring however, this proved to be detrimental for long running experiments as Cu dust particulates accumulated on the fibre optic head. This coating of Cu dust limited light collection and hence for the rest of this thesis, a telescope array was assembled to collect light from the Cu plasma and coupled to the fibre optic and is shown in fig. 4.17(b).

The light collected by the fibre optic was routed first through the filter shown in fig. 4.20. This short-pass filter was added to remove any reflected $\lambda = 795\,$nm light from the Legend that coupled into the fibre optic. Using a bifurcated fibre optic with a diameter $D_c = 1000\,\mu$m and numerical appeture of $NA = 0.39$ [133]. This bifurcated fibre optic covered a wavelength range of $300 - 1200\,$nm [133]. This bifurcated fibre optic was used to send light to both a Thorlabs DET210 photodiode with a rise time, t_r, of $t_r = 1\,$ns (shown in fig.4.17(a)) and a spectrometer (either the USB2000 Ocean Optics shown in fig.4.17(c) or the Princeton Instruments Acton SP2500) [134]. The light sent to the photodiode was used to measure the PL time duration with an oscilloscope (see fig. 4.18). The oscilloscope was triggered off of the Legend Elite system. The light sent to the spectrometers was used to obtain the spectra for both the Legend pulse shown in fig. 4.19, the noise floor in fig. 4.21 and the Cu-LIBP in fig. 4.22-5.1.

The Legend pulse used in both PE and ablation was characterized using a Princeton Instruments Acton SP2500 spectrometer and a knife edge measurement was used to estimate the initial spot-size before being focused by the $F = 200\,$mm lens in fig. 4.18. The results of spectral features are shown in table 4.1 and a Gaussian fit to the data collected in fig.4.19 gave a central wavelength, λ, $\lambda = 795\,$nm with a spectral bandwidth of $\Delta\lambda = 25\,$nm.

One major issue with performing PL and spectral measurements is that the reflection from the Legend pulse does couple to the fibre optic shown in fig. 4.17(b), this means the Cu-LIBP PL signal is initially polluted with Legend light. To resolve this, required the

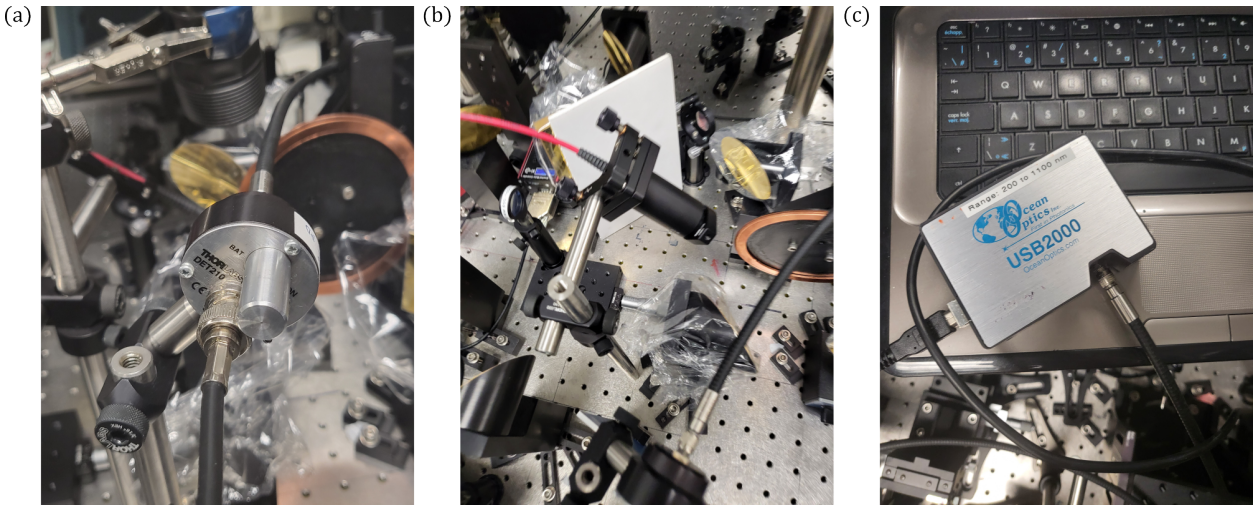

Figure 4.17: Fig. (a) The Thorlabs DET210 photodiode used in the collection of the PL curves the model shown has a response time of $t_r = 1\,\text{ns}$. Fig. (b) the fibre optic with a telescope array used to gather light emission for the latter-half of the data collection. Fig. (c) an Ocean Optics USB 2000 spectrometer; it is one of the two models of spectrometer used in this thesis.

addition of a short-pass filter to remove the reflected Legend $\lambda = 795\,\text{nm}$ light. In this thesis, a short-pass filter with a cutoff wavelength of $\lambda_c = 650\,\text{nm}$ was selected and is shown in fig. 4.20. Fig. 4.19-4.21 shows that the filter is so effective at removing the Legend reflection that the spectra for the ambient vs the reflected pulse plus the filter are indistinguishable. Furthermore, no spectral information regarding the Cu-LIBP is lost as the key spectral features are clustered around $\lambda = 530\,\text{nm}$ (see fig.4.22 and ref. [76]). Thus, the short-pass filter with $\lambda_c = 650\,\text{nm}$ shown in fig. 4.20 successfully decouples Cu-LIBP PL from the Legend reflection and was subsequently used during the ablation process.

The position of the fibre optic shown in fig. 4.17(b) was calibrated by maximizing the intensity of the Legend reflection spectrum off the Cu-ring shown in fig. 4.13. This was achieved using the OceanOptics USB2000 spectrometer shown in fig. 4.17(c). To do this, required the temporary removal of the short-pass filter with a wavelength cutoff of $\lambda_c = 650\,\text{nm}$ shown in fig. 4.20 and the $F = 200\,\text{mm}$ lens to prevent preemptive ablation. To reduce the effect of ambient light, the lights in the lab were shut off. After the signal of the Legend reflection was sufficiently maximized, the short-pass filter shown in fig.4.20 was slotted back into the filter holder. The sample holder shown in fig. 4.13 was rotated at an angular velocity of $\nu = 0.06\,^\circ/\text{s}$ to provide a fresh surface for ablation. Minor adjustments

Δl (mm)	D_g (grooves/mm)	$\Delta\lambda_r$ (nm)	b (nm)
0.2	1200	0.33	750

Table 4.3: Settings of the Princeton Instruments Acton SP2500 used. The grating used in the measurement of the spectra seen in fig. 4.19 and fig. 5.1 had an associated blaze of $b = 750\,\text{nm}$ and focal length of $F = 500\,\text{mm}$. $\Delta\lambda_r$ was calculated using eqn. 4.10.

were sometimes made to either the XYZ-translation stage or to the fibre optic position to maximize plasma PL signal during the experimental run. Once a satisfactory spectra or PL signal was collected, a beam block was flipped up to stop ablation and data was subsequently collected from either the oscilloscope or the computer desktop.

Two spectrometers were used in this work: (1) a OceanOptics USB2000 spectrometer (shown in fig. 4.17(c)) and (2) a Princeton Instruments Action SP2500 spectrometer. The former spectrometer (spectrometer (1)) was used for calibration in-between ablation runs as mentioned in the prior paragraph and to gauge the effects of the short-pass filter (fig.4.22). All major measurements of the Cu-LIBP spectra, and the Legend pulse characterization were accomplished with the latter spectrometer (spectrometer (2)). The spectral resolution of a spectrometer is given by [135],

$$\Delta\lambda_r = \frac{\Delta l}{F D_g}. \tag{4.10}$$

Where $\Delta\lambda_r$ is the spectral resolution, Δl is the slit-width, F the focal length, and D_g the dispersion of the grating in grooves per millimetre [135]. For this thesis the measurements performed using the Princeton Instruments Acton SP2500 (fig. 4.19 and fig. 5.1) grating 2 was used which had a dispersion of $D_g = 1200\,\text{g/mm}$ with a blaze, b, of $b = 750\,\text{nm}$. The settings for the Princeton Instruments Acton SP2500 spectrometer are shown in table 4.3.

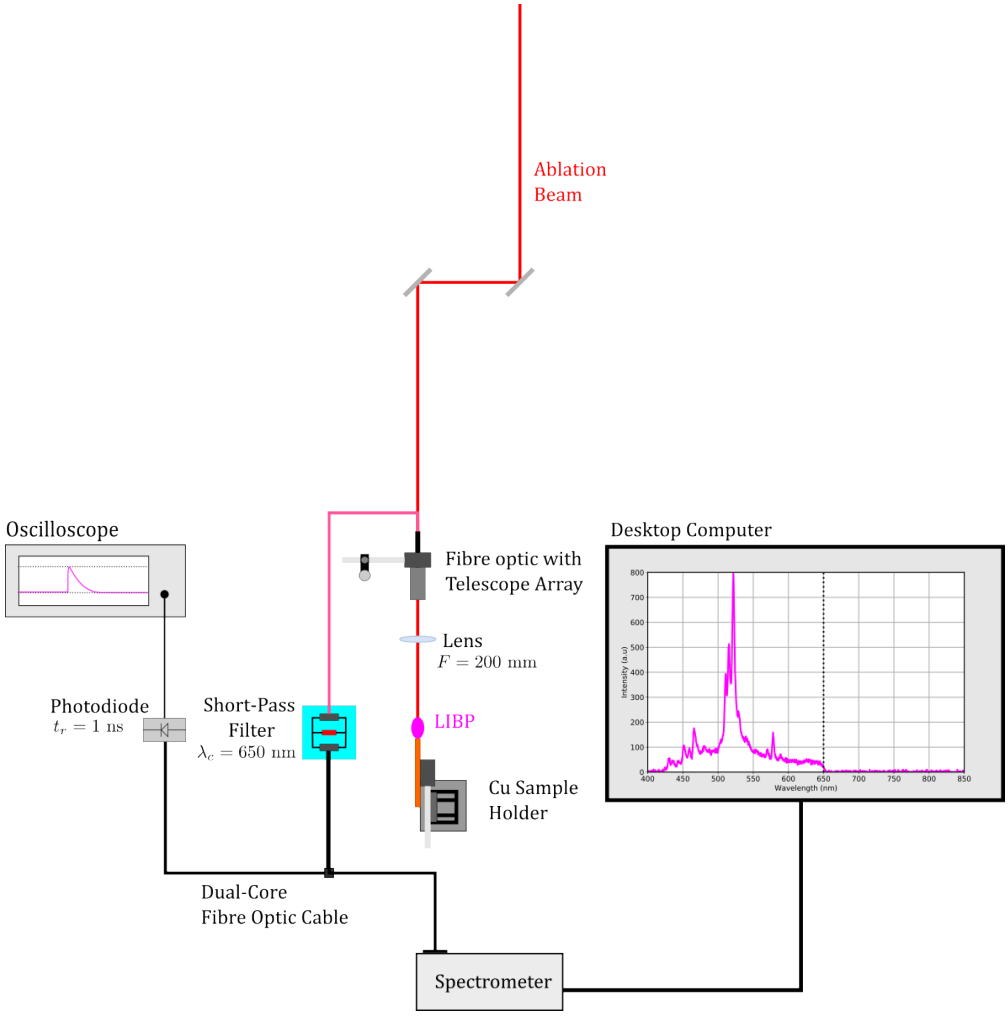

Figure 4.18: Schematic of the PL and spectrum collection setup. In this setup the fibre optic with a telescope array (shown in fig. 4.17(b)) collects both the LIBP PL and Legend reflection. To remove the Legend reflection, the light is routed through the short-pass filter (shown in fig. 4.20) with a wavelength cutoff of $\lambda_c = 650\,\text{nm}$. The PL is then routed to both a photodiode (shown in fig. 4.17(a)) and a spectrometer (shown fig. 4.17(c) and fig. [fig num]). The LIBP PL signal is measured and recorded with the photodiode and oscilloscope respectively. The spectra is measured and recorded with the spectrometer and a desktop computer respectively.

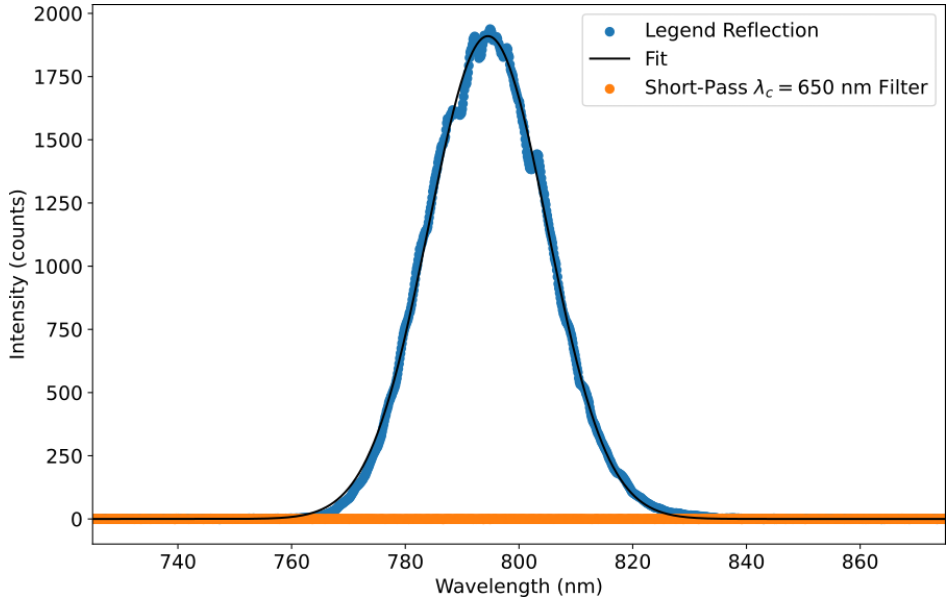

Figure 4.19: The measured reflection from the Legend pulse used for ablation and PE coupled to the fibre optic shown in fig. 4.17(b) over the range $720\,\text{nm} \leq \lambda \leq 880\,\text{nm}$. Fitting the curve using a Gaussian gave a central frequency, λ, of $\lambda = 795\,\text{nm}$, a pulsewidth, $\Delta\lambda$ (taken here to be equal to the FWHM), $\Delta\lambda = 25\,\text{nm}$. Given it's relatively high count number, the legend reflection drowns out the plasma PL. This necessitated the addition of a short-pass filter shown in fig. 4.20 with a wavelength cutoff of $\lambda_c = 650\,\text{nm}$ to remove it. The addition of the short-pass filter resulted in a signal indistinguishable from the background (see fig. 4.21). These signals were measured using the Acton SP2500 spectrometer. For this measurement the focusing lens was removed.

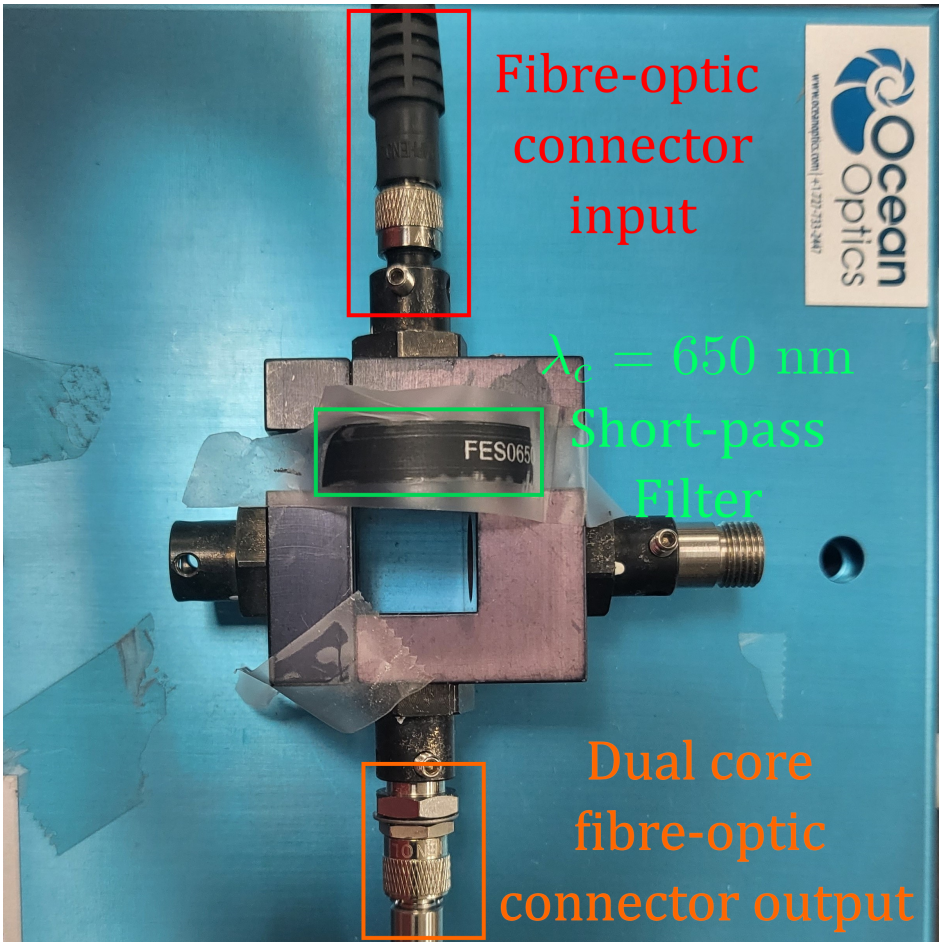

Figure 4.20: The short-pass filter. Light from the PL passes through the short-pass filter with a wavelength cutoff of $\lambda_c = 650\,\text{nm}$ to remove the Legend $\lambda = 795\,\text{nm}$ light that has coupled to the fibre optic in addition to the plasma PL. Without this filter, measurement of the LIBP PL is not feasible. After passing through the filter, the PL emission is then coupled to a dual core fibre optic which routes the light to both the photodiode (shown in fig. 4.17(a)) and one of the two spectrometers. For this measurement the focusing lens was removed.

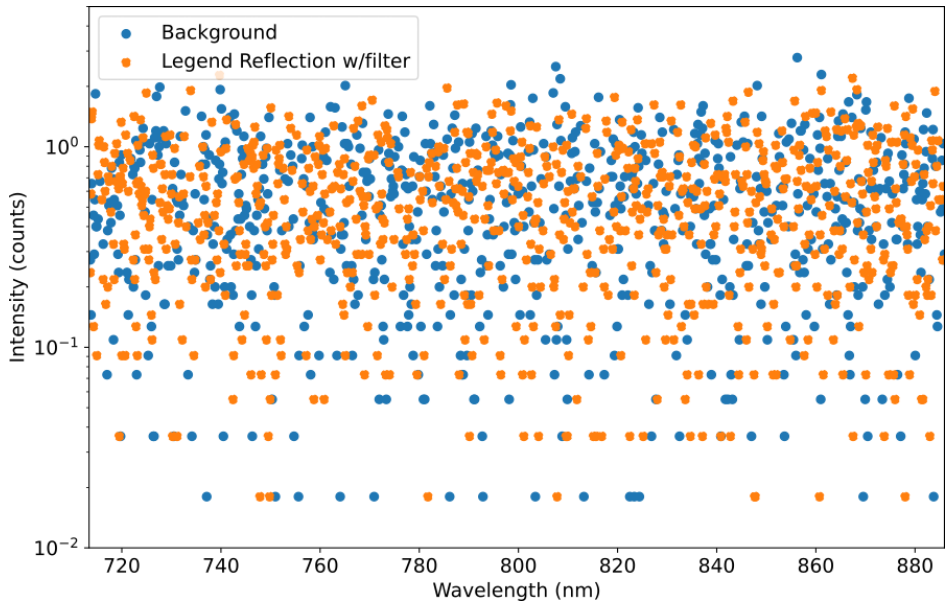

Figure 4.21: The noise floor of the ambient background with the short-pass filter sampled over the same range $720\,\text{nm} \leq \lambda \leq 880\,\text{nm}$. This figure shows that adding the short-pass filter with a wavelength cutoff of $\lambda_c = 650\,\text{nm}$ results in a signal indistinguishable from the noise floor. This figure demonstrates that the filter shown in fig. 4.20 is successful at removing reflected $\lambda = 795\,\text{nm}$ light. This means in practice that any measured PL signal seen will not have any contribution from the Legend, i.e., it is possible to decouple the Legend reflection from the LIBP PL. See fig. 4.22 for demonstration of the filtration with Cu-LIBP PL.

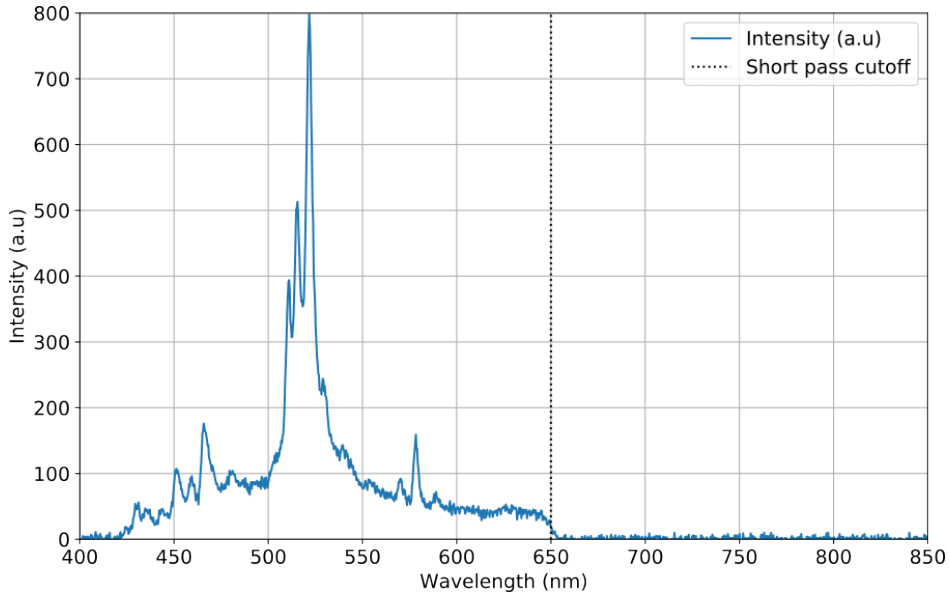

Figure 4.22: Filter with Cu-LIBP PL spectra. This figure shows that the addition of the short-pass filter with a wavelength cutoff of $\lambda_c = 650\,\text{nm}$ (shown in fig.4.20) does not remove the LIBP PL spectra. This proves that the Legend reflection can be decoupled from the Cu-LIBP PL.

4.4 Methods of Emissive Terahertz Characterization in Laser-Induced Plasmas

Results from the Cu-LIBP PL using the methods outlined in the section prior showed that the duration of PL emission was relatively short lived. This made transmissive approaches such as the one outlined in section 4.2 difficult and this forced the development of the emissive approach. As mentioned prior, this approach was motivated by the work of Gao et al., who claimed that they observed a half-cycle THz pulse from a fs-ablated Cu rotating sheet [49]. This required a re-design and re-tooling of the setups shown in fig. 4.10, 4.11, and 4.14.

To re-design and re-tool the setups shown in fig. 4.10, 4.11, and 4.14, a few features had to be changed; first, the use of the VMRA system was abandoned completely. Everything was triggered off of the Legend Elite system the parameters of which are shown in table 4.1. This was necessary because in the Emissive approach shown in fig. 4.26 the LIP (either an EHP or LIBP) acts as the source of THz emission and hence there is no need for an external THz probe which was provided by a GaAs THz-SED pumped by the VMRA system. The second major change is that another beam from the Legend was brought in to do the electro-optic sampling. Because of the higher power, the Legend had to be attenuated using several ND filters along the EOS line shown in fig. 4.26. The third major change was that the coarse delay stage position for the Legend was moved. This was necessary as the EOS and PE lines had to temporally coincide at the same point in time (termed the t_0 point). This t_0 was obtained initially with the help of the Thorlabs DET210 photodiode and the oscilloscope used in the prior section for the PL duration measurements using the reflection off a beam block just before the ZnTe crystal. This gave the rough estimate of where t_0 was with a seperation of at least $\Delta t_p = 300\,\text{ps}$ between the pulses. The final change between the transmissive setup and the emissive setup shown in fig. 4.26, is that the pump line was delayed with a fine delay stage while the EOS line was held fixed.

To pinpoint where t_0 was exactly, the GaAs based THz-SED shown in fig. 4.23 was placed along the THz collection path shown in fig. 4.26 and a broad sweep across the delay stage was performed with the lock-in amplifier running in R-mode. R-mode is a mode of the lock-in amplifier where it measures just the amplitude of the signal, i.e., $R = \sqrt{X^2 + Y^2}$, where

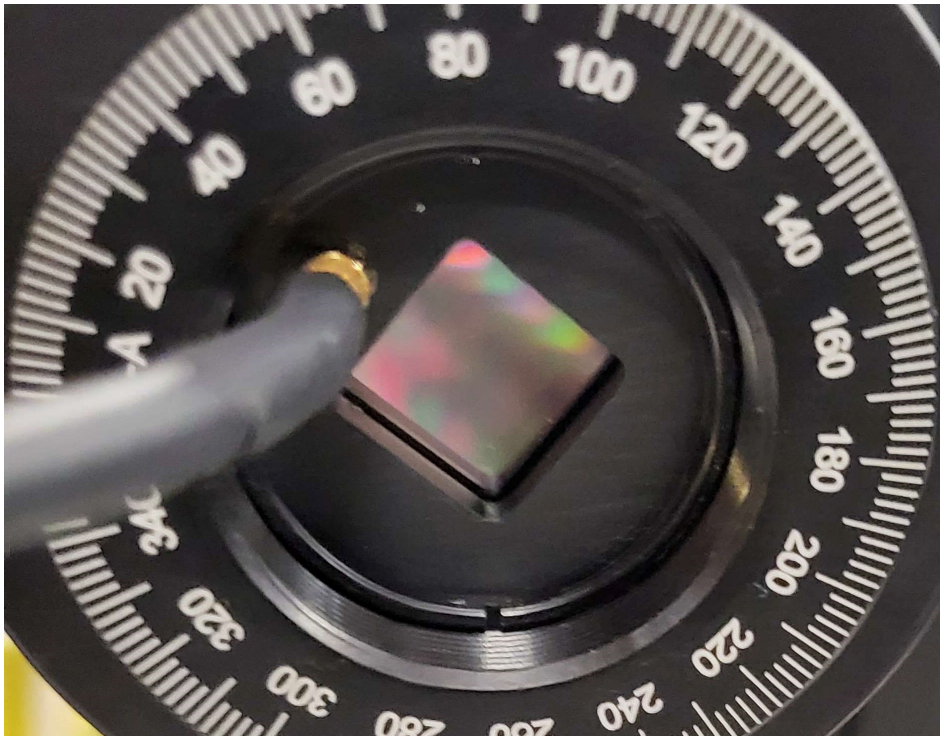

Figure 4.23: A GaAs based THz-SED. This THz-SED was placed along the THz collection path to imitate a LIP source. The shiny surface shown here is PE by the $\lambda = 795\,\text{nm}$ Legend pulse which releases photoexcited carriers which are then driven across the surface by a bias voltage across it. For the calibration of the emissive THz setup, the voltage across the THz-SED was set to $V = 1.7\,\text{V}$ with a current of $I_{\text{pc}} = 0.01\,\text{mA}$.

X and Y are the vector components of the output signal [129]. Once a spike was detected in R-mode, the lock-in amplifier was set back to $A - B$ mode so a proper measurement of the single-cycle THz pulse from the THz-SED could be preformed. The result of this calibration measurement is shown in fig.4.24-4.25. The success of this calibration measurement indicated that emissive THz spectroscopy scheme shown in fig. 4.26 worked and from here the next step was to proceed to benchmark using PE semiconductors.

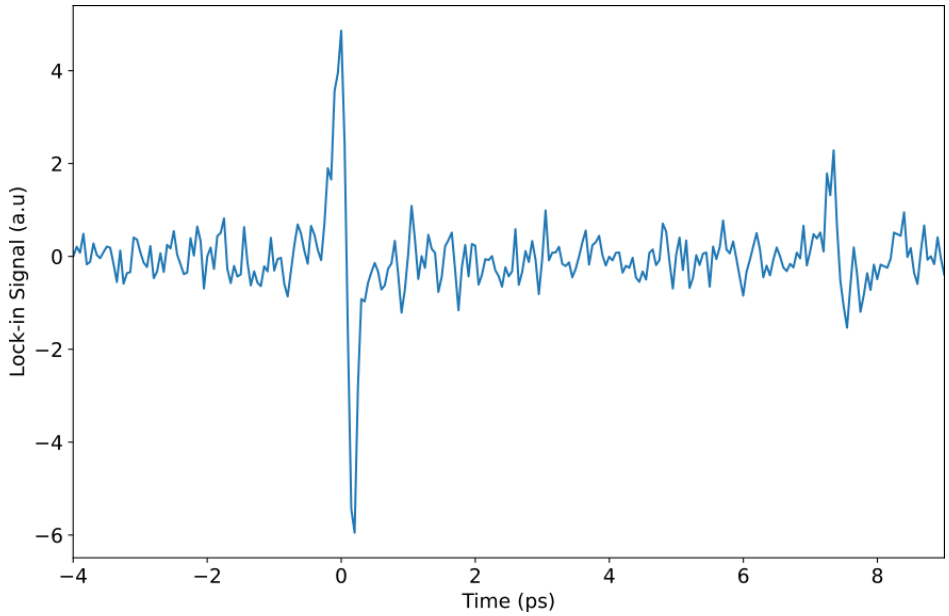

Figure 4.24: Time domain of the THz pulse from the GaAs THz-SED. The detection of this pulse indicated that emissive spectroscopy scheme shown in fig. 4.26 worked. This THz pulse was obtained by fixing the EOS line while delaying the PE line. The lock-in amplifier settings used to obtain this signal was a time constant of $\tau_L = 100\,\text{ms}$ and a sensitivity of $V_L = 10\,\mu\text{V}$.

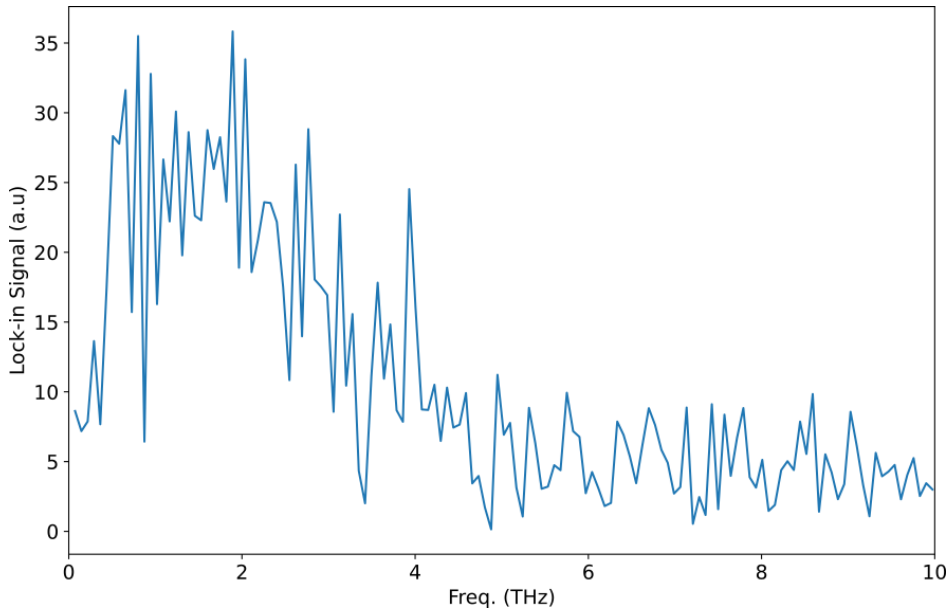

Figure 4.25: The frequency domain of the THz pulse from the GaAs THz-SED shown in fig. 4.24. The detection of this pulse indicated that emissive spectroscopy scheme shown in fig. 4.26 worked. This THz pulse was obtained by fixing the EOS line while delaying the PE line. The bandwidth of THz pulse is $\Delta f \simeq 4\,\text{THz}$.

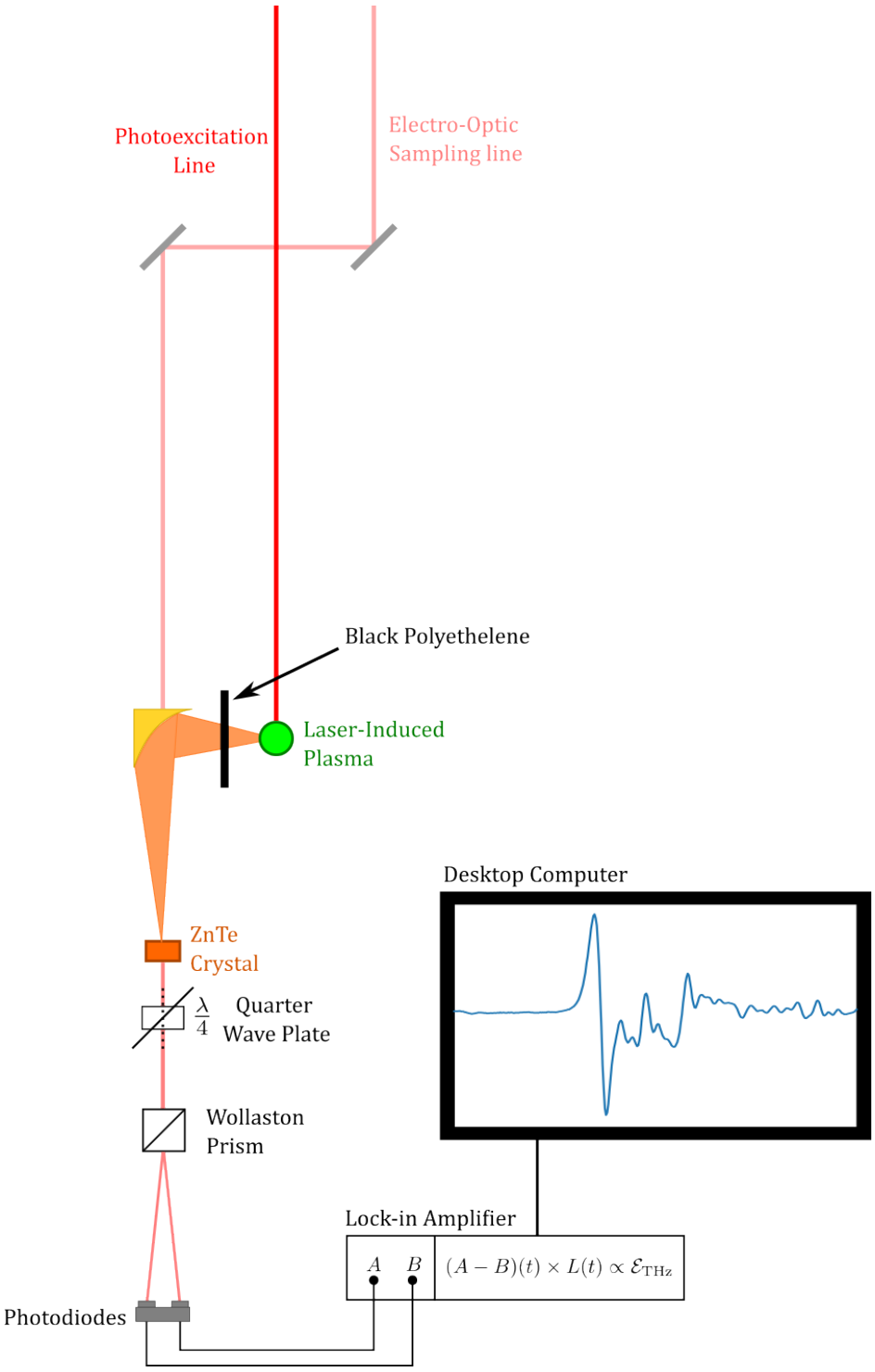

Figure 4.26: A basic schematic of the emissive THz approach. In this approach it is assumed that the LIP (either an EHP or LIBP) acts as a source of THz radiation. In this setup, only the Legend Elite system was used. The PE/Ablation line was delayed with respect to the EOS line. It was shown through the detection of a THz pulse from a THz-SED (see fig. 4.24-4.25) placed along the THz collection path that emissive detection is possible.

4.4.1 Terahertz Emission from Semiconductors

To detect THz emission in semiconductors the setup was arranged according to fig. 4.27. The PE beam was chopped at a rate of $f_c = 500\,\mathrm{Hz}$, and it was at this rate that the lock-in amplifier was fixed to. The average PE-beam power was measured to be around $\langle P \rangle \simeq 102\,\mathrm{mW}$. To emulate the effect of a point source, the PE-beam was clipped using an iris aperture. For the balancing of the photodiodes the lock-in amplifier was set to a time constant of $\tau_L = 30\,\mathrm{ms}$ and a sensitivity of $V_L = 1\,\mathrm{mV}$. The semiconductor wafer was mounted at 45° to the oncoming PE beam as shown in fig. 4.27.

To align the semiconductor wafer and laser to the THz focus, a white paper slip was placed in a wafer holder and it was placed near the THz focus at a 45° angle to the oncoming PE beam. The guiding laser emulated the path followed by the THz pulse, and was tightest at the focus of the Off-axis parabolics. It is to this location that the paper slip in the wafer holder was placed. The PE beam was then adjusted until the spot of the guiding laser overlapped with the PE beam spot. Once the overlap between the guiding laser spot and PE beam had been achieved, the wafer holder was clamped down to the optic table and the paper slip was swapped out with the semiconducting wafer.

THz emission was then checked for by PE the semiconductor wafer and performing a broad sweep across the pump delay stage in R-mode. If a signal was found, the lock-in amplifier was immediately switched to $A - B$ mode and a full scan of the pulse was done. There were in total three semiconductors samples from which THz emission was checked: Undoped GaAs, InAs (111) p-type 2n doped, and GaAs p-type 2n doped $\langle 111 \rangle$. The scan settings of which are displayed in table 4.4. Of the three samples tested, only the InAs (111) p-type 2n doped and GaAs p-type 2n doped $\langle 111 \rangle$ yielded any THz emission. The lock-in amplifier settings from the GaAs p-type 2n doped $\langle 111 \rangle$ were used initially in the detection of THz emission in Cu-LIBPs as it was the lowest sensitivity at which THz emission was detected. However, when THz emission in Cu-LIBP was detected this saturated the lock-in amplifier and the settings had to be subsequently changed.

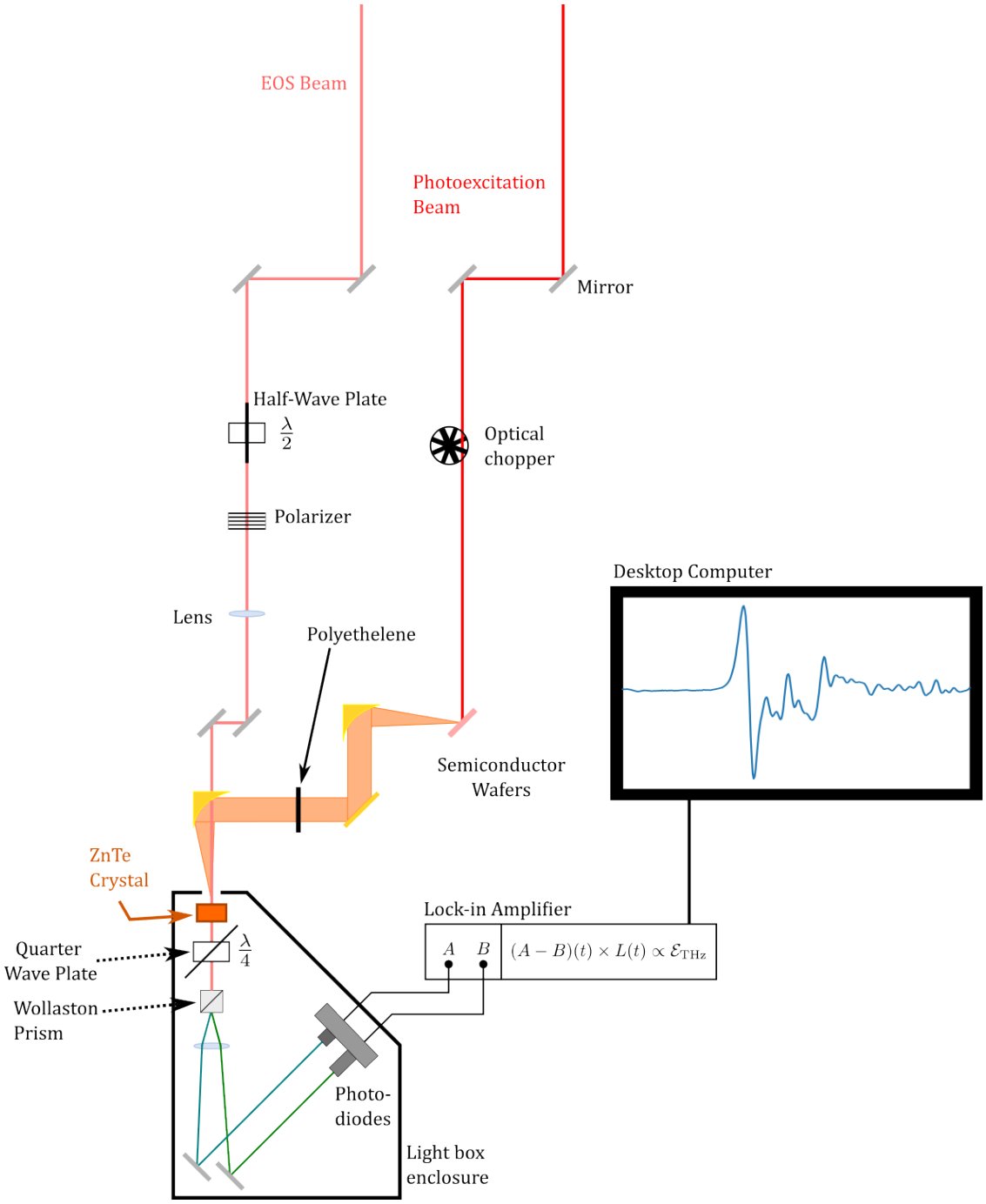

Figure 4.27: The setup used to study THz emission in semiconductors. In this setup, the EOS beam was fixed with respect to the PE beam and the PE beam was chopped at a rate of $f_c = 500\,\mathrm{Hz}$. The polyethylene shown along the THz path prevents coupling of the reflected PE beam to the ZnTe. The semiconductors were set at an angle of $\theta = 45°$ with respect to the oncoming PE beam. The half-wave plate and polarizer in addition to ND filters attached to the lens attenuated EOS beam to prevent damage to the ZnTe crystal.

Sample	V_L (μV)	τ_L (ms)
Undoped GaAs	10	100
InAs (111) p-type 2n doped	200	100
GaAs p-type 2n doped $\langle 111 \rangle$	2	300

Table 4.4: Lock-in amplifier settings and samples used in the detection of THz emission from semiconductors. Note that GaAs is an intrinsically n-type semiconductor.

4.4.2 THz Emission from Cu Laser-Induced Breakdown Plasma

The ablation beam was chopped at a frequency of $f_c = 500\,\text{Hz}$, and it was at this rate that the lock-in amplifier was fixed to. The oncoming ablation beam light was focused using a focal length of $F = 200\,\text{mm}$ as with the transmissive THz experiment in subsection 4.2.2 giving an absorbed fluence of $\Phi \simeq 3.82\,\text{J/cm}^2$. As with the transmissive THz experiment in subsection 4.2.2 the Cu-sample holder was rotated at an angular velocity of $\nu = 0.06\,^\circ/\text{s}$ to guarantee a fresh surface for ablation. As mentioned prior, there was no significant pre-pulse to make a preformed plasma as was done in experiments done by Hamster et al. and Sagisaka et al. [50–52]. This means that any THz emission seen must be arising from the rapid expansion of charge into air alone, as the femtosecond pulse does not interact with the plasma as it did in Hamster et al. or Sagisaka et al. [8; 10; 50–52].

Note that orientation of the Cu-Sample holder was at an angle of $\theta = 20^\circ$ with respect to a oncoming vertically polarized ablation beam that was initially (fig. 4.28(a)). This angle was chosen because of a similar experiment performed by Gao et al.. In the letter Gao et al. orientated a rotating Cu-sheet at this angle with respect to the oncoming laser [49]. There is a danger by placing the sample at the orientation shown in fig. fig. 4.28(a) as there is potential for coupling from optical rectification in the metal [68; 69]. To eliminate THz generation due to optical rectification, the sample was orientated at normal incidence (fig. 4.28(b)). To prevent the coupling of the $\lambda = 795\,\text{nm}$ ablation beam to the photodiodes, polyethylene was added along the THz collection path as shown in fig. 4.30.

While consistent and repeated THz emission was achieved from the ablation of the Cu disk mounted on the smaple holder shown in fig. 4.13, an issue encountered was that the stage position at which THz emission occurred drifted by as much as $\Delta x \simeq 0.05\,\text{mm}$ ($\delta t \simeq 0.3\,\text{ps}$) between scans. This made averaging of the THz waveforms infeasible, individual scans could

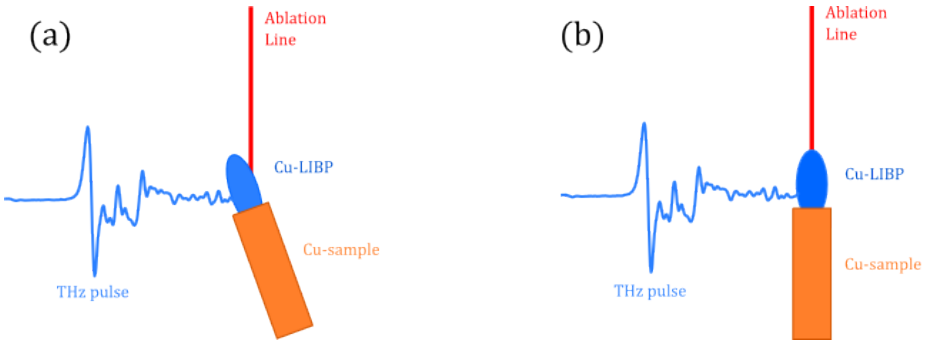

Figure 4.28: The orientations of the Cu-ring at (a) $\theta = 20°$ and at (b) normal incidence. The orientation shown in fig. (a) has the potential for THz generation from optical rectification to couple into the signal, while in orientation (b) this coupling is eliminated. Both orientations were tested over the course of the experiment.

be collected, but not averaged waveforms during a run. The author suspects that this could be due to the fact that the Cu-ring was jutting into and out of the focus slightly causing the peak drift seen in fig. 4.29. This is because the Cu-ring is not totally centred on the sample holder, and at times, the Cu-ring had fallen off and had to be re-attached. Another possible contribution, is that irregularities at the surface of the Cu-ring could contribute to the peak shift, for as noted by Y.R. Shen, local surface defects could change the resulting electric field [70].

For the balancing of the photodiodes the lock-in amplifier was set to a time constant of $\tau_L = 30\,\text{ms}$ and a sensitivity of $V_L = 1\,\text{mV}$. The lock-in amplifier settings selected for the scanning THz waveforms were a time constant of $\tau_L = 300\,\text{ms}$ and a sensitivity of $V_L = 20\,\mu\text{V}$.

Figure 4.29: A photo of the LabVIEW program used in the data collection of THz waveforms from the Cu-LIBP during a run. In this photo Cu-LIBP THz emission peak is shifting by as much as $\Delta x \simeq 0.05\,\mathrm{mm}$ ($\delta t \simeq 0.3\,\mathrm{ps}$). This shifting of the peak makes averaging the THz waveform infeasible. This could arise to due to the position of the Cu-ring jutting into and out of the laser focus slightly, irregularities at the surface of the Cu-ring, or both.

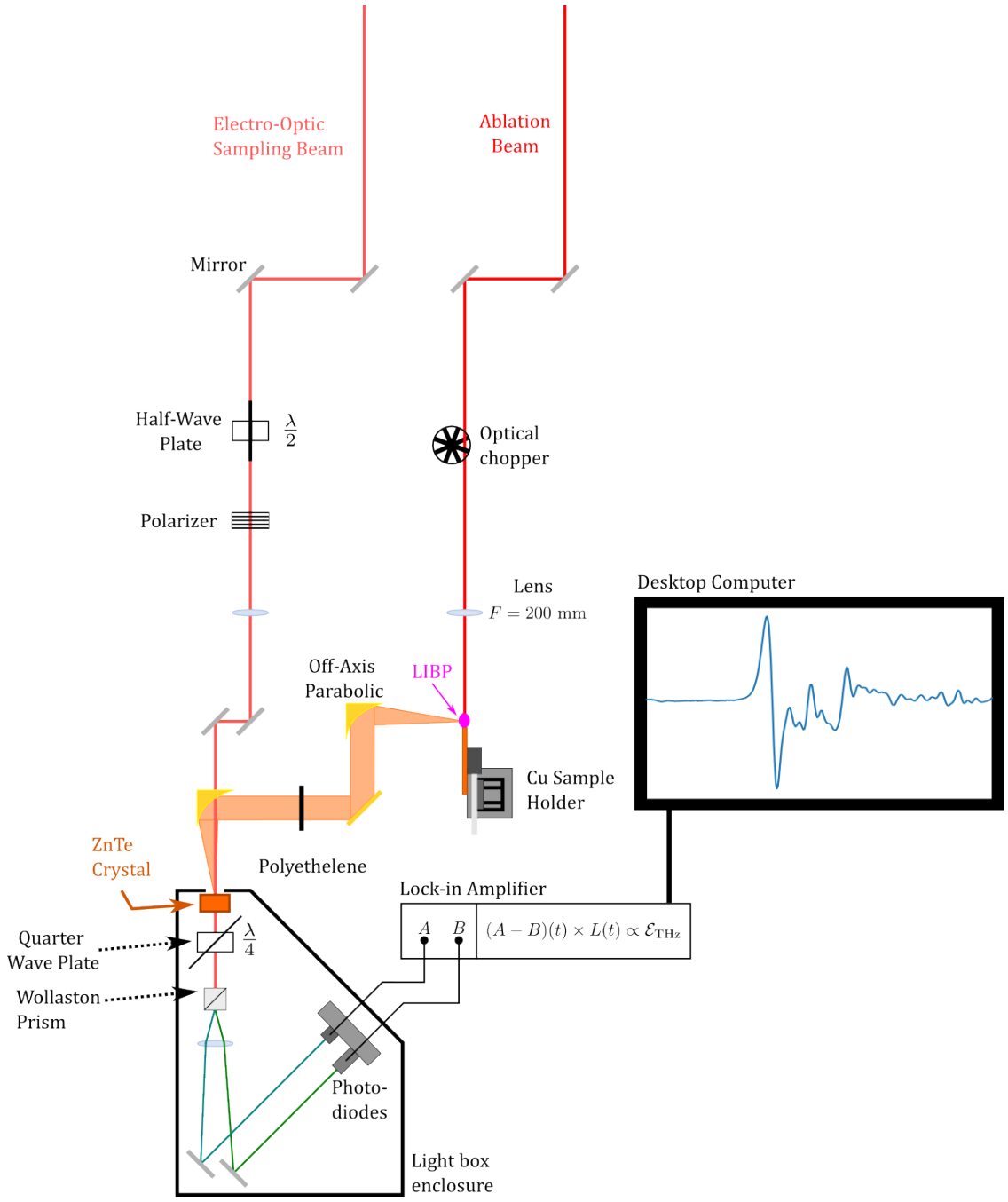

Figure 4.30: A schematic of the setup used for the detection of THz emission in a Cu-LIBP. In this setup, the EOS beam was fixed with respect to the ablation beam and the ablation beam was chopped at a rate of $f_c = 500\,\mathrm{Hz}$. Note that the source Cu-Sample holder was initially orientated at an angle shown in fig. 4.28(a) and was later switched to the orientation shown in fig. 4.28(b). This resulted in THz pulses with differing spectral features. As with the schematic shown in fig. 4.27, the half-wave plate and polarizer in addition to ND filters attached to the lens attenuated the EOS beam to prevent damage to the ZnTe crystal.

Chapter 5

Results: Terahertz Transmission in Laser-Induced Plasmas

As stated in the introduction, the goal of this thesis was to see if LIBPs could be investigated using THz pulses. Initially, this was performed using an experimental setup suited for transmissive probing. This approach was implemented using the setups shown in figures 4.11 and 4.14. Based on the success achieved in detecting THz modulation with semiconductors, the hope was that this could then extend to solid target LIBP. This proved unfruitful for two reasons: As shown by the results obtained here, the PL lifetime proved to be shorter than anticipated (on the order $\tau_0 \sim 20\,\mathrm{ns}$ ($t_{\mathrm{PL}} \sim 100\,\mathrm{ns}$)), a regime that for reasons stated later proved inaccessible with our stage delays.

Presented in this chapter are the results of the time-integrated spectra, the PL lifetime, and THz transmission in semiconductors. The latter two of which hinted that as the setup stood, transmissive THz spectroscopy was not feasible the reasons of which will be elaborated on within this chapter. The conclusions of this chapter then pushed this thesis towards more emissive approaches based on the work of Gao et al. who showed that THz emission can occur within an LIBP [49]. This changed the direction of the work towards monitoring THz emission which proved successful in both the case of semiconductors and Cu-LIBP.

5.1 Time Integrated Spectra and Photoluminescence of Cu target Laser-Induced Breakdown Plasmas

To help gauge the viability of using single-cycle THz pulses for ambient probing of Cu-LIBPs it is necessary to estimate the lifetime of the plume. However, such a metric is ill-defined and there is no consensus on what constitutes the lifetime of a LIBP. As discussed prior in section 2.2, the descision is made to use the PL lifetime. For it is over these time scales that charge carriers have separated and are undergoing recombination (see fig.5.1-5.2) and bremsstrahlung processes, emitting light in the process [12; 83]. Thus, it is over the time light is emitted that the existence of a plasma state can be readily verified and for the purposes of this work, the lifetime of the LIBP is taken to be the duration over which light is emitted.

To benchmark and qualitatively describe the Cu-LIBP PL emission, the spectra of the Cu-LIBP were taken and are shown in fig. 5.1-5.2.

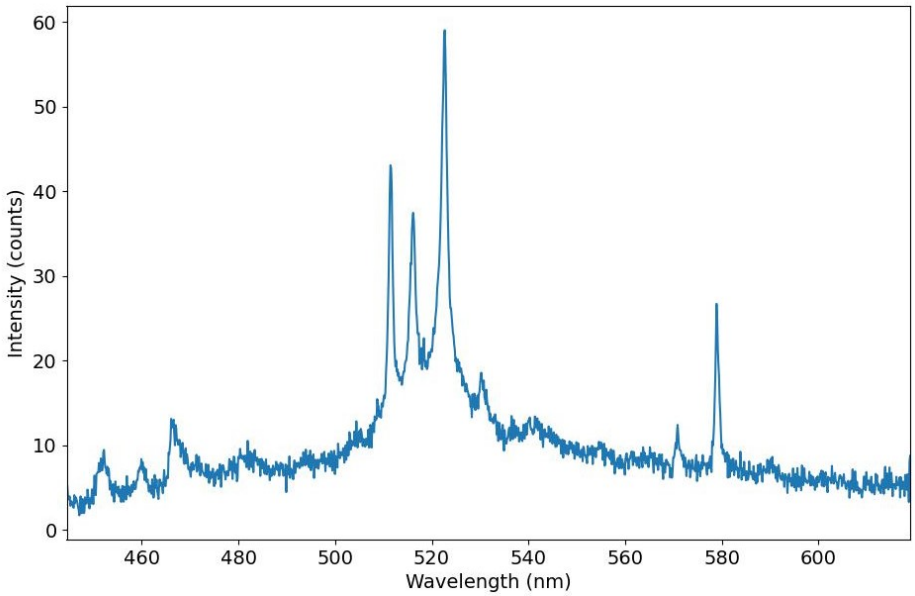

Figure 5.1: Cu-LIBP time integrated spectra centred around $\lambda = 530\,\text{nm}$ collected with the Acton SP2500 Spectrometer. The three main lines centred around $\lambda \sim 520\,\text{nm}$ are the neutral transitions lines corresponding to bound-bound transitions within neutral excited Cu atoms [76].

From fig. 5.1-5.2 it is apparent that continuum emission is present and in the case of fig.

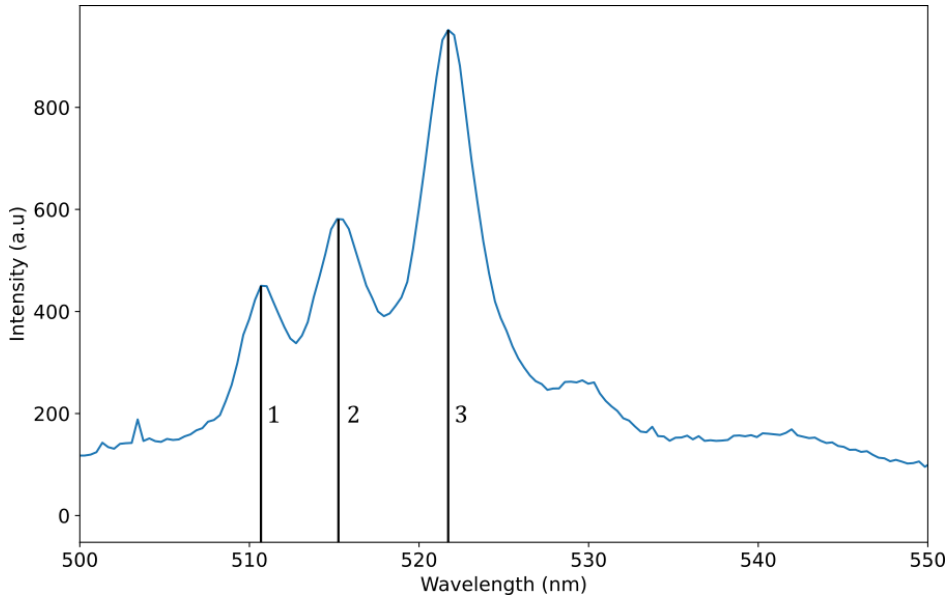

Figure 5.2: A close up of the three main Cu-neutral lines centred around $\lambda \sim 520\,\text{nm}$ taken with the OceanOptics USB2000 spectrometer. These lines represent bound-bound transitions inside excited neutral Cu atoms. The numbered solid black lines correspond to the locations of the three main peaks and are given in table 5.1.

Line	λ_{LV} (nm)	λ_{MV} (nm)	% Difference
1	510.32	510.68	0.07
2	515.25	515.17	0.02
3	521.96	521.71	0.05

Table 5.1: Table comparing the experimentally measured values, λ_{MV}, in this thesis to those of literature values, λ_{LV}, reported in ref. [76]. This indicate that the spectra shown in fig. 5.1-5.2 match closely with what has been reported prior given the negligible per cent difference between them.

5.2, it was so dominant that the main neutral transition lines reported in ref. [76; 136; 137] were only partially resolved. Since the first ionization energy of Cu is relatively high, occuring at $U_I = 7.73\,\text{eV} \mapsto \lambda = 160\,\text{nm}$ it is not possible with either the OceanOptics USB200 or the Princeton Instruments Acton SP2500 spectrometer to detect the first ionization line at $\lambda = 160\,\text{nm}$ [136; 137]. Barring possible X-ray contributions, the spectra in fig. 5.1-5.2 indicate that the light emission detected is dominated by bound-bound transitions, that is by spontaneous emission of excited atoms and ions inside the plasma (see Appendix B and ref. [10; 83] for details). These lines occur around $\lambda \sim 520\,\text{nm}$ as the lines present in fig. 5.1 most closely match Cu I emission lines reported by ref. [76; 136; 137].

As for the photoluminescence (PL), shown in fig. 5.3 and 5.4 it appears to decay exponentially as $I_{\mathrm{PL}} \propto e^{-t/\tau_0}$. Where τ_0 is the PL lifetime. The response of the scope is taken to be Gaussian thus, any resulting curve can be thought of as the convolution of a Gaussian and an exponential decay, which eqn. 2.12 gives as,

$$\begin{aligned} I(t) = g(t,\tau) * I_{\mathrm{PL}}(\tau) &= A_0 \int_{-\infty}^{+\infty} d\tau \theta(\tau - t_0) \exp\left[-\frac{(t-\tau-t_0)^2}{2t_w^2}\right] \exp\left[-\frac{\tau}{\tau_0}\right] \\ &= g(t,\tau) * I_{\mathrm{PL}}(\tau) = A_0 \int_{t_0}^{+\infty} d\tau \exp\left[-\frac{(t-\tau-t_0)^2}{2t_w^2}\right] \exp\left[-\frac{\tau}{\tau_0}\right]. \end{aligned} \tag{5.1}$$

Where $\theta(\tau - t_0)$ is the Heaviside step function, t_0 is the time at which the detector sees Cu-LIBP PL, A_0 is a constant, and t_w is the standard-deviation of the Gaussian scope-response. It is related to the full-width-at-half-maximum according to, FWHM $= 2\sqrt{2\ln(2)}t_w$. By solving integral eqn. 5.1 numerically, an approximate τ_0 can be obtained. This is what is done in the fits of the PL curves shown in fig. 5.3-5.4. It is of note that the integral given by eqn. 5.1 can be solved analytically, and the solution is,

$$I(t) = g(t,\tau) * I_{\mathrm{PL}}(\tau) = I_0 \mathrm{e}^{-\frac{t}{\tau_0}} \left(1 + \mathrm{erf}\left[\frac{\sqrt{2}}{2}\left(\frac{t-2t_0}{t_w} - \frac{t_w}{\tau_0}\right)\right]\right) \tag{5.2}$$

Where, I_0 is a constant defined as,

$$I_0 = \sqrt{\frac{2\pi}{2}} t_w A_0 \exp\left[\frac{t_0}{\tau_0} + \frac{t_w^2}{2\tau_0^2}\right].$$

For the derivation of eqn. 5.2 see Appendix D section D.1. The overall result of fitting the PL curves shown in fig. 5.3-5.4 show that for pump powers on the order of $P = 135 - 205\,\mathrm{mW}$ yield $\tau_0 \simeq 20\,\mathrm{ns}$. Note that the full-width at-half-maximum (FWHM) was used in the fitting process. At lower fluences the fitting routine used breaks down see fig. 5.4 giving $\tilde{\chi}^2 \gg 1$ indicating poorer fit quality.

The fitting routine was implemented using a few in-house classes coded in python centred around the `scipy` API (the documentation for which can be found in ref. [138]). The general outline of the algorithm routine is as follows: data for the traces shown in fig. 5.3-5.4 were

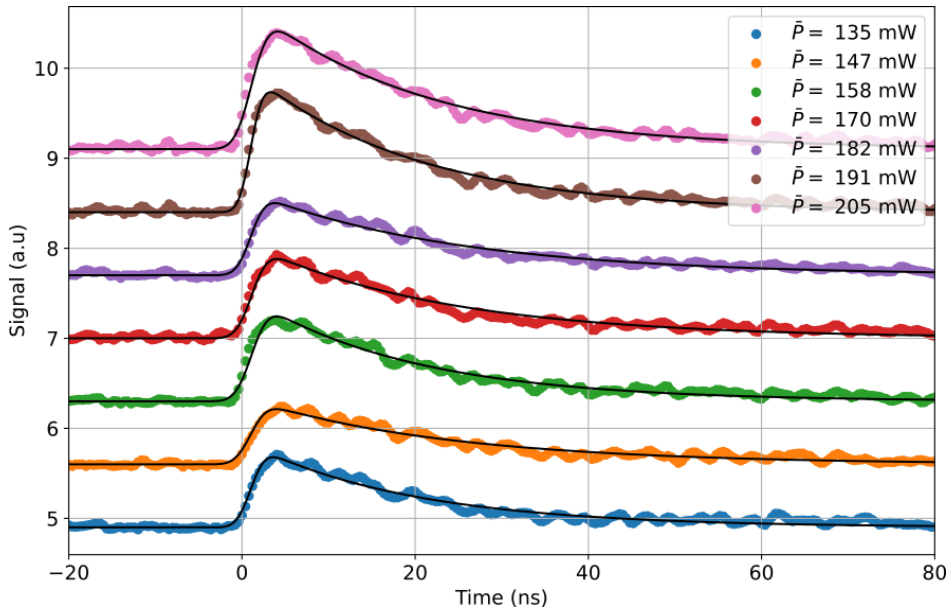

Figure 5.3: Time integrated PL curves for various high fluences. The curves were fit to eqn. 2.12 Fit parameters for each curve are shown in table 5.2. All the curves here have $\tau_0 \simeq 20\,\text{ns}$. Varying the pump (and with it the fluence) power in this range did little to increase

retrieved using the in-house `rtrvPLdata` which performed the necessary pre-processing and cleaning (e.g. removing noise and cutting off unnecessary zeros). `rtrvPLdata` then returned the cleaned dataset and the standard deviation of the noise floor, `sigma`. The cleaned dataset was then past to the `scipy.optimize.curve_fit` method; the bounds for the fit parameters for the method were $A_0 \in [0, 10\,\text{mV/ns}]$, $\tau_0 \in [0, 30\,\text{ns}]$, FWHM $\in [0, 6\,\text{ns}]$, and $t_0 \in [0, 2\,\text{ns}]$ the `maxfev` parameter was set to `maxfev=6000` to allow sufficient passes for convergence. The `scipy.optimize.curve_fit` method would then return two arrays: `popt` and `pcov`. The former being the optimized fit parameters and the latter being the covariance matrix of the parameters. To get the errors `pcov` was evaluated as, `perr=np.sqrt(np.diag(pcov))`. The reduced chi-squared, $\tilde{\chi}^2$, was simultaneously calculated using the in-house `redchisq` method which took the fitted signal trace and the `sigma` parameter as inputs. This process was then repeated for the next trace.

What fig. 5.3 and tab. 5.2 indicates that for fs-ablation, the Cu-LIBP exists on the order of $\tau_0 \simeq 20\,\text{ns}$ which is too short a time frame for THz probing to occur. To see why this is a limiting factor consider that the length of delay needed for a THz pulse to sample Cu-LIBPs

$\langle P \rangle$ (mW)	A_0 (mV/ns)	τ_0 (ns)	t_{PL} (ns)	FWHM (ns)	$\tilde{\chi}^2$
135	0.30 ± 0.01	19.2 ± 0.3	96 ± 2	3.0 ± 0.1	1.04
147	0.20 ± 0.01	23.7 ± 0.3	118 ± 2	3.4 ± 0.2	0.87
158	0.32 ± 0.01	19.0 ± 0.2	95 ± 1	3.5 ± 0.1	0.83
170	0.30 ± 0.01	22.5 ± 0.3	113 ± 1	3.4 ± 0.2	1.21
182	0.29 ± 0.01	23.8 ± 0.2	119 ± 1	3.1 ± 0.1	0.64
191	0.59 ± 0.02	19.6 ± 0.2	98 ± 1	2.6 ± 0.1	1.00
205	0.43 ± 0.01	20.2 ± 0.2	101 ± 1	3.6 ± 0.1	0.98

Table 5.2: Fit parameters and the $\tilde{\chi}^2$ value of each fit of the time integrated PL curves shown in fig.5.3. Uncertainty in $\langle P \rangle$ is constant and is $u(\langle P \rangle) = \pm 1\,\mathrm{mW}$. Varying the fluence here did little to increase the overall PL lifetime, τ_0.

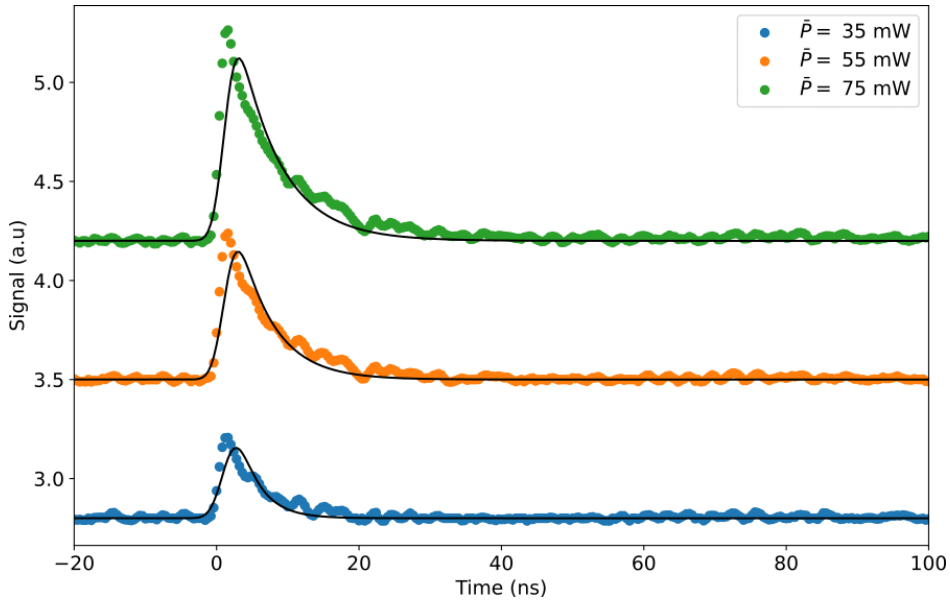

Figure 5.4: Time integrated PL curves for lower fluences. The curves were fit to eqn. 2.12. Fit parameters for each curve are shown in table 5.3. These curves in general are of poorer quality fit in comparison to the high-fluence results shown in fig. 5.3.

$\langle P \rangle$ (mW)	A_0 (mV/ns)	τ_0 (ns)	t_{PL} (ns)	FWHM (ns)	$\tilde{\chi}^2$
35	0.38 ± 0.01	4.9 ± 0.1	24.5 ± 0.5	3.3 ± 0.1	2.94
55	0.50 ± 0.02	5.9 ± 0.1	29.5 ± 0.5	3.2 ± 0.1	5.16
75	0.64 ± 0.02	7.4 ± 0.1	37 ± 0.5	3.0 ± 0.1	10.0

Table 5.3: Fit parameters and the $\tilde{\chi}^2$ value of each fit of the time integrated PL curves shown in fig.5.4. The data presented here suggests more variation in the PL-lifetime with the pump power, albeit with minimal improvement.

is given by,

$$\Delta x = \frac{c\Delta t}{2},$$

where $c = 300\,\text{mm/ns}$ and is the speed of light in air to be able to probe the Cu-LIBP with a duration on the order of, $\tau_0 \simeq 20\,\text{ns}$ implies that the delay is at least $\Delta t = 20\,\text{ns}$ this means that the length of delay required is,

$$\Delta x = \frac{c\Delta t}{2} = \frac{(300\,\text{mm/ns})\,(20\,\text{ns})}{2} = 3 \times 10^4\,\text{mm} = 3\,\text{m}$$

At the time of writing and experimentation, we do not have access to a fine delay stage of this length. This means that given the current limitations of space and material, it is not possible to probe the dynamics of fs-pulse induced LIBP from solid targets. One possible workaround that is hinted at in Mingareev et al., is to use a multi-pass delay stage called a Herriot cell [139]. A Herriot cell consists of two high reflectivity mirrors which form a cavity that traps the input light bouncing it back and forth for a number of N passes before releasing it [139]. Mingareev et al. used a Herriot cell to perform shadowgraphy on a fs-ablated Al and Cu [139]. The same concept could be extended to THz spectroscopy to probe nanosecond-microsecond phenomena by delaying the THz generation line. There does remain the issue of diffusion of solid target LIBP plume expansion into the ambient air. For if there is not sufficient expansion into the focus of the plume at a time when there are enough carriers to sample, the THz pulse will not be able to probe the LIBP as the plasma will be too diffuse. Ideally, for THz probing the plume should at least be on the order of $l \sim 1\,\text{mm}$.

A brief survey of the literature indicates that this should not be too great a concern. For example, Freeman et al. using ICCD measurements gave a typical fully extended plume a lateral length of about $l \simeq 2.5\,\text{mm}$ under ambient conditions [140]. Though Freeman et al. is unclear exactly when the image they gave was taken, so it is hard to gauge roughly how dense the plume is. Electron shadowgraphy measurements performed by Centurion et al. indicate that within the first ~ 30 picoseconds, there is rapid plume expansion to at least $l \sim 0.45\,\text{mm}$ under ambient conditions [92]. For the case of Cu-LIBP specifically, Wang et al.'s ICCD measurements do give a plume at an extent of $l \simeq 1\,\text{mm}$ at a time of 800 ns after ablation

with a corresponding density of approximately, $n_e \simeq 7 \times 10^{17}\,\mathrm{cm}^{-3}$ [11]. Wang et al.'s results taken by themselves do seem to indicate that there is both sufficient length, and sufficient electron number density for THz probing, given how THz spectroscopy was performed for inductively-coupled plasmas, with densities on the order of $n_e \sim 10^{11} - 10^{16}\mathrm{cm}^{-3}$ [27–31].

The main bottleneck for transmissive THz probing of LIBPs is then just the timing. Using the results from fig. 5.3 and table 5.2 gives the full Cu-LIBP PL lifetime is on the order of $t_{\mathrm{PL}} \simeq 100\,\mathrm{ns}$. This makes it very difficult to probe using the setup outlined in chapter 4 section 4.2 as the EHP to which the setup was calibrated to have full conductivity lifetimes, t_c, ranging from $t_c \simeq 6 - 348\,\mu\mathrm{s}$. (For discussion on the relative timing see section 5.2)

Possible sources of error could come from one of two sources: (1) the stand-off distance at which the fibre optic was placed (2) the angle at which PL was collected. For (1) there is a noted dependency on the intensity of light meaning that slight changes to the fibre position could result in significant reduction in the overall signal [47; 141]. For (2) the angular dependency was neglected and this could also cause a loss of PL signal [141]. The reason why the distance and angle of the fibre-optic matters, is as Lin et al. mentions, the LIBP characteristics vary dramatically with distance from the target surface in all directions [141]. Lin et al. observed very different spectral intensities at different fibre-optic angles and polar distances, with optimal distances and angles being between $15\,\mathrm{mm} \leq r \leq 35\,\mathrm{mm}$ and $\theta = 50^\circ$ with respect to the sample plane [141]. Lin et al.'s results are not shocking. To understand why this is so it helps to recall that the time-averaged intensity of light is [142],

$$I = \frac{1}{2} c \epsilon_0 \mathcal{E}^2. \tag{5.3}$$

Due to the rapid separation of charges at the early times in a LIBP, a distinct ion-front and electron-front form in the LIBP at the early times [89–93]. This local separation of positive and negative charge can be thought of as a transient dipole [143]. Thus, a model of the Cu-LIBP electric field could be a dipole in the near-field. The electric field of a perfect dipole, $\vec{\mathcal{E}}_d$, in spherical coordinates is given as [143],

$$\vec{\mathcal{E}}_d\,(r, \theta) = \frac{p}{4\pi\epsilon_0 r^3} \left[2\cos^2(\theta)\hat{r} + \sin(\theta)\hat{\theta} \right], \tag{5.4}$$

where $p = qd$ is the dipole moment magnitude, with d being the separation between the positive and negative charge clouds. Taking the dot product of eqn. 5.4 with itself gives ,

$$\vec{\mathcal{E}}_d \cdot \vec{\mathcal{E}}_d = \mathcal{E}_d^2 = \left(\frac{p}{4\pi\epsilon_0 r^3}\right)^2 \left(4\cos^2(\theta) + \sin^2(\theta)\right) = \left(\frac{p}{4\pi\epsilon_0 r^3}\right)^2 \left(3\cos^2(\theta) + 1\right).$$

Substituting this result into eqn. 5.3 gives the intensity of the Cu-LIBP as,

$$I_d = \frac{1}{2} c\epsilon_0 \mathcal{E}_d^2 = \frac{c\epsilon_0}{2}\left(\frac{p}{4\pi\epsilon_0 r^3}\right)^2 \left(3\cos^2(\theta) + 1\right) = \frac{c}{2\epsilon_0}\left(\frac{p}{4\pi}\right)^2 \frac{\left(3\cos^2(\theta) + 1\right)}{r^6}.$$

$$\therefore I_d \propto \frac{\left(3\cos^2(\theta) + 1\right)}{r^6} \tag{5.5}$$

What eqn. 5.5 indicates is that the intensity of light from a Cu-LIBP falls off as $I_d \propto 1/r^6$ with the distance. While the exact dependency of LIBP light intensity may not be, $I_d \propto 1/r^6$, it illustrates why ref. [47; 141] all noticed variation with the collected plasma PL with distance. This could translate to greater intensities, and possibly longer decay times if the fibre-optic was placed closer. In this thesis, the distance between the fibre-optic tip and the plasma was roughly $l \sim 40\,\text{mm} - 50\,\text{mm}$. This was outside the optimal range mentioned by Lin et al. ($15\,\text{mm} \leq r \leq 35\,\text{mm}$) [141]. Despite this limitation, the timescales over which I_{PL} decayed were on the order of $t_{\text{PL}} \sim 100\,\text{ns}$, which matches Verhoff et al.'s observation that the emission intensity from fs-ablated brass, an alloy of copper and zinc, was very weak after $\sim 100\,\text{ns}$ [8]. Thus, the PL-intensity curves observed in fig. 5.3-5.4 are within reason. In conclusion, taking these values as a lower order estimate of PL emission, indicate that PL and by extension, the plasma is relatively short lived in comparison to the EHP in semiconductors discussed in the next section. If $\tau_0 \simeq 20\,\text{ns}$ the stage length needed is $\Delta x = 3\,\text{m}$ to access those time scales, which was beyond our experimental capabilities. Even if the plasma is longer lived than what is indicated here, these results still point towards the need for proper time delays between the arrival of the THz pulse and plasma formation.

5.2 Terahetz Transmission in Semiconductors

For the benchmarking of the asynchronous THz transmissive approach outlined in chapter 4 section 4.2, semiconductors GaAs and Si were PE to form an EHP analgous to the Cu-LIBP. The goal with this experiment was to show that a $\Delta\mathcal{T}$ could be obtained, for if this approach worked in semiconductor EHPs, it should translate over to LIBPs. While a $\Delta\mathcal{T}$ was obtained for both the cases of PE GaAs and Si (see fig. 5.5 and 5.7), both have conductivity lifetimes, τ_c, on the order of $\tau_c \simeq 1-70\,\mu$s which is substantially larger than the $\tau_0 \simeq 20\,$ns PL lifetime seen in the previous section. Making detection for the case of EHPs easier than Cu-LIBPs.

As with the Cu-LIBP PL, it was assumed that the $-\Delta\mathcal{T}$ shown in fig. 5.5 and 5.7 decays exponentially $-\Delta\mathcal{T} \propto e^{-t/\tau_c}$. If again, the response of the scope is taken to be Gaussian any resulting curve can be thought of as the convolution of a Gaussian and an exponential decay. The result is identical to eqn. 5.1 with the substitution $\tau_0 \mapsto \tau_c$. Furthermore, as with the Cu-LIBP PL lifetime, we can define a full conductivity lifetime, t_c which is equal to five time constants of τ_c, i.e., $t_c = 5\tau_c$. The resulting $-\Delta\mathcal{T}$ for Si and GaAs are shown in fig. 5.5 and 5.7.

A type II Chebyshev polynomial filter was applied to the Si conductivity lifetime shown in fig. 5.5. This was done to get an approximate fit, otherwise the fitting routine developed in section 5.1 proved to be infeasible as it would not converge or improperly fit the unifiltered curve shown in fig. 5.5. This choice of filtration is further justified when the Fourier transformed spectrum of fig. 5.5, shown in fig. 5.6, is considered. Fig. 5.6 indicated that the bulk of the signal comes from lower-frequency components less than the cutoff frequency, f_c, of $f_c = 0.05\,$MHz with higher frequency components contributing to the noise. The GaAs conductivity lifetime required no equivalent filtration to perform the fit, and the fit proceeded without the use of a filter. The results for the fits shown in eqn. 5.5 and 5.7 are given in table 5.4.

By setting the delay stage such that the $-\Delta\mathcal{T}$ was maximized, it was possible to then vary the average laser power, $\langle P\rangle$, used to pump the Si-wafer and observe changes in the negative average differential THz transmission, $-\langle\Delta\mathcal{T}\rangle$. The results of which are shown in fig. 5.8. Fig. 5.8 shows linear behaviour between the $\langle P\rangle$ and $-\langle\Delta\mathcal{T}\rangle$ until some critical

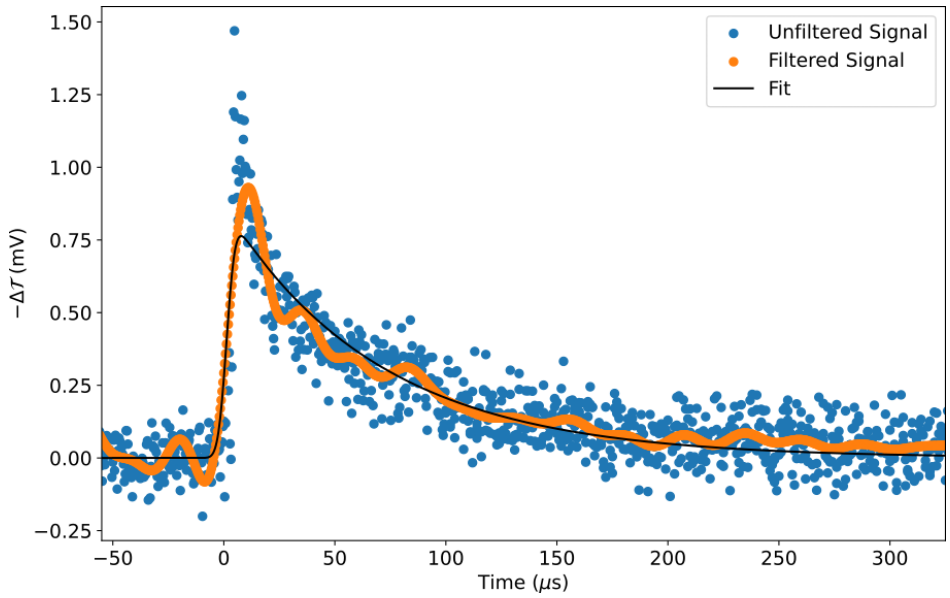

Figure 5.5: The conductivity lifetime of an electron-hole plasma in PE-Si. Here $-\Delta\mathcal{T}$ is the negative differential transmission. Due to noise in the signal, a low-pass type II Chebyshev polynomial filter of order, N, of $N = 12$ power, a cutoff frequency, f_c, of $f_c = 12\,\text{MHz}$ and a roll-off, A_s, of $A_s = 85\,\text{dB}$ was applied to the signal. This was done so an estimate of the conductivity lifetime could be obtained by fitting to the filtered signal. The fit parameters are given in table 5.4. Data was collected using an oscilloscope.

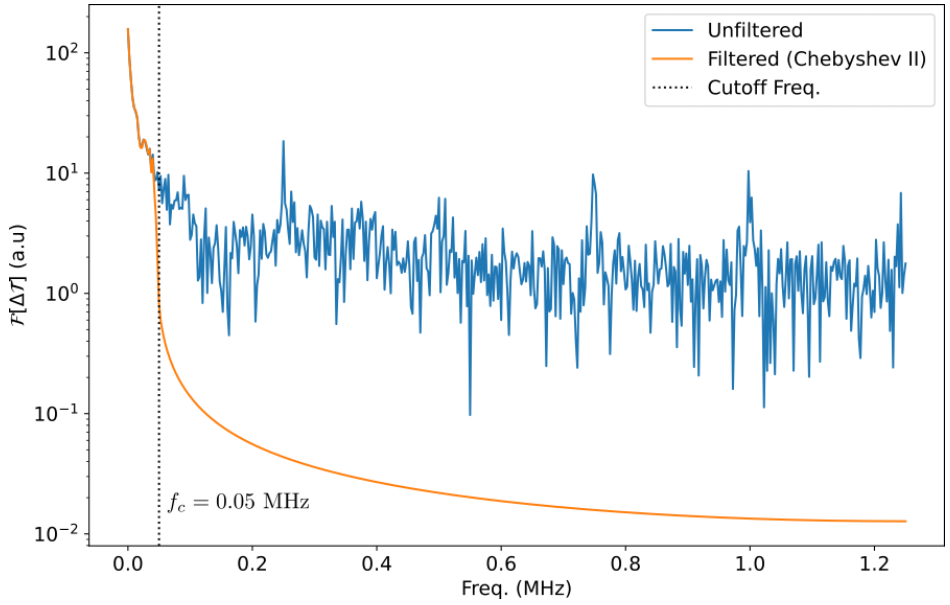

Figure 5.6: Fig. 5.5 in the frequency domain. As is evident from the figure, past $f_c = 0.05\,\text{MHz}$, the bulk of the frequency components contribute to noise in the signal. This motivated the use of th low-pass type II Chebyshev polynomial filter.

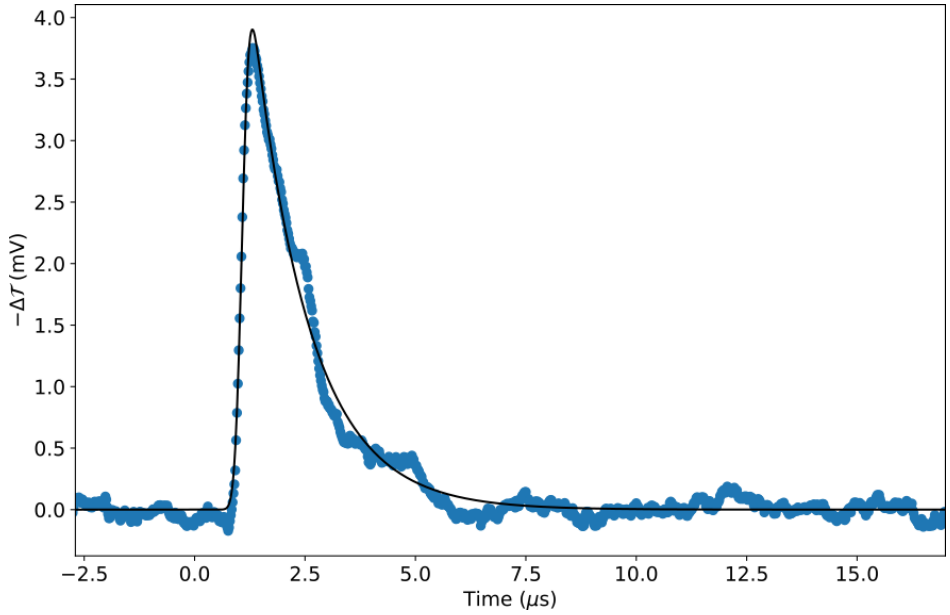

Figure 5.7: The conductivity lifetime of an EHP in PE-GaAs. Fit parameters are shown in table 5.4. Unlike the PE-Si shown in fig. 5.5, no filter was applied to the signal. The fit parameters are given in table 5.4. Data was collected using an oscilloscope.

Sample	A_0 (mV/μs)	t_0 (μs)	τ_c (μs)	t_c (μs)	FWHM (μs)	$\tilde{\chi}^2$
GaAs	35.5 ± 0.8	1.079 ± 0.002	1.27 ± 0.01	6.35 ± 0.05	0.30 ± 0.01	2.21
Si	0.12 ± 0.01	1.3 ± 0.1	69.6 ± 0.8	348 ± 4	7.1 ± 0.4	1.04

Table 5.4: Fit parameters and the $\tilde{\chi}^2$ value of the $-\Delta\mathcal{T}$ fits shown in fig.5.8 and 5.7. The Si results came from the fits to the filtered signal. Note that no filtering was performed on the GaAs signal.

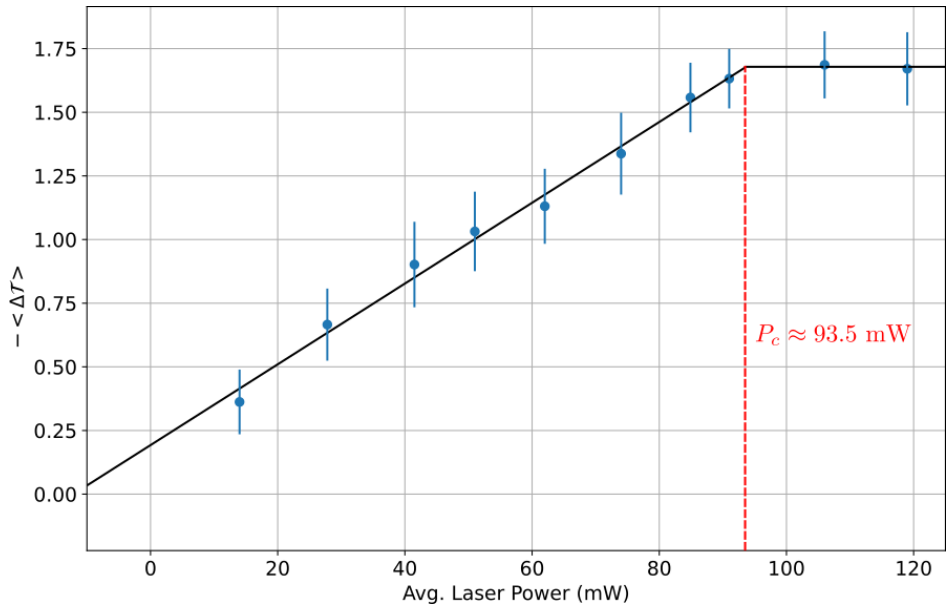

Figure 5.8: Measurement of the THz modulation in the presence of an EHP in PE Si for varying optical pump power. Here $-\langle\Delta\mathcal{T}\rangle$ is the negative average differential transmission obtained from a lock-in amplifier read-out. The error bars are the standard deviation in the $-\langle\Delta\mathcal{T}\rangle$ signal and range from $u\left(-\langle\Delta\mathcal{T}\rangle\right) \simeq \pm 0.1 - 0.2$. Uncertainty in optical pump power is constant and is $u\left(P\right) = \pm 0.1\,\mathrm{mW}$. The black line is the fit given by eqn. 5.6. Initial linear behaviour from $P = 27.8 - 93.5\,\mathrm{mW}$ ($E_p = 27.8 - 93.5\,\mu\mathrm{J}$) implies an increase in the free-carriers for screening. The saturation at $P_c \simeq 93.5\,\mathrm{mW}$ at which point, indicates that the maximal number of free-carriers have been released and more cannot be pumped. The saturation value is $-\langle\Delta\mathcal{T}\rangle = -\Delta\mathcal{T}_s = 1.68 \pm 0.03$.

power, P_c. This P_c was estimated to occur at $P_c \simeq 93.5\,\mathrm{mW}$. Past P_c the $-\langle\Delta\mathcal{T}\rangle$ became saturated and was found to be equal to $-\langle\Delta\mathcal{T}\rangle = -\Delta\mathcal{T}_s = 1.68 \pm 0.03$. This behaviour can be modelled according to the following phenomenological expression,

$$-\langle\Delta\mathcal{T}\rangle\left(P\right) = \begin{cases} \beta_0 P + \Delta\mathcal{T}_m & \text{for } P < P_c \\ -\Delta\mathcal{T}_s & \text{for } P \geq P_c, \end{cases} \tag{5.6}$$

where β_0 is the slope and is $\beta_0 = (1.6 \pm 0.1) \times 10^{-2}\mathrm{mW}^{-1}$ and $\Delta\mathcal{T}_m$ is the minimal differential transmission observable and is $\Delta\mathcal{T}_m \approx 0.19 \pm 0.03$. The fitting of eqn. 5.6 was implemented using the `scipy.optimize.curve_fit` method from the `scipy` API (the documentation for which can be found in ref. [138]).

The observation of a saturation behaviour in fig.5.8 can be explained as follows: when a

semiconductor is being PE, electrons are promoted to the conduction band, while holes go to the valence band as illustrated in fig. 3.1 [113; 114]. The probability of these transitions between the conduction and valence band occur is given by Fermi's golden rule [113],

$$w_{i\to f} = \frac{2\pi}{\hbar}|\langle f|\,\mathcal{H}'\,|i\rangle|^2 g\left(\hbar\omega\right) \tag{5.7}$$

where, $\mathcal{H}'$, is the interaction Hamiltonian and $g\left(\hbar\omega\right)$ is the joint density of states for electrons and holes and is given by [113],

$$g\left(\hbar\omega\right) = \frac{1}{2\pi^2}\left(\frac{2\mu}{\hbar^2}\right)^{3/2}\left(\hbar\omega - E_G\right)^{1/2}. \tag{5.8}$$

Where $\hbar\omega$ is the incident photon energy such that $\hbar\omega \geq E_G$ and μ is the reduced electron-hole mass [113],

$$\frac{1}{\mu} = \frac{1}{m_e^*} + \frac{1}{m_h^*},$$

where m_e^* and m_h^* are the effective electron and hole masses respectively. The under PE $\mathcal{H}'$ is described semi-classically as an electric-dipole transition, $\mathcal{H}' = -e\mathbf{r}\cdot\vec{\mathcal{E}}_0$ where $\mathbf{r}$ is the position operator; this form of the Hamiltonian is called the electric-dipole approximation [113; 144]. The derivation of this approximation is given in ref. [144]. What is important for this thesis is to note that because $\vec{\mathcal{E}}_0$ is just a constant electric field from the laser, meaning that eqn. 5.7 can be re-written as [113; 144],

$$\begin{aligned} w_{i\to f} = \frac{2\pi}{\hbar}|\langle f|\,\mathcal{H}'\,|i\rangle|^2 g\left(\hbar\omega\right) = \frac{2\pi}{\hbar}\left|\langle f|\,(-e\mathbf{r})\cdot\vec{\mathcal{E}}_0\,|i\rangle\right|^2 g\left(\hbar\omega\right) \\ \therefore w_{i\to f} = \frac{2\pi}{\hbar}\left(e\mathcal{E}_0\right)^2|\langle f|\,\mathbf{r}\,|i\rangle|^2 g\left(\hbar\omega\right). \end{aligned} \tag{5.9}$$

The task is to now relate the laser field, $\mathcal{E}_0$ to the laser power. To do this, recall that the time-averaged energy flow through a surface with a normal at $\hat{z}$ is given by the time-averaged Poynting vector [142],

$$\langle\mathbf{S}\rangle = \frac{1}{2}c\epsilon_0\mathcal{E}_0^2\hat{z} = I\hat{z}. \tag{5.10}$$

power, P in turn is related to $\langle \mathbf{S} \rangle$ through the integral [145],

$$\langle P \rangle = \int \langle \mathbf{S} \rangle \cdot d\vec{A}, \tag{5.11}$$

where $d\vec{A}$ is the surface area under consideration, in this instance, $d\vec{A} = sdsd\phi\hat{z}$ which corresponds to the an integration over the area the laser spot covers the semiconductor. Evaluating eqn. 5.11 gives,

$$\begin{aligned} \langle P \rangle = \int \langle \mathbf{S} \rangle \cdot d\vec{A} = \frac{1}{2} c\epsilon_0 \mathcal{E}_0^2 \int_0^{r_0} \int_0^{2\pi} sdsd\phi = \frac{\pi r_0^2}{2} c\epsilon_0 \mathcal{E}_0^2 = \frac{\pi r_0^2}{2Z_0} \mathcal{E}_0^2 \\ \langle P \rangle = \frac{\pi r_0^2}{2Z_0} \mathcal{E}_0^2 \implies \therefore \mathcal{E}_0^2 = \frac{2Z_0}{\pi r_0^2} \langle P \rangle , \end{aligned} \tag{5.12}$$

where Z_0 is the impedance of free-space and is $Z_0 = 377\,\Omega$ and r_0 is the laser spot-size radius. Substituting eqn. 5.12 into eqn. 5.9 gives,

$$\begin{aligned} \therefore w_{i\to f} = \frac{Z_0}{\hbar} \left(\frac{2e}{r_0} \right)^2 \langle P \rangle \left| \langle f | \, \mathbf{r} \, | i \rangle \right|^2 g\left(\hbar\omega\right) \\ w_{i\to f} = \frac{Z_0}{\hbar} \left(\frac{2e}{r_0} \right)^2 \langle P \rangle \left| \langle f | \, \mathbf{r} \, | i \rangle \right|^2 \frac{1}{2\pi^2} \left(\frac{2\mu}{\hbar^2} \right)^{3/2} \left(\hbar\omega - E_G \right)^{1/2} . \end{aligned} \tag{5.13}$$

What eqn. 5.13 shows is that $w_{i\to f} \propto \langle P \rangle$; by increasing $\langle P \rangle$, the probability of a transition between the conduction and valence band and thus, the likelihood of an electron-hole pair being created as illustrated in fig. 3.1 increases. This explains the initial linear behaviour seen in fig. 5.8, for by pumping the Si wafer at higher powers, the probability of a transition, and with it, free-carriers being released, increases. These free-carriers then screen the oncoming THz pulses travelling through the wafer, leading to a rising $-\langle \Delta\mathcal{T} \rangle$.

The onset of saturation at P_c in fig. 5.8 can be explained using the Pauli exclusion principle. The Pauli exclusion principle states that no two electrons can occupy the same state [146]. For the case of semiconductors there exists a very large, but finite number of states that the electrons can occupy in the conduction band [113]. Increasing $w_{i\to f}$ increases the likelihood that the conduction band occupancy will be filled [113], thus past a certain threshold, no new transitions can take place as the band is already filled and no two electrons can occupy the same state. When this comes about, the maximum number of free-carriers

capable of screening the oncoming THz pulse have been released, and subsequently $-\langle\Delta\mathcal{T}\rangle = -\Delta\mathcal{T}_s$.

By being continually pumped, an EHP is sustained and the oncoming THz pulses are attenuated as seen in fig. 5.5, 5.7, and 5.8. Varying the pump delay time and repeated sampling of the THz pulse via EOS, the conductivity and collision times could be measured using the Drude model as per ref. [22; 23; 25; 59]. For the purposes of this thesis though, the interest lies not in re-creating the results seen in ref. [22; 23; 25; 59], but in observing a $-\Delta\mathcal{T}$ like the ones shown in fig. 5.5 and 5.7 for the case of a Cu-LIBP. The significance of this is that a figure similar to that of fig. 5.5 and 5.7 would mean that conductivity measurements in semiconductors could just as easily apply to LIBPs. Therefore, no attempt was made in this thesis to extract conductivities, σ_1 and σ_2 from the Si and GaAs samples.

Furthermore, because the area of ablation is finite containing a finite amount of electrons and ions, an analogous saturation behaviour given by eqn. 5.6 and shown in fig. 5.8 could also arise. This conjecture is rooted in Park et al.'s experiments, which observed saturation behaviour in charge measurements for ionized planar Cu samples at around $\Phi \simeq 1\,\mathrm{kJ/cm^2}$ [71].

However, over the course of the investigation period, no such analogous results like those shown in fig. 5.5, 5.7, and 5.8 were replicated in a Cu-LIBP. The reasoning as to why this asynchronous technique worked in semiconductors but failed for Cu-LIBPs arises from the orders of magnitude difference between the full conductivity lifetime, t_c, which is $t_c \simeq 6 - 348\,\mu\mathrm{s}$ and the full PL lifetime, t_{PL}, which was found to be $t_{\mathrm{PL}} \simeq 100\,\mathrm{ns}$. This massive difference in the lifetimes made it unlikely for Cu-LIBP to be probed using the asynchronous methods outlined in chapter 4 section 4.2. This is because the period between plasma formation in both cases is $T_p = 2\,\mathrm{ms}$ meaning that only every 2 ms is there a LIP (either EHP or LIBP) available for sampling and the VMRA responsible for THz generation, only produces THz pulses $T_p = 4\,\mu\mathrm{s}$. This makes it more likely for the THz pulse to "see" the EHP (with $t_c \simeq 6 - 348\,\mu\mathrm{s}$) but not the LIBP (with $t_{\mathrm{PL}} \simeq 100\,\mathrm{ns}$) (see fig. 5.9). To put it another way, measurement of microsecond scale processes, such as the conductivity lifetimes shown in this section, are just easier to measure with microsecond timing between the pulses, than nanosecond scale process, such as the Cu-LIBPs.

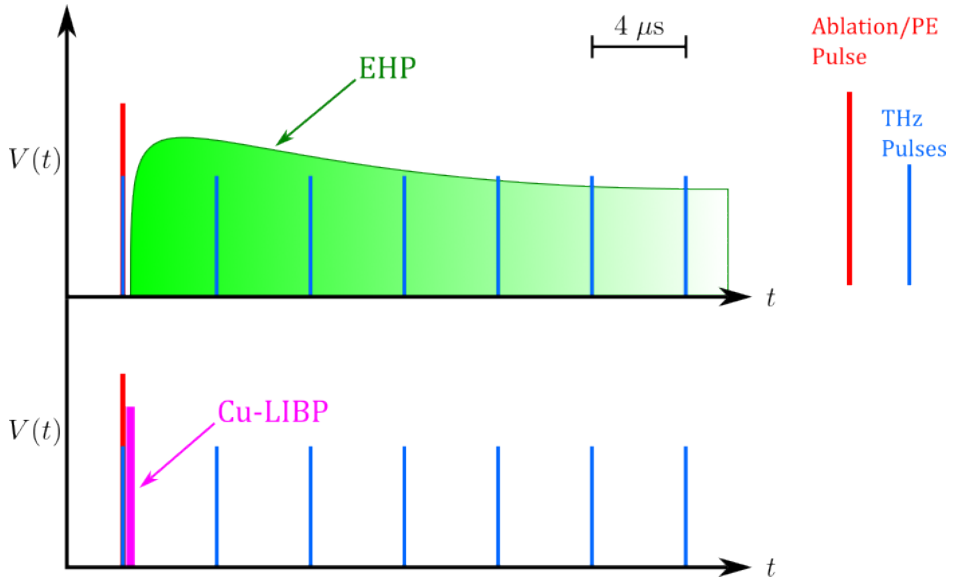

Figure 5.9: A graphical explanation of the difficulties encountered with sampling a Cu-LIBP. The timing diagram is on a $4\,\mu$s scale. While it is not impossible to detect the Cu-LIBP, shifting the arrival of the THz pulses requires a delay of at least $\Delta x = 3\,\mathrm{m}$ which is not feasible with the setup used. Note that THz pulses could arrive later or earlier with respect to the Ablation/PE pulses due to the random phase between the Legend and VMRA systems.

Chapter 6

Results: Terahertz Emission in Laser-Induced Plasmas

6.1 THz Emission in Cu target Laser-Induced Breakdown Plasmas

THz emission has been observed in gaseous target plasmas and solid target plasmas first by Hamster et al. in 1993 [51]. Cook and Hochstrasser later refined the technique for gaseous targets leading to the development of Four Wave Mixing (FWM) which is now a widespread technique for THz emission [123; 147]. Coherent THz emission from a solid target though was first detected by Yuan Gao in 2008 using EOS [49]. Strangely though, there was little follow up to Gao's observations with most of the work discussing detection of THz radiation from a solid target plasma using a bolometer, but not the half-cycle or even full-cycle pulse [50; 53; 54; 56]. Though there is the notable exception of Li et al. who was able to observe a full cycle THz pulse using a relativistic laser [55].

Curiously though, neither Li or Gao are concerned with non-linear effects arising from the interaction between light and the solid target [49; 55]. Both Li and Gao have their samples mounted at an angle to the oncoming PE-beam, and at such an angle contributions due to optical rectification are non-negilgable [49; 55; 68]. However as noted by Anisimov et al. in their letter on ultrashort pulse interactions, thermionic emission and the photoelectric

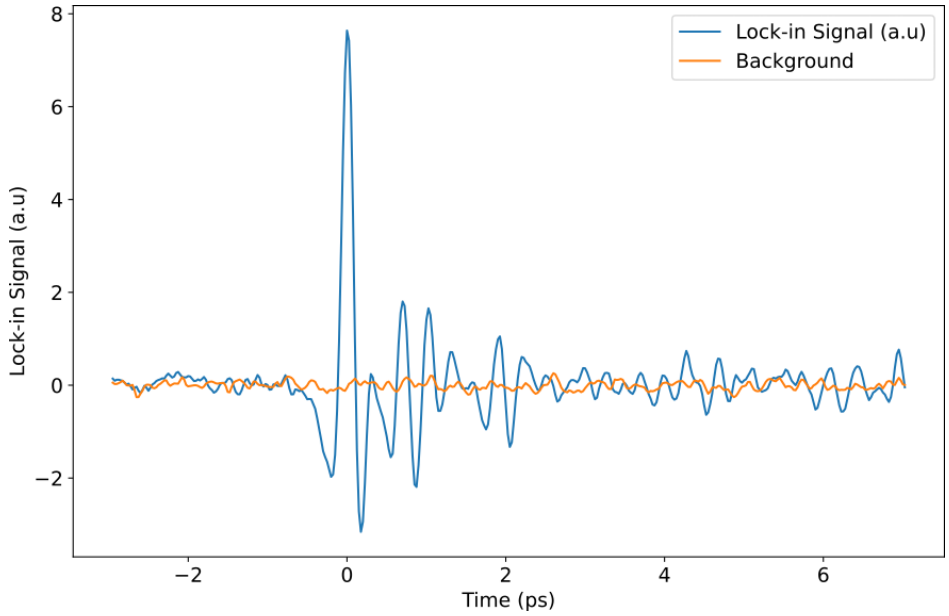

Figure 6.1: The time domain of a single-cycle Cu-LIBP THz pulse measured with the Cu-ring target orientated at an angle shown in the inset of fig. 6.2. Lock-in amplifier settings used in the detection of this pulse were a sensitivity of $V_L = 20\,\mu$V and a time constant of $\tau_L = 300\,$ms.

effect do not just disappear [84]. The same could also be said of other processes such as optical rectification, which has been observed in metals [68; 69]. Still though this raises the possibility that the THz waveform seen in the works of Li and Gao arise not from the solid target LIBP as Gao and Li claim, but from a non-linear optical effect from the bulk.

To see if such contributions from non-linear bulk processes are present the Cu-ring mount shown in fig.4.30 was set at an angle of $\theta = 20°$ (see inset of fig. 6.2) to the oncoming laser as per the work of Gao et al. [49]. This yielded the waveform shown in fig. 6.1 which resembles the InAs waveform shown in fig. 6.7. This result has one of three possible interpretations: (1) space-charge separation between ions and electrons in a LIBP produces a THz transient in a manner analogous to the photo-Dember effect in InAs, (2) both the space-charge field and nonlinear bulk processes (e.g., optical rectification) shown in fig. 6.1 contribute to THz emission, (3) nonlinear effects in the solid target are solely responsible for the single-cycle THz pulse shown in fig. 6.1. Of these three interpretations of fig. 6.1, the (3) can be ruled out definitively. This is because, in the second part of this experiment, the angle between the Cu-ring sample mount and the oncoming ablation beam was orientated at normal incidence

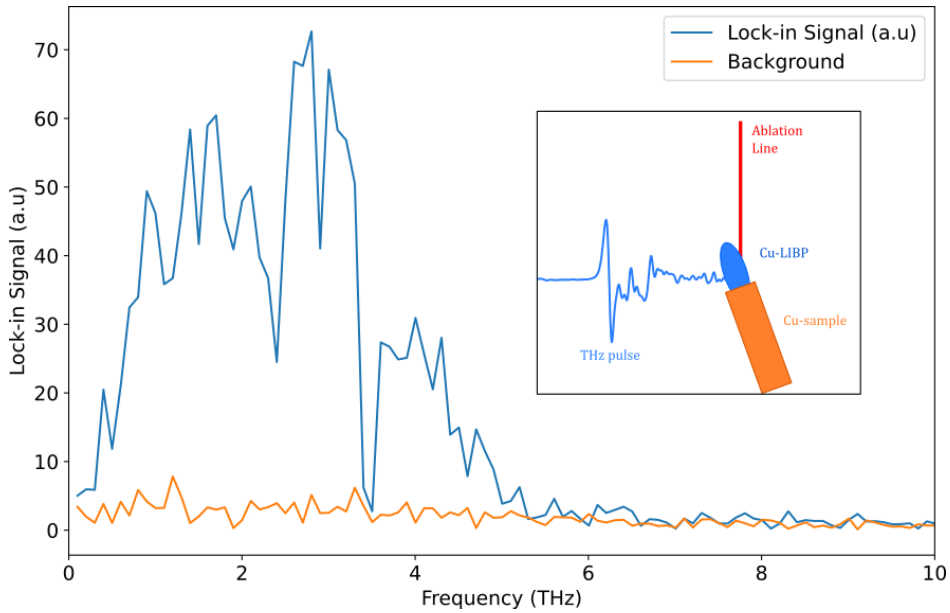

Figure 6.2: The frequency domain of the Cu-LIBP THz pulse with the Cu-ring target held at an angle, θ, $\theta = 20°$, to the oncoming ablation pulse during measurement. Inset: the orientation of the Cu-ring target during the measurement. Comparison to fig. 6.4 shows a loss of frequency components. This indicates possible coupling between non-linear bulk processes, e.g., optical rectification, into the signal.

(see inset of fig. 6.4). By changing the orientation of the sample to be at normal incidence to the oncoming ablation pulse, any signal contributions from optical rectification disappear [60]. This means that any THz emission seen should arise from the rapid space-charge separation in the LIBP plume alone, or at the very least, the bulk of the emission should emerge from the space-charge separation documented in ref. [91–93]. The detection of THz radiation at normal incidence as shown in fig. 6.3-6.4 indicates that the space-charge field is responsible for the majority of THz emission. Given the absence of the frequency components shown in fig. 6.2 in fig. 6.4, most likely interpretation of the physical mechanisms present in fig. 6.1-6.2 is that of interpretation (2). Meanwhile, for fig. 6.3-6.4 (1) is the most sound given how the orientation is set to normal incidence. Note though that this interpretation is barring possible contributions from a hypothetical photocurrent arising from electron motion in the metal (see chapter 2 section 2.4).

Some form of orientation dependency on the THz emission in a LIBP has been seen before in the work of Du Fei et al. in ref. [54]. In their work, Du Fei et al. noticed that depending on where the bolometer was placed, the THz energy per solid angle could differ

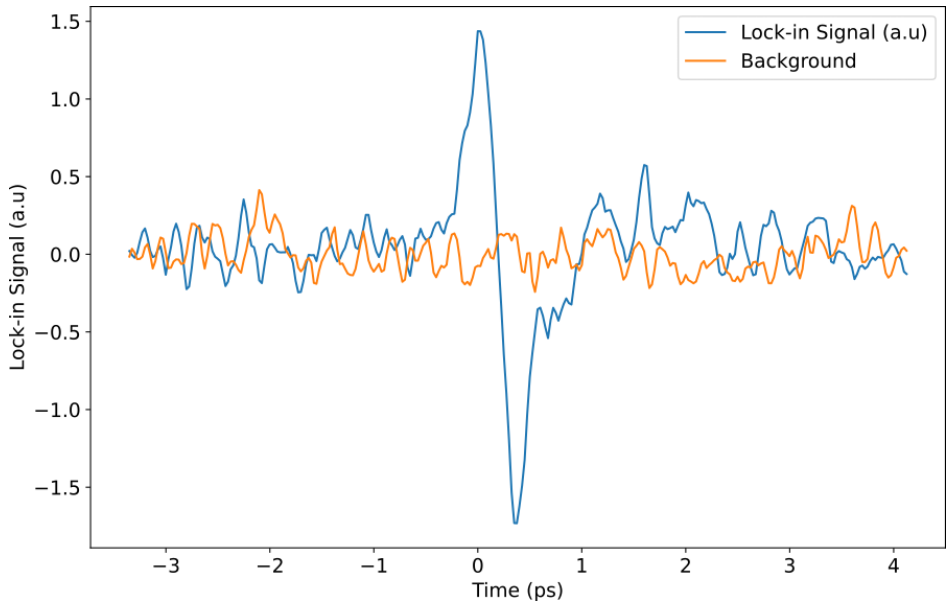

Figure 6.3: The time domain of a single-cycle Cu-LIBP THz pulse measured with the Cu-ring target orientated at normal incidence. The orientation is shown in the inset of fig. 6.2. Lock-in amplifier settings used in the detection of this pulse were a sensitivity of $V_L = 20\,\mu$V and a time constant of $\tau_L = 300\,$ms.

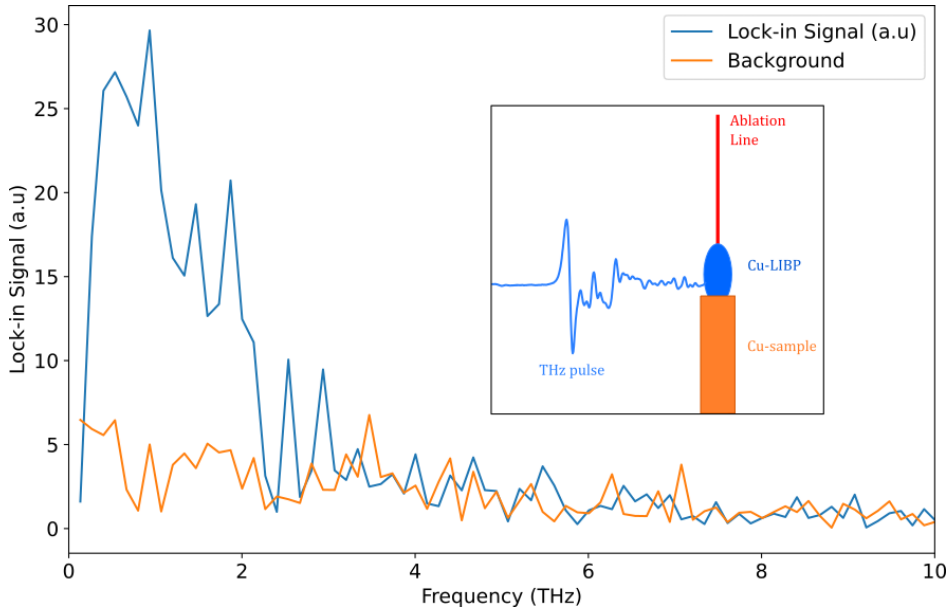

Figure 6.4: The frequency domain of the Cu-LIBP THz pulse with the Cu-ring target held at normal incidence to the oncoming ablation pulse during measurement. Inset: the orientation of the Cu-ring target during the measurement. Comparison to fig. 6.2 shows a loss of frequency components. This indicates possible coupling between non-linear bulk processes, e.g., optical rectification, into the signal.

by as much as a factor of 10 when sweeping over a 90° angle [54]. It should be noted though that Du Fei et al. did not measure the THz waveform, only the THz energy dependency at three different orientations of their bolometer with respect to the target; with the target itself being held fixed [54]. Furthermore, a key difference between Du Fei et al. and this thesis, is that in Du Fei et al.'s case, as with Sagisaka et al. and Hamster et al., there was a pre-formed plasma which was then subsequently driven by a femtosecond pulse which is not the case here [50–52; 54]. To the best of the author's understanding, the vanishing of THz frequency components from a solid-target LIBP, such as those shown in fig. 6.1-6.4 has not been documented in the literature.

With regards as to how emissive approaches relying on the rapid space-charge separation could aid in the detection of water content in a target, the author is inconclusive. For classical THz detection of water content relies on transmissive THz techniques [13; 16; 17]. Furthermore, to the best of the author's knowledge, no one has proposed emissive THz approaches as a viable means of detecting water content. Thus, more work needs to be done to develop emissive detection of water content. A possible experiment that could be preformed is to ablate samples of varying water concentration and compare this to a THz pulse fired from a PCA. The THz pulse from the PCA would serve as a measure of the background humidity in the lab. If the depths of the THz waveform troughs in the frequency domain become deeper (similar to what is seen in fig. 1.3) with samples of increasing water content, it would show that emissive THz detection of water content is viable, especially if the troughs persist after subtraction from the background PCA THz waveform.

6.2 Terahertz Emission in Semiconductors

THz emission in photoexcited semiconductors is a well established process and forms the basis for PCA THz emitter structures like the one shown in fig. 4.7. The goal in this experiment was to see if the experimental setup shown in fig. 4.27 could detect THz emission of any kind and in the process corroborate literature observations such as those reported by ref. [60–63; 65; 66].

There were in total four semiconductors samples from which THz emission was checked:

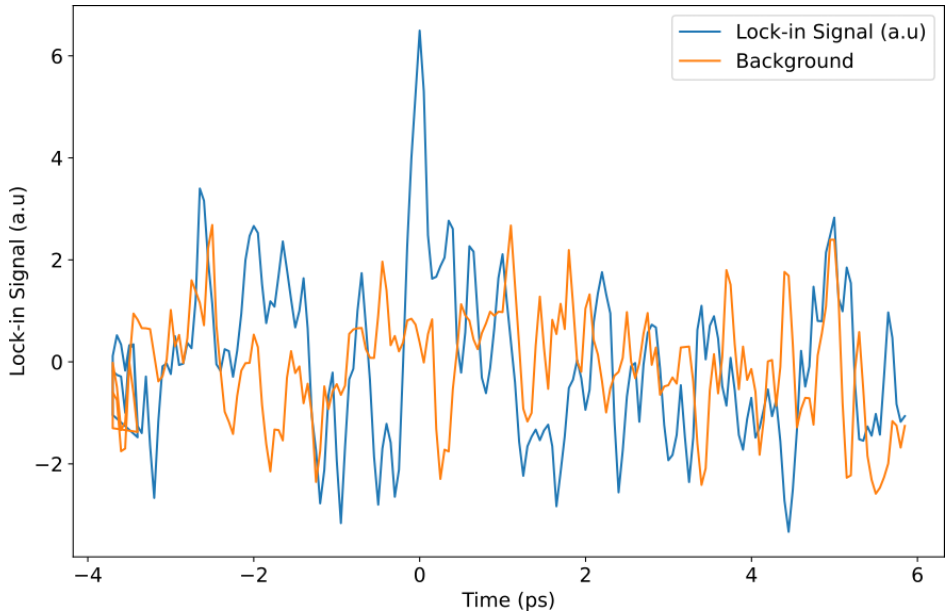

Figure 6.5: The time domain of the PE GaAs p-type 2n doped ⟨110⟩ sample THz pulse. THz emission here is just above the background. The lock-in amplifier settings used for the detection of THz emission in this sample are $V_L = 2\,\mu$V sensitivity and a time constant of, $\tau_L = 300\,$ms.

Undoped GaAs, InP, InAs (111) p-type 2n doped, and GaAs p-type 2n doped ⟨110⟩. From the undoped GaAs and InP no THz emission of any kind was detected. While THz emission from PE GaAs p-type 2n doped ⟨110⟩ was found (see fig. 6.5-6.6) it was difficult to detect and closer to the noise floor of the lock-in amplifier as seen in fig. 6.5-6.6. The lock-in amplifier settings (see table 4.4) used for the detection of THz emision from PE GaAs p-type 2n doped ⟨110⟩ were used to provide a lower bound for the detection of THz emission in Cu-LIBPs shown in fig. 6.1-6.4.

In contrast to GaAs p-type 2n doped ⟨110⟩, InAs (111) p-type 2n doped showed incredibly strong emission with a relatively large signal-to-noise as seen in fig. 6.7-6.8. The frequency domain (fig. 6.8) of InAs (111) p-type 2n indicates that the THz pulse has a bandwidth of $\Delta f \sim 4\,$THz. The lock-in amplifier settings (see table 4.4) used for the detection of THz emision from PE InAs (111) p-type 2n were used to provide an upper bound for the detection of THz emission in Cu-LIBPs shown in fig. 6.1-6.4.

All samples under study were placed at a $\theta = 45°$ angle (see fig. 4.27), at this angle optical rectification within the sample is maximized [60]. So it is possible that the THz emission seen

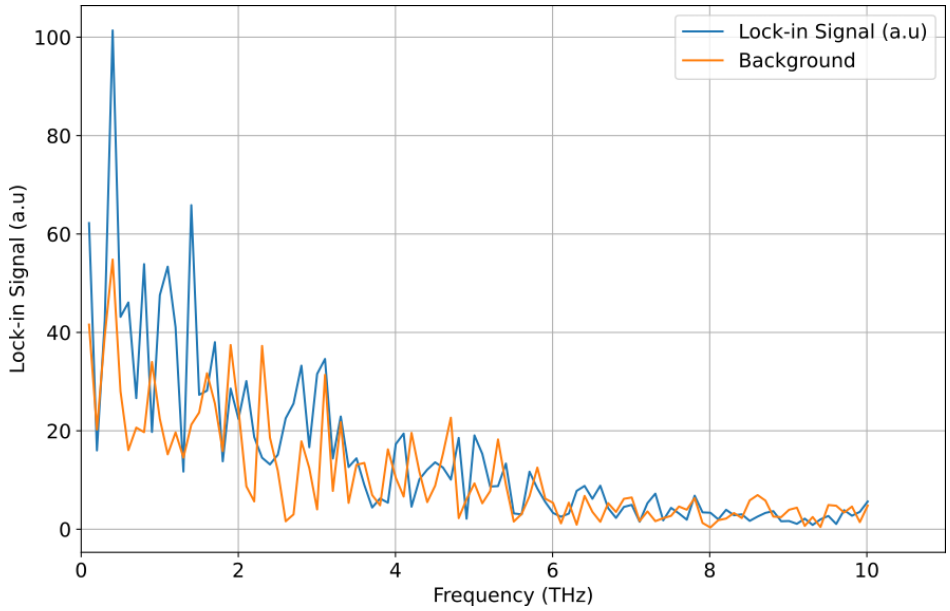

Figure 6.6: The frequency domain of the PE GaAs p-type 2n doped ⟨110⟩ sample THz pulse. Here it is evident that a few frequencies are above the background floor, but the background still screens much of the THz emission from the sample. The settings used for this sample were used as the upper calibration bound for emissive THz detection in Cu-LIBPs.

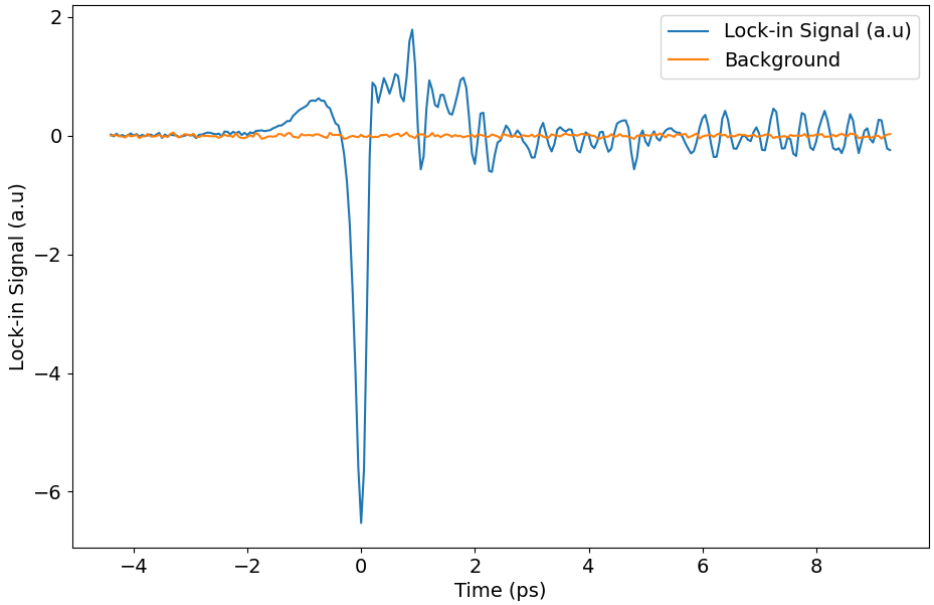

Figure 6.7: The time domain of the PE InAs (111) p-type 2n doped THz pulse. THz emission here is well above the background and is very strong. The lock-in amplifier settings used for the detection of THz emission in this sample are a $V_L = 200\,\mu$V sensitivity and a time constant $\tau_L = 300\,$ms.

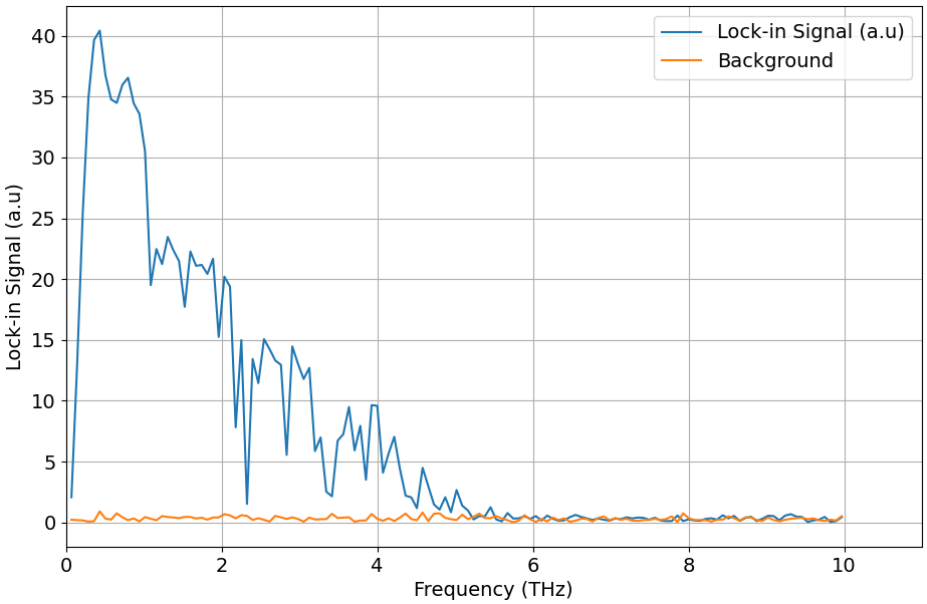

Figure 6.8: The frequency domain of the PE InAs (111) p-type 2n doped sample THz pulse. From this figure it is evident that the THz emission is strong. The THz pulse here has a frequency bandwidth of $\Delta f \sim 4.5\,\mathrm{THz}$. The settings used for this sample were used as the upper calibration bound for emissive THz detection in Cu-LIBPs.

in fig. 6.5-6.8 have non-negligible contributions from optical rectification [60]. As for the predominant THz generation mechanisms in each of the samples used, GaAs is a primarily surface-field emitter at wavelengths of $\lambda = 800\,\mathrm{nm}$ meaning that the resulting currents are driven by a built-in static surface-field, $\vec{\mathcal{E}}_s$ [61; 63; 65; 66]. This static surface-field arises from Fermi-level pinning [118]. If this is the case, the surge current can be expressed as [61],

$$\vec{J} \approx e\left(\mu_e n_e + \mu_h n_h\right)\vec{\mathcal{E}}_s. \tag{6.1}$$

InAs meanwhile is a primarily photo-Dember emitter [60–63]. In the photo-Dember effect, electrons and holes diffuse into the bulk of the semiconductor forming a transient dipole due to the large difference in mobility between the holes and electrons [60–63]. In the case of the photo-Dember effect, the surge current can be expressed as [61],

$$\vec{J} \approx e\left(D_e \boldsymbol{\nabla} n_e - D_h \boldsymbol{\nabla} n_h\right) \quad \text{where} \quad D_i = \frac{\mu_i k_B T_i}{e} \quad i = e, h. \tag{6.2}$$

Both of eqn. 6.1 and 6.2 are directly proportional to the THz field, i.e., $\mathcal{E}_{THz} \propto \partial J/\partial t$ [60–

63; 65; 66]. What is significant for this thesis, is that the results shown in 6.5-6.8 is that they show emissive THz detection using the approach outlined in chapter 4 section 4.4 worked for at least the case of PE semiconductor EHPs. This established a basis from which it was then possible to move unto monitoring THz emission from Cu-LIBPs; giving the results shown in fig. 6.1-6.4.

Chapter 7

Conclusions

In this thesis, methods for using single-cycle THz pulses for the study LIBPs were investigated by one of two means: (1) transmissive THz aproaches (THz pulse is sent through the plasma) and (2) emissive THz approaches (THz emission from the plasma is monitored). Both approaches were implemented to asses the feasibility of an all-optical means by which stand-off water detection could be preformed alongside LIBS. This is motivated by observations that THz pulses are highly sensitive to water molecule rotational and vibrational modes [13; 15; 16]. Ideally, this would give rise to a hybrid THz-LIBS unit that could be used in-situ to measure both target elemental composition and water content. To benchmark both approaches, EHPs arising from PE of semiconductors were used.

Results from simulations assuming a vacuum, and the predominance of electron-ion collisions and collisionless cases (fig. 2.3-2.9) in LIBPs and results from inductively coupled plasmas in ref. [27–30], along with the work of Mics et al. and Chen et al. for gaseous and solid-target LIBPS in ref. [31; 33] indicated that the transmissive THz approaches should be theoretically possible albeit, heavily attenuated. The asynchronous transmissive method outlined in chapter 4 section 4.2 was successful in producing a measurable $-\Delta\mathcal{T}$ conductivity spectra in PE Si (fig. 5.5) and GaAs (fig. 5.7). By fixing the fine delay stages to the peak of the THz pulse from the PCA emitter shown in fig. 4.7, and subsequently varying the average pump power, $\langle P \rangle$, a saturation behaviour in the average differential transmission $\langle \Delta\mathcal{T} \rangle$ around $\langle P \rangle \simeq 90\,\mathrm{mW}$ appeared (fig. 5.8) for the case of PE Si. The emergence of both a $-\Delta\mathcal{T}$ conductivity spectrum similar to the ones shown in fig. 5.5 and 5.7 and saturation

behaviour in the $\langle -\Delta\mathcal{T} \rangle$ with the pump power were subsequently expected to be found for the case of a Cu-LIBP. The speculation for the saturation behaviour being based on the findings of Park et al. who noticed that the ionic charge they measured from ps-ablated planar Cu began to saturate around $\Phi \sim 1\,\mathrm{kJ/cm^2}$ [71].

However, neither an equivalent $-\Delta\mathcal{T}$ spectrum or saturation behaviour analogous to those seen in fig. 5.5, 5.7, and 5.8 were found for the case of Cu-LIBPs induced by fs-ablation. This prompted an investigation of the PL lifetimes of the Cu-LIBP seen in fig. 5.3 - 5.4. The PL lifetime was chosen as the metric to gauge the overall duration of plasma effects because it is the time frame over which the existence plasma effects could be readily verified to at least a first order. Fits to the high fluence PL curves shown in fig. 5.3 gave PL lifetimes on the order of $\tau_0 \simeq 20\,\mathrm{ns}$. This value of $\tau_0 \simeq 20\,\mathrm{ns}$ is far lower than the conductivity lifetimes found from PE GaAs and SI EHPs, which were around, $\tau_c \simeq 1 - 70\,\mu\mathrm{s}$. This discrepancy between the Cu-LIBP PL lifetime and the conductivity lifetime of Si and GaAs EHPs indicates that it is highly likely that the Cu-LIBP is dissipating in between the arrival of THz pulses. This means that a major limitation that must be overcome for the development of transmissive methods for water detection in solid-target LIBPs is controlling the relative timing between the ablation pulses, plasma ignition, and the arrival of THz pulses. An appropriate delay needed to resolve this, in the case of this thesis, is a delay stage of length $\Delta x = 3\,\mathrm{m}$, which was not experimentally feasible.

The difficulty surrounding transmissive THz approaches then pushed the direction of this thesis towards emissive approaches. The basis for this was the work of Gao et al. who observed THz emission from a fs-ablated Cu-LIBP [49]. Emissive approaches, while untested for the detection of water content, were investigated in order to bypass the difficulty associated with synchronization across picosecond to microsecond timescales the transmissive approaches have. Hence, attention was shifted towards emissive approaches. In both the case of PE semiconductor EHPs and fs-ablated Cu-LIBPs, emissive detection of single-cycle THz pulse was seen (fig. 6.5-6.8 and fig. 6.1-6.4).

The results from Cu-LIBPs seen in fig. 6.1-6.4 could not be sufficiently explained by the models proposed by Hamster et al. and Sagisaka et al.; this is due to the fact that in both cases Hamster et al. and Sagisaka et al. use an amplified stimulated emission

pulse and a pre-pulse to make a preformed plasma which they subsequently driven with the main fs-pulse [50–52]. For the emissive experiments outlined in this thesis make no use of such pulsse to produce a plasma. The ablation and subsequent plasma ignition was accomplished solely through the use of a pulse of pulsewidth $\tau_p = 70\,\text{fs}$ and central wavelength of $\lambda = 795\,\text{nm}$. Assuming there a non-negligible pre-pulse it would not be sufficient for it to induce a pre-formed plasma in the case of this thesis. This is because for typical contrast ratios from the Legend system used are $E_{pp}/E_p \simeq 1/500$ the which for typical absorbed fluences, of $\Phi_0 = 3.82\,\text{J/cm}^2$, the absorbed fluence for any pre-pulse would be $\Phi_{pp} = 7.64\,\text{mJ/cm}^2$ which is well below the threshold fluences quoted by Nolte et al. for fs-ablated Cu ($140\,\text{mJ/cm}^2 \leq \Phi_0 \leq 460\,\text{mJ/cm}^2$) and the threshold quoted by Hashida et al. for fs-ablated Cu at pulse-widths of $\tau_p = 70\,\text{fs}$ ($\Phi_0 = 18\,\text{mJ/cm}^2$) [72; 74].

Instead, the author posits that the likely origin of the THz emission seen in, fig. 6.1-6.4, arises from a space-charge effect analogous to the photo-Dember effect such as the one seen in the InAs pulse (fig. 6.7-6.8). This motivated the development of a rudimentary model, described in chapter 2 section 2.4 based off of the assertion that there exists some proportionality constant, η_C, between the photon density, n_p, and the charge carriers, n_c, which is termed the charge-carrier production efficiency ($\eta_C \equiv n_p\,(t)\,/n_c\,(t)$). This toy model successfully re-created a single-cycle THz pulse (see fig. 2.11). This theoretical speculation is grounded firmly in prior experimental work, as a such a space-charge effect in LIBPs is not only well documented, it has been shown to even occur over picosecond timescales [89; 91–93]. However, a more complete model needs to be developed.

Another possible source to consider though of THz radiation could come from nonlinear optical effects, such as optical rectification or alternatively, a possible photocurrent. Initially, following the work of Gao et al. in ref. [49], the orientation of the Cu-ring was set at an angle of $\theta = 20°$ to the oncoming ablation beam. At such an angle, contributions to the THz generation from optical rectification are known to occur, even in PE metals [67–69]. Kadlec et al. even noted that for the case of PE gold and silver, that THz emission occured regardless of PE beam polarization [68]. To verify that the THz emission seen in fig. 6.1-6.2 arises from the suspected space-charge effect, and not solely from optical rectification the orientation was changed so that the oncoming beam was at normal incidence, at this orientation no possible

contributions from optical rectification can occur [60]. Thus, the continued persistence of THz emission seen in fig. 6.3-6.4 lends credence to the interpretation that coherent THz emission in LIBPs predominantly arises from the space-charge effect. To the best of the author's knowledge, the frequency component orientation dependency seen upon comparing fig. 6.2 to fig. 6.4 has not been documented before in literature. Though it is worth noting that Du Fei et al. noted that there was an orientation dependency upon the emitted THz energy [54]. Though in the case of Du Fei et al., the sample orientation was not changed, only the angle of the detector [54].

As for the feasiblity of a hybrid THz-LIBS standoff detector, there are two possible directions future investigations must take: (1) solve the synchronization problem associated with the transmissive approach or (2) further develop the emissive approach. Direction (1) has the distinct advantage of that transmissive THz detection of water content already has a basis in literature [13; 14; 16]. The disadvantage of trying to apply transmissive THz techniques to LIBPs is that, unlike the ambient air or a propane plume used in ref. [16], a LIBP is a rapidly disappearing target so more effort needed to resolve the synchronization between ablation pulse arrival, THz probing, and plasma ignition. Direction (2) meanwhile does not require the same degree of synchronization due to the fact that the source of THz emission is the LIBP itself. For emissive THz approaches to be viable for application in a hybrid THz-LIBS standoff detector, it must be shown first that the troughs in a LIBP THz pulse are due to water content in the LIBP plume, not from the ambient environment. If this can be shown, then emissive approaches would pave the way for an all-optical hybrid THz-LIBS detection system capable of measuring both elemental composition and water content in a target.

Neither the transmissive or emissive THz approach though has been fully ruled out by the findings in this thesis. More work is needed to develop a firm conclusion vis-a-vis the feasibility for an all-optical hybrid THz-LIBS detection system capable of measuring both elemental composition and water content in a target. Furthermore, the disappearance of frequency components between fig. 6.2 and fig. 6.4 warrants further investigation in of itself. For there are many possible ultrafast processes that occur beyond optical rectification and the space-charge effect that need to be decoupled from one another (see ref. [75; 84]

for details) for a more complete understanding of photoexcitation, ablation, and plasma evolution.

Bibliography

[1] Yingchao Huang, Sivanandan S Harilal, Abdul Bais, and Amina E Hussein. Progress toward machine learning methodologies for laser-induced breakdown spectroscopy with an emphasis on soil analysis. *IEEE Transactions on Plasma Science*, 2023.

[2] S Rosenwasser, G Asimellis, B Bromley, R Hazlett, J Martin, T Pearce, and A Zigler. Development of a method for automated quantitative analysis of ores using libs. *Spectrochimica Acta Part B: Atomic Spectroscopy*, 56(6):707–714, 2001.

[3] Gustavo Nicolodelli, Jader Cabral, Carlos Renato Menegatti, Bruno Marangoni, and Giorgio S Senesi. Recent advances and future trends in libs applications to agricultural materials and their food derivatives: an overview of developments in the last decade (2010–2019). part i. soils and fertilizers. *TrAC Trends in Analytical Chemistry*, 115:70–82, 2019.

[4] David A. Cremers, Rosalie A. Multari, and Andrew K. Knight. Encyclopedia of analytical chemistry. In *Laser-induced Breakdown Spectroscopy*, pages 1–26. John Wiley & sons, Ltd., 2016.

[5] Roger C Wiens, Shiv K Sharma, Justin Thompson, Anupam Misra, and Paul G Lucey. Joint analyses by laser-induced breakdown spectroscopy (libs) and raman spectroscopy at stand-off distances. *Spectrochimica Acta Part A: Molecular and Biomolecular Spectroscopy*, 61(10):2324–2334, 2005.

[6] SS Harilal, MC Phillips, DH Froula, KK Anoop, RC Issac, and FN Beg. Optical diagnostics of laser-produced plasmas. *Reviews of Modern Physics*, 94(3):035002–1–035002–40, 2022.

[7] AE Hussein, PK Diwakar, SS Harilal, and A Hassanein. The role of laser wavelength on plasma generation and expansion of ablation plumes in air. *journal of applied physics*, 113(14):143305, 2013.

[8] B Verhoff, SS Harilal, JR Freeman, PK Diwakar, and A Hassanein. Dynamics of femto- and nanosecond laser ablation plumes investigated using optical emission spectroscopy. *Journal of Applied Physics*, 112(9):093303, 2012.

[9] SS Harilal, N Farid, JR Freeman, PK Diwakar, NL LaHaye, and A Hassanein. Background gas collisional effects on expanding fs and ns laser ablation plumes. *Applied Physics A*, 117(1):319–326, 2014.

[10] SS Harilal, BE Brumfield, NL LaHaye, KC Hartig, and MC Phillips. Optical spectroscopy of laser-produced plasmas for standoff isotopic analysis. *Applied Physics Reviews*, 5(2):021301, 2018.

[11] Mengmeng Wang, Lan Jiang, Sumei Wang, Qitong Guo, Feng Tian, Zhuyuan Chu, Jin Zhang, Xin Li, and Yongfeng Lu. Multiscale visualization of colloidal particle lens array mediated plasma dynamics for dielectric nanoparticle enhanced femtosecond laser-induced breakdown spectroscopy. *Analytical chemistry*, 91(15):9952–9961, 2019.

[12] VN Rai and SN Thakur. Chapter 4: Physics of plasma in laser-induced breakdown spectroscopy. In *Laser-induced breakdown spectroscopy*, pages 83–111. Elsevier press Amsterdam, 2007.

[13] Martin Van Exter, Ch Fattinger, and D Grischkowsky. Terahertz time-domain spectroscopy of water vapor. *Optics letters*, 14(20):1128–1130, 1989.

[14] Yun-Shik Lee. Introduction. In *Principles of Terahertz Science and Technology*, pages 1–9. Springer Science and Business Media, 2009.

[15] Yun-Shik Lee. Basic theories of terahertz interactions with matter. In *Principles of Terahertz Science and Technology*, pages 10–50. Springer Science and Business Media, 2009.

[16] RA Cheville and D Grischkowsky. Far-infrared terahertz time-domain spectroscopy of flames. *Optics letters*, 20(15):1646–1648, 1995.

[17] Yihong Yang, Mahboubeh Mandehgar, and D Grischkowsky. Determination of the water vapor continuum absorption by thz-tds and molecular response theory. *Optics Express*, 22(4):4388–4403, 2014.

[18] Agata Mendys, Michał Kański, Ali Farah-Sougueh, Stéphane Pellerin, Bartłomiej Pokrzywka, and Krzysztof Dzierżega. Investigation of the local thermodynamic equilibrium of laser-induced aluminum plasma by thomson scattering technique. *Spectrochimica Acta Part B: Atomic Spectroscopy*, 96:61–68, 2014.

[19] José A Bittencourt. Chapter 7: The equilibrium state. In *Fundamentals of Plasma Physics 3rd Edition*, pages 161–187. Springer Science & Business Media, 2004.

[20] Gabriele Cristoforetti, Alessandro De Giacomo, M Dell'Aglio, Stefano Legnaioli, Elisabetta Tognoni, Vincenzo Palleschi, and Nicolo Omenetto. Local thermodynamic equilibrium in laser-induced breakdown spectroscopy: beyond the mcwhirter criterion. *Spectrochimica Acta Part B: Atomic Spectroscopy*, 65(1):86–95, 2010.

[21] G Cristoforetti, E Tognoni, and LA Gizzi. Thermodynamic equilibrium states in laser-induced plasmas: From the general case to laser-induced breakdown spectroscopy plasmas. *Spectrochimica Acta Part B: Atomic Spectroscopy*, 90:1–22, 2013.

[22] DG Cooke, FA Hegmann, EC Young, and T Tiedje. Electron mobility in dilute gaas bismide and nitride alloys measured by time-resolved terahertz spectroscopy. *Applied physics letters*, 89(12):122103–1–122103–3, 2006.

[23] DG Cooke, AN MacDonald, A Hryciw, J Wang, Q Li, A Meldrum, and FA Hegmann. Transient terahertz conductivity in photoexcited silicon nanocrystal films. *Physical Review B*, 73(19):193311, 2006.

[24] KPH Lui and FA Hegmann. Ultrafast carrier relaxation in radiation-damaged silicon on sapphire studied by optical-pump–terahertz-probe experiments. *Applied Physics Letters*, 78(22):3478–3480, 2001.

[25] David G Cooke, A Nicole MacDonald, Aaron Hryciw, Al Meldrum, Juan Wang, Q Li, and Frank A Hegmann. Ultrafast terahertz conductivity of photoexcited nanocrystalline silicon. *Journal of Materials Science: Materials in Electronics*, 18(1):447–452, 2007.

[26] Rupert Huber, F Tauser, A Brodschelm, M Bichler, G Abstreiter, and A Leitenstorfer. How many-particle interactions develop after ultrafast excitation of an electron–hole plasma. *Nature*, 414(6861):286–289, 2001.

[27] SP Jamison, Jingling Shen, DR Jones, RC Issac, B Ersfeld, D Clark, and DA Jaroszynski. Plasma characterization with terahertz time–domain measurements. *Journal of applied physics*, 93(7):4334–4336, 2003.

[28] BH Kolner, PM Conklin, RA Buckles, NK Fontaine, and RP Scott. Time-resolved pulsed-plasma characterization using broadband terahertz pulses correlated with fluorescence imaging. *Applied Physics Letters*, 87(15):151501, 2005.

[29] BH Kolner, RA Buckles, PM Conklin, and RP Scott. Plasma characterization with terahertz pulses. *IEEE Journal of Selected Topics in Quantum Electronics*, 14(2):505–512, 2008.

[30] Ayumi Ando, Tomoko Kurose, Vivien Reymond, Katsuhisa Kitano, Hideaki Kitahara, Keisuke Takano, Masahiko Tani, Masanori Hangyo, and Satoshi Hamaguchi. Electron density measurement of inductively coupled plasmas by terahertz time-domain spectroscopy (thz-tds). *Journal of Applied Physics*, 110(7):073303–1–073303–8, 2011.

[31] Zoltan Mics, Filip Kadlec, Petr Kužel, Pavel Jungwirth, Stephen E Bradforth, and V Ara Apkarian. Nonresonant ionization of oxygen molecules by femtosecond pulses: plasma dynamics studied by time-resolved terahertz spectroscopy. *The Journal of chemical physics*, 123(10):104310, 2005.

[32] K Yetal Kim, B Yellampalle, JH Glownia, AJ Taylor, and G Rodriguez. Measurements of terahertz electrical conductivity of intense laser-heated dense aluminum plasmas. *Physical review letters*, 100(13):135002, 2008.

[33] Zhijiang Chen, CB Curry, R Zhang, F Treffert, N Stojanovic, S Toleikis, R Pan, M Gauthier, E Zapolnova, LE Seipp, Y.Y. Tsui, et al. Ultrafast multi-cycle terahertz measurements of the electrical conductivity in strongly excited solids. *Nature communications*, 12(1638):1–8, 2021.

[34] Yong Tan, Hang Zhao, Rui Zhang, Yuejin Zhao, Cunlin Zhang, Xi-Cheng Zhang, and Liangliang Zhang. Transient evolution of quasifree electrons of plasma in liquid water revealed by optical-pump terahertz-probe spectroscopy. *Advanced Photonics*, 3(1):015002–1–015002–7, 2021.

[35] Mark Fox. Chapter 7: Free electrons. In *Optical Properties of Solids 2nd Edition*, pages 180–210. Oxford University Press, 2010.

[36] Umran S Inan and Marek Goł kowski. Chapter 7: Collisions and plasma conductivity. In *Principles of Plasma Physics for Engineers and Scientists*, pages 152–166. Cambridge university press, 2011.

[37] R Bowers and MC Steele. Plasma effects in solids. *Proceedings of the IEEE*, 52(10):1105–1112, 1964.

[38] Klaus Sokolowski-Tinten and Dietrich von der Linde. Generation of dense electron-hole plasmas in silicon. *Physical Review B*, 61(4):2643, 2000.

[39] JA Van Vechten, Ro Tsu, and FW Saris. Nonthermal pulsed laser annealing of si; plasma annealing. *Physics Letters A*, 74(6):422–426, 1979.

[40] Monique Combescot and Julien Bok. Electron-hole plasma generation and evolution in semiconductors. *Journal of Luminescence*, 30(1-4):1–17, 1985.

[41] Ellen J Yoffa. Dynamics of dense laser-induced plasmas. *Physical review B*, 21(6):2415–2425, 1980.

[42] José A Bittencourt. Chapter 10: Plasma conductivity and diffusion. In *Fundamentals of Plasma Physics 3rd Edition*, pages 238–262. Springer Science & Business Media, 2004.

[43] J. R. Hook and H. E. Hall. Chapter 5: Semiconductors. In *Solid State Physics 2nd Edition*, pages 131–166. John Wiley & Sons, 1991.

[44] Richard D Mattuck. The many body problem for everybody. In *A Guide to Feynman Diagrams in the Many-Body Problem*, page 4. Courier Corporation, 1992.

[45] J Hopwood. Review of inductively coupled plasmas for plasma processing. *Plasma Sources Science and Technology*, 1(2):109–116, 1992.

[46] David A Cremers and Rosemarie C Chinni. Laser-induced breakdown spectroscopy—capabilities and limitations. *Applied Spectroscopy Reviews*, 44(6):457–506, 2009.

[47] Nobuyuki Kawahara, JL Beduneau, T Nakayama, Eiji Tomita, and Y Ikeda. Spatially, temporally, and spectrally resolved measurement of laser-induced plasma in air. *Applied Physics B*, 86:605–614, 2007.

[48] BK Ofori-Okai, A Descamps, J Lu, LE Seipp, A Weinmann, SH Glenzer, and Z Chen. Toward quasi-dc conductivity of warm dense matter measured by single-shot terahertz spectroscopy. *Review of Scientific Instruments*, 89(10):10D109–1–10D109–5, 2018.

[49] Yuan Gao, Tara Drake, Zhiyuan Chen, and Matthew F DeCamp. Half-cycle-pulse terahertz emission from an ultrafast laser plasma in a solid target. *Optics letters*, 33(23):2776–2778, 2008.

[50] A Sagisaka, H Daido, S Nashima, S Orimo, K Ogura, M Mori, A Yogo, J Ma, I Daito, AS Pirozhkov, et al. Simultaneous generation of a proton beam and terahertz radiation in high-intensity laser and thin-foil interaction. *Applied Physics B*, 90(3):373–377, 2008.

[51] H Hamster, A Sullivan, S Gordon, W White, and RW Falcone. Subpicosecond, electromagnetic pulses from intense laser-plasma interaction. *Physical review letters*, 71(17):2725, 1993.

[52] H Hamster, A Sullivan, S Gordon, and RW Falcone. Short-pulse terahertz radiation from high-intensity-laser-produced plasmas. *Physical Review E*, 49(1):671–677, 1994.

[53] A Gopal, P Singh, S Herzer, A Reinhard, A Schmidt, U Dillner, T May, H-G Meyer, W Ziegler, and GG Paulus. Characterization of 700 μj t rays generated during high-power laser solid interaction. *Optics Letters*, 38(22):4705–4707, 2013.

[54] Fei Du, Chun Li, MuLin Zhou, WeiMin Wang, LuNing Su, Yi Zheng, XuLei Ge, YuTong Li, JingLong Ma, XiaoLong Liu, et al. Angular distribution of terahertz emission from laser interactions with solid targets. *Science China Information Sciences*, 55:43–48, 2012.

[55] YT Li, C Li, ML Zhou, WM Wang, F Du, WJ Ding, XX Lin, F Liu, ZM Sheng, XY Peng, et al. Strong terahertz radiation from relativistic laser interaction with solid density plasmas. *Applied Physics Letters*, 100(25):254101, 2012.

[56] Yixing Geng, Dongyu Li, Siyuan Zhang, Minjian Wu, Tong Yang, Dan Wang, Lixin Yan, Jungao Zhu, Xiyao Hu, Yanying Zhao, et al. Strong enhancement of coherent terahertz radiation by target ablation using picosecond laser pulses. *Physics of Plasmas*, 27(11):113104, 2020.

[57] P Uhd Jepsen, David G Cooke, and Martin Koch. Terahertz spectroscopy and imaging–modern techniques and applications. *Laser & Photonics Reviews*, 5(1):124–166, 2011.

[58] Frank A Hegmann, Oksana Ostroverkhova, and David G Cooke. Chapter 7: Probing organic semiconductors with terahertz pulses. In *Photophysics of Molecular Materials: From Single Molecules to Single Crystals*, pages 367–428. John Wiley & Sons, Ltd, 2006.

[59] DG Cooke, FA Hegmann, Yu I Mazur, WQ Ma, X Wang, Zh M Wang, GJ Salamo, M Xiao, TD Mishima, and MB Johnson. Anisotropic photoconductivity of ingaas quantum dot chains measured by terahertz pulse spectroscopy. *Applied physics letters*, 85(17):3839–3841, 2004.

[60] Ping Gu, Masahiko Tani, Shunsuke Kono, Kiyomi Sakai, and X-C Zhang. Study of terahertz radiation from inas and insb. *Journal of Applied Physics*, 91(9):5533–5537, 2002.

[61] JN Heyman, N Coates, A Reinhardt, and Gottfried Strasser. Diffusion and drift in terahertz emission at gaas surfaces. *Applied physics letters*, 83(26):5476–5478, 2003.

[62] Kai Liu, Jingzhou Xu, Tao Yuan, and X-C Zhang. Terahertz radiation from inas induced by carrier diffusion and drift. *Physical Review B*, 73(15):155330, 2006.

[63] Michael B Johnston, DM Whittaker, A Corchia, AG Davies, and Edmund H Linfield. Simulation of terahertz generation at semiconductor surfaces. *Physical Review B*, 65(16):165301, 2002.

[64] X-C Zhang and DH Auston. Optoelectronic measurement of semiconductor surfaces and interfaces with femtosecond optics. *Journal of applied physics*, 71(1):326–338, 1992.

[65] X-C Zhang, JT Darrow, BB Hu, DH Auston, MT Schmidt, P Tham, and ES Yang. Optically induced electromagnetic radiation from semiconductor surfaces. *Applied physics letters*, 56(22):2228–2230, 1990.

[66] X-C Zhang, Binbin B Hu, Justin T Darrow, and David H Auston. Generation of femtosecond electromagnetic pulses from semiconductor surfaces. *Applied Physics Letters*, 56(11):1011–1013, 1990.

[67] Filip Kadlec, Petr Kužel, and Jean-Louis Coutaz. Study of terahertz radiation generated by optical rectification on thin gold films. *Optics letters*, 30(11):1402–1404, 2005.

[68] Filip Kadlec, Petr Kužel, and Jean-Louis Coutaz. Optical rectification at metal surfaces. *Optics letters*, 29(22):2674–2676, 2004.

[69] DJ Hilton, RD Averitt, CA Meserole, GL Fisher, DJ Funk, JD Thompson, and AJ Taylor. Terahertz emission via ultrashort-pulse excitation of magnetic metal films. *Optics letters*, 29(15):1805–1807, 2004.

[70] Y.R. Shen. Optical breakdown. In *The Principles of Nonlinear Optics*, pages 528–539. John Wiley & Sons, 1984.

[71] CO Park, HW Lee, TD Lee, and JK Kim. Multiphoton ionization of aluminum and copper planar target. *Applied physics letters*, 52(5):368–370, 1988.

[72] Stefan Nolte, Cl Momma, H Jacobs, A Tünnermann, Boris N Chichkov, Bernd Wellegehausen, and Herbert Welling. Ablation of metals by ultrashort laser pulses. *JOSA B*, 14(10):2716–2722, 1997.

[73] K Furusawa, K Takahashi, H Kumagai, K Midorikawa, and M Obara. Ablation characteristics of au, ag, and cu metals using a femtosecond ti: sapphire laser. *Applied Physics A*, 69(1):S359–S366, 1999.

[74] M Hashida, AF Semerok, O Gobert, G Petite, Y Izawa, et al. Ablation threshold dependence on pulse duration for copper. *Applied surface science*, 197:862–867, 2002.

[75] JP Girardeau-Montaut and C Girardeau-Montaut. Theory of ultrashort nonlinear multiphoton photoelectric emission from metals. *Physical Review B*, 51(19):13560–13567, 1995.

[76] Yu Li, Changhong Hu, Hanzhuang Zhang, Zhankui Jiang, and Zhongshan Li. Optical emission enhancement of laser-produced copper plasma under a steady magnetic field. *Applied optics*, 48(4):B105–B110, 2009.

[77] X Zeng, XL Mao, R Greif, and RE Russo. Experimental investigation of ablation efficiency and plasma expansion during femtosecond and nanosecond laser ablation of silicon. *Applied Physics A*, 80(2):237–241, 2005.

[78] Ursel Fantz. Basics of plasma spectroscopy. *Plasma sources science and technology*, 15(4):S137–S147, 2006.

[79] NM Kuznetsov and Yu P Raizer. Recombination of electrons in a plasma expanding into a vacuum. *Journal of Applied Mechanics and Technical Physics*, 6(4):6–12, 1965.

[80] Takashi Fujimoto and RWP McWhirter. Validity criteria for local thermodynamic equilibrium in plasma spectroscopy. *Physical Review A*, 42(11):6588, 1990.

[81] Hans R. Griem. Thermodynamic equilibrium relations. In *Principles of Plasma Spectroscopy*, pages 212–220. Elsevier, 1996.

[82] Stanley Byron, Robert C Stabler, and Paul I Bortz. Electron-ion recombination by collisional and radiative processes. *Physical Review Letters*, 8(9):376, 1962.

[83] Joachim Oxenius. Thermal equilibrium and detailed balance. In *Kinetic Theory of Particles and Photons*, pages 1–34. Springer Science and Business Media, 1986.

[84] SI Anisimov, BL Kapeliovich, TL Perelman, et al. Electron emission from metal surfaces exposed to ultrashort laser pulses. *Zh. Eksp. Teor. Fiz*, 66(2):375–377, 1974.

[85] IN Arutyunyan, GA Asbar'yan, and VA Pogasyan. Multi-photon processes in the focus of an intense laser beam with expansion of the interactive region taken into consideration. *Sov. Phys. JETP*, 31:548–550, 1970.

[86] Paul A Anderson. The work function of copper. *Physical Review*, 76(3):388–390, 1949.

[87] SE v Kirkwood, AC Van Popta, YY Tsui, and R Fedosejevs. Single and multiple shot near-infrared femtosecond laser pulse ablation thresholds of copper. *Applied Physics A*, 81:729–735, 2005.

[88] LV Keldysh. Ionization in the field of a strong electromagnetic wave. *Sov. Phys. JETP*, 20(5):1307–1314, 1965.

[89] JS Pearlman and GH Dahlbacka. Charge separation and target voltages in laser-produced plasmas. *Applied Physics Letters*, 31(7):414–417, 1977.

[90] JE Crow, PL Auer, and JE Allen. The expansion of a plasma into a vacuum. *Journal of Plasma Physics*, 14(1):65–76, 1975.

[91] Yasuaki Okano, Yoichiro Hironaka, Ken-ichi Kondo, and Kazutaka G Nakamura. Electron imaging of charge-separated field on a copper film induced by femtosecond laser irradiation. *Applied Physics Letters*, 86(14):141501–1–141501–3, 2005.

[92] Martin Centurion, Peter Reckenthaeler, Sergei A Trushin, Ferenc Krausz, and Ernst E Fill. Picosecond electron deflectometry of optical-field ionized plasmas. *Nature Photonics*, 2(5):315–318, 2008.

[93] Junjie Li, Xuan Wang, Zhaoyang Chen, Richard Clinite, Samuel S Mao, Pengfei Zhu, Zhengming Sheng, Jie Zhang, and Jianming Cao. Ultrafast electron beam imaging of femtosecond laser-induced plasma dynamics. *Journal of Applied Physics*, 107(8):083305–1–083305–6, 2010.

[94] José A Bittencourt. Chapter 11: Some basic plasma phenomena. In *Fundamentals of Plasma Physics 3rd Edition*, pages 269–291. Springer Science & Business Media, 2004.

[95] Hans R Griem. Validity of local thermal equilibrium in plasma spectroscopy. *Physical Review*, 131(3):1170, 1963.

[96] A De Giacomo, R Gaudiuso, M Dell'Aglio, and A Santagata. The role of continuum radiation in laser induced plasma spectroscopy. *Spectrochimica Acta Part B: Atomic Spectroscopy*, 65(5):385–394, 2010.

[97] Curtis Hemenway, Richard W. Henry, and Martin Caulton. Gaseous processes. In *Physical Electronics 2nd Edition*, pages 172–202. John Wiley & Sons, 1967.

[98] M Mattioli. Recombination processes during the expansion of a laser-produced plasma. *Plasma Physics*, 13(1):19, 1971.

[99] Joachim Oxenius. Kinetic equations of particles. In *Kinetic Theory of Particles and Photons*, pages 35–65. Springer Science and Business Media, 1986.

[100] PT Rumsby and JWM Paul. Temperature and density of an expanding laser produced plasma. *Plasma Physics*, 16(3):247, 1974.

[101] Owen Bishop. Topic 4 - capacitors. In *Electronics-circuits and systems*, page 31–38. Routledge, 4 edition, 2011.

[102] Mark Fox. Chapter 1: Introduction. In *Optical Properties of Solids 2nd Edition*, pages 1–24. Oxford University Press, 2010.

[103] J.D. Huba. Coulomb logarithm. In *NRL Plasma Formulary*, pages 34–37. United States Navy: Naval Research Laboratory, 2011.

[104] Max Born and Emil Wolf. *Optics of metals*, page 735–789. Cambridge University Press, 7 edition, 2019.

[105] Mark Fox. Chapter 5: Luminescence. In *Optical Properties of Solids 2nd Edition*, pages 113–136. Oxford University Press, 2010.

[106] Ralph H Fowler. The analysis of photoelectric sensitivity curves for clean metals at various temperatures. *Physical review*, 38(1):45–56, 1931.

[107] Lee A DuBridge. Theory of the energy distribution of photoelectrons. *Physical Review*, 43(9):727–741, 1933.

[108] Yang Zhou and Peng Zhang. A quantum model for photoemission from metal surfaces and its comparison with the three-step model and fowler–dubridge model. *Journal of Applied Physics*, 127(16):164903–1–164903–11, 2020.

[109] Chenjie An, Rui Zhu, Jun Xu, Yaqi Liu, Xiaopeng Hu, Jiasen Zhang, and Dapeng Yu. Increase of intrinsic emittance induced by multiphoton photoemission from copper cathodes illuminated by femtosecond laser pulses. *AIP Advances*, 8(5):055225–1–055225–7, 2018.

[110] Baerbel Rethfeld, Dmitriy S Ivanov, Martin E Garcia, and Sergei I Anisimov. Modelling ultrafast laser ablation. *Journal of Physics D: Applied Physics*, 50(19):1–39, 2017.

[111] von R Kronig and J Korringa. Zur theorie der bremsung schneller geladener teilchen in metallischen leitern. *Physica*, 10(6):406–418, 1943.

[112] Maurice Glicksman. Plasmas in solids. In *Solid state physics*, volume 26, pages 275–427. Elsevier, 1971.

[113] Mark Fox. Chapter 3: Interband absorption. In *Optical Properties of Solids 2nd Edition*, pages 62–91. Oxford University Press, 2010.

[114] Andreas Othonos. Probing ultrafast carrier and phonon dynamics in semiconductors. *Journal of applied physics*, 83(4):1789–1830, 1998.

[115] Curtis Hemenway, Richard W. Henry, and Martin Caulton. The band theory of solids. In *Physical Electronics 2nd Edition*, pages 221–239. John Wiley & Sons, 1967.

[116] Y.R. Shen. Generation and detection of broadband terahertz pulses. In *Principles of Terahertz Science and Technology*, pages 51–116. Springer Science and Business Media, 2009.

[117] Mark Fox. Chapter 11: Nonlinear optics. In *Optical Properties of Solids 2nd Edition*, pages 295–326. Oxford University Press, 2010.

[118] Zhen Zhang and John T Yates Jr. Band bending in semiconductors: chemical and physical consequences at surfaces and interfaces. *Chemical reviews*, 112(10):5520–5551, 2012.

[119] Peter R Smith, David H Auston, and Martin C Nuss. Subpicosecond photoconducting dipole antennas. *IEEE Journal of Quantum Electronics*, 24(2):255–260, 1988.

[120] M Bass, PA Franken, JF Ward, and G Weinreich. Optical rectification. *Physical Review Letters*, 9(11):446, 1962.

[121] Robert W Boyd. *Nonlinear optics, 3rd Edition*. Academic press, 2008.

[122] A Rice, Y Jin, XF Ma, X-C Zhang, David Bliss, J Larkin, and M Alexander. Terahertz optical rectification from¡ 110¿ zinc-blende crystals. *Applied physics letters*, 64(11):1324–1326, 1994.

[123] Yun-Shik Lee. *Principles of terahertz science and technology*. Springer Science and Business Media, 2009.

[124] Daniel R Ward, Falco Hüser, Fabian Pauly, Juan Carlos Cuevas, and Douglas Natelson. Optical rectification and field enhancement in a plasmonic nanogap. *Nature nanotechnology*, 5(10):732–736, 2010.

[125] Kotaro Kajikawa, Yusuke Nagai, Yuichi Uchiho, Gopakumar Ramakrishnan, Nishant Kumar, Gopika KP Ramanandan, and Paul CM Planken. Terahertz emission from surface-immobilized gold nanospheres. *Optics letters*, 37(19):4053–4055, 2012.

[126] Qi Wu and X-C Zhang. Free-space electro-optic sampling of terahertz beams. *Applied Physics Letters*, 67(24):3523–3525, 1995.

[127] Mark Fox. Chapter 2: Classical propagation. In *Optical Properties of Solids 2nd Edition*, pages 28–57. Oxford University Press, 2010.

[128] Jelic Vedran. *Imaging Ultrafast Dynamics on the Atomic Scale with a Terahertz Scanning Tunneling Microscope*. PhD thesis, University of Alberta, Edmonton, AB, Canada, Spring 2018.

[129] Unknown. *MODEL SR830 DSP Lock-In Amplifier*. Stanford Research Systems Inc., Sunnyvale, California, United States of America, 1993.

[130] Takeshi Yasui, Eisuke Saneyoshi, and Tsutomu Araki. Asynchronous optical sampling terahertz time-domain spectroscopy for ultrahigh spectral resolution and rapid data acquisition. *Applied Physics Letters*, 87(6):061101–1–061101–3, 2005.

[131] Peter B Johnson and R. W. Christy. Optical constants of the noble metals. *Physical review B*, 6(12):4370–4379, 1972.

[132] Unknown. *FP600ERT Specification Sheet*. Thorlabs, Newton, New Jersey, United States of America, 2022.

[133] Unknown. *FT1000EMT Specification Sheet*. Thorlabs, Newton, New Jersey, United States of America, 2022.

[134] Unknown. *DET210-High Speed Silicon Detector Specification Sheet*. Thorlabs, Newton, New Jersey, United States of America, 2005.

[135] Ivan Pelant and Jan Valenta. Chapter 2: Experimental techniques of luminescence spectroscopy. In *Luminescence Spectroscopy of Semiconductors*, pages 9–78. Oxford University Press, 2012.

[136] Chunli Gao, Qi Min, Jinzhu Liu, Susu Hu, Ying Du, Yanhong Wu, Shiquan Cao, Duixiong Sun, Chenzhong Dong, and Maogen Su. Time evolution of copper-aluminum alloy laser-produced plasmas in vacuum. *Journal of Quantitative Spectroscopy and Radiative Transfer*, 274:107855, 2021.

[137] N Konjević and WL Wiese. Experimental stark widths and shifts for spectral lines of neutral and ionized atoms. *Journal of physical and chemical reference data*, 19(6):1307–1385, 1990.

[138] Scipy api documentation. https://docs.scipy.org/doc/scipy/reference/. Accessed: 2023-05-11.

[139] Ilja Mingareev and Alexander Horn. Time-resolved investigations of plasma and melt ejections in metals by pump-probe shadowgrpahy. *Applied Physics A*, 92(4):917–920, 2008.

[140] JR Freeman, SS Harilal, PK Diwakar, B Verhoff, and A Hassanein. Comparison of optical emission from nanosecond and femtosecond laser produced plasma in atmosphere and vacuum conditions. *Spectrochimica Acta Part B: Atomic Spectroscopy*, 87:43–50, 2013.

[141] Qingyu Lin, Xu Wang, Guanghui Niu, Hongjun Lai, Xiaoqin Zhu, Kunping Liu, Tao Xu, and Yixiang Duan. Angular-based spatially resolved laser-induced breakdown spectroscopy: a new technique for the effective enhancement of signals without an external time delay system. *Chinese science bulletin*, 59:3377–3384, 2014.

[142] David J. Griffiths. Chapter 9: Electromagnetic waves. In *Introduction to Electrodynamics*, pages 382–435. Pearson, 4 edition, 2012.

[143] David J. Griffiths. Chapter 3: Potentials. In *Introduction to Electrodynamics*, pages 113–166. Pearson, 4 edition, 2012.

[144] Mark Fox. Appendix b: Quantum theory of radiative absorption and emission. In *Optical Properties of Solids 2nd Edition*, pages 340–347. Oxford University Press, 2010.

[145] David J. Griffiths. Chapter 11: Radiation. In *Introduction to Electrodynamics*, pages 466–501. Pearson, 4 edition, 2012.

[146] Curtis Hemenway, Richard W. Henry, and Martin Caulton. Bound particles. In *Physical Electronics 2nd Edition*, pages 15–32. John Wiley & Sons, 1967.

[147] DJ Cook and RM Hochstrasser. Intense terahertz pulses by four-wave rectification in air. *Optics letters*, 25(16):1210–1212, 2000.

[148] Hans R. Griem. Thermodynamic equilibrium and statistical mechanics. In *Principles of Plasma Spectroscopy*, pages 187–220. Cambridge University Press, 1996.

[149] Carlos Aragón and Jose Antonio Aguilera. Characterization of laser induced plasmas by optical emission spectroscopy: A review of experiments and methods. *Spectrochimica Acta Part B: Atomic Spectroscopy*, 63(9):893–916, 2008.

[150] Sun Kwok. Fundamental concepts of radiation. In *Physics and Chemistry of the Interstellar Medium*, pages 21–49. University Science Books, 2007.

[151] John D Hey. Criteria for local thermal equilibrium in non-hydrogenic plasmas. *Journal of Quantitative Spectroscopy and Radiative Transfer*, 16(1):69–75, 1976.

[152] JF Kephart, RP Godwin, and GH McCall. Bremsstrahlung emission from laser-produced plasmas. *Applied Physics Letters*, 25(2):108–109, 1974.

[153] J Yu, Z Jiang, JC Kieffer, and A Krol. Hard x-ray emission in high intensity femtosecond laser–target interaction. *Physics of plasmas*, 6(4):1318–1322, 1999.

[154] Sun Kwok. Continuum radiation in the gas phase. In *Physics and Chemistry of the Interstellar Medium*, pages 171–172. University Science Books, 2007.

[155] C Hirlimann. Pulsed optics. In *Femtosecond Laser Pulses: Principles and Experiments 2nd Edition*, pages 31–32. Springer, 2005.

Appendix A

Local Thermodynamic Equilibrium in Laser-Induced Breakdown Spectroscopy

Before discussing LTE in detail it helps to define what is meant by thermodynamic equilibrium (TE) first as LTE is a sub-case of TE. When a plasma exists in TE, the whole system composed of electrons, atoms, ions, and radiation can be fully described by statistical mechanics, where the equilibrium distributions are characterized by the same temperature [20]. Under TE, the interactions in the plasma can be described by the Maxwell-Boltzmann distribution and the moments thereof [19],

$$f(v) = n\left(\frac{m_s}{2\pi k_B T}\right)^{3/2} \exp\left[-\frac{mv^2}{2k_B T}\right]. \tag{A.1}$$

In a multi-species plasma eqn. A.1 holds for all species under TE [19]. If TE exists, then the atomic state distribution function (ASDF), is described by the Boltzmann distribution [20; 148],

$$n_j = n_s \frac{g_j \exp(-\beta E_j)}{\mathcal{Z}(T)}. \tag{A.2}$$

Where n_j is the population of the $j-th$ principle quantum number level, $\beta = (k_B T)^{-1}$, and g_j is is the quantum degeneracy of the $j-$th level, and $\mathcal{Z}(T)$ is the partition function of the

atomic level system [20; 148]. $\mathcal{Z}(T)$ given by [148],

$$\mathcal{Z}(T) = \sum_j g_j \exp(-\beta E_j). \tag{A.3}$$

Under TE, the population of different ionization stages, under typical LIBS conditions is described by the Saha equation [20; 149],

$$n_e \frac{n^{(Z)}}{n^{(Z-1)}} = \frac{2}{\lambda_e^3} \frac{\mathcal{Z}^{(Z-1)}(T)}{\mathcal{Z}^{(Z)}(T)} \exp\left(\beta \left[E_\infty^{(Z-1)} - \Delta E_\infty^{(Z-1)}\right]\right). \tag{A.4}$$

Here (Z) and $(Z-1)$ refers to the (Z)-th ionization and the $(Z-1)$ ionization levels while $\Delta E_\infty^{(Z-1)}$ is the correction quantity for interactions in plasmas [20; 149]. While λ_t is the thermal de-Broglie length [83],

$$\lambda_t = \sqrt{\frac{2\pi\beta\hbar^2}{m}} = \sqrt{\frac{2\pi\hbar^2}{m k_B T}}.$$

Eqn. A.4 gives a means by which two ionic lines (or one neutral line and an ionic line) maybe related to one another and can be used to estimate the electron and ionic densities within the plasma. Under TE, the photon energy is described by a Planck function given by [144; 150],

$$u(\omega, T) = \frac{\hbar\omega^3}{\pi^2 c^3} \frac{1}{e^{\beta\hbar\omega} - 1}. \tag{A.5}$$

As can be inferred from eqn. A.1 - A.5 and stated earlier, under TE the temperature of the ions, electrons, atoms, and photons emitted from the plasma all can be described by a characteristic temperature T, i.e., $T_e = T_i = T_A = T_\omega$ [20]. This can occur provided that the Principle of Detailed Balance (PDB) holds [20; 83].

The PDB states that for a dilute gas under TE, for every initial state i and final state f, each reaction $i \to f$ is exactly counterbalanced by its inverse reaction $f \to i$ [20; 83]. As J. Oxenius describes in ref. [83] the PDB has the following corollaries: (1) global balancing in both reactions and velocity ranges, (2) the reciprocity relations hold, and (3) sufficiently low density of gas [83]. To elaborate further, (1) implies there is not just global balancing in the reactions (e.g. $\mathrm{H}(2p) + \mathrm{e} \leftrightarrows \mathrm{H}(3d) + \mathrm{e}$) but balancing in the velocity range of the particles

involved [83]. Corollary (2) entails that the validity of the PDB depends on the validity of the quantum mechanical reciprocity relation $w(i \to f) = w(f \to i)$ [83]. Where $w(i \to f)$ is the transition probability per unit time for the transition $|i\rangle \to |f\rangle$ between quantum states i and f [83]. Corollary (3) stipulates that the density of gas must be sufficiently low enough so that the particle quantum states are well defined and the state of the gas as a whole is specified by the occupation numbers of one-particle states [83].

Provided that all three points are met the PDB is fulfilled, and the plasma can be said to exist within a state of TE [83]. This enables one to use methods from statistical mechanics to characterize the dynamics of the plasma. As noted by Cristoferreti et al, when photons escape from typical laboratory plasmas, their energy deviates from the Planck function given by eqn. A.5 [20]. However, if the energy lost by radiation is smaller than what is involved in the other processes eqn. A.1-A.4 are still valid descriptions of the system and a new equilibrium is established where-in $T_e = T_i = T_A \neq T_\omega$ [20; 83]. LTE in this regard can be viewed then as claiming that the particles composing the plasma are in TE with each other while the photons emitted are not in TE, thus LTE refers strictly to the particles within the plasma but not the photons [83; 95]. This can be met provided that the following criteria hold which is discussed in the next section.

A.1 Local Thermodynamic Equilibrium Considerations

The criteria for LTE in an inhomogenous transient plasma at its most general can be stated as the following set of conditions [20; 95],

$$\frac{|n_e(t+\tau) - n_e(t)|}{n_e(t)} \ll 1 \quad \frac{|T(t+\tau) - T(t)|}{T(t)} \ll 1 \tag{A.6}$$

$$\frac{|n_e(r) - n_e(r+d)|}{n_e(r)} \ll 1 \quad \frac{|T(r) - T(r+d)|}{T(r)} \ll 1 \tag{A.7}$$

. Where d and τ is the equilibrium length and equilibriation time-scale between two energy levels defined in ref. [95]. What criteria A.6-A.7 imply is that variation in temperature and electron density with time and distance are so minimal, that for all intents in purposes they do not exist. Under criteria A.6-A.7 the plasma is in a temporal steady state that is spatially

uniform and the relationship between ion populations in the Z and $Z-1$ states is given by eqn. A.4 and is termed complete LTE (CLTE) [80]. In CLTE collisional depopulation processes dominate over radiative depopulation processes $\sim 10\times$ [95]. For optically thin plasmas CLTE occurs if the electron density is such that [95],

$$n_e \gtrsim 9.2 \times 10^{17} Z^7 \sqrt{\frac{k_B T}{E_H^{(Z)}}} \left(\frac{E_2 - E_1}{E_H^{(Z)}} \right)^3 \left[\mathrm{cm}^{-3} \right] . \tag{A.8}$$

Where $E_H^{(Z)} = Z^2 \mathrm{e}^2 / 2a_0$ is the ionization energy of the hydrogenic ion [95]. Note criterion A.8 could be further relaxed by an order of magnitude if that resonance line is self-absorbing [95]. For optically thick plasmas CLTE occurs if the electron density is such that [95],

$$n_e \gtrsim 10^{17} Z^7 \sqrt{\frac{k_B T}{E_H^{(Z)}}} \left(\frac{E_2 - E_1}{E_H^{(Z)}} \right)^3 \left[\mathrm{cm}^{-3} \right] . \tag{A.9}$$

However, criteria A.8 - A.9 are fulfilled only for plasmas consisting of a singly ionized species [81; 95]. To remedy this, John D. Hey introduced an effective gaunt factor $\langle g \rangle$ which he defines as [151],

$$\langle g \rangle \equiv \exp\left(\frac{E_{j'} - E_j}{k_B T_e} \right) \int_{\frac{1}{2} m v_0^2}^{+\infty} g \exp\left(-\frac{m v_i^2}{2 k_B T_e} \right) d \left(\frac{m v_i^2}{2 k_B T_e} \right)$$

and re-wrote criterion A.8-A.9 as [151],

$$n_e \gtrsim \frac{2.55 \times 10^{17}}{\langle g \rangle} \sqrt{\frac{k_B T_e}{E_H}} \left(\frac{E_2 - E_1}{E_H} \right)^3 \left[\mathrm{cm}^{-3} \right] . \tag{A.10}$$

Hey's formalism though neglects the possible existence of metastable levels lying between the ground state and the upper level of the resonance line which occurs widely in many atomic species [151] (in the same paper though he does generalize to metastable states see ref. [151]). This list of criterion may seem rather strange at first glance as typically what is quoted in the literature is not the names of Hey and Griem and their criterion but McWhirter. This is because confusingly all three of the aforementioned criteria are all called McWhirter criteria [18]. These McWhirter criterion tend to vary between authors (compare ref. [20] to [18]).

Yet even if CLTE mentioned here fails to hold this does not mean that the LTE approximation cannot be applied. The LTE model and eqn. A.1 - A.4 can still hold provided that the majority of atoms occupy a set of sufficiently highly excited states. The critical quantum number associated with the minimal state above which the excited atoms in a plasma must occupy was derived by Byron et al is [80–82],

$$j_B = \left(\frac{Z^2 R_H}{3k_B T}\right)^{1/2} = \left(\frac{Z^2 E_H}{3k_B T}\right)^{1/2}. \tag{A.11}$$

Where R_H is the Rydberg constant and E_H is the ground state ionization energy of the hydrogen atom. It is at j_B (termed here as the "Byron level") that rapidly colliding electrons become comparable to the energy $k_B T$ [81]. If the majority of excited atoms are in a state with principle quantum number j exist at or above j_B then (i.e. if $j \geq j_B$) there exists a partial local thermodynamic equilibrium (PLTE) [80; 81]. Practically what this entails is that for plasmas whom the majority of excited atomic species exist at or above the Byron level the deviations from eqn. A.4 are only $\pm 10\%$ [80; 81]. While there have been subsequent corrections to Byron et al's definition of what the critical principle quantum number is (see ref. [80; 81]); it's worth repeating here in the original form as it captures fundamentally the same physics as later corrections and gives PLTE a definition that ties it back to atomic transitions within the plasma. If a plasma is said to exist within PLTE the electron density is such that [95],

$$n_e \gtrsim 7.4 \times 10^{18} \frac{Z^7}{j^{17/2}} \left(\frac{k_B T}{E_H^{(Z)}}\right) \quad \left[\mathrm{cm}^{-3}\right] \tag{A.12}$$

. Criterion A.12 holds for helium, hydrogen and in hydrogenic atoms in states $j \geq j_B$ [81; 95]. It is worth noting though that Griem in his monograph (see ref. [81]) mentions that there is still controversy surrounding a McWhirter criterion for PLTE [81]. Even if a criteria in the style of Griem, Hey and McWhirter is agreed upon, there is no guarantee that the LTE approximation even holds partially [20].

This is because the McWhirter criteria regardless of their form, are a necessary but not sufficient condition for the existence of LTE, as the criterion listed in A.6 - A.7 must still hold. It is fully possible to satisfy the McWhirter criterion but fail criteria A.6 - A.7. In the

case of criteria A.6 plasma plume evolution could be too fast, resulting in electrons and the atoms not reaching thermodynamic equilibrium, for this reason Cristoferreti has cautioned against measurements with a detection delay-time shorter than 1.3 μs for at least the case of nanosecond ablation [20]. Lastly, for multi-element plasmas, there exists the bizarre case of LTE holding for some elements, but not others [20]. It is for this reason that Griem defined a diffusion length d that must be shorter than the variation length over the relaxation time [20; 95]. If even one of the constituents of a multi-element plasma violates criterion A.7, the plasma as a whole is no longer in LTE as the constituent is far exceeding the diffusion length over the relaxation time , implying a non-thermal process [20; 95]. Even for the case of homogeneous and stationary plasmas, high ionization degree of the plasma after breakdown causes an imbalance between the ionization and recombination processes, violating the PDB, resulting in strong deviations from eqn. A.4; forcing researchers to choose gating times on the order of the relaxation time [20].

Thus, with regards to LTE the McWhirter criterion can only describe if it does not exist, not if it does exist. Furthermore there are certain ranges over which LTE maybe an appropriate description but breakdown at earlier and later times (see ref. [18]). The important thing to note is that it is not sufficient to verify the LTE state with the McWhirter criteria, it must be used in conjunction with other methods before the LTE approximation can be applied. LIBPs spectra from later or earlier times and multi-element plasmas, should therefore be approached with caution. To quote verbatim Cristoforetti in his 2010 review, "Considering the characteristics of many laser-induced plasmas [LIBPs], the right question should be not whether equilibrium conditions exist, but rather how far we are from equilibrium [20]."

Appendix B

Light Emission Processes in Laser-Induced Breakdown Plasmas

LIBPs have three main mechanisms by which emission of light can occur: free-free radiation (FFRs) (i.e. Bremsstrahlung Emission), free-bound transitions (FBTs) (a.k.a Radiative Recombination), and bound-bound transitions (BBTs) (a.k.a Spontaneous/Stimulated Emission) [12; 99]. Another prominent mechanism is dielectronic recombination [99]. However, this process is similar to FBTs and is ommitted here for the sake of brevity; see ref. [99] for details.

FFR is the radiation emitted by a light particle (typically an electron) is deflected by another heavier particle (e.g. ions and/or neutral atoms). This occurs because a sudden change in the particles momenta leads to the emission of light, hence it's alternate name *Bremsstrahlung radiation* which from German translates literally into English as "breaking radiation" [99]. For the case of an electron interacting with a heavier particle the conservation of energy reads [99],

$$\frac{1}{2}m_e v_i^2 = \frac{1}{2}m_e v_f^2 + \hbar\omega. \tag{B.1}$$

A FFR process has a reaction given by [99],

$$A + \mathrm{e}\,(v_i) \longrightarrow A + \mathrm{e}\,(v_f) + \hbar\omega \quad \text{where} \quad v_i > v_f.$$

Where A is some heavy particle (usually an atom) [99]. For a pictorial representation of

FFR see fig. B.1. Under local thermodynamic equilibrium (LTE), FFR is balanced by its inverse process: free-free absorption or Inverse Bremsstrahlung [99]. For free-free absorption the process is [99]:

$$A + \mathrm{e}\,(v_i) + \hbar\omega \longrightarrow A + \mathrm{e}\,(v_f) \quad \text{where} \quad v_i > v_f.$$

FFR contributes to both broad spectrum continuum emission and X-ray radiation [96; 152–154]. Free-bound transitions or radiative recombination occurs when an electron recombines

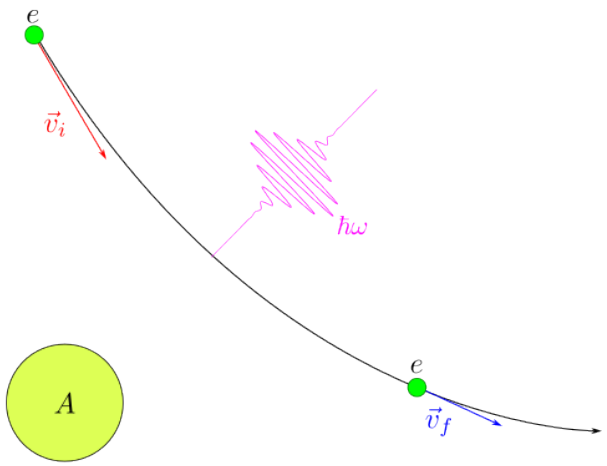

Figure B.1: Pictorial representation of free-free emission. The electron's trajectory is altered by the atom resulting in a deflection which changes the kinetic energy of the electron resulting in the emission of light with energy given by eqn. B.1.

with an ion forming a neutral atom resulting in the emission of a photon with an energy given by [99; 154],

$$\hbar\omega = \frac{1}{2}m_e v^2 + \frac{\hbar\omega_1}{j^2}. \tag{B.2}$$

Where j is the the $j-$th energy level [154]. A FBT process has a reaction given by [99],

$$A^+ + \mathrm{e}\,(v) \longrightarrow A + \hbar\omega.$$

Under LTE, a FBT is balanced by its inverse process: photoionization. For photoionization the process is [99]:

$$A + \hbar\omega \longrightarrow A^+ + \mathrm{e}\,(v)\,.$$

Pictorially, a FBT looks like fig. B.2. FBT emits light over a broad range of wavelengths contributing to the continuum emission seen in many LIBS experiments [96; 154].

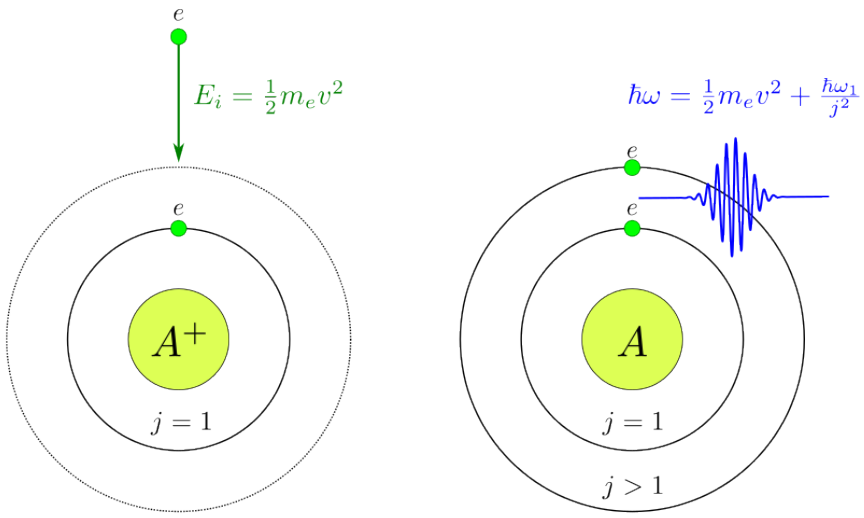

Figure B.2: Pictorial representation of free-bound emission. In this picture, an electron is absorbed by an ion A^+ at some outer energy level $j > 1$ leading to the emission of light equal to eqn. B.2.

BBTs in contrast to FFE or FBTs radiation emitted in a BBT is not continuous but discrete [83]. This is because emission from BBT corresponds to transitions between some excited energy level j' to a lower energy level j over some radiative lifetime of the excited state τ within atomic species [83]. In this description, BBTs are nothing more than stimulated/spontaneous emission processes and the light emitted from them is given by the difference between energy levels $\hbar\omega = E_{j'} - E_j$ which occur within the excited atoms and molecules inside the plasma [83]. For a pictorial representation see fig. B.3. Of the three processes just described only FFE or FBT have the potential to produce THz emission as they are both the primary contributors to continuum emission which by definition includes THz radiation, while BBT maps to discrete atomic transitions within an excited atom. However based on spectral emission alone, one would not be able to detect THz radiation from a LIBP because of the predominance of continuum emission as it would be "smeared out" in the THz range and would be fundamentally indistinguishable from the background. Note this does not mean though that THz emission cannot be seen from a plasma, just not using

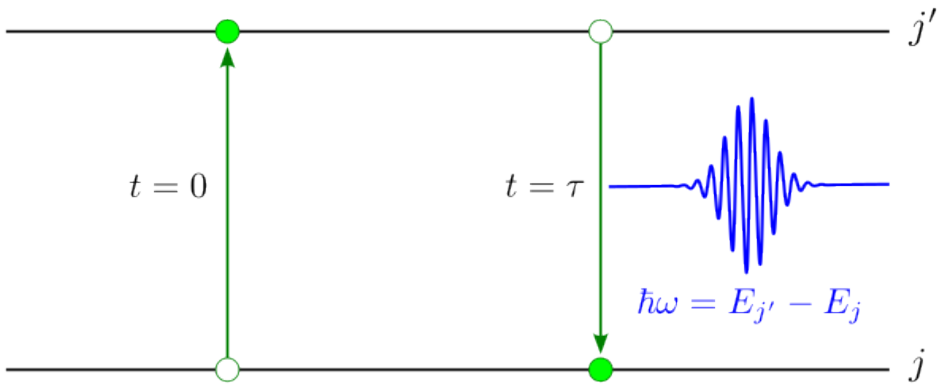

Figure B.3: Pictorial representation of a bound-bound transition process. BBTs give rise to the lines seen in a LIBS spectrum and correspond to intra-atomic transitions. The energy emitted after some relaxation time, τ, by these intra-atomic transitions is $\hbar\omega = E_{j'} - E_j$, where j' is the upper energy level and j is the lower energy level.

LIBS.

Appendix C

Optical Properties of a Plasma Slab

Calculating the optical properties of the LIBP plume required first a calculation of the conductivity which is given by [35],

$$\tilde{\sigma} = \frac{\sigma_0}{1 + (\omega\tau)^2} + i\frac{\sigma_0\omega\tau}{1 + (\omega\tau)^2} = \sigma_1 + i\sigma_2 \quad \text{where} \quad \sigma_0 = \frac{n_e e^2 \tau}{m_e}. \tag{C.1}$$

Where ω is the angular frequency and τ is the collisional time provided by eqn. 2.15-2.16 [103],

$$\Pi_{e,i} = 23 - \ln\left(Z\sqrt{\frac{n_e}{T_e}}\right) \quad \text{where} \quad T_i\frac{m_e}{m_i} < T_e < 10Z^2 \ \text{eV}$$
$$\tau \simeq 3.44 \times 10^5 \frac{T_e^{3/2}}{n_e \Pi_{e,i}}.$$

Once $\tilde{\sigma}$ is known the real and imaginary components of the dielectric constant, ϵ_1 and ϵ_2 respectively, can be calculated according to [35],

$$\tilde{\epsilon} = 1 - \frac{\sigma_2}{\epsilon_0\omega} + i\frac{\sigma_1}{\epsilon_0\omega} = \epsilon_1 + i\epsilon_2. \tag{C.2}$$

From the results of eqn. C.2, it is then possible to calculate the indicies of refraction, n_1 & n_2 2.17,

$$n_1 = \frac{1}{\sqrt{2}}\left(\sqrt{\epsilon_1^2 + \epsilon_2^2} + \epsilon_1\right)^{1/2}, \quad n_2 = \frac{1}{\sqrt{2}}\left(\sqrt{\epsilon_1^2 + \epsilon_2^2} - \epsilon_1\right)^{1/2}.$$

The results of 2.17 can then be used to calculate the reflectivity R and transmissivity T_t given by eqn. 2.18 [102],

$$R = \frac{(n_1 - 1)^2 + n_2^2}{(n_1 + 1)^2 + n_2^2}, \quad T_t = \frac{(1 - R)^2\, \mathrm{e}^{-\alpha l}}{1 - R^2 \mathrm{e}^{-2\alpha l}}.$$

The penetration depth, δ, is then [102],

$$\delta = \frac{c}{2n_2\omega} = \frac{c}{4\pi n_2 f} = \frac{1}{\alpha}$$

The plots of eqn. C.1-C.2 are shown in fig. C.1-C.2.

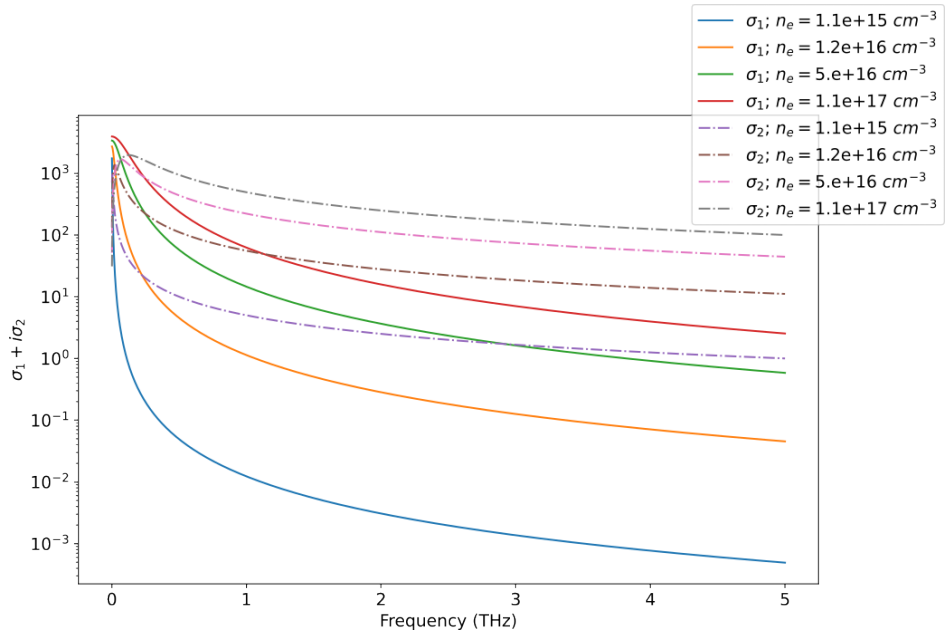

Figure C.1: The real and imaginary components of the LIBP conductivity calculated according to eqn.C.1 over the bandwidth of the ZnTe used in this thesis. These results could then be fed into eqn.C.2 to obtain the dielectric constant over the same frequency range.

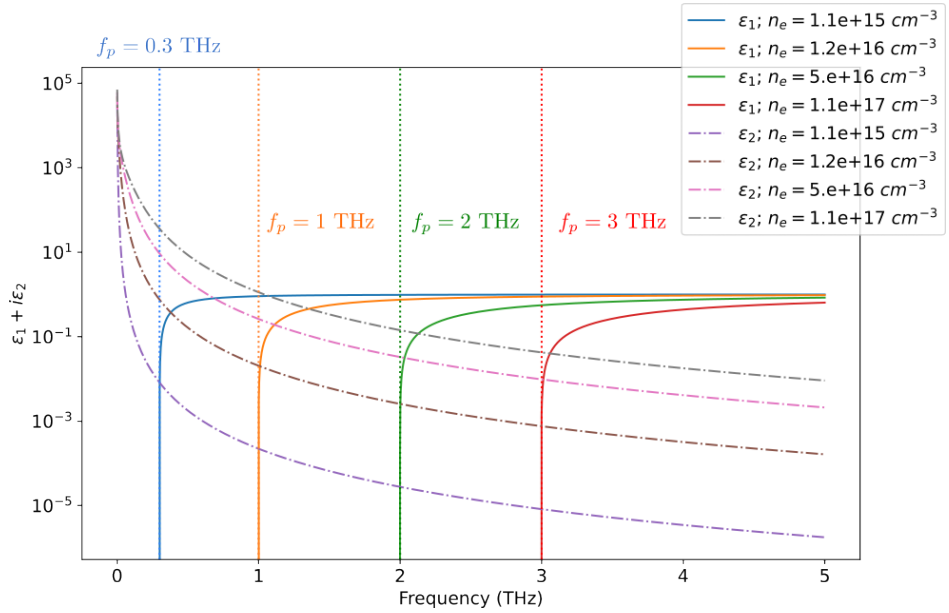

Figure C.2: The real and imaginary components of the dielectric constant calculated according to eqn.C.2 over the bandwidth of the ZnTe used in this thesis. These results could then be fed into eqn.2.17 to obtain the refractive indicies over the same frequency range. Note, how at the plasma frequency, f_p the real component over-takes the imaginary component.

Appendix D

Derivations

D.1 Derivation of The Plasma PL-response Signal (eqn. 5.2)

It was assumed that the time integrated PL shown in fig. 5.3 decays exponentially,

$$I_{\mathrm{PL}} \propto e^{-t/\tau_0}$$

The response of the scope is Gaussian in nature ergo, any resulting curve can be thought of as the convolution of a Gaussian and an exponential decay, therefore,

$$\begin{aligned} I(t) = g(t) * I_{\mathrm{PL}}(t) &= A_0 \int_{-\infty}^{+\infty} d\tau \theta(\tau - t_0) \exp\left[-\frac{(t-\tau-t_0)^2}{2t_w^2}\right] \exp\left[-\frac{\tau}{\tau_0}\right] \\ &= g(t) * I_{\mathrm{PL}}(t) = A_0 \int_{t_0}^{+\infty} d\tau \exp\left[-\frac{(t-\tau-t_0)^2}{2t_w^2}\right] \exp\left[-\frac{\tau}{\tau_0}\right]. \end{aligned}$$

Here $\theta(\tau - t_0)$ is the Heaviside step function & A_0 is some constant with units of mV/ns. Performing the substitution $\tau' = \tau + t_0$ and centering the time window at t_0 gives the integral,

$$I(t) = g(t) * I_{\mathrm{PL}}(t) = A_0 \int_0^{+\infty} d\tau' \exp\left[-\frac{(t-\tau')^2}{2t_w^2}\right] \exp\left[-\frac{\tau' - t_0}{\tau_0}\right]$$
$$= A_0 \int_0^{+\infty} d\tau' \exp\left[-\frac{(t-\tau')^2}{2t_w^2} - \frac{\tau' - t_0}{\tau_0}\right] = A_0 e^{t_0/\tau_0} \int_0^{+\infty} d\tau' \exp\left[-\frac{(t-\tau')^2}{2t_w^2} - \frac{\tau'}{\tau_0}\right]$$
$$= A_0 e^{t_0/\tau_0} \int_0^{+\infty} d\tau' \exp\left[-\frac{1}{2t_w^2}\left((t-\tau')^2 + \frac{2t_w^2\tau'}{\tau_0}\right)\right] = A_0 e^{t_0/\tau_0} \int_0^{+\infty} d\tau' \exp\left[-\frac{p(\tau')}{2t_w^2}\right].$$

Next, rewrite $p(\tau')$ by completing the square,

$$p(\tau') = (t-\tau')^2 + \frac{2t_w^2}{\tau_0}\tau' = t^2 - 2t\tau' + \tau'^2 + \frac{2t_w^2\tau'}{\tau_0} = t^2 - 2t\tau' + \frac{2t_w^2\tau'}{\tau_0} + \tau'^2$$
$$= t^2 - \left(2t - \frac{2t_w^2}{\tau_0}\right)\tau' + \tau'^2 = \left(\tau' + \frac{1}{2}\left(2t - \frac{2t_w^2}{\tau_0}\right)\right)^2 - \frac{1}{4}\left(2t - \frac{2t_w^2}{\tau_0}\right)^2 + t^2$$
$$= \left(\tau' + \left(t - \frac{t_w^2}{\tau_0}\right)\right)^2 - \left(t - \frac{t_w^2}{\tau_0}\right)^2 + t^2$$
$$\therefore p(\tau') = \left(\tau' + \left(t - \frac{t_w^2}{\tau_0}\right)\right)^2 - \left(t - \frac{t_w^2}{\tau_0}\right)^2 + t^2$$

Substituting back into the integral gives,

$$I(t) = A_0 e^{t_0/\tau_0} \int_0^{+\infty} d\tau' \exp\left[-\frac{p(\tau')}{2t_w^2}\right]$$
$$= A_0 \mathrm{e}^{t_0/\tau_0} \int_0^{+\infty} d\tau' \exp\left[-\frac{1}{2t_w^2}\left(\left(\tau' + \left(t - \frac{t_w^2}{\tau_0}\right)\right)^2 - \left(t - \frac{t_w^2}{\tau_0}\right)^2 + t^2\right)\right]$$
$$= A_0 \mathrm{e}^{t_0/\tau_0} \exp\left[\frac{1}{2t_w^2}\left(t - \frac{t_w^2}{\tau_0}\right)^2 - \frac{t^2}{2t_w^2}\right] \int_0^{+\infty} d\tau' \exp\left[-\frac{1}{2t_w^2}\left(\tau' + \left(t - \frac{t_w^2}{\tau_0}\right)\right)^2\right]$$
$$= A_0 \mathrm{e}^{t_0/\tau_0} \exp\left[\frac{1}{2t_w^2}\left(t^2 - 2t\frac{t_w^2}{\tau_0} + \frac{t_w^4}{\tau_0^2}\right) - \frac{t^2}{2t_w^2}\right] \int_0^{+\infty} d\tau' \exp\left[-\frac{1}{2t_w^2}\left(\tau' + \left(t - \frac{t_w^2}{\tau_0}\right)\right)^2\right]$$
$$= A_0 \exp\left[\frac{t_0}{\tau_0} - \frac{t}{\tau_0} + \frac{t_w^2}{2\tau_0^2}\right] \int_0^{+\infty} d\tau' \exp\left[-\frac{1}{2t_w^2}\left(\tau' + \left(t - \frac{t_w^2}{\tau_0}\right)\right)^2\right]$$
$$I(t) = A_0 \exp\left[\frac{t_0}{\tau_0} - \frac{t}{\tau_0} + \frac{t_w^2}{2\tau_0^2}\right] I(\tau')$$

The task is to now evaluate $I(\tau')$ or cast it into the form of an integral that is a definition of a known function. To do this, re-write the integral over the original domain from t_0 to ∞:

$$I(\tau') = I(\tau + t_0) = \int_{t_0}^{+\infty} d\tau \exp\left[-\frac{1}{2t_w^2}\left(\tau + t_0 + \left(t - \frac{t_w^2}{\tau_0}\right)\right)^2\right]$$

This integral is similar in form to the definition of the error function,

$$\text{erf}(x) = 1 - \frac{2}{\sqrt{\pi}}\int_x^{+\infty} du e^{-u^2} \implies \int_x^{+\infty} du e^{-u^2} = \frac{\sqrt{\pi}}{2}\left(1 - \text{erf}(x)\right).$$

By the definition above (using an appropriate substitution), the resulting integral is,

$$I(\tau + t_0) = \frac{\sqrt{2\pi}}{2}\left(1 + \text{erf}\left[\frac{\sqrt{2}}{2}\left(\frac{t}{t_w} - \frac{2t_0}{t_w} - \frac{t_w}{t_0}\right)\right]\right).$$

This means that altogether,

$$I(t) = \frac{\sqrt{2\pi}}{2} A_0 \exp\left[\frac{t_0}{\tau_0} - \frac{t}{\tau_0} + \frac{t_w^2}{2\tau_0^2}\right]\left(1 + \text{erf}\left[\frac{\sqrt{2}}{2}\left(\frac{t}{t_w} - \frac{2t_0}{t_w} - \frac{t_w}{t_0}\right)\right]\right)$$

$$\therefore I(t) = I_0 e^{-\frac{t}{\tau_0}}\left(1 + \text{erf}\left[\frac{\sqrt{2}}{2}\left(\frac{t}{t_w} - \frac{2t_0}{t_w} - \frac{t_w}{t_0}\right)\right]\right)$$

Which is identical to eqn. 5.2.

D.2 Derivation of the Gaussian Pulse Bandwidth Relation (eqn. 4.8)

The relationship between frequency and time in a Gaussian pulse is constrained by the inequality [155],

$$\tau_p \Delta f \geq 0.441. \tag{D.1}$$

Taking expression D.1 to be equal gives τ_p as,

$$\tau_p = \frac{0.441}{\Delta f}. \tag{D.2}$$

The task is now to determine the relationship between Δf and $\Delta\lambda$. This is so that an equivalent expression to eqn. D.2 in terms of $\Delta\lambda$ maybe found. To do so consider the relation, $\lambda = c/f$, taking the absolute value of the derivative with respect to f gives,

$$\frac{\mathrm{d}\lambda}{\mathrm{d}f} = \frac{\mathrm{d}}{\mathrm{d}f}\left(\frac{c}{f}\right) = -\frac{c}{f^2} = -\frac{\lambda}{f} \implies \left|\frac{\mathrm{d}\lambda}{\mathrm{d}f}\right| = \frac{\lambda}{f}$$

Taking the limit as $\mathrm{d}\lambda \longrightarrow \infty$ and $\mathrm{d}f \longrightarrow \infty$ gives,

$$\frac{\Delta\lambda}{\Delta f} = \frac{\lambda}{f} \implies \frac{\Delta\lambda}{\lambda} = \frac{\Delta f}{f} \implies \therefore \frac{1}{\Delta f} = \frac{\lambda}{f\Delta\lambda} = \frac{\lambda_0^2}{c\Delta\lambda} \tag{D.3}$$

Eqn. D.3 then allows one to write eqn. D.2 as,

$$\tau_p = \frac{0.441}{\Delta f} = 0.441\frac{\lambda^2}{c\Delta\lambda} \tag{D.4}$$

Which is identical to eqn. 4.8.